A New Technique for Characterizing Multi-Temperature Convection with Application in Building Energy Simulation

by

Seyed Sepehr Mohaddes Foroushani

A thesis
presented to the University of Waterloo
in fulfillment of the
thesis requirement for the degree of
Doctor of Philosophy
in
Mechanical and Mechatronics Engineering

Waterloo, Ontario, Canada, 2017

Examining Committee Membership

The following served on the Examining Committee for this thesis. The decision of the Examining Committee is by majority vote.

External Examiner	Dr. MARILYN LIGHTSTONE Professor (McMaster University)
Supervisors	Dr. JOHN WRIGHT Professor
	Dr. DAVID NAYLOR Professor
	Dr. MICHAEL COLLINS Professor
Internal Members	Dr. GEORGE RAITHBY Professor Emeritus
	Dr. SEAN PETERSON Associate Professor
Internal-external Member	Dr. DANIEL STASHUK Professor

Author's Declaration

I hereby declare that I am the sole author of this thesis. This is a true copy of the thesis, including any required final revisions, as accepted by my examiners.

I understand that my thesis may be made electronically available to the public.

Abstract

Glazing systems with attachments such as shades and insect screens are known as complex fenestration systems (CFS). The ASHRAE Window Attachment Tool (ASHWAT) for modeling heat transfer through a CFS are based on a general network of thermal resistors. In these models, convective heat transfer at the indoor side of a CFS with an indoor-mounted attachment is represented by a delta resistor-network. The heat transfer coefficients that characterize this network cannot be calculated using the conventional methods, i.e. based only on the knowledge of the total heat transfer rates at the temperature nodes. Currently, approximate relations based on known limits and experience are used in ASHWAT to estimate the indoor-side convection coefficients.

The CFS problem is part of the broader class of multi-temperature convection, i.e. problems entailing exclusively isothermal and adiabatic boundary conditions. Driven by the desire to calculate the convection coefficients of the CFS problem with improved accuracy, this thesis is devoted to the study of multi-temperature convection. An extension of the Newton law of cooling is proposed to formulate the multi-temperature convection problem in terms of multiple driving temperature differences. Consequently, the problem is characterized by multiple *paired* heat transfer coefficients. A technique dubbed dQdT was developed to obtain the paired heat transfer coefficients. The dQdT technique is based on a baseline solution to the full set of governing equations and subsequent solutions to the linearized energy equation with perturbed boundary conditions. dQdT can be implemented in both analytical and numerical solutions. In addition to enabling the extended Newton formulation, the dQdT technique provides a basis for determining the applicability of the resistor-network model to a convection problem. The validity of dQdT was demonstrated in several ways.

The extended Newton formulation and the dQdT technique were applied to a wide range of convection problems: forced and free convection, internal and external flows, laminar

and turbulent flows, hydrodynamically developed and hydrodynamically developing flows, constant- and variable-property flows. The extended Newton formulation was shown to be advantageous compared to the traditional formulation; it leads to a presentation of the solution that is more consistent with the physics of the problem while revealing more detail about the thermal phenomenon. Moreover, using the dQdT results improved correlations for the classical problems of convection in heated annuli and vertical channels were developed.

Finally, the dQdT technique was applied to calculate the heat transfer coefficients of the CFS problem. It was shown that while the current ASHWAT estimates are in good agreement with the dQdT results for a CFS entailing a roller blind, there is a potential for improving the ASHWAT estimates for a CFS entailing a venetian blind. Using dQdT, the convection coefficients of a wide range of CFS configurations can now be accurately calculated.

Acknowledgements

First and foremost, I would like to express my sincerest gratitude towards my supervisors, Dr. John Wright and Dr. David Naylor. Without their support, encouragement and understanding, the completion of this work would not have been nearly possible for me.

I would like to acknowledge the financial support of the NSERC Smart Net-zero Energy Buildings Strategic Research Network, the University of Waterloo and the CFD Society of Canada, which made it possible for me to fully dedicate my time, attention and energy to the research reported in this thesis.

I would also like to thank the respected examiners for reviewing this thesis and providing insightful feedback.

Finally, I would like to thank the many great teachers, peers and students whom I have had the privilege to work with and learn from.

Table of Contents

List of Figures

List of Tables

Nomenclature

A	Surface area
B	Eigencoefficient
b	Glass-shade spacing
C	Functionality coefficient
c	Local functionality coefficient
c_p	Constant-pressure specific heat
D	Diameter
D_h	Hydraulic diameter
f	Eigenfunction
Gr	Grashof number
g	Gravitational acceleration
H	Height
h	Heat transfer coefficient
k	Thermal conductivity, Turbulence kinetic energy (Chapter 9)
L	Spacing; Distance
$\dot{m}$	Mass flow rate
$\overline{\mathrm{Nu}}$	Average Nusselt number
Nu	Local Nusselt number
n	Summation index

Pe	Peclet number
Pr	Prandtl number
p	Pressure
Q	Heat transfer rate
q	Heat flux
Re	Reynolds number
r	Radius, Radial coordinate
r_T	Temperature ratio
S	Conduction shape factor
T	Temperature
u	Velocity in x-direction
v	Velocity in y- or r-direction
W	Width
w	Slat width
X	Inverse Graetz number
x	Axial/longitudinal coordinate
Y	Dimensionless lateral coordinate
y	Lateral coordinate

Greek Letters

β	Volumetric expansion coefficient
δ	Perturbation; small change
ε	Turbulence energy dissipation rate
θ	Dimensionless temperature
λ	Eigenvalue, Thermal conductivity (Chapter 9)

μ	Dynamic viscosity
ν	Kinematic viscosity
ρ	Density
ϕ	Radius ratio
ω	Specific turbulence energy dissipation rate

Subscripts

0	Free-stream/inlet/far-field flow
1	Isothermal surface
2	Isothermal surface
a	Ambient air
g	Glass/glazing
fd	Fully developed
i	The isothermal boundary at T_i
j	The isothermal boundary at T_j
ij	Paired; between i and j
m	Mean
s	Shading layer/attachment

Superscripts

(1)	Fundamental solution of the first kind
(k)	Iteration number

List of Abbreviations

ASHRAE	American Society of Heating, Refrigerating & Air-conditioning Engineers
ASHWAT	ASHRAE Window Attachment Tool
CFS	Complex Fenestration System
RHS	Right-Hand Side
SHGC	Solar Heat Gain Coefficient

Chapter 1

Introduction

1.1 The ASHWAT Models

In 2009, ASHRAE research project RP-1311 concluded with the ASHRAE Window Attachment Tool, ASHWAT (Wright et al. 2009): a comprehensive set of energy simulation models for Complex Fenestration System (CFS), i.e. glazing systems with attachments such as slat-type shades, drapes, roller blinds and insect screens. The ASHWAT project was in many aspects a success. ASHWAT predictions of solar transmission and solar heat gain coefficient (SHGC) have been compared with indoor solar simulator measurements and good agreement has been obtained (Kotey et al. 2009). The ASHWAT models have been implemented in the ASHRAE Toolkit (HBX version) and other building energy simulation software (e.g. Wright et al. 2011, Lomanowski & Wright 2012). Using ASHWAT, an extensive set of tabulated shade performance data have been generated, now appearing in the ASHRAE *Handbook of Fundamentals* (ASHRAE 2013). In addition, projects undertaken since the completion of RP-1311 have demonstrated that the ASHWAT models can be used in time-step building energy simulation with little computational cost, while retaining full design flexibility and the possibility of real-time shade operation (Wright et al. 2011, Lomanowski & Wright 2012).

A key element of ASHWAT is a very general thermal-resistor network used to calculate the overall heat transfer coefficient (U-factor) and SHGC of a CFS for any combination of indoor/outdoor temperatures (air and mean radiant), and any level/direction of incident solar flux (beam and diffuse) (Collins & Wright 2006, Wright 2008). In this network, each layer of the CFS is represented by a node at the corresponding temperature, connected to other layers (nodes) through radiative and convective thermal resistances. See Figure 1.1. In the resistor network shown in this figure, a glazing/attachment layer at T_i is connected to indoor and outdoor air through radiative (r) and convective (c) resistors. The main feature of this approach is that it allows heat transfer between a node, T_i, and *any* other node. The portion of this resistor network corresponding to the indoor side of a CFS is of interest to the present thesis.

1.2 The Delta Network

The presence of an indoor-mounted attachment adds complexities to heat transfer in a window system which must be considered in modeling. Many attachments, e.g. venetian blinds, drapery with open-weave fabric and insect screens, allow transmission of radiation — solar or longwave. Therefore, radiant exchange can take place directly between the glazing (T_i) and the indoor surfaces ($T_{\mathrm{m,in}}$), "bypassing" the attachment layer in between. Likewise, air may flow through and/or around any attachment, allowing "direct" convective heat transfer between T_i and $T_{\mathrm{a,in}}$.

In Figure 1.2, the indoor portion of the resistor network of a CFS with an indoor-mounted attachment is shown. This network pertains to the "centre-glass" region of the window, i.e. away from the frame and edge seals, wherein the temperature of the glazing layer is uniform and heat transfer can be treated as one-dimensional. This network is comprised of three nodes representing the indoor-side glass surface (T_{g}), the attachment (T_{s}), and the indoor air (T_{a}). Each pair of nodes is connected through a convective resistor.

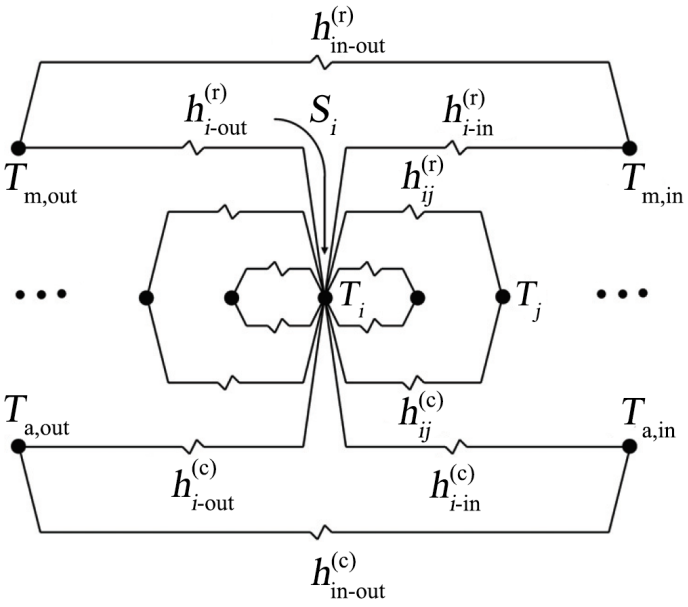

Figure 1.1: The general resistor network of ASHWAT (Wright 2008): A layer at T_i is connected to indoor and outdoor air through radiative (r) and convective (c) resistors. T_{a}: Air temperature, T_{m}: Mean radiant temperature, S_i: Solar radiation absorbed at T_i

In Figure 1.2, the convective resistors are characterized by the respective heat transfer coefficients. Note that each convective resistor exists in parallel with a radiative resistor. In other words, a similar delta network describes radiant exchange at the indoor side.

The delta network shown in Figure 1.2 is advantageous in that it reveals detailed information about the heat transfer phenomenon and provides the possibility of generating accurate solar-thermal performance data for the CFS. Specifically, the resistor-network formulation makes it possible to calculate SHGC and U-factor of a CFS for any combination of environment temperatures and any level of insolation. This is not possible using the traditional irradiance-radiosity approach for tracking longwave radiant exchange. The resistor-network model is computationally advantageous too, especially in the context of time-step building energy simulation. See the papers by Wright (2008) and Foroushani et al. (2015a) for detailed discussion of these advantages.

The indoor-side network, shown in Figure 1.2, is only a small part of the complex network of the entire CFS (Figure 1.1). Moreover, heat transfer at the indoor side is usually

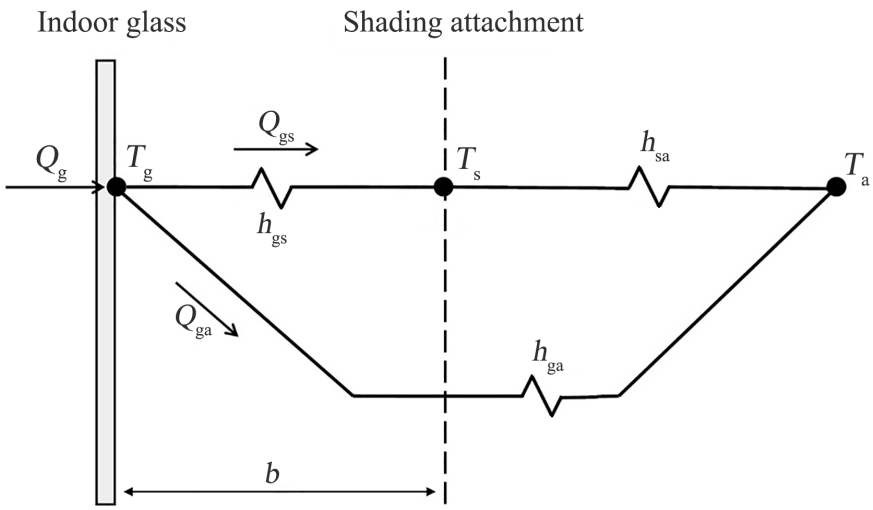

Figure 1.2: The resistor network of convection at the indoor side of a complex fenestration system (g: glazing, s: shading attachment, a: indoor air)

dominated by radiant exchange. Therefore, the performance of the ASHWAT models and the whole-building energy simulations is unlikely to be sensitive to the indoor-side convection coefficients. This was suspected during the development of the ASHWAT models and later demonstrated through a sensitivity analysis (Foroushani et al. 2016).

Nonetheless, compared to the other components of ASHWAT, the calculation of h_{gs}, h_{sa} and h_{ga}, the heat transfer coefficients that characterize the delta network of Figure 1.2, does not enjoy the same level of fundamental grounding. Currently, approximate estimates based on known limits and experience are used in ASHWAT to evaluate these coefficients. These estimates will be discussed and examined in detail in Chapter 10. In fact, the first suggestion made in the final report of RP-1311 (Wright et al. 2009) for future research was to develop "more detail and accuracy regarding indoor surface and glazing/shading layer channel convective heat transfer coefficients". When the ASHWAT models were developed the research on the thermal performance of window attachments was at an early stage. The heat transfer literature yields virtually no information on the resistor-network modeling of complex convection problems and evaluating the convective resistances involved. Surprisingly, it was revealed upon further examination that the

three convection coefficients corresponding to the delta network of Figure 1.2 cannot be determined using conventional methods. The formulation of this problem and development of solutions were the original motivation for the research reported in this thesis.

1.3 Multi-Temperature Convection

The problem of convection at the indoor side of a CFS comprises three *isothermal* boundaries: the glazing at T_{g}, the attachment at T_{s}, and the far-field air at T_{a}. Moreover, the isothermal boundaries of the CFS problem are all in thermal "communication". In other words, the temperature of each node influences heat transfer at each of the other two nodes. The success of the ASHWAT models is in large part due to the recognition and proper modeling of this feature.

But the CFS problem is not unique in these respects. In various heat transfer problems, the thermal problem entails exclusively isothermal and adiabatic boundary conditions. In such cases, heat transfer at each isothermal boundary is in general influenced by all the boundary temperatures. Convection in passages with isothermal walls and over isothermal surfaces are common examples. Thus, a class of heat transfer problems can be identified under the title of *multi-temperature convection problems*. The three-temperature problem of convection at the indoor side of a CFS is an example of this class.

1.4 Scope

The present research was undertaken to study convection at the indoor side of a complex fenestration system and calculate the three convection coefficients that characterize the corresponding delta network with improved detail and accuracy. It was revealed however that the CFS problem belongs to the broader class of multi-temperature convection problems. Furthermore, it became clear that the lack of detailed calculation methods

for the indoor-side convection coefficients in ASHWAT is not merely a weakness of these models; it is a general shortcoming of the conventional methods used in the study of convection. The scope of the study was accordingly expanded to the general problem of multi-temperature convection.

The research reported in this thesis was conducted with three overarching goals:

i) Formulating "the problem of multi-temperature convection" and exploring possible solutions.

ii) Developing a methodology for calculating the heat transfer coefficients of the CFS problem.

iii) Assessing the current ASHWAT estimates for the convection coefficients of the CFS problem.

1.5 Overview

This thesis is organized in eleven chapters. In the following two chapters, the theoretical basis of the work is presented. An extension of the Newton law of cooling is proposed as a general formulation of multi-temperature convection (Chapter 2). A new technique, dubbed dQdT, is developed to calculate the corresponding heat transfer coefficients. The theory concludes with an examination of the resistor-network model of convection (Chapter 3). In Chapters 4-9, several classical problems are revisited using the extended Newton formulation and the dQdT technique. In Chapter 10, dQdT is applied to calculate the heat transfer coefficients of convection at the indoor side of complex fenestration systems and assess the ASHWAT estimates. In the concluding summary, Chapter 11, highlights of the work and suggestions for future research are presented. In seven appendices, additional information such as computer codes, tabulated solution data and a mathematical theorem are presented.

A great portion of the results presented in this work is based on numerical solutions. Effort has been made to present a complete set of information (computational domain, discretization, solution schemes, validation, etc.) for each numerical solution. However, depending on the context and purpose of study, such information is presented with different levels of detail. For instance, due to its simplicity, the finite-difference solution to the asymmetric Graetz problem (Chapter 2) is not scrutinized in great detail. This solution is chiefly used for demonstration. On the other hand, the finite-volume solutions to the problem of free convection in a vertical channel, used to develop new heat transfer correlations, are examined and validated in much greater detail.

Although effort has been made to maintain consistency throughout this thesis, there are some differences in notation from one chapter to another. This is because the dQdT results presented in most chapters are based on, or at least compared to, existing solutions from the literature. Priority was given to consistency within each chapter. Hence, differences in the notations and definitions used by different authors have led to minor discrepancies in the present work. For example, the temperature ratio, r_T, is defined differently in Chapters 4 and 8.

Most of the material presented in Chapter 4 on the asymmetric Graetz problem has been published in the *AIAA Journal of Thermophysics & Heat Transfer* (Foroushani et al. 2017a). The results presented in Chapters 5 and 6 for the annulus problem along with parts of the mathematical development presented in Chapter 2 appear in another publication in the *Journal of Thermophysics & Heat Transfer* (Foroushani et al. 2017b). The material on laminar free convection in a vertical channel (Chapter 8) and the full development of the dQdT technique (Chapter 2) have been published in the third paper of the series in the *Journal of Thermophysics & Heat Transfer* (Foroushani et al. 2017c). The dQdT results for CFS configurations with a roller blind (Chapter 10) were presented at the ASHRAE Winter Conference 2017 (Foroushani et al. 2017d).

Chapter 2

Mathematical Formulation of Multi-Temperature Convection

2.1 The Newton Formulation

According to the Newton law of cooling, the rate of convective heat transfer is directly proportional to a driving temperature difference. Since most convection problems entail fluid flow over surfaces, this temperature difference is usually the difference between surface and fluid temperatures. The Newton law of cooling is expressed mathematically by introducing a proportionality coefficient, known as the convection heat transfer coefficient, h, as shown in Equation 2.1. In this equation, Q_1 is the heat transfer rate at the surface, A is the surface area, and T_1 and T_0 denote the surface and fluid temperatures respectively.

$$Q_1 = hA(T_1 - T_0) = hA\,\Delta T \tag{2.1}$$

Equation 2.1 is hereinafter called the "Newton formulation".

The "direction" of heat transfer is designated by a sign convention. Throughout this thesis, $Q_1 > 0$ designates heat transfer *from* the surface, while $Q_1 < 0$ corresponds to heat transfer *to* the surface. The heat transfer coefficient is hence never negative; $h \geq 0$.

Note that although h is introduced as a proportionality coefficient, it is not necessarily a constant. In other words, the relation between the heat transfer rate and temperature difference is not necessarily linear. Any nonlinearity in Q_1 with respect to T_1 or T_0 is contained in h.

Further note that tacit in the Newton formulation is the assumption that convective heat transfer occurs in a setting with two representative temperatures, T_0 and T_1. A standard example is heat transfer in flow over an isothermal flat plate, shown schematically in Figure 2.1. In this case, the free-stream temperature and the surface temperature are the two representative temperatures. Note that the free-stream flow and the plate surface are two isothermal boundaries; T_0 and T_1 are boundary temperatures. In connection to the mathematical formulation of the problem, these two isothermal boundaries constitute the boundary conditions of the differential energy equation.

Obviously, not all convection problems entail isothermal boundaries — flows or surfaces. In fact, the isothermal assumption is in most cases an idealization because uniform temperature distributions are rarely encountered. It is however usual to represent a non-uniform temperature boundary by some average temperature.

Moreover, in many cases the thermal condition at a surface is determined by the temperature gradient, i.e. heat flux, rather than temperature. In this case, non-uniform temperature distributions are usually encountered. In the case of isoflux surface conditions too, the Newton formulation is typically applied by using an average temperature to represent the surface.

Even if only prescribed-temperature boundaries are involved and the isothermal idealization is invoked, many heat transfer problems are described by more than two

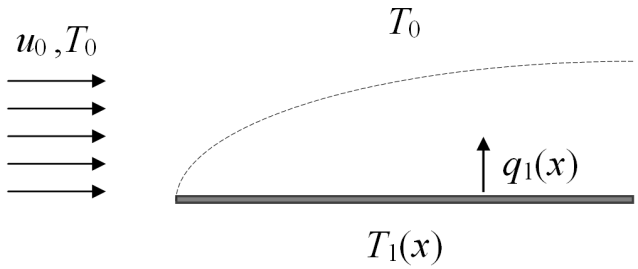

Figure 2.1: Schematic of flow over an isothermal flat plate

isothermal boundaries, hence entailing more than two representative temperatures. A common example is convective heat transfer in asymmetrically heated passages, e.g. the parallel-plate channel shown in Figure 2.2. If the flow enters the channel at a uniform temperature, T_0, and the walls are at temperatures T_1 and T_2, the thermal boundary conditions entail the set of three independent temperatures: $\{T_0, T_1, T_2\}$. Heat transfer in the channel is hence determined by three boundary temperatures.

The Newton formulation (Equation 2.1) needs be reconciled with the presence of three representative temperatures. It is conventional to construct a single temperature difference through a combination of the independent (and sometimes dependent) temperatures. For example, the mean wall temperature, $T_{\text{wm}} = (T_1 + T_2)/2$, is used to represent the channel walls. The total heat transfer in the channel is hence expressed as shown in Equation 2.2.

$$Q_1 + Q_2 = hA(T_{\text{wm}} - T_0) \tag{2.2}$$

In internal-flow problems, e.g. convection in an isothermal pipe, instead of T_0, the mean fluid temperature, T_{m}, is usually used to represent the fluid flow. The choice of T_{m} as a representative temperature is advantageous because it leads to a constant heat transfer coefficient which contains important information from the solution of the energy equation, namely the mean fluid temperature. Note that T_{m} is a dependent variable.

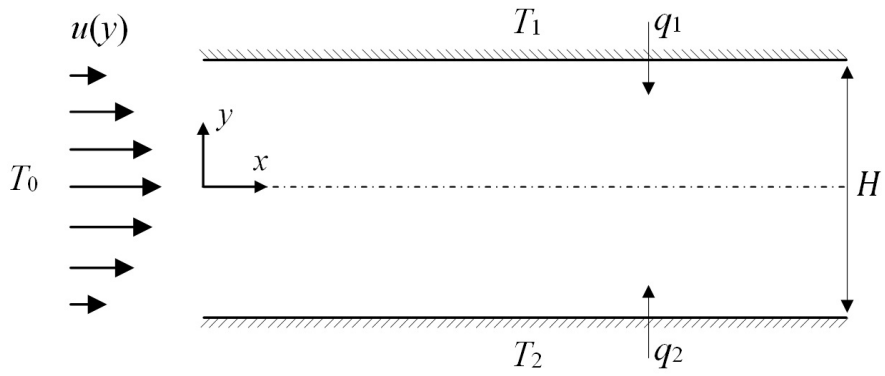

Figure 2.2: Schematic of flow in a parallel-plate channel with isothermal walls

Using T_{m} to represent the flow, the Newton formulation of heat transfer in the channel shown in Figure 2.2 is expressed as shown in Equation 2.3.

$$Q_1 + Q_2 = hA(T_{\mathrm{wm}} - T_{\mathrm{m}}) \tag{2.3}$$

As will be demonstrated in Chapters 4 and 5, using T_{m} to represent the flow in problems entailing multiple (more than two) isothermal boundaries can be problematic. Presently, attention is devoted to a proper extension of the Newton formulation exclusively in terms of the independent, boundary temperatures.

2.2 The Newton Formulation Extended

It is known from the mathematics of the problem that heat transfer in the configuration shown in Figure 2.2 is influenced by all the three independent temperatures, i.e. the set of boundary temperatures, $\{T_i\}$. More precisely, the rate of heat transfer at either wall and the rate of total heat transfer to the fluid are all functions of $\{T_i\}$. This observation is supported by laboratory and numerical experiments. Equation 2.4 is the mathematical expression of this observation.

$$Q_i = Q_i\big(\{T_i\}\big) \tag{2.4}$$

As suggested by the Newton formulation, it is the driving temperature difference, i.e. the *difference* between the boundary temperatures, that determines the heat transfer rate. In the case of multiple boundary temperatures, there are also multiple temperature differences. In the three-temperature arrangement of Figure 2.2, for example, there are three temperature differences: $\Delta T_{10} = T_1 - T_0$, $\Delta T_{20} = T_2 - T_0$ and $\Delta T_{12} = T_1 - T_2$. The functional relation between $\{Q_i\}$ and $\{T_i\}$ can accordingly be rewritten as shown in Equation 2.5 to emphasize the role of the temperature differences.

$$Q_i = Q_i\big(\{\Delta T_{ij}\}\big) \tag{2.5}$$

Note that obtaining Equation 2.5 from Equation 2.4 mathematically entails merely a linear change of variables.

To recast Equation 2.5 into a form analogous to the Newton formulation (Equation 2.1), Q_i can be expanded into a linearized summation with ΔT_{ij} explicitly factored out of each term. See Equation 2.6.

$$Q_i = \sum_j C_{ij}\Delta T_{ij} = \sum_j C_{ij}(T_i - T_j) \tag{2.6}$$

Any nonlinearity with respect to $\{T_i\}$ is contained in $\{C_{ij}\}$. But no assumptions are made regarding the form of $\{C_{ij}\}$. Equation 2.6 is hereinafter called the "extended Newton formulation". Equation 2.1 is a special case of Equation 2.6.

The coefficient C_{ij} characterizes the relationship between Q_i and the driving temperature difference ΔT_{ij}. It is hence appropriate to call C_{ij} a "functionality coefficient".

The subscript ij is introduced to indicate that C_{ij} corresponds to the dependence of Q_i on a specific temperature difference, ΔT_{ij}.

Applying the extended Newton formulation to the three-temperature example of convection in an asymmetrically heated channel (Figure 2.2), the rate of heat transfer at the walls can be written as:

$$\begin{aligned} Q_1 &= C_{10}(T_1 - T_0) + C_{11}(T_1 - T_1) + C_{12}(T_1 - T_2) \\ &= C_{10}(T_1 - T_0) + C_{12}(T_1 - T_2) \end{aligned} \tag{2.7}$$

$$\begin{aligned} Q_2 &= C_{20}(T_2 - T_0) + C_{21}(T_2 - T_1) + C_{22}(T_2 - T_2) \\ &= C_{20}(T_2 - T_0) + C_{21}(T_2 - T_1) \end{aligned} \tag{2.8}$$

Likewise for the rate of total heat transfer from the fluid;

$$\begin{aligned} Q_0 &= C_{00}(T_0 - T_0) + C_{01}(T_0 - T_1) + C_{02}(T_0 - T_2) \\ &= C_{01}(T_0 - T_1) + C_{02}(T_0 - T_2) \end{aligned} \tag{2.9}$$

Note that Q_0 is the rate of total heat transfer to the fluid, obtained from an overall energy balance on the system. Further note that there is no clear area of heat transfer corresponding to Q_0. Therefore, to maintain generality, instead of using heat transfer coefficients and areas, the extended Newton formulation (Equation 2.6) was postulated by introducing functionality coefficients, $\{C_{ij}\}$.

The traditional formulation relies on an equivalent or effective temperature difference, which is not unique. Therefore, $\{Q_i\}$ can be formulated in different ways. A possible formulation is:

$$\begin{cases} Q_1 = h_1 A_1 (T_1 - T_{\mathrm{m}}) \\ \\ Q_2 = h_2 A_2 (T_2 - T_{\mathrm{m}}) \end{cases}$$

Although the existence of multiple heat transfer rates is acknowledged in the traditional formulation, each heat transfer rate is characterized in terms of a *single* heat transfer coefficient. As a result, an amalgam of independent and dependent temperatures is used to forge an "effective" temperature difference for each heat transfer rate. As mentioned earlier, such a temperature difference is not unique. In the extended Newton formulation, on the other hand, only independent temperatures appear. Moreover, the contribution of each temperature difference is explicitly represented by a separate term.

2.3 Characterizing the Functionalities: The Problem of Multi-Temperature Convection

After presenting the Newton formulation, Incropera et al. (2007) state that the study of any convection problem reduces ultimately to "a study of the means by which h may be determined". Similarly, with the extended Newton formulation in place, the task will be the determination of the functions $\{C_{ij}\}$ to quantitatively characterize the relation between $\{Q_i\}$ and $\{T_i\}$.

The convection heat transfer coefficient, h, is a post-processing parameter. In other words, in the study of a convection problem, depending on the boundary conditions, Q or ΔT is calculated or measured. Then, h is calculated by rearranging Equation 2.1:

$$h = \frac{Q}{A\,\Delta T}$$

Similarly, in a multi-temperature arrangement, $\{Q_i\}$ can be determined for a given $\{T_i\}$. This is, in principle, the only information available to evaluate $\{C_{ij}\}$. Applying the extended Newton formulation, a system of equations is obtained with $\{C_{ij}\}$ unknown. For a problem with N isothermal boundaries, this system entails N equations and $N(N-1)$ unknowns. Clearly, for $N > 2$ this is an under-determined problem that cannot be solved

for $\{C_{ij}\}$. This is, in essence, the problem of multi-temperature convection; when more than two isothermal boundaries exist, the functionality coefficients cannot in general be determined based on the information available from conventional methods, i.e. from the heat transfer rates, $\{Q_i\}$. Consider, for instance, the extended Newton formulation of the three-temperature problem of flow in a parallel-plate channel with isotherm walls, presented in Equations 2.7-2.9. These three equations entail six unknowns — the six functionality coefficients that characterize the problem.

Note that implicit in the resistor-network model used in ASHWAT is the assumption that the two functionality coefficients pertaining to a pair of isothermal boundaries are equal, i.e. $C_{ij} = C_{ji}$. For the CFS problem, this is equivalent to: $h_{ij} = h_{ji}$. As will be discussed in following chapters, this is *not* necessarily the case; it is only true under certain conditions. Nevertheless, even with the assumption that $C_{ij} = C_{ji}$, the problem of multi-temperature convection persists. Although the number of unknowns would be reduced to N, the overall energy balance of the system reduces the number of the independent equations to $N - 1$. For a three-temperature problem, for example, setting $C_{ij} = C_{ji}$ in Equations 2.7-2.9 leads to a system of two equations and three unknowns.

2.4 The dQdT Technique

Reconsider Equation 2.7:

$$Q_1 = C_{10}(T_1 - T_0) + C_{12}(T_1 - T_2)$$

Differentiating the expression above with respect to T_0, Equation 2.10 is obtained.

$$\frac{\partial Q_1}{\partial T_0} = -C_{10} + \frac{\partial C_{10}}{\partial T_0}(T_1 - T_0) + \frac{\partial C_{12}}{\partial T_0}(T_1 - T_2) \tag{2.10}$$

Therefore, C_{10} can be obtained from Equation 2.10, if the second and third terms on the RHS are driven to zero. This, in turn, is achieved if;

$$\frac{\partial C_{10}}{\partial T_0} = \frac{\partial C_{12}}{\partial T_0} = 0$$

For the general nonlinear case, i.e. for most problems, the condition above does not hold. However, this condition can be *forced* by *treating* C_{10} and C_{12} as *constants* when differentiating Q_1 with respect to T_0. In mathematical notation:

$$C_{10} = -\frac{\partial Q_1}{\partial T_0}\bigg|_{C_{ik}=\text{const}} \tag{2.11}$$

Likewise, the functionality coefficient C_{12} can be obtained by differentiating Equation 2.7 with respect to T_2, while treating C_{10} and C_{12} as constants;

$$C_{12} = -\frac{\partial Q_1}{\partial T_2}\bigg|_{C_{ik}=\text{const}} \tag{2.12}$$

In general, the functionality coefficient C_{ij} of a multi-temperature convection problem can be calculated as:

$$C_{ij} = -\frac{\partial Q_i}{\partial T_j}\bigg|_{C_{ik}=\text{const}} \tag{2.13}$$

The procedure of evaluating the functionality coefficient C_{ij} in terms of the partial derivative $\partial Q_i/\partial T_j$ according to Equation 2.13 is hereinafter called "the dQdT technique", or simply "dQdT". This procedure is demonstrated in the following examples.

2.4.1 Two-Temperature Example: Convection at an Isothermal Vertical Flat Plate

Consider the classical problem of laminar convection at an isothermal flat plate. The problem is described by two boundary temperatures: the plate temperature, T_1, and the free-stream/far-field temperature, T_0. It is hence classified as a "two-temperature" problem.

Equation 2.14 is the Newton formulation of heat transfer at the plate, Q_1, obtained by applying Equation 2.6.

$$Q_1 = C_{10}(T_1 - T_0) \tag{2.14}$$

Comparing Equations 2.1 and 2.14, it is evident that in this two-temperature problem, the functionality coefficient C_{10} is the product of the heat transfer coefficient, h, and the plate surface area, A. For a two-temperature problem, once Q_1 is known, h or C_{10} can be readily calculated by rearranging Equation 2.1 or 2.14; there is no need for dQdT. In this section, the dQdT technique is nonetheless applied for demonstration and validation.

For forced convection, i.e. in the absence of buoyancy, the average Nusselt number is obtained using the similarity solution (Blasius 1908) to the hydrodynamic problem. The result is a function of the Reynolds number, Re, and the Prandtl number, Pr. See Equation 2.15.

$$\mathrm{Nu} = \frac{Q_1}{k(T_1 - T_0)} = 0.664\,\mathrm{Re}^{1/2}\,\mathrm{Pr}^{1/3} \tag{2.15}$$

Therefore, the heat transfer rate (per unit depth) at the plate is:

$$Q_1 = 0.664\,\mathrm{Re}^{1/2}\,\mathrm{Pr}^{1/3}\,k\,(T_1 - T_0) \tag{2.16}$$

Comparing Equations 2.14 and 2.16, C_{10} is obtained;

$$C_{10} = \frac{Q_1}{T_1 - T_0} = 0.664\, k\, \mathrm{Re}^{1/2}\, \mathrm{Pr}^{1/3} \tag{2.17}$$

To obtain C_{10} using dQdT, Equation 2.16 must be differentiated with respect to T_0. See Equation 2.18.

$$C_{10} = -\frac{\partial Q_1}{\partial T_0}\bigg|_{C_{10}=\text{const}} = 0.664\, k\, \mathrm{Re}^{1/2}\, \mathrm{Pr}^{1/3} \tag{2.18}$$

The two approaches produce the same result.

In the presence of buoyancy, i.e. for free convection, the boundary-layer solution by Ostrach (1953) gives the average Nusselt number based on the plate height (H) as shown in Equation 2.19. In this equation, Φ is a function of Pr only and $\mathrm{Gr} = g\beta(T_1 - T_0)H^3/\nu^2$.

$$\mathrm{Nu} = \frac{Q_1}{k(T_1 - T_0)} = \frac{4}{3}\Phi\, \mathrm{Gr}^{1/4} \tag{2.19}$$

Therefore, the heat transfer rate (per unit depth) at the plate is given as shown in Equation 2.20.

$$Q_1 = \left[\frac{4}{3}\Phi\, \mathrm{Gr}^{1/4}\, k\right](T_1 - T_0) \tag{2.20}$$

The functionality coefficient C_{10} can then be obtained as shown in Equation 2.21.

$$C_{10} = \frac{Q_1}{T_1 - T_0} = \frac{4}{3}\, k\, \Phi\, \mathrm{Gr}^{1/4} \tag{2.21}$$

To obtain C_{10} using dQdT, Equation 2.20 must be differentiated with respect to T_0 *while treating the contents of the square brackets as constants*;

$$\begin{aligned} C_{10} &= -\frac{\partial Q_1}{\partial T_0}\bigg|_{C_{10}=\text{const}} \\ &= -\frac{\partial}{\partial T_0}\left\{\left[\frac{4}{3}\,k\,\Phi\,\text{Gr}^{1/4}\right](T_1 - T_0)\right\}_{\text{Gr}=\text{const}} \\ &= \frac{4}{3}\,k\,\Phi\,\text{Gr}^{1/4} \end{aligned} \tag{2.22}$$

The validity of dQdT for this two-temperature is confirmed by comparing Equations 2.21 and 2.22.

Note that if the $C_{10} = \text{const}$ constraint is relaxed;

$$-\frac{\partial Q_1}{\partial T_0} = \frac{5}{3}\,k\,\Phi\,\text{Gr}^{1/4} \tag{2.23}$$

Comparing Equations 2.22 and 2.23, it is seen that relaxing the $C_{ik} = \text{const}$ constraint leads to a bias error of 25%.

Also note that applying the Newton formulation, the rate of heat transfer from the fluid, Q_0, can be written as shown in Equation 2.24.

$$Q_0 = C_{01}(T_0 - T_1) \tag{2.24}$$

Nonetheless, the energy balance of this two-temperature arrangement requires: $Q_0 = -Q_1$. Hence, Equations 2.14 and 2.24 lead to: $C_{10} = C_{01}$. In other words, this two-temperature problem is fully characterized by a single functionality coefficient, C_{10}. This argument can

be extended to any two-temperature convection problem. As stated earlier, it is for $N > 2$ that the problem of multi-temperature convection arises. A three-temperature example is therefore in order at this point.

2.4.2 Three-Temperature Example: Hydrodynamically Developed Laminar Flow in a Parallel-Plate Channel with Isothermal Walls

Consider the configuration shown in Figure 2.2: a hydrodynamically developed laminar flow at a uniform temperature, T_0, enters the channel formed between two semi-infinite parallel plates maintained at temperatures T_1 and T_2, separated by distance H. The thermal boundary conditions of the problem are described by three independent temperatures: $\{T_0, T_1, T_2\}$. There are also three heat transfer rates of interest: heat transfer rate at the walls, Q_1 and Q_2, and the rate of total heat transfer from the fluid, Q_0. The extended Newton formulation (Equation 2.6) yields:

$$\begin{cases} Q_0 = C_{01}(T_0 - T_1) + C_{02}(T_0 - T_2) \\ Q_1 = C_{10}(T_1 - T_0) + C_{12}(T_1 - T_2) \\ Q_2 = C_{20}(T_2 - T_0) + C_{21}(T_2 - T_1) \end{cases} \tag{2.25}$$

The heat transfer rates, $\{Q_i\}$, can be determined using analytical or numerical solutions. Nonetheless, the system of equations above is under-determined with three equations and six unknowns; it cannot be solved for $\{C_{ij}\}$. dQdT is required.

With constant fluid properties, negligible conduction in the x-direction and negligible viscous dissipation, the energy equation for hydrodynamically developed laminar flow is reduced to Equation 2.26.

$$\rho u_{\mathrm{fd}} c_p \frac{\partial T}{\partial x} = k \frac{\partial^2 T}{\partial y^2} \tag{2.26}$$

The boundary conditions of the problem are:

$$\begin{aligned} x = 0 \quad &; \quad T = T_0 \\ y = H/2 \quad &; \quad T = T_1 \\ y = -H/2 \quad &; \quad T = T_2 \end{aligned} \tag{2.27}$$

Hatton & Turton (1962) obtained an analytical solution to Equation 2.26 subject to the conditions of Equation 2.27 in the form shown in Equation 2.28.

$$\theta = Y - \sum_{n=1}^{\infty} B_n f_n \exp\left(-\frac{8}{3} \lambda_n^2 X \right) \tag{2.28}$$

In Equation 2.28, θ is the dimensionless temperature defined in Equation 2.29 with $T_{\mathrm{wm}} = (T_1 + T_2)/2$, Y is the dimensionless lateral coordinate: $Y = 2y/H$, and X is the dimensionless stream-wise coordinate, defined in Equation 2.30 where $\mathrm{Re} = \left[\rho u_{\mathrm{m}} (2H)\right]/\mu$. B_n, f_n and λ_n are, respectively, the eigencoefficients, eigenfunctions and eigenvalues of the Sturm-Liouville system obtained by applying separation of variables.

$$\theta = \frac{T - T_{\mathrm{wm}}}{T_1 - T_{\mathrm{wm}}} \tag{2.29}$$

$$X = \frac{2x}{H} \left(\frac{1}{\mathrm{Re}\,\mathrm{Pr}} \right) \tag{2.30}$$

The solution by Hatton & Turton (1962) will be discussed in Chapter 4 in more detail. Here, it is used to derive analytical expressions for $\{Q_i\}$ and demonstrate the dQdT technique.

With the temperature distribution known from Equation 2.28, heat flux at either wall can be obtained by differentiation. See Equations 2.31 and 2.32 wherein the sign convention introduced earlier is observed.

$$\begin{aligned} q_1 &= \frac{k}{H}(T_1 - T_2)\left(\frac{\partial \theta}{\partial Y}\right)_{Y_1} \\ &= \frac{k}{H}(T_1 - T_2)\left[1 - \sum_{n=1}^{\infty} B_n \left(\frac{\partial f_n}{\partial Y}\right)_{Y=1} \exp\left(-\frac{8}{3}\lambda_n^2 X\right)\right] \end{aligned} \tag{2.31}$$

$$\begin{aligned} q_2 &= -\frac{k}{H}(T_1 - T_2)\left(\frac{\partial \theta}{\partial Y}\right)_{Y_2} \\ &= \frac{k}{H}(T_1 - T_2)\left[1 - \sum_{n=1}^{\infty} B_n \left(\frac{\partial f_n}{\partial Y}\right)_{Y=-1} \exp\left(-\frac{8}{3}\lambda_n^2 X\right)\right] \end{aligned} \tag{2.32}$$

Heat fluxes can then be integrated from the channel inlet to any location x to calculate the (per unit depth) heat transfer rates at the walls. See Equation 2.33.

$$\begin{aligned} Q_i &= \int_0^x |q_i| \, \mathrm{d}x \\ &= \frac{k}{H}(T_1 - T_2) \int_0^x \left[1 - \sum_{n=1}^{\infty} B_n \left(\frac{\partial f_n}{\partial Y}\right)_{Y_i} \exp\left(-\frac{8}{3}\lambda_n^2 X\right)\right] \mathrm{d}x \qquad (i = 1, 2) \end{aligned} \tag{2.33}$$

With a change of the integration variable, the summation can be integrated as shown in Equation 2.34.

$$\int \left[\sum_{n=1}^{\infty} B_n \left(\frac{\partial f_n}{\partial Y} \right) \exp\left(-\frac{8}{3}\lambda_n^2 X \right) \right] \mathrm{d}x$$

$$= \mathrm{Re}\,\mathrm{Pr} \left(\frac{H}{2} \right) \sum_{n=1}^{\infty} \left[B_n \left(\frac{\partial f_n}{\partial Y} \right) \int \exp\left(-\frac{8}{3}\lambda_n^2 X \right) \mathrm{d}X \right] \tag{2.34}$$

$$= \mathrm{Re}\,\mathrm{Pr} \left(\frac{H}{2} \right) \sum_{n=1}^{\infty} \left[-\frac{3B_n}{8\lambda_n^2} \left(\frac{\partial f_n}{\partial Y} \right) \exp\left(-\frac{8}{3}\lambda_n^2 X \right) \right]$$

The wall heat transfer rates are therefore obtained as shown in Equations 2.35 and 2.36.

$$Q_1 = \mathrm{Re}\,\mathrm{Pr}\,\frac{k(T_1 - T_2)}{2} \left\{ X - \sum_{n=1}^{\infty} \frac{3B_n}{8\lambda_n^2} \left(\frac{\partial f_n}{\partial Y} \right)_{Y=1} \left[1 - \exp\left(-\frac{8}{3}\lambda_n^2 X \right) \right] \right\} \tag{2.35}$$

$$Q_2 = -\mathrm{Re}\,\mathrm{Pr}\,\frac{k(T_1 - T_2)}{2} \left\{ X - \sum_{n=1}^{\infty} \frac{3B_n}{8\lambda_n^2} \left(\frac{\partial f_n}{\partial Y} \right)_{Y=-1} \left[1 - \exp\left(-\frac{8}{3}\lambda_n^2 X \right) \right] \right\} \tag{2.36}$$

The rate of total heat transfer from the fluid is then obtained from an energy balance. See Equation 2.37.

$$Q_0 = -Q_1 - Q_2$$

$$= -\mathrm{Re}\,\mathrm{Pr}\,\frac{k(T_1 - T_2)}{2} \left\{ \sum_{n=1}^{\infty} \frac{3B_n}{8\lambda_n^2} \left[\left(\frac{\partial f_n}{\partial Y} \right)_{Y=1} - \left(\frac{\partial f_n}{\partial Y} \right)_{Y=-1} \right] \left[1 - \exp\left(-\frac{8}{3}\lambda_n^2 X \right) \right] \right\} \tag{2.37}$$

Equations 2.35-2.37 provide analytical expressions for $\{Q_i\}$. To evaluate $\{C_{ij}\}$ using dQdT, these expressions must be differentiated according to Equation 2.13. It must be noted in carrying out this operation that, as shown by Hatton & Turton (1962), the even eigencoefficients, $\{B_{\mathrm{E},n}\}$, are directly proportional to the temperature ratio, r_T (defined in Equation 2.38), while the odd eigencoefficients are independent of $\{T_i\}$.

$$r_T = \frac{T_0 - T_{\mathrm{wm}}}{T_1 - T_{\mathrm{wm}}} \tag{2.38}$$

Applying dQdT, the functionality coefficients C_{10} and C_{12}, for example, are obtained as shown in Equations 2.39 and 2.40.

$$\begin{aligned} C_{10} &= -\left.\frac{\partial Q_1}{\partial T_0}\right|_{C_{ik}=\mathrm{const}} \\ &= \mathrm{Re}\,\mathrm{Pr}\,k \left\{ \sum_{n=1}^{\infty} \frac{3}{8\lambda_n^2} \left(\frac{\partial B_n}{\partial \theta_0}\right) \left(\frac{\partial f_n}{\partial Y}\right)_{Y=1} \left[1 - \exp\left(-\frac{8}{3}\lambda_n^2 X\right)\right] \right\} \end{aligned} \tag{2.39}$$

$$\begin{aligned} C_{12} &= -\left.\frac{\partial Q_1}{\partial T_2}\right|_{C_{ik}=\mathrm{const}} \\ &= \mathrm{Re}\,\mathrm{Pr}\,k \left\{ X - \sum_{n=1}^{\infty} \frac{3B_n}{8\lambda_n^2} \left(\frac{\partial f_n}{\partial Y}\right)_{Y=1} \left[1 - \exp\left(-\frac{8}{3}\lambda_n^2 X\right)\right] \right. \\ &\qquad \left. - \sum_{n=1}^{\infty} \frac{3}{8\lambda_n^2} \left(\frac{\partial B_n}{\partial \theta_2}\right) \left(\frac{\partial f_n}{\partial Y}\right)_{Y=1} \left[1 - \exp\left(-\frac{8}{3}\lambda_n^2 X\right)\right] \right\} \end{aligned} \tag{2.40}$$

This is a constant-property forced convection problem. Therefore, the energy equation is linear and the $C_{ik} = \mathrm{const}$ constraint is automatically satisfied. The implementation

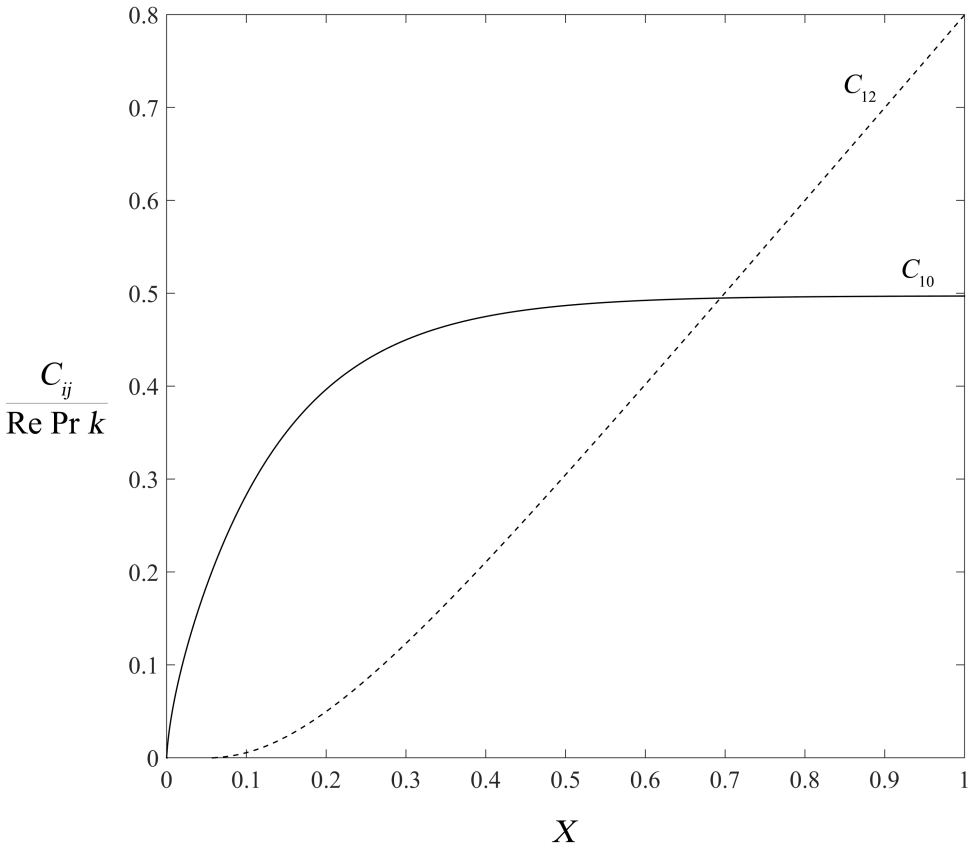

Figure 2.3: dQdT results for hydrodynamically developed laminar flow in a parallel-plate channel with isothermal walls

of this constraint, which is crucial to the dQdT technique, in the case of variable fluid properties and/or free convection will be discussed in following sections.

A closer examination of the dQdT results for C_{10} and C_{12} helps demonstrate the utility and validity of the extended Newton formulation, i.e. characterizing heat transfer in terms of $\{C_{ij}\}$. The dQdT results are plotted in Figure 2.3 using the eight eigencoefficients, eigenvalues and eigenfunction derivatives given by Hatton & Turton (1962).

Recall that C_{ij} characterizes the effect of ΔT_{ij} on Q_i. More specifically, C_{ij} quantifies the sensitivity of Q_i to the boundary temperature T_j. Moreover, note that C_{10} and C_{12} include the area of the heat-transfer surface, A_1, which increases linearly with X. Therefore, the slope of the curves shown in Figure 2.3 is a better representation of the thermal

development of the flow. In this light, the curves shown in Figure 2.3 have a clear physical interpretation. Near the channel inlet, T_2 has almost no impact on Q_1, reflected by $C_{12} = \partial C_{12}/\partial X = 0$ for $X \lesssim 0.1$. However, moving downstream, as the boundary layers thicken and the flow approaches the thermally developed limit, the effect of T_2 on Q_1 increases. In other words, as the boundary layer developed along the wall at T_2 starts to interact with the boundary layer along the wall at T_1, the effect of T_2 on Q_1 increases. As the flow reaches thermal development, C_{12} approaches to a straight line. In the thermally developed limit, heat transfer in the channel is dominated by conduction between the walls.

The evolution of the temperature profile and variation of heat transfer in the channel are also reflected in the trend of C_{10}. In the thermally developing region, particularly for $X \lesssim 0.2$, Q_1 is significantly influenced by the inlet temperature, T_0. Therefore C_{10} has a very large slope for $X \lesssim 0.2$. In the thermally developed limit (essentially for $X \gtrsim 0.6$), C_{10} becomes nearly horizontal; the effect of T_1 reaches its maximum and remains constant. As noted earlier, heat transfer in the thermally developed region is dominated by conduction between the walls – across the flow – and hence Q_1 is independent of T_0.

2.5 Numerical Implementation of dQdT

In Section 2.4, the dQdT technique was developed and demonstrated assuming analytical expressions for $\{Q_i\}$ can be obtained. In other words, the development presented earlier is only useful when an analytical solution to the energy equation is at hand. But analytical solutions are rarely available. Numerical solutions, on the other hand, can be obtained for a wide range of configurations and flow conditions. The dQdT technique is therefore of limited utility unless it can be applied numerically, i.e. the partial differentiation of Equation 2.13 evaluated based on numerical solutions.

Reconsider Equation 2.13:

$$C_{ij} = -\frac{\partial Q_i}{\partial T_j}\bigg|_{C_{ik}=\text{const}}$$

The derivative $\partial Q_i/\partial T_j$ can be approximated as shown in Equation 2.41.

$$\frac{\partial Q_i}{\partial T_j} \approx \frac{\delta Q_i}{\delta T_j} \tag{2.41}$$

In Equation 2.41, δT_j denotes a finite perturbation in the boundary temperature T_j, and δQ_i is the resulting change in the heat transfer rate Q_i. The accuracy of Equation 2.41 depends on the curvature of the $Q_i(T_j)$ function and the size of δT_j. See Equation 2.42.

$$\frac{\partial Q_i}{\partial T_j} = \frac{\delta Q_i}{\delta T_j} - \frac{\partial^2 Q_i}{\partial T_j^2}(\delta T_j) + \mathrm{O}(\delta T_j^2) \tag{2.42}$$

According to Equation 2.42, Equation 2.41 is a close approximation if the perturbation δT_j is small. The effect of the $C_{ik} = \text{const}$ constraint on the accuracy of this approximation remains to be examined.

Deriving the extended Newton formulation, no assumptions were made regarding the form of the functionality coefficients $\{C_{ij}\}$. It is helpful at this point to examine the nature of $\{C_{ij}\}$ more closely. The rate of convective heat transfer is a function of geometry, velocity field, fluid properties and boundary temperatures. This can be established by examining the governing equations. Hence, for a given geometry, $\{Q_i\}$ is function of the velocity field, fluid properties and boundary temperatures. The extended Newton formulation is thus, in a sense, grouping the effects of velocity field and fluid properties in $\{C_{ij}\}$ on the one hand, and those of the boundary temperatures in $\{\Delta T_{ij}\}$ on the other hand. Note that this grouping is not a "separation" of the effects; $\{T_i\}$ can influence $\{C_{ij}\}$ through thermal effects on the velocity field, i.e. buoyancy, or temperature-dependent

fluid properties. But the $C_{ik} = \text{const}$ constraint suppresses this influence. In other words, the $C_{ik} = \text{const}$ constraint removes the nonlinearities of the energy equation. Therefore, dQdT is, in essence, the procedure of linearizing Q_i and then differentiating the result with respect to T_j.

If Q_i is linearized, i.e. when the $C_{ik} = \text{const}$ constraint is enforced, the curvature term becomes zero; $\partial^2 Q_i / \partial T_j^2 = 0$. Equation 2.42 then becomes:

$$\left.\frac{\partial Q_i}{\partial T_j}\right|_{C_{ik}=\text{const}} = \left.\frac{\delta Q_i}{\delta T_j}\right|_{C_{ik}=\text{const}} \tag{2.43}$$

In a numerical solution, the linearization of the energy equation, i.e. suppressing the temperature dependence of the velocity field and fluid properties, can be done by "fixing" the velocity field and fluid properties. In order to do this, a "baseline" solution is first obtained to the full set of the governing equations for the given boundary conditions, $\{T_i\}$, and the heat transfer rate Q_i is calculated. Next, the boundary temperature T_j is changed to $T_j^* = T_j + \delta T_j$ and a new solution to the energy equation *only* is obtained using the velocity and fluid-property fields of the baseline solution. The new heat transfer rate Q_i^* and its change with respect to the baseline case are calculated; $\delta Q_i = Q_i^* - Q_i$. The functionality coefficient C_{ij} is then obtained as shown in Equation 2.44.

$$C_{ij} = -\left.\frac{\delta Q_i}{\delta T_j}\right|_{C_{ik}=\text{const}} \tag{2.44}$$

Alternatively, Equation 2.44 may be derived based on the interpretation of dQdT as a tool for generating additional equations to close the under-determined system of equations resulting from the extended Newton formulation. The dQdT technique was originally conceived using this approach, as described below.

The extended Newton formulation of the heat transfer rate Q_i, obtained from the baseline solution, gives:

$$Q_i = \sum_k C_{ik}(T_i - T_k)$$

Likewise, Q_i^*, the heat transfer rate obtained from solving the energy equation with perturbed boundary conditions, $\{T_k^*\}$, while retaining the velocity field and fluid properties of the baseline solution, can be written as:

$$Q_i^* = \sum_k C_{ik}^*(T_i^* - T_k^*)$$

However, because the velocity field and fluid properties of the baseline solution are retained, i.e. the $C_{ik} = \text{const}$ constraint is enforced; $C_{ik} = C_{ik}^*$. Therefore:

$$\begin{aligned}
\delta Q_i &= Q_i^* - Q_i \\
&= \sum_k C_{ik}^*(T_i^* - T_k^*) - \sum_k C_{ik}(T_i - T_k) \\
&= \sum_k C_{ik}\big[(T_i^* - T_i) + (T_k - T_k^*)\big]
\end{aligned}$$

Hence, by choosing $\{T_k^*\} = \{T_k + \delta T_k \,\big|\, \forall k \neq j \,;\, \delta T_k = 0\}$;

$$\delta Q_i = C_{ij}(T_j - T_j^*)$$

And therefore:

$$C_{ik} = -\frac{\delta Q_i}{\delta T_j}\bigg|_{C_{ik}=\text{const}}$$

2.5.1 Numerical dQdT — Examples

Free Convection at an Isothermal Vertical Flat Plate

In Section 2.4.1, dQdT was applied to an analytical solution to the two-temperature problem of laminar free convection at an isothermal vertical flat plate. In this section, the same problem is used to demonstrate the numerical implementation of dQdT.

To apply dQdT numerically, a baseline solution to the full set of governing equations must first be obtained. The commercial CFD code ANSYS Fluent 14.0 (ANSYS 2011a,b) was used to obtain second-order finite volume solutions to the mass, momentum and energy equations in the computational domain shown in Figure 2.4. The PRESTO! algorithm for pressure discretization, SIMPLE scheme for handling the pressure-velocity coupling and the Boussinesq approximation for density were used. The boundary conditions used in the CFD solution are shown in Figure 2.4.

After the baseline numerical solution was obtained, the total heat transfer rate (per unit depth) at the plate, Q_1, was calculated. For a two-temperature problem, once Q_1 is known, C_{10} can be directly calculated as shown in Equation 2.45.

$$C_{10} = \frac{Q_1}{T_1 - T_0} \tag{2.45}$$

Next, to apply dQdT, the ambient temperature, T_0, was changed by δT_0 and a new solution was obtained by updating the temperature field only, while retaining the velocity field of the baseline solution. In Fluent, this can be easily done by selecting only the energy equation in the "Equations" section, under "Solution Controls". The new heat transfer rate at the plate, Q_1^*, and the change, $\delta Q_1 = Q_1^* - Q_1$, were calculated. C_{10} was then obtained as shown in Equation 2.44.

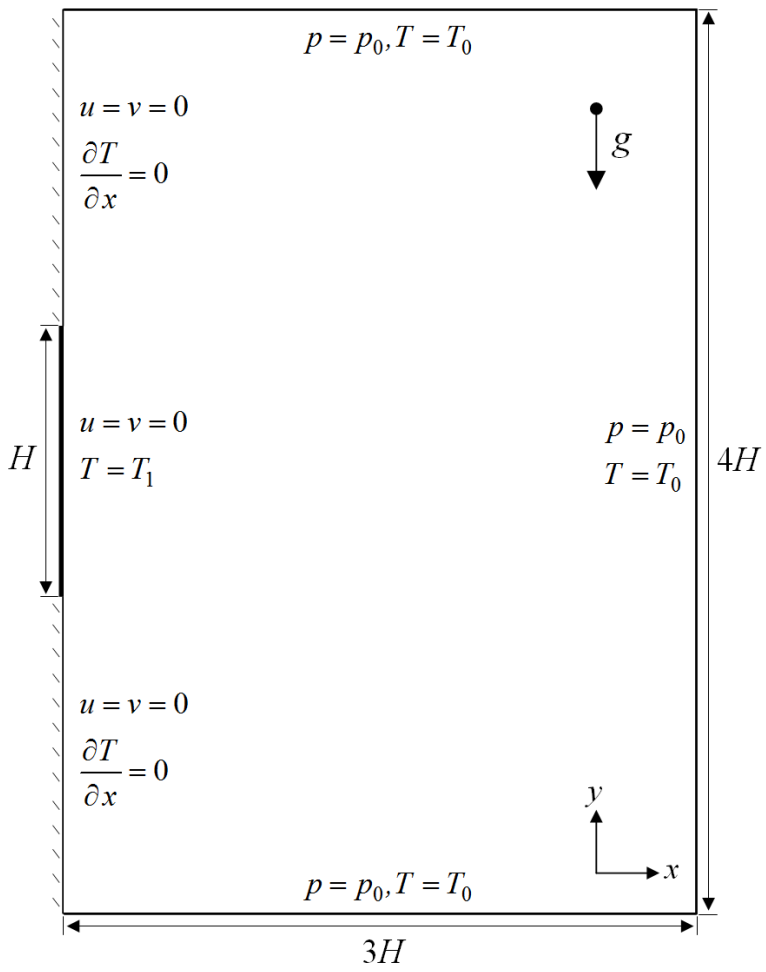

Figure 2.4: Computational domain for free convection at an isothermal vertical flat plate

At Ra $= 10^5$, for example, with $H = 0.1\,\text{m}$, $T_1 = 310\,\text{K}$, $T_0 = 300\,\text{K}$, and $k = 0.0255$ W/(mK), the baseline CFD solution yielded a heat transfer rate of $Q_1 = 2.3681$ W/m. Therefore, based on Equation 2.45;

$$C_{10} = \frac{Q_1}{T_1 - T_0} = \frac{2.3681}{310 - 300} = 0.2368\,\frac{\text{W}}{\text{mK}}$$

Then, T_0 was changed to $T_0^* = 299\,\text{K}$ and the solution to the energy equation only was updated using the velocity field of the baseline solution. The new rate of heat transfer at the plate was calculated: $Q_1^* = 2.6050$ W/m. Hence, based on Equation 2.44;

$$C_{10} = -\frac{\delta Q_1}{\delta T_0}\bigg|_{C_{10}=\text{const}} = \frac{2.6050 - 2.3681}{300 - 299} = 0.2369\,\frac{\text{W}}{\text{mK}}$$

When the far-field temperature was perturbed to $T_0^* = 299\,\text{K}$ and an updated solution was obtained to the *full* set of the governing equations, i.e. with the $C_{ik} = \text{const}$ constraint relaxed, the new heat transfer rate was $Q_1^* = 2.6649$ W/m. Therefore:

$$\delta Q_1 = Q_1^* - Q_1 = 0.2968\,\frac{\text{W}}{\text{m}}$$

And;

$$C_{10} = -\frac{\delta Q_1}{\delta T_0} = 0.2968\,\frac{\text{W}}{\text{mK}}$$

Hence, for this problem, relaxing the $C_{ik} = \text{const}$ constraint leads to a 25.3% error, which is in agreement with the analytical result derived in Section 2.4.1.

In Figure 2.5, the results of Equations 2.44 and 2.45 are compared to the boundary-layer solution by Ostrach (1953) (Equation 2.19) for $10^2 \leq \text{Ra} \leq 10^9$ and $\text{Pr} = 0.7$. The results are reported in the dimensionless form, C_{10}/k, which is, in this two-temperature case, equivalent to the traditional average Nusselt number. To evaluate Equation 2.19 the approximate curve-fit relation proposed by Oosthuizen & Naylor (1999) was used to calculate Φ. The dQdT results match the algebraic results (Equation 2.45) exactly, while in close agreement with the boundary-layer solution. Note that the dQdT and algebraic results are based on solutions to the full elliptic energy equation, hence the small discrepancy with the parabolic boundary-layer solution. This discrepancy is pronounced for lower flow rates ($\text{Ra} < 10^3$) where diffusion in the y-direction becomes significant. The close agreement between the results validates Equation 2.44.

It was stated earlier that the accuracy of Equation 2.42 depends on the size of the perturbation, δT_j. Nevertheless, since fixing the velocity field and the fluid properties

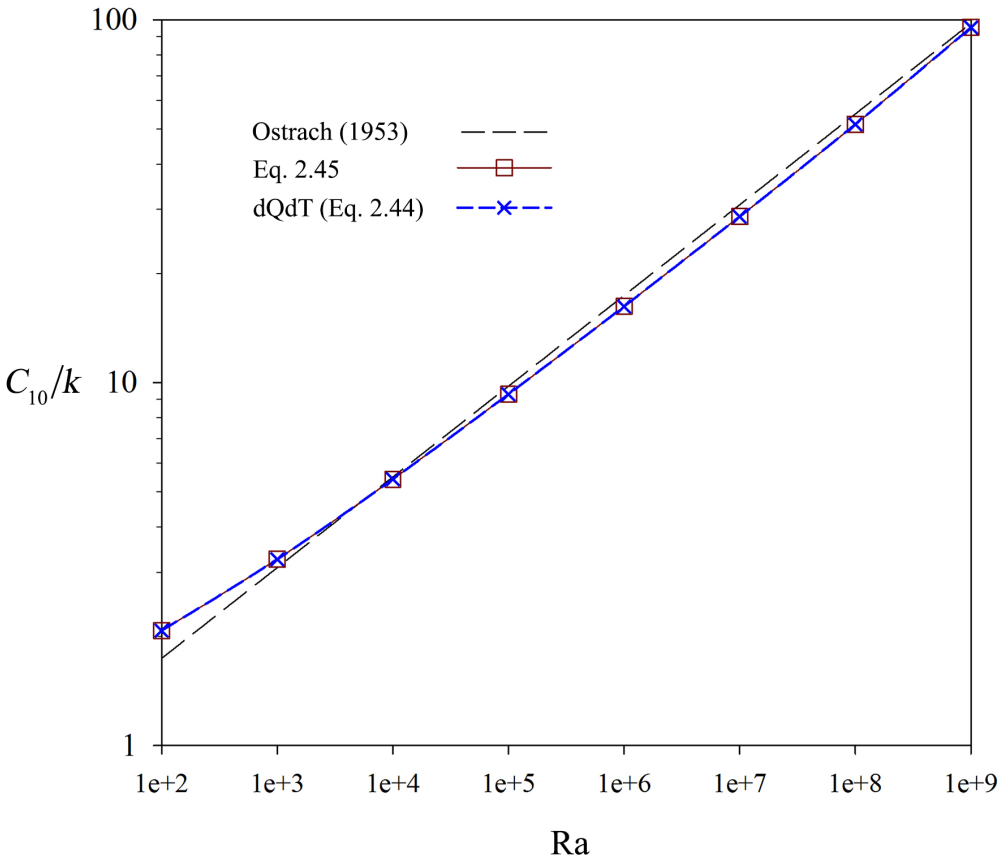

Figure 2.5: The functionality coefficient of laminar free convection at an isothermal vertical flat plate (Pr=0.7)

linearizes the energy equation, i.e. $\partial^2 Q_i/\delta T_j^2 = 0$, the size of δT_j does not matter when performing dQdT. Note however that numerical considerations preclude very small perturbations; given the numerical errors of the solution, δT_j must be large enough that δQ_i can be reliably calculated. This can be seen from Table 2.1 wherein C_{10} obtained by using different values of δT_0 in the dQdT operation are presented for the example discussed earlier $\left[H = 0.1 \text{ m}, T_1 = 310 \text{ K}, T_0 = 300 \text{ K}, \text{ and } k = 0.0255 \text{ W/(mK)}\right]$. The error was calculated based on the algebraic results (Equation 2.45): $C_{10} = 0.2368$ W/(mK). For $\delta T_0 \geq 0.01$, dQdT yields nearly identical results regardless of the size of δT_0.

Table 2.1: Results of dQdT with different perturbations sizes
[Free convection at an isothermal flat plate ($\mathrm{Ra} = 10^5, \mathrm{Pr} = 0.7$)]

T_0^* [K]	δT_0 [K]	Q_1^* [W/m]	C_{10}/k [-]	Error [%]
305.000	5.000	1.1841	9.2868	0.00
302.000	2.000	1.8945	9.2868	0.00
301.000	1.000	2.1313	9.2867	0.00
299.000	-1.000	2.6050	9.2869	0.00
300.500	0.500	2.2497	9.2866	0.00
300.100	0.100	2.3445	9.2856	-0.01
300.010	0.010	2.3658	9.2749	-0.13
300.001	0.001	2.3679	9.1765	-1.19

Hydrodynamically Developed Laminar Flow in a Parallel-Plate Channel with Isothermal Walls

Also examined in Section 2.4 as an example was the problem of hydrodynamically developed laminar flow in an asymmetrically heated parallel-plate channel. As noted earlier, because this is a forced-convection problem with constant fluid properties, the $C_{ik} = \text{const}$ constraint is automatically satisfied. Therefore, to obtain $\{C_{ij}\}$ using numerical dQdT, it is sufficient to obtain a solution to the mass and momentum equations; then the energy equation must be solved with the original boundary conditions, $\{T_i\}$, as well as with perturbed boundary conditions, $\left\{T_i + \delta T_i \,\middle|\, \forall i \neq j\,;\, \delta T_i = 0\right\}$. No special measures are necessary to enforce the $C_{ik} = \text{const}$ constraint. Moreover, since the flow enters the channel hydrodynamically fully developed, the procedure is reduced to obtaining solutions to the energy equation.

Introducing the non-dimensional variables shown in Equation 2.46, the parabolic energy equation (Equation 2.26) can be expressed in non-dimensional form as shown in Equation 2.47.

$$\begin{cases} U = \dfrac{u_{\mathrm{fd}}}{u_{\mathrm{m}}} \\ \theta = \dfrac{T - T_0}{T_1 - T_0} \\ X = \dfrac{2x}{H}\left(\dfrac{1}{\mathrm{Re\ Pr}}\right) \\ Y = \dfrac{2y}{H} \end{cases} \tag{2.46}$$

$$\frac{U}{4}\left(\frac{\partial\theta}{\partial X}\right) = \frac{\partial^2\theta}{\partial Y^2} \tag{2.47}$$

The 1/4 factor appears in Equation 2.47 since the Reynolds number based on the channel hydraulic diameter ($2H$) is used to define X.

The non-dimensional boundary conditions are:

$$\begin{aligned} X = 0 \quad &; \quad \theta = \theta_0 = 0 \\ Y = 1 \quad &; \quad \theta = \theta_1 = 1 \\ Y = -1 \quad &; \quad \theta = \theta_2 = \frac{T_2 - T_0}{T_1 - T_0} \end{aligned} \tag{2.48}$$

Using the finite-difference formulation, the PDE of Equation 2.47 becomes:

$$U_{m,n}\frac{\theta_{m,n} - \theta_{m-1,n}}{4(\Delta X)} = \frac{\theta_{m,n+1} - 2\theta_{m,n} + \theta_{m,n-1}}{(\Delta Y)^2} \tag{2.49}$$

The explicit formulation then gives the temperature of the node (m, n), with first- and second-order accuracy in X and Y respectively, as shown in Equation 2.50. The superscript (k) denotes the iteration number.

$$\theta_{m,n}^{(k)} = \left[\frac{U_{m,n}}{4(\Delta X)} + \frac{2}{(\Delta Y)^2}\right]^{-1}\left[\frac{\theta_{m,n+1}^{(k-1)} + \theta_{m,n-1}^{(k-1)}}{(\Delta Y)^2} + \frac{U_{m,n}}{4(\Delta X)}\theta_{m-1,n}^{(k-1)}\right] \tag{2.50}$$

A MATLAB code was developed to obtain a numerical solution to Equation 2.47 using a forward-marching iteration scheme based on Equation 2.50. See Appendix A. Solutions were obtained for the boundary conditions shown in Equation 2.48 as well as for two additional cases with $\delta\theta_0 = 0.1$ and $\delta\theta_2 = 0.1$. The functionality coefficients were then calculated using Equation 2.44.

The results are plotted in Figure 2.6. It can be seen that the numerical dQdT results for C_{10} and C_{12} are in good agreement with the analytical dQdT results. The small discrepancy between the results is due to the truncation error in evaluating the series expressions of the analytical solution as well as the discretization error in the numerical solution. The overall agreement of the numerical and analytical results indicates the validity of numerical dQdT (Equation 2.44).

2.6 Characterizing the Functionalities: Special Cases

It was stated in Section 2.3 that for an N-temperature problem, the extended Newton formulation leads to a system of N equations with the $N(N-1)$ functionality coefficients, $\{C_{ij}\}$, unknown. For $N > 2$, this system is under-determined. The dQdT technique was developed to address this problem. In special cases, however, the number of unknowns may be reduced and the original system of equations solved.

2.6.1 Special Case: Symmetry

A functionality coefficient depends on geometry, velocity field and fluid properties. Therefore, if there is symmetry in geometry, velocity field and fluid properties, some functionality coefficients must be equal. In the parallel-plate channel (Figure 2.2), for example, with the fluid properties assumed to be constant and the velocity profile known to be symmetric about the channel centerline ($y = 0$), there is symmetry in the thermal interaction of the two walls. Therefore, the influence of T_2 on Q_1 is expected to be the same as the influence of T_1 on Q_2. Recalling that C_{ij} quantifies the sensitivity of Q_i to T_j, the preceding argument leads to: $C_{12} = C_{21}$. Moreover, symmetry indicates that the two wall temperatures must have the same influence on the rate of total heat transfer to fluid; $C_{01} = C_{02}$. Finally, heat transfer at the walls must be similarly influenced by the inlet temperature; $C_{10} = C_{20}$.

Note that dQdT can be utilized to confirm the observations above regarding symmetry. For example, compare the analytical expression found for C_{10} in Section 2.4.2 (Equation 2.39) to Equation 2.51, the dQdT result for C_{20}. It is shown in Chapter 4, using the eigencoefficients and eigenfunction derivatives given by Hatton & Turton (1962), that these two expressions are equivalent.

$$\begin{aligned} C_{20} &= -\left.\frac{\delta Q_2}{\delta T_0}\right|_{C_{ik}=\text{const}} \\ &= -\text{Re}\,\text{Pr}\,k\left\{\sum_{n=1}^{\infty}\frac{3}{8\lambda_n^2}\left(\frac{\partial B_n}{\partial \theta_0}\right)\left(\frac{\partial f_n}{\partial Y}\right)_{Y=-1}\left[1-\exp\left(-\frac{8}{3}\lambda_n^2 X\right)\right]\right\} \end{aligned} \tag{2.51}$$

In the following, the symmetry between the walls will be used to obtain the functionality coefficients algebraically.

Rewriting the Newton formulation of the channel problem (Equation 2.25) while taking note of symmetry between the walls, equations below are obtained:

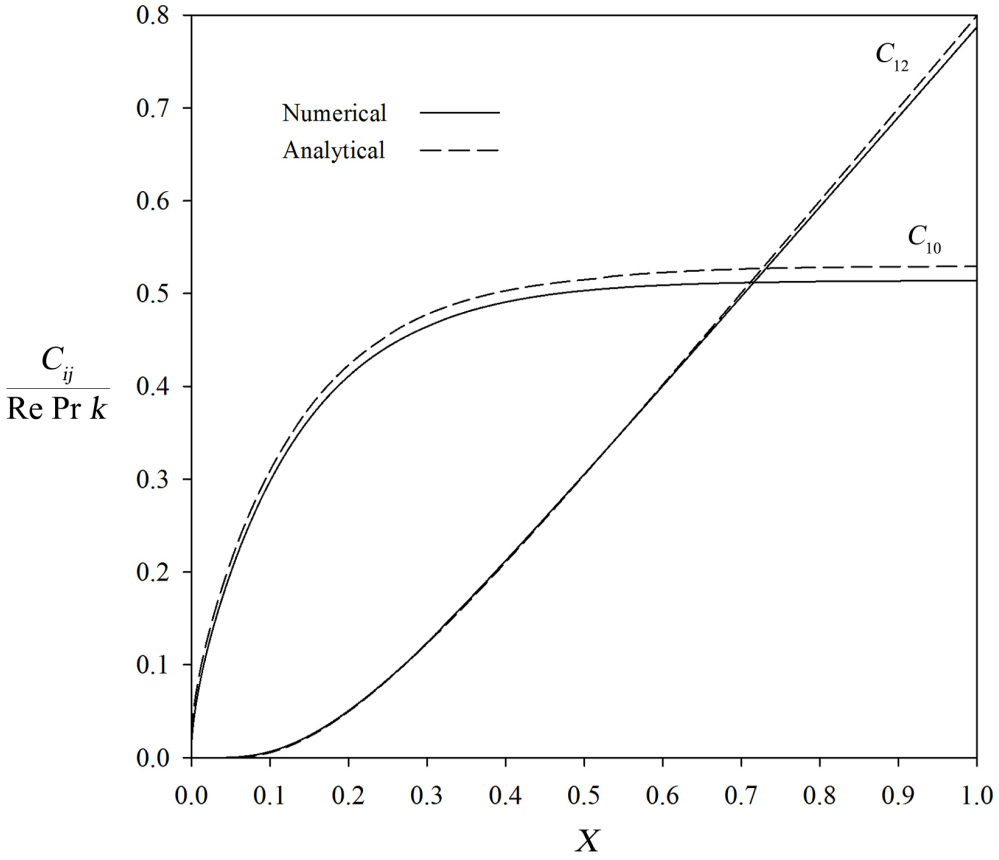

Figure 2.6: Functionality coefficients of hydrodynamically developed laminar flow in a channel with isothermal walls – Analytical and numerical dQdT results

$$\begin{cases} Q_0 = C_{01}(T_0 - T_1) + C_{01}(T_0 - T_2) \\ Q_1 = C_{10}(T_1 - T_0) + C_{12}(T_1 - T_2) \\ Q_2 = C_{10}(T_2 - T_0) + C_{12}(T_2 - T_1) \end{cases} \tag{2.52}$$

These equations form a system of three equations with three unknowns: C_{01}, C_{10} and C_{12}. Rearranging the first equation, C_{01} can be obtained as shown in Equation 2.53.

$$C_{01} = C_{02} = \frac{Q_0}{2T_0 - T_1 - T_2} \tag{2.53}$$

Summing the second and third equations, C_{10} is obtained as shown in Equation 2.54.

$$C_{10} = C_{20} = \frac{Q_1 + Q_2}{T_1 + T_2 - 2T_0} \tag{2.54}$$

Finally, with C_{10} known, the second equation can be solved for C_{12}. See Equation 2.55.

$$C_{12} = C_{21} = \frac{Q_1 - C_{10}(T_1 - T_0)}{T_1 - T_2} \tag{2.55}$$

Equations 2.53-2.55 can be used in conjunction with the expressions found for $\{Q_i\}$ in Section 2.4.2 to derive analytical expressions for $\{C_{ij}\}$. Using Equations 2.35, 2.36 and 2.54, for instance, C_{10} is obtained as shown in Equation 2.56.

$$\begin{aligned} C_{10} &= \frac{Q_1 + Q_2}{T_1 + T_2 - 2T_0} \\ &= -\mathrm{Re}\,\mathrm{Pr}\,\frac{k}{2}\left(\frac{T_1 - T_2}{T_1 + T_2 - 2T_0}\right) \\ &\times \left\{ \sum_{n=1}^{\infty} \frac{3B_n}{8\lambda_n^2} \left[\left(\frac{\partial f_n}{\partial Y}\right)_{Y=1} - \left(\frac{\partial f_n}{\partial Y}\right)_{Y=-1} \right] \left[1 - \exp\left(-\frac{8}{3}\lambda_n^2 X \right) \right] \right\} \\ &= \mathrm{Re}\,\mathrm{Pr}\,\frac{k}{2r_T} \left\{ \sum_{n=1}^{\infty} \frac{3B_n}{8\lambda_n^2} \left[\left(\frac{\partial f_n}{\partial Y}\right)_{Y=1} - \left(\frac{\partial f_n}{\partial Y}\right)_{Y=-1} \right] \left[1 - \exp\left(-\frac{8}{3}\lambda_n^2 X \right) \right] \right\} \end{aligned} \tag{2.56}$$

Denoting the even and odd eigenfunctions by subscripts "E" and "O" respectively, the relations below can be written by definition:

$$\begin{cases} \left.\dfrac{\partial f_{\mathrm{E},n}}{\partial Y}\right|_{Y=1} = -\left.\dfrac{\partial f_{\mathrm{E},n}}{\partial Y}\right|_{Y=1} \\ \\ \left.\dfrac{\partial f_{\mathrm{O},n}}{\partial Y}\right|_{Y=1} = \left.\dfrac{\partial f_{\mathrm{O},n}}{\partial Y}\right|_{Y=1} \end{cases}$$

Therefore, Equation 2.56 leads to:

$$C_{10} = \mathrm{Re}\,\mathrm{Pr}\,\frac{k}{r_T}\left\{\sum_{n=1}^{\infty}\frac{3B_{\mathrm{E},n}}{8\lambda_{\mathrm{E},n}^2}\left(\frac{\partial f_{\mathrm{E},n}}{\partial Y}\right)_{Y=1}\left[1-\exp\left(-\frac{8}{3}\lambda_{\mathrm{E},n}^2 X\right)\right]\right\} \tag{2.57}$$

In Section 2.4.2 (Equation 2.39) the expression below was obtained for C_{10} by applying dQdT:

$$C_{10} = \mathrm{Re}\,\mathrm{Pr}\,k\left\{\sum_{n=1}^{\infty}\frac{3}{8\lambda_n^2}\left(\frac{\partial B_n}{\partial\theta_0}\right)\left(\frac{\partial f_n}{\partial Y}\right)_{Y=1}\left[1-\exp\left(-\frac{8}{3}\lambda_n^2 X\right)\right]\right\}$$

Examining the expressions given by Hatton & Turton (1962) for $\{B_n\}$, it can be shown that:

$$\begin{cases} \dfrac{\partial B_{\mathrm{E},n}}{\partial\theta_0} = \dfrac{B_{\mathrm{E},n}}{r_T} \\ \\ \dfrac{\partial B_{\mathrm{O},n}}{\partial\theta_0} = 0 \end{cases}$$

Therefore, Equations 2.39 and 2.57 are equivalent. The symmetry argument presented in this section is hence verified.

2.6.2 Special Case: Linearity

A functionality coefficient depends on geometry, velocity field and fluid properties. Therefore, in a linear problem, i.e. in the absence of thermal effects on the velocity field and fluid properties, $\{C_{ij}\}$ is independent of $\{T_i\}$. This means that in linear problems, $\{C_{ij}\}$ evaluated for a certain set of boundary temperatures, $\{T_i\}$, is the unique and universal set applicable to any $\{T_i\}$. Therefore, to find the functionality coefficient C_{ij}, it is sufficient to obtain the heat transfer rate Q_i for $\{T_k \,|\, \forall k \neq j \,;\, T_k = T_i\}$. Applying Equation 2.6, Q_i can then be written as:

$$Q_i = \sum_k C_{ik}(T_i - T_k) = C_{ij}(T_i - T_j) \qquad (\forall k \neq j \,;\, T_k = T_i)$$

Hence, C_{ij} can be calculated as:

$$C_{ij} = \frac{Q_i}{T_i - T_j} \qquad (\forall k \neq j \,;\, T_k = T_i) \tag{2.58}$$

The numerical scheme developed earlier for hydrodynamically developed laminar flow in a parallel-plate channel with isothermal walls can be used to demonstrate Equation 2.58. For instance, C_{10} can be obtained by setting $\theta_1 = \theta_2 = 1$ and $\theta_0 = 0$. In this case, the numerical solution yielded the non-dimensional heat transfer rate at $X = 0.5$ to be:

$$\left(\frac{1}{\mathrm{Re\ Pr}}\right)\frac{Q_1}{k(T_1 - T_0)} = 0.4934$$

According to Equation 2.58, C_{10} in this case is:

$$\frac{C_{10}}{\mathrm{Re\,Pr}\,k} = \frac{0.4934}{1 - 0} = 0.4934$$

The analytical and numerical dQdT results (Figure 2.6) for $C_{10}/(\mathrm{Re}\,\mathrm{Pr}\,k)$ at $X = 0.5$ were respectively 0.5149 and 0.4938. Equation 2.58 is thus validated.

Similarly, to obtain C_{12} using Equation 2.58, a numerical solution was obtained for $\theta_1 = \theta_0 = 1$, $\theta_2 = 0$. In this case, Q_1 at $X = 0.5$ was:

$$\left(\frac{1}{\mathrm{Re}\ \mathrm{Pr}}\right)\frac{Q_1}{k(T_1 - T_0)} = 0.3056$$

Therefore:

$$\frac{C_{12}}{\mathrm{Re}\,\mathrm{Pr}\,k} = \frac{0.3056}{1-0} = 0.3056$$

As a further check on Equation 2.58, compare the result above to the analytical and numerical dQdT results (Figure 2.6) for $C_{12}/(\mathrm{Re}\,\mathrm{Pr}\,k)$ at $X = 0.5$: 0.3047 and 0.3054. The close agreement of these results, again, verifies Equation 2.58.

2.7 Summary

In multi-temperature convection problems, heat transfer takes place between more than two isothermal boundaries. In this case, the Newton law of cooling must be reconciled with the presence of multiple boundary temperatures. Traditionally, this is done by combining various independent (and sometimes dependent) temperatures of the problem to construct an effective temperature difference. In this chapter, an extension of the Newton law of cooling was proposed to formulate a multi-temperature convection problem exclusively in terms of the independent, boundary temperatures. This formulation leads to additional parameters, dubbed functionality coefficients, each characterizing the effect of one boundary temperature on the heat transfer rate at another isothermal boundary. The dQdT technique was developed and validated to calculate the functionality coefficients.

This technique entails a baseline solution to full set of governing equations and subsequent solutions to the energy equation with perturbed boundary conditions. dQdT can be implemented in both analytical and numerical solutions.

Chapter 3

The Resistor-Network Model

Steady, one-dimensional heat conduction with no internal generation and constant thermophysical properties is often modeled using a network of thermal resistors. This approach is sometimes extended to cases of convective or radiative heat transfer, usually at the boundaries of a domain in which heat conduction is of interest. A common example is the composite wall, shown schematically in Figure 3.1 along with the corresponding resistor network.

In a unique extension of the resistor-network approach, the ASHWAT models for heat transfer through complex fenestration systems were developed based on a general network of thermal resistors (Wright 2008, Wright et al. 2009, Barnaby et al. 2009). The general resistor-network used in ASHWAT was briefly introduced in Chapter 1. The ASHWAT resistor-network is unique in two aspects. First, the network is used to model convection and radiation. Second, the problem of convection at the indoor side of a CFS is particularly unique in that heat transfer can take place between all the isothermal boundaries. Consequently, in the corresponding resistor network, also introduced in Chapter 1, all the temperature nodes are connected, forming a delta network. Contrast the resistor network of Figure 3.1 with the one shown in Figure 1.2; in Figure 3.1 there is

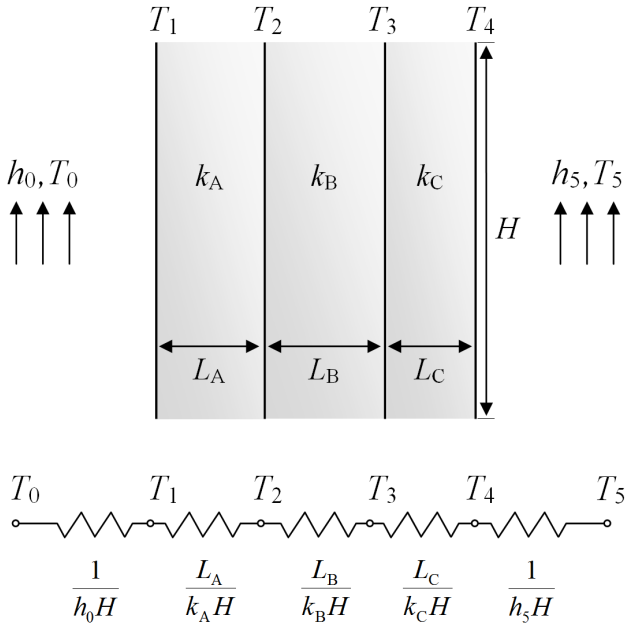

Figure 3.1: The thermal-resistor network of heat transfer in a composite wall with convection at the boundaries

no connection between non-adjacent nodes (e.g. T_0 and T_2), "bypassing" the intermediate layers (T_1).

The resistor-network model used in ASHWAT has been successful in predicting the energy performance of fenestration systems as well as characterizing the solar/thermal performance of different shading attachments. It is also computationally advantageous in time-step building energy simulation (Wright et al. 2011, Lomanowski & Wright 2012). Motivated by the notable success and advantage of ASHWAT, the extension of the resistor-network model to the general problem of multi-temperature convection is explored in this chapter.

3.1 The Electrical Analogy

The concept of thermal resistance, and by extension using arrays of thermal resistors to represent a heat transfer problem, is based on the analogy between the diffusion of electrical

charge and diffusive heat transfer. An important feature of electrical current, and therefore a criterion for the validity of the electrical analogy, is that it is a scalar. This has two important implications: 1) electrical current obeys the rule of algebraic summation, and 2) there is reciprocity of current between any two nodes directly connected in an electrical circuit. In other words, the current from node i to j is equal in magnitude to the current in reverse direction, from j to i.

Therefore, the validity of the electrical analogy, and hence the resistor-network model, can be determined by examining the algebraic summation and reciprocity of heat transfer. These requirements do not impose any restrictions on the mode of heat transfer.

3.2 Resistor-Network Model of Convection

Consider a fluid flow entering with a uniform temperature the channel formed between two parallel isothermal plates. As discussed in Chapter 2, the extended Newton formulation of the problem gives:

$$\begin{cases} Q_0 = C_{01}(T_0 - T_1) + C_{02}(T_0 - T_2) \\ Q_1 = C_{10}(T_1 - T_0) + C_{12}(T_1 - T_2) \\ Q_2 = C_{20}(T_2 - T_0) + C_{21}(T_2 - T_1) \end{cases} \tag{3.1}$$

In Chapter 2, dQdT was applied to find C_{10} and C_{12} of the channel problem. As will be shown in Chapter 4, applying dQdT to obtain the other functionality coefficients of the problem, it can be shown that: $C_{ij} = C_{ji}$. Alternatively, the algebraic relations derived in Chapter 2 (Section 2.6.1) based on the symmetry argument can be used to confirm $C_{ij} = C_{ji}$.

For example, consider the relations for C_{01} and C_{10} (Equations 2.53 and 2.54):

$$C_{01} = \frac{Q_0}{2T_0 - T_1 - T_2}$$

$$C_{10} = \frac{Q_1 + Q_2}{T_1 + T_2 - 2T_0}$$

Recalling the overall energy balance of the channel;

$$Q_0 = -Q_1 - Q_2$$

It is shown that: $C_{01} = C_{10}$.

With $C_{ij} = C_{ji}$ Equation 3.1 can be rewritten as:

$$\begin{cases} Q_0 = C_{10}(T_0 - T_1) + C_{20}(T_0 - T_2) \\ Q_1 = C_{10}(T_1 - T_0) + C_{12}(T_1 - T_2) \\ Q_2 = C_{20}(T_2 - T_0) + C_{12}(T_2 - T_1) \end{cases} \tag{3.2}$$

The equations above constitute the nodal current (energy) balances of the delta resistor-network shown in Figure 3.2. In this network, the nodes at T_1 at T_2 represent the isothermal channel walls. The third node, at T_0, represents the fluid flow.[1] Note that T_0 is the only independent (boundary) temperature corresponding to the flow. The temperature nodes are connected through three convective resistances, characterized by the functionality coefficients, $\{C_{ij}\}$. To borrow the electrical-circuit terminology, C_{ij} is the conductance of the leg connecting T_i and T_j. The term $C_{ij}(T_i - T_j)$ is then the "thermal current" through this leg, i.e. between T_i and T_j. Introducing $Q_{ij} = C_{ij}(T_i - T_j)$, Equation 3.2 can be written in the general form shown in Equation 3.3.

[1] Although T_0 is the inlet temperature, this node does not correspond to a specific physical location; it represents the fluid flow throughout the channel.

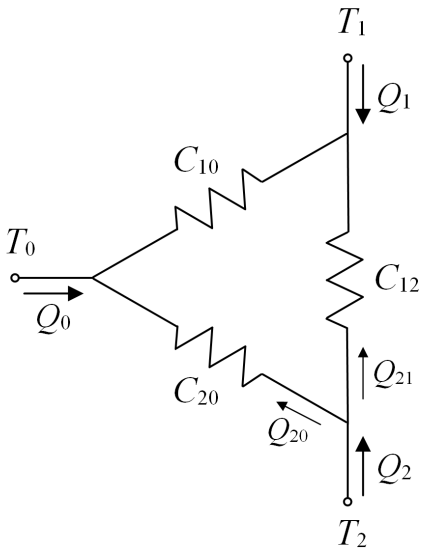

Figure 3.2: The resistor network of flow in a channel with isothermal walls

$$Q_i = \sum_j C_{ij}(T_i - T_j) = \sum_j Q_{ij} \tag{3.3}$$

Hence, the extended Newton formulation ensures that the thermal current at each isothermal boundary does obey the rule of algebraic summation. With $C_{ij} = C_{ji}$, there is reciprocity of thermal current between the nodes; $|Q_{ij}| = |Q_{ji}|$. Therefore the resistor-network model is applicable.

It is helpful at this point to examine a multi-temperature convection problem that cannot be represented by a network of convective resistors, i.e. a problem wherein algebraic summation or reciprocity of thermal currents is not satisfied. Consider cross flow over two parallel cylinders with isothermal surfaces, in "tandem" arrangement. See Figure 3.3.

The flow is characterized by the Reynolds number, Re, defined in Equation 3.4 wherein u_0 denotes the free-stream velocity.

$$\mathrm{Re} = \frac{\rho u_0 D_1}{\mu} \tag{3.4}$$

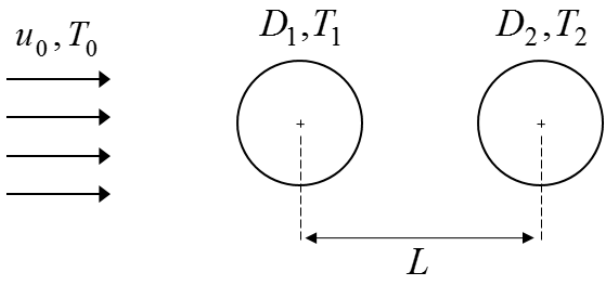

Figure 3.3: Schematic of cross flow over a pair of isothermal cylinders in tandem

Equation 3.1 gives the Newton formulation of heat transfer also for this three-temperature problem. Therefore, the algebraic summation of thermal currents is satisfied. The reciprocity of current is however contingent on the condition that $C_{ij} = C_{ji}$.

It is known from the physics of the problem that (in the subsonic regime), due to the position of the cylinders in the flow, the influence of T_1 on $\{Q_i\}$ is larger than the influence of T_2, simply because T_1 is upstream of T_2. Recalling that C_{ij} quantifies the sensitivity of Q_i to T_j, it is hence expected that: $C_{21} > C_{12}$. dQdT can be used to verify this result.

The commercial solver ANSYS Fluent was used to implement dQdT numerically and calculate the functionality coefficients of the problem. Solutions were generated for $D_1 = D_2 = L/2$, $\mathrm{Pr} = 0.7$ and $0 \leq \mathrm{Re} < 60$. This range of Re was chosen in order to maintain the flow laminar and steady, and the numerical solutions straightforward. The detailed discussion of the CFD solutions is deferred to Chapter 7. Presently, attention is focused on the dQdT results.

The dQdT results for the cylinder-cylinder functionality coefficients, C_{12} and C_{21}, are plotted in Figure 3.4. At $\mathrm{Re} = 0$, i.e. for pure conduction between the cylinders, the coefficients correspond to the conduction shape factor of two parallel cylinders of equal diameter in an infinite medium and at the given spacing; $C_{21}/k = C_{12}/k = S = 2.3$. For $\mathrm{Re} > 0$, however; $C_{21} > C_{12}$. In other words, in the presence of advection, the effect of T_1 on Q_2 is larger than the effect of T_2 on Q_1. Therefore, the reciprocity of thermal currents

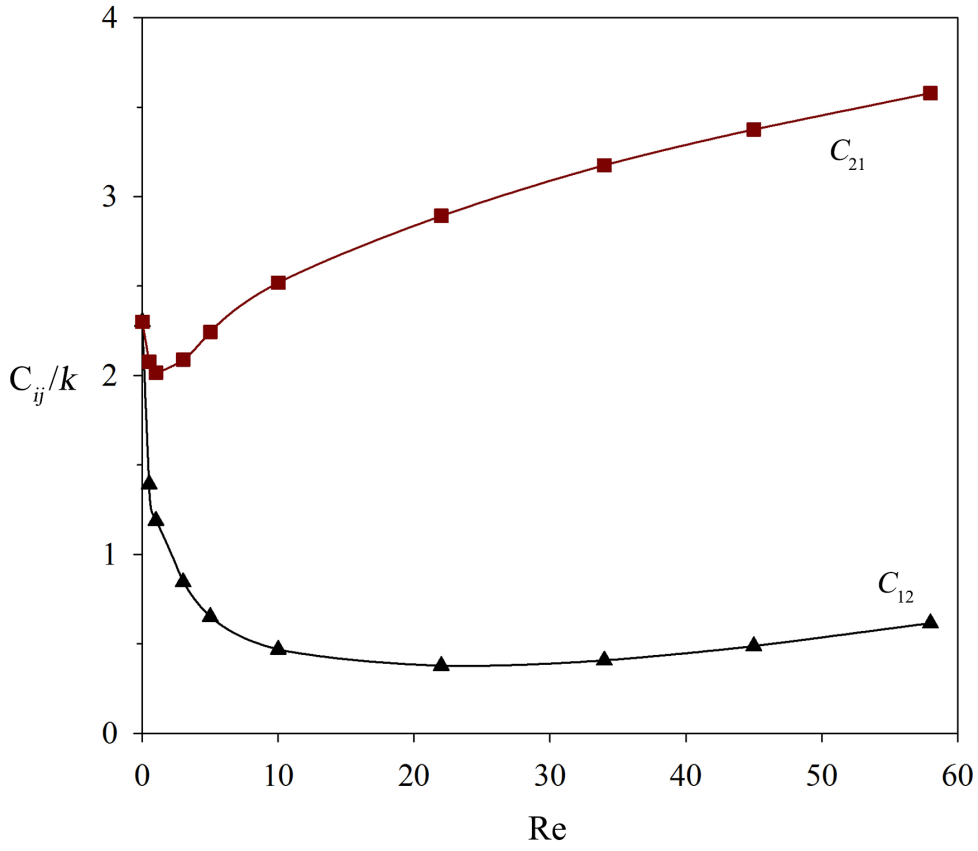

Figure 3.4: Cylinder-cylinder functionality coefficients of cross flow over cylinders Tandem alignment ($D_1 = D_2 = L/2$, Pr = 0.7)

does not exist; the configuration shown in Figure 3.3 cannot be represented by a network of convective resistors.

Consider now the cylinders in side-by-side arrangement, shown in Figure 3.5. The numerical dQdT results for the cylinder-cylinder functionality coefficients of this configuration are shown in Figure 3.6. In this case, $C_{12} = C_{21}$. This results was expected due to the symmetric position of the cylinders in the flow field. Likewise, it can be shown that: $C_{10} = C_{01}$ and $C_{20} = C_{02}$. Therefore, the reciprocity of thermal currents is satisfied and the multi-temperature problem *can* be represented by the delta resistor network of Figure 3.2.

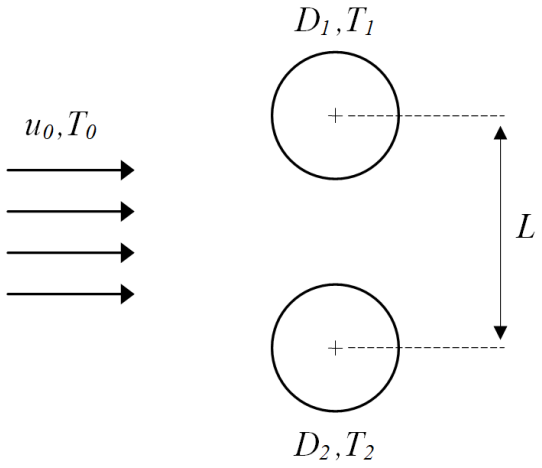

Figure 3.5: Schematic of cross flow over a pair of side-by-side isothermal cylinders

The examples above show the utility of the dQdT technique in establishing the validity of the resistor-network model for a multi-temperature convection problem.

3.3 The "Split" of Heat Transfer

In earlier publication, e.g. Foroushani et al. (2017b,c), the thermal current $Q_{ij} = C_{ij}(T_i - T_j)$ in the resistor-network model was dubbed a "paired" heat transfer rate and interpreted as the rate of heat transfer between the nodes at T_i and T_j. Nevertheless, "splitting" convective heat transfer into paired components, i.e. breaking Q_i into components $\{Q_{ij}\}$, may not be completely valid. An important distinction between electrical current and heat transfer must be emphasized. Electrical current is the *process* of the transport of electrons — an *entity*. Heat transfer, on the other hand, is a process with no corresponding entity. Note that this is also a point of departure between heat transfer and mass transfer. At a conceptual level, therefore, the analogy between the diffusion of electrical charge and heat transfer seems incomplete.

An implication of this phenomenological distinction is that the paired thermal current Q_{ij} may not have a clear physical meaning, especially in convective heat transfer where the

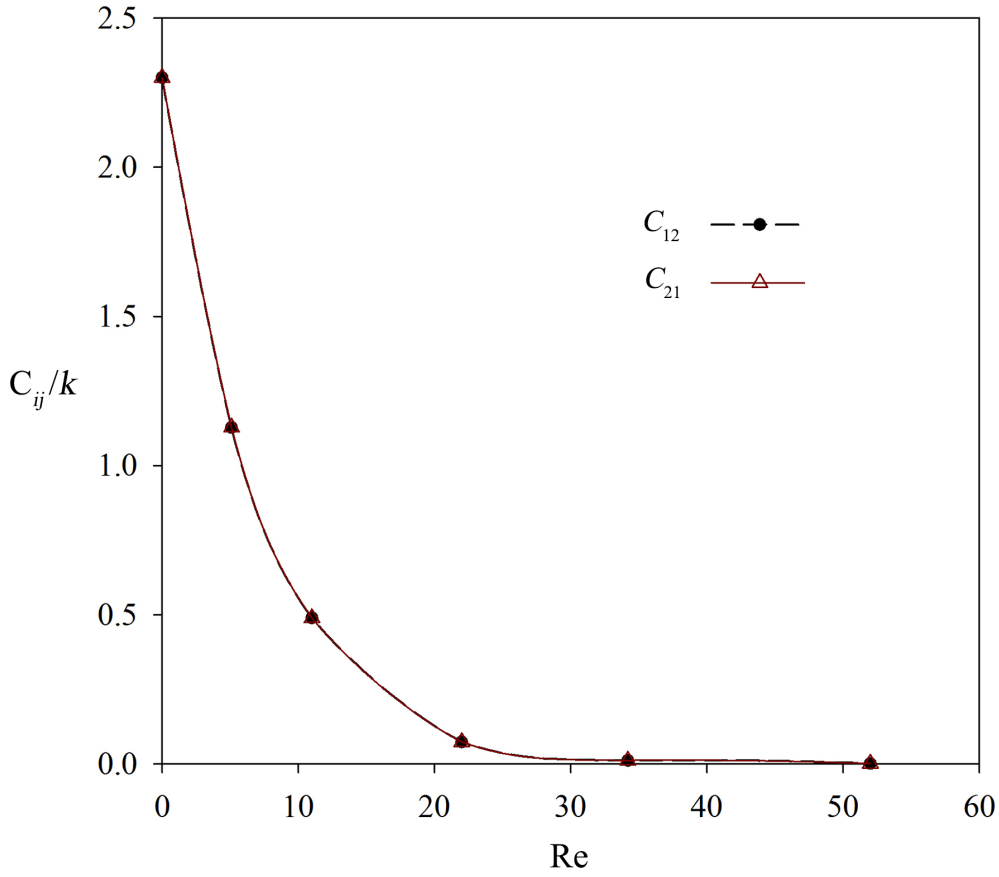

Figure 3.6: Cylinder-cylinder functionality coefficients of cross flow over cylinders Side-by-side alignment ($L = 2D_1 = 2D_2$, Pr = 0.7)

fluid flow acts as an intermediate medium between solid surfaces. Note that this ambiguity does not exist in radiation. In fact, the classical theory of thermal radiation is centered on tracking and resolving the split of heat transfer between different surfaces and media. Likewise, heatlines provide a graphical tool for tracking heat transfer in the conduction regime and resolving the split of heat transfer.

But splitting convective heat transfer is not as straightforward. In the channel problem, for example, there is heat transfer at the channel walls (Q_1 and Q_2) and there is heat transfer to the fluid (Q_0). Near the channel inlet, before the thermal boundary layers merge, heat transfer takes place between either wall and the fluid. Conversely, in the thermally developed limit, there is no *net* heat transfer to the fluid; heat transfer occurs

between the walls. In general, however, it seems impossible to track the heat transfer at a wall to determine where it "ends up" — the fluid or the other wall.

Aside from conceptual difficulty, resolving the split of heat transfer entails also a difficult practical problem which is, in essence, equivalent to the problem of multi-temperature convection, discussed in Chapter 2. The extension of heatlines for visualizing convective heat transfer (Kimura & Bejan 1983) seemed, at first sight, a viable option for tracking heat transfer. However, because of their dependence on *a* reference temperature (in the advection term), convection heatlines are not unique (Trevisan & Bejan 1987). This limits the utility of the heatline method significantly.

The dQdT technique resolves the *practical* aspect of the split of heat transfer; with $\{C_{ij}\}$ known, the paired heat transfer rates, $\{Q_{ij}\}$, can be easily calculated. The conceptual question must nonetheless be considered carefully. In other words, separating convective heat transfer into paired components, e.g. wall-to-wall, $Q_{12} = C_{12}(T_1 - T_2)$, or wall-to-fluid, $Q_{10} = C_{10}(T_1 - T_0)$, may not be valid outside the context of the resistor-network model, i.e. beyond the metaphor of paired thermal currents.

3.4 Summary

Some multi-temperature convection problems may be represented by a network of convective resistors. The dQdT technique provides a means for assessing the validity of this model. If there is reciprocity between the functionality coefficients, i.e. $C_{ij} = C_{ji}$, the resistor-network model is applicable; the multi-temperature problem can be modeled as a network of temperature nodes representing the isothermal boundaries. The functionality coefficients, $\{C_{ij}\}$, are the conductances of this network. However, the paired thermal current through the legs of this network may not have a clear physical interpretation.

Chapter 4

The Asymmetric Graetz Problem Revisited

Flow in heated passages has been a classical topic of interest in heat transfer due mainly to its application in the design and analysis of heat exchangers. For fluids with a high Prandtl number (oils, organic liquids, etc.) or cases where the fluid passes through an unheated section first, hydrodynamic development may occur well before thermal development. In this case, the thermal analysis of the flow is done assuming a fully developed velocity profile.

In 1882, Graetz published a solution to the problem of heat transfer in an isothermal pipe for a hydrodynamically developed laminar flow with negligible axial conduction and viscous dissipation (Graetz 1882). This solution is considered to be the first analytical solution to a convection problem. Accordingly, the problem of convective heat transfer in hydrodynamically developed laminar flow in a passage with isothermal walls is known as the Graetz problem.

In recent years, the emergence of such devices as microchannels and fuel cells has renewed the interest in the Graetz problem. Numerous variations and extensions of the

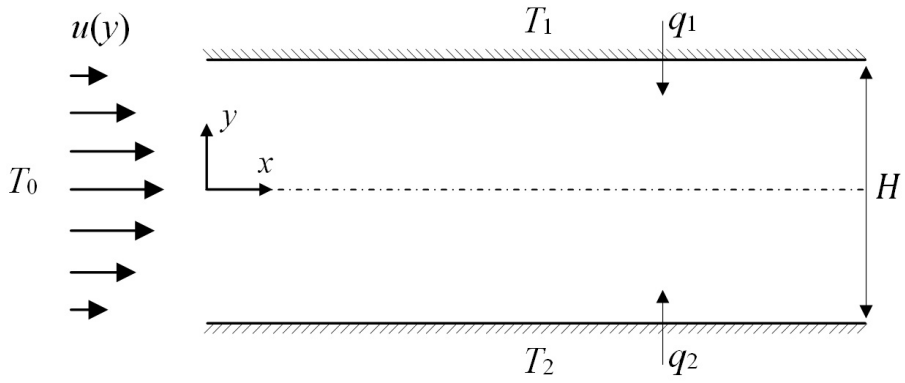

Figure 4.1: Schematic of hydrodynamically developed flow
in a parallel-plate channel with isothermal walls

problem have been studied; several analytical and numerical solutions have been published. Recent reviews of the Graetz-problem literature can be found in the papers by Ryzhkov (2013) and Haddout & Lahjomri (2015). A classical solution from the literature is of particular interest in this chapter.

Consider a hydrodynamically developed laminar flow at a uniform temperature, T_0, entering the channel formed between two semi-infinite parallel plates maintained at temperatures T_1 and T_2, separated by distance H. See Figure 4.1. In general, the walls may be heated "asymmetrically", i.e. $T_1 \neq T_2$. Hence, the problem of calculating the rate of heat transfer in the configuration shown in Figure 4.1 is known as the asymmetric Graetz problem.

4.1 The Analytical Solution

With constant fluid properties, negligible conduction in the x-direction and negligible viscous dissipation, the energy equation for laminar flow is reduced to Equation 4.1.

$$\rho u_{\mathrm{fd}} c_p \frac{\partial T}{\partial x} = k \frac{\partial^2 T}{\partial y^2} \tag{4.1}$$

The fully developed laminar velocity profile, u_{fd}, is given by Equation 4.2.

$$u_{\text{fd}} = -\frac{1}{2\mu}\left(\frac{\mathrm{d}p}{\mathrm{d}x}\right)\left(\frac{H^2}{4} - y^2\right) \tag{4.2}$$

The boundary conditions of the problem are:

$$\begin{aligned} x = 0 \quad &; \quad T = T_0 \\ y = H/2 \quad &; \quad T = T_1 \\ y = -H/2 \quad &; \quad T = T_2 \end{aligned} \tag{4.3}$$

The problem is described by three isothermal boundaries. It is hence a three-temperature problem. A temperature ratio is often used to specify the ordering of $\{T_i\}$. Equation 4.4 shows a common definition (Hatton & Turton 1962) with $T_{\text{wm}} = (T_1 + T_2)/2$.

$$r_T = \frac{T_0 - T_{\text{wm}}}{T_1 - T_{\text{wm}}} \tag{4.4}$$

Hatton & Turton (1962) applied separation of variables to obtain an analytical solution to Equation 4.1 subject to the conditions of Equation 4.3. See Equation 4.5.

$$\theta = Y - \sum_{n=1}^{\infty} B_n f_n \exp\left(-\frac{8}{3}\lambda_n^2 X\right) \tag{4.5}$$

In Equation 4.5, θ is the dimensionless temperature defined in Equation 4.6 and Y is the dimensionless lateral coordinate: $Y = 2y/H$. X is the inverse Graetz number, defined in Equation 4.7, representing the stream-wise coordinate.

$$\theta = \frac{T - T_{\text{wm}}}{T_1 - T_{\text{wm}}} \tag{4.6}$$

$$X = \frac{2x}{H}\left(\frac{1}{\mathrm{Re}\,\mathrm{Pr}}\right) \tag{4.7}$$

The flow is characterized by the Reynolds number defined in Equation 4.8.

$$\mathrm{Re} = \frac{\rho u_{\mathrm{m}}(2H)}{\mu} \tag{4.8}$$

The first term of the solution shown in Equation 4.5, Y, is the linear, fully developed temperature profile. The second term is the series solution to a Sturm-Liouville system, with B_n, f_n and λ_n denoting the eigencoefficients, eigenfunctions and eigenvalues, respectively. Hatton & Turton (1962) have presented the first eight eigenvalues of the problem.

Hatton & Turton (1962) used the solution to the temperature field, $\theta(x, y)$, to derive a series expression for the mean fluid temperature, T_{m}. The evolution of T and T_{m} along the channel is shown in Figure 4.2 for a sample case with $T_0 < T_1 < T_2$. This figure reveals important aspects of the thermal development of the flow. At the channel inlet the fluid temperature is uniform: $T(x = 0) = T_0$. Moving downstream, due to heat transfer from the walls the temperature profile evolves, approaching a linear profile in the $x \to \infty$ limit. The variation of heat flux at the walls, q_1 and q_2, can be determined by examining the temperature gradient, $\partial T/\partial y$, at the walls. In the thermally developed limit;

i) The temperature profile becomes linear with:

$$\lim_{x\to\infty} \frac{\partial T}{\partial y} = \frac{T_1 - T_2}{H}$$

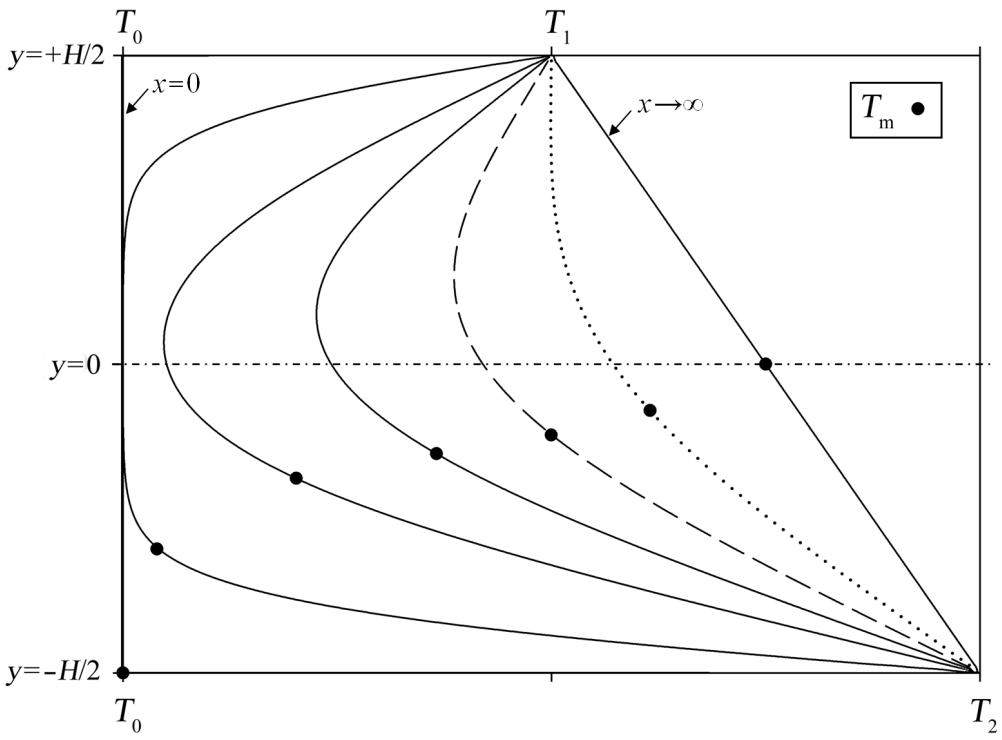

Figure 4.2: Evolution of temperature profile and mean fluid temperature (T_{m}) in the asymmetric Graetz problem ($r_T = 3$)

ii) The mean fluid temperature reaches the mean wall temperature:

$$\lim_{x\to\infty} T_{\mathrm{m}} = T_{\mathrm{wm}}$$

iii) The net heat flux to the fluid decays to zero:

$$\lim_{x\to\infty} (q_1 + q_2) = \frac{k}{H}(T_1 - T_2) - \frac{k}{H}(T_1 - T_2) = 0$$

Attention is usually focused on the thermally developing region where the temperature profile evolves and the net heat transfer to the fluid takes place.

4.2 Traditional Formulation

In the paper by Hatton & Turton (1962), results are presented in terms of local Nusselt numbers, Nu_1 and Nu_2, defined in Equation 4.9.

$$\mathrm{Nu}_i = \frac{q_i}{T_i - T_\mathrm{m}}\left(\frac{2H}{k}\right) \qquad (i = 1, 2) \tag{4.9}$$

The expressions presented by Hatton & Turton (1962) for Nu_1 and Nu_2 are reproduced in Equations 4.10 and 4.11. Note the emergence of r_T in these expressions.

$$\begin{aligned}\mathrm{Nu}_1 = \Bigg\{ 1 - 2r_T \sum_{n=1}^{\infty} \frac{1}{\lambda_{\mathrm{E}n}} \left[\frac{(\partial f_{\mathrm{E}n}/\partial y)_{Y=1}}{(\partial f_{\mathrm{E}n}/\partial \lambda_{\mathrm{E}n})_{Y=1}}\right] \exp(-8\lambda_{\mathrm{E}n}^2 X/3) \\ + 2\sum_{n=1}^{\infty} \frac{1}{\lambda_{\mathrm{O}n}} \left[\frac{(\partial f_{\mathrm{O}n}/\partial y)_{Y=1}}{(\partial f_{\mathrm{O}n}/\partial \lambda_{\mathrm{O}n})_{Y=1}}\right] \exp(-8\lambda_{\mathrm{O}n}^2 X/3) \Bigg\} \Bigg/ \\ \left\{ \frac{1}{4} - \frac{3r_T}{4} \sum_{n=1}^{\infty} \frac{1}{\lambda_{\mathrm{E}n}^3} \left[\frac{(\partial f_{\mathrm{E}n}/\partial y)_{Y=1}}{(\partial f_{\mathrm{E}n}/\partial \lambda_{\mathrm{E}n})_{Y=1}}\right] \exp(-8\lambda_{\mathrm{E}n}^2 X/3) \right\}\end{aligned} \tag{4.10}$$

$$\begin{aligned}\mathrm{Nu}_2 = \Bigg\{ 1 + 2r_T \sum_{n=1}^{\infty} \frac{1}{\lambda_{\mathrm{E}n}} \left[\frac{(\partial f_{\mathrm{E}n}/\partial y)_{Y=1}}{(\partial f_{\mathrm{E}n}/\partial \lambda_{\mathrm{E}n})_{Y=1}}\right] \exp(-8\lambda_{\mathrm{E}n}^2 X/3) \\ + 2\sum_{n=1}^{\infty} \frac{1}{\lambda_{\mathrm{O}n}} \left[\frac{(\partial f_{\mathrm{O}n}/\partial y)_{Y=1}}{(\partial f_{\mathrm{O}n}/\partial \lambda_{\mathrm{O}n})_{Y=1}}\right] \exp(-8\lambda_{\mathrm{O}n}^2 X/3) \Bigg\} \Bigg/ \\ \left\{ \frac{1}{4} + \frac{3r_T}{4} \sum_{n=1}^{\infty} \frac{1}{\lambda_{\mathrm{E}n}^3} \left[\frac{(\partial f_{\mathrm{E}n}/\partial y)_{Y=1}}{(\partial f_{\mathrm{E}n}/\partial \lambda_{\mathrm{E}n})_{Y=1}}\right] \exp(-8\lambda_{\mathrm{E}n}^2 X/3) \right\}\end{aligned} \tag{4.11}$$

In Figure 4.3, a plot of $\{\mathrm{Nu}_i\}$ for various temperature ratios is reproduced from the work of Hatton & Turton (1962). Several important observations can be made about this

plot. First, even though q_1 is both continuous and finite for $X > 0$, Nu_1 has a singularity at some finite distance downstream of the channel ($X > 0$) if $r_T > 1$. This singularity is in addition to the singularity at the channel inlet ($X = 0$) which is caused by the singularity in the heat flux. The extra singularity arises because the driving temperature difference used to define Nu_1 (Equation 4.9) is based on T_m. When $T_0 < T_1 < T_2$, for instance, Nu_1 becomes indefinite in the location where $T_\mathrm{m} = T_1$. Moreover, Nu_1 changes sign through this singularity, which is non-physical; q_1 does not change sign until the temperature gradient normal to the wall becomes zero, i.e. at a local adiabatic point where $\mathrm{Nu}_1 = 0$. As shown by Mitrović et al. (2006), the singularity point where $T_\mathrm{m} = T_1$ (dashed curve in Figure 4.2), is distinct from the local adiabatic point (dotted curve). As pointed out in different sources, e.g. Nield (2004), the singularities seen in Figure 4.3 reduce the utility of the results. To address this deficiency, Nield (2004) proposed a Nusselt number based on the total heat flux, $(q_1 + q_2)$, and the difference between the mean wall and fluid temperatures, $(T_\mathrm{wm} - T_\mathrm{m})$. Both $(q_1 + q_2)$ and $(T_\mathrm{wm} - T_\mathrm{m})$ decay continuously to zero as the flow approaches its thermally developed limit. Therefore, the extra singularity is eliminated.

The second, and more important, observation about Figure 4.3 is that $\{\mathrm{Nu}_i\}$ depends on r_T. This is unexpected. In the two-temperature case of symmetrically heated walls, i.e. for $T_1 = T_2$, the Nusselt number can be expressed as $\mathrm{Nu} = \mathrm{Nu}(\mathrm{Re},\mathrm{Pr})$. Given that the only difference between the asymmetric and symmetric cases is an additional non-homogeneous (but linear) boundary condition, the nature of the solutions should be the same. In other words, it is expected that in the case of $T_1 \neq T_2$ too the solution could be expressed in terms of Nusselt numbers that are independent of r_T. The results presented by Hatton & Turton (1962) exhibit this feature only in the thermally developed limit:

$$\lim_{X\to\infty} \mathrm{Nu}_1 = \lim_{X\to\infty} \mathrm{Nu}_2 = 4$$

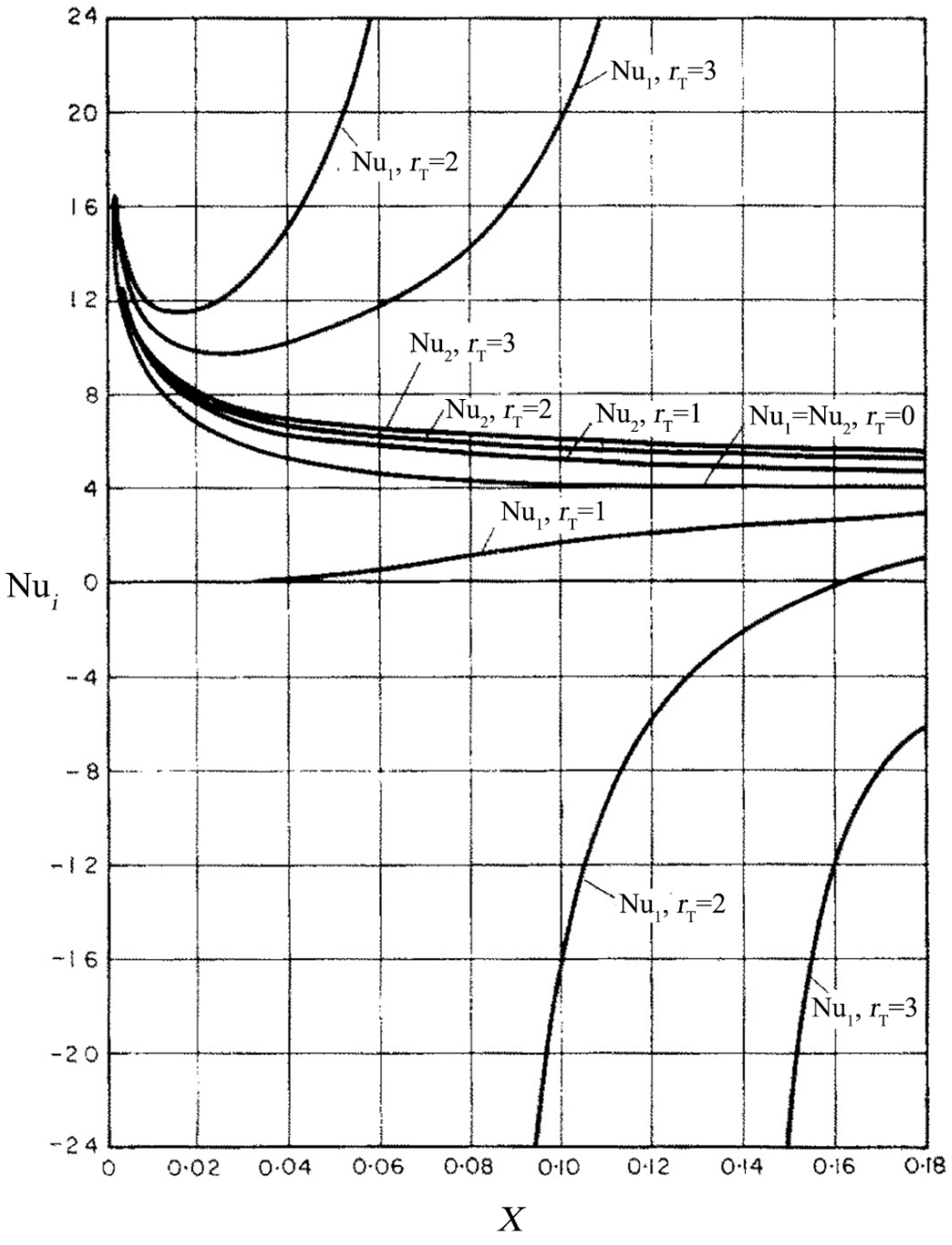

Figure 4.3: Local Nusselt numbers of the asymmetric Graetz problem (Hatton & Turton 1962) [Reproduced with permission; labels modified to match current nomenclature]

The modified Nusselt number proposed by Nield (2004) is also independent of r_T only in the thermally developed limit.

Finally, Figure 4.3 may be misleading by suggesting that the thermal development length of the flow is a function of r_T. As will be demonstrated, this is not the case.

4.3 Extended Newton Formulation

The foregoing discussion demonstrates shortcomings of using a single heat transfer coefficient for a multi-temperature convection problem — the traditional formulation. Now consider the extended Newton formulation of the problem:

$$Q_i = \sum_j C_{ij}(T_i - T_j)$$

Each of the three heat transfer rates is characterized by two functionality coefficients. In Chapter 2, dQdT was applied to obtain C_{10} and C_{12}:

$$C_{10} = \mathrm{Re}\,\mathrm{Pr}\,k\left\{\sum_{n=1}^{\infty}\frac{3}{8\lambda_n^2}\left(\frac{\partial B_n}{\partial\theta_0}\right)\left(\frac{\partial f_n}{\partial Y}\right)_{Y=1}\left[1-\exp\left(-\frac{8}{3}\lambda_n^2 X\right)\right]\right\}$$

$$C_{12} = -\mathrm{Re}\,\mathrm{Pr}\,k\left\{X-\sum_{n=1}^{\infty}\frac{3B_n}{8\lambda_n^2}\left(\frac{\partial f_n}{\partial Y}\right)_{Y=1}\left[1-\exp\left(-\frac{8}{3}\lambda_n^2 X\right)\right]\right.$$
$$\left.-\sum_{n=1}^{\infty}\frac{3}{8\lambda_n^2}\left(\frac{\partial B_n}{\partial\theta_2}\right)\left(\frac{\partial f_n}{\partial Y}\right)_{Y=1}\left[1-\exp\left(-\frac{8}{3}\lambda_n^2 X\right)\right]\right\}$$

4.3.1 Average Paired Nusselt Numbers

An average paired Nusselt number may be defined as shown in Equation 4.12 to express $\{C_{ij}\}$ in dimensionless form. The term "paired" emphasizes the idea that $\overline{\mathrm{Nu}}_{ij}$ corresponds to a specific pair of isothermal boundaries and distinguishes it from the traditional "total" Nusselt number.

$$\overline{\mathrm{Nu}}_{ij} = \frac{C_{ij}}{k}\left(\frac{2H}{x}\right) \tag{4.12}$$

Using the expressions obtained on Chapter 2 and Equation 4.12, $\overline{\mathrm{Nu}}_{10}$ and $\overline{\mathrm{Nu}}_{12}$, the paired Nusselt numbers characterizing heat transfer at the upper wall (Q_1), are:

$$\overline{\mathrm{Nu}}_{10} = \frac{4}{X}\sum_{n=1}^{\infty}\frac{3}{8\lambda_n^2}\left(\frac{\partial B_n}{\partial\theta_0}\right)\left(\frac{\partial f_n}{\partial Y}\right)_{Y=1}\left[1-\exp\left(-\frac{8}{3}\lambda_n^2 X\right)\right] \tag{4.13}$$

$$\begin{aligned}\overline{\mathrm{Nu}}_{12} = -\frac{4}{X}\Bigg\{ & X - \sum_{n=1}^{\infty}\frac{3B_n}{8\lambda_n^2}\left(\frac{\partial f_n}{\partial Y}\right)_{Y=1}\left[1-\exp\left(-\frac{8}{3}\lambda_n^2 X\right)\right] \\ & - \sum_{n=1}^{\infty}\frac{3}{8\lambda_n^2}\left(\frac{\partial B_n}{\partial\theta_2}\right)\left(\frac{\partial f_n}{\partial Y}\right)_{Y=1}\left[1-\exp\left(-\frac{8}{3}\lambda_n^2 X\right)\right]\Bigg\}\end{aligned} \tag{4.14}$$

dQdT can be used to obtain expressions for all $\overline{\mathrm{Nu}}_{ij}$. See Equations 4.15-4.18.

$$\begin{aligned}\overline{\mathrm{Nu}}_{20} &= \frac{C_{20}}{k}\left(\frac{2H}{x}\right) \\ &= \frac{1}{k}\left(\frac{2H}{x}\right)\left[-\frac{\partial Q_2}{\partial T_0}\right]_{C_{ik}=\text{const}} \\ &= \frac{4}{X}\sum_{n=1}^{\infty}\frac{3}{8\lambda_n^2}\left(\frac{\partial B_n}{\partial\theta_0}\right)\left(\frac{\partial f_n}{\partial Y}\right)_{Y=-1}\left[1-\exp\left(-\frac{8}{3}\lambda_n^2 X\right)\right]\end{aligned} \tag{4.15}$$

$$
\begin{aligned}
\overline{\mathrm{Nu}}_{21} &= \frac{C_{21}}{k}\left(\frac{2H}{x}\right) \\
&= \frac{1}{k}\left(\frac{2H}{x}\right)\Big[-\frac{\partial Q_2}{\partial T_1}\Big]_{C_{ik}=\text{const}} \\
&= -\frac{4}{X}\Bigg\{X - \sum_{n=1}^{\infty}\frac{3B_n}{8\lambda_n^2}\left(\frac{\partial f_n}{\partial Y}\right)_{Y=-1}\Big[1-\exp\Big(-\frac{8}{3}\lambda_n^2 X\Big)\Big] \\
&\qquad - \sum_{n=1}^{\infty}\frac{3}{8\lambda_n^2}\left(\frac{\partial B_n}{\partial \theta_1}\right)\left(\frac{\partial f_n}{\partial Y}\right)_{Y=-1}\Big[1-\exp\Big(-\frac{8}{3}\lambda_n^2 X\Big)\Big]\Bigg\}
\end{aligned}
\tag{4.16}
$$

$$
\begin{aligned}
\overline{\mathrm{Nu}}_{01} &= \frac{C_{01}}{k}\left(\frac{2H}{x}\right) \\
&= \frac{1}{k}\left(\frac{2H}{x}\right)\Big[-\frac{\partial Q_0}{\partial T_1}\Big]_{C_{ik}=\text{const}} \\
&= -\frac{4}{X}\Bigg\{\sum_{n=1}^{\infty}\frac{3}{8\lambda_n^2}\left(\frac{\partial B_n}{\partial \theta_1}\right)\Big[\left(\frac{\partial f_n}{\partial Y}\right)_{Y=1} - \left(\frac{\partial f_n}{\partial Y}\right)_{Y=-1}\Big]\Big[1-\exp\Big(-\frac{8}{3}\lambda_n^2 X\Big)\Big]\Bigg\}
\end{aligned}
\tag{4.17}
$$

$$
\begin{aligned}
\overline{\mathrm{Nu}}_{02} &= \frac{C_{02}}{k}\left(\frac{2H}{x}\right) \\
&= \frac{1}{k}\left(\frac{2H}{x}\right)\Big[-\frac{\partial Q_0}{\partial T_2}\Big]_{C_{ik}=\text{const}} \\
&= \frac{4}{X}\Bigg\{\sum_{n=1}^{\infty}\frac{3}{8\lambda_n^2}\left(\frac{\partial B_n}{\partial \theta_2}\right)\Big[\left(\frac{\partial f_n}{\partial Y}\right)_{Y=1} - \left(\frac{\partial f_n}{\partial Y}\right)_{Y=-1}\Big]\Big[1-\exp\Big(-\frac{8}{3}\lambda_n^2 X\Big)\Big]\Bigg\}
\end{aligned}
\tag{4.18}
$$

Note that as discussed in Chapter 2, the symmetry in the geometry, velocity field and the fluid properties can be used to reduce the number of unknowns in the system of equations resulting from the extended Newton formulation. The functionality coefficients can then be obtained algebraically, without dQdT. This approach was taken in an earlier work (Foroushani et al. 2017a) to derive the functionality coefficients of the asymmetric Graetz problem.

As shown in Chapter 3 (Section 3.2), there is reciprocity between the functionality coefficients of the asymmetric Graetz problem: $C_{ij} = C_{ji}$. Therefore: $\overline{\mathrm{Nu}}_{ij} = \overline{\mathrm{Nu}}_{ji}$.

Furthermore, it was shown in Chapter 2 that due to symmetry: $C_{10} = C_{20}$. Therefore: $\overline{\mathrm{Nu}}_{10} = \overline{\mathrm{Nu}}_{20}$. These results were confirmed by evaluating Equations 4.13-4.18 using the eigencoefficients, eigenfunction derivatives and eigenvalues given by Hatton & Turton (1962).

Reciprocity and symmetry of the functionality coefficients mean:

i) The problem can be represented by a delta network of three convective resistances. See Figure 4.4. In this context, Q_{ij}, the thermal current between T_i and T_j, can be calculated as:

$$Q_{ij} = C_{ij}(T_i - T_j) = \left(\frac{kx}{2H}\right)\overline{\mathrm{Nu}}_{ij}(T_i - T_j)$$

ii) The heat transfer problem is fully characterized by two paired Nusselt numbers: a "wall-fluid" Nusselt number ($\overline{\mathrm{Nu}}_{10} = \overline{\mathrm{Nu}}_{20} = \overline{\mathrm{Nu}}_{01} = \overline{\mathrm{Nu}}_{02}$) and a "wall-wall" Nusselt number ($\overline{\mathrm{Nu}}_{12} = \overline{\mathrm{Nu}}_{21}$).

Using the eigencoefficients, eigenfunction derivatives and eigenvalues given by Hatton & Turton (1962), the analytical expressions shown in Equations 4.19 and 4.20 were derived for $\{\overline{\mathrm{Nu}}_{ij}\}$. As expected, no dependence on $\{T_i\}$ is observed. The paired Nusselt numbers depend only on X, i.e. a combination of geometry, flow rate and fluid properties.

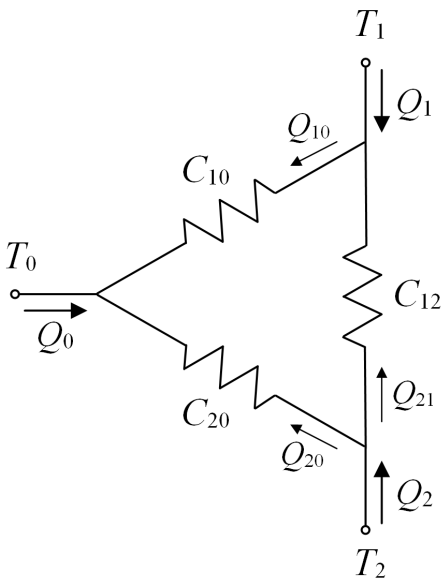

Figure 4.4: The resistor network of the asymmetric Graetz problem

$$\begin{aligned}\overline{\mathrm{Nu}}_{10} = \frac{1}{X}\Big[1 &- 0.9104\exp(-7.54X) - 0.0532\exp(-85.73X) \\ &- 0.0152\exp(-249.27X) - 0.0068\exp(-498.15X) \\ &- 0.0038\exp(-832.39X) - 0.0024\exp(-1251.93X) \\ &- 0.0016\exp(-1756.80X) - 0.0012\exp(-2347.03X)\Big]\end{aligned} \tag{4.19}$$

$$\overline{\mathrm{Nu}}_{12} = \frac{1}{X}\Big[2X - 0.4 + 0.4552\exp(-7.54X) - 0.0733\exp(-35.96X) + 0.0266e\exp(-85.73X) - 0.0131\exp(-156.83X) + 0.0076\exp(-249.27X) - 0.0049\exp(-363.04X) + 0.0034\exp(-498.15X) - 0.0025\exp(-654.59X) + 0.0019\exp(-832.39X) - 0.0001\exp(-1031.47X) + 0.0012\exp(-1251.93X) - 0.0009\exp(-1493.69X) + 0.0007\exp(-1756.80X) - 0.0007\exp(-2041.25X) + 0.0006\exp(-2347.03X) - 0.0005\exp(-2674.81X)\Big] \tag{4.20}$$

Equations 4.19 and 4.20 are plotted in Figure 4.5. The evolution of the temperature field in the channel can be used to explain this plot. As shown in Figure 4.2, near the inlet there is a core of fluid flowing at T_0 which is not affected by heat transfer from the walls. Downstream where the thermal boundary layers merge, this core shrinks and the temperature profile eventually evolves into a linear profile which is independent of T_0. Accordingly, $\overline{\mathrm{Nu}}_{10}$ starts from infinity at the inlet, reflecting the singularity in heat flux, and decays to zero in the thermally-developed limit where there is zero net heat transfer to the fluid. The variation of $\overline{\mathrm{Nu}}_{12}$ follows a different trend. Near the inlet where the boundary layers are thin, the walls do not "communicate" thermally; $\overline{\mathrm{Nu}}_{12} \approx 0$ for $0 \leq X \leq 0.05$. On the other hand, for $X > 0.05$, as the two thermal boundary layers become thicker, $\overline{\mathrm{Nu}}_{12}$ increases, approaching the pure-condition limit. Since the channel hydraulic diameter, $2H$, was used to define $\overline{\mathrm{Nu}}_{ij}$ (Equation 4.12);

$$\lim_{X\to\infty} \overline{\mathrm{Nu}}_{12} = 2$$

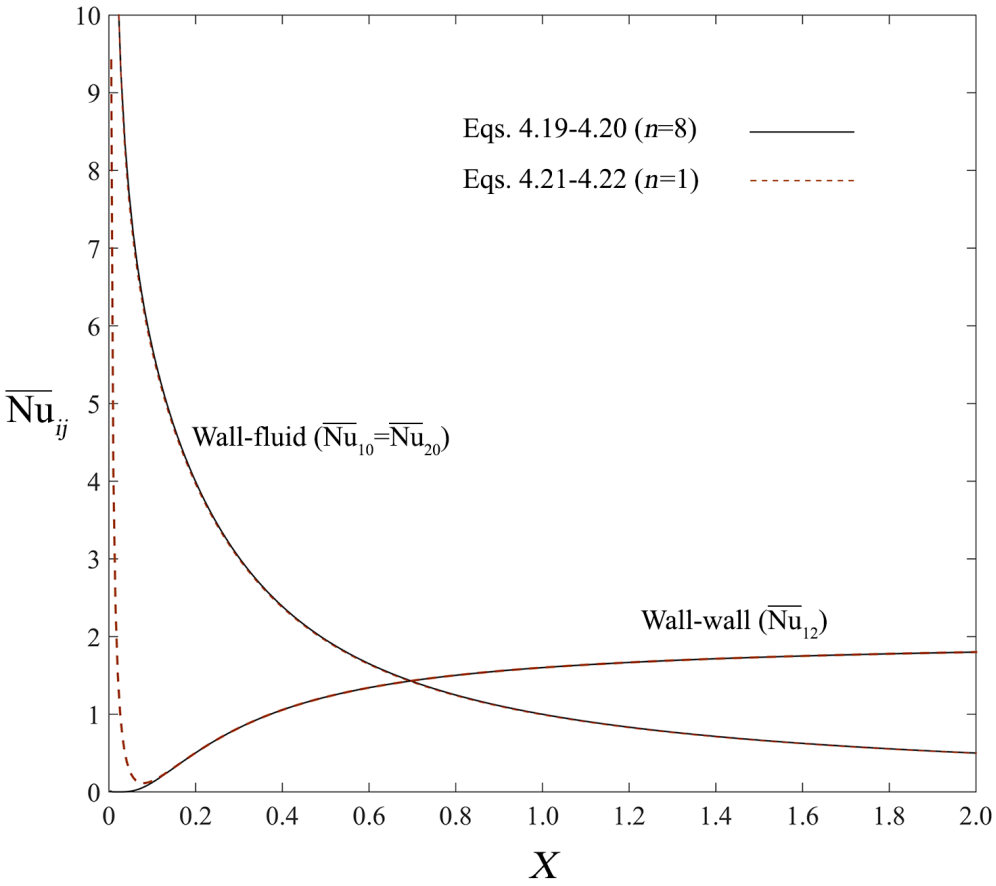

Figure 4.5: Average paired Nusselt numbers of the asymmetric Graetz problem

In addition to having better consistency with the physics of the problem, the paired Nusselt numbers are also easier to use compared to the total Nusselt numbers. Equations 4.19 and 4.20 can be readily evaluated in a spreadsheet. Moreover, these expressions can be used for any $\{T_i\}$, including the two-temperature case ($T_1 = T_2$). In Section 4.4, the utility of these results is demonstrated in sample calculations.

Calculations can be further simplified by using only the first series term ($n = 1$) to approximate $\{\overline{\mathrm{Nu}}_{ij}\}$. See Equations 4.21 and 4.22.

$$\overline{\mathrm{Nu}}_{10} \approx \frac{1 - 0.9104\exp(-7.54X)}{X} \tag{4.21}$$

$$\overline{\mathrm{Nu}_{12}} \approx 2 - \frac{0.4 - 0.4552\exp(-7.54X)}{X} \tag{4.22}$$

The expressions above are also plotted in Figure 4.5. It can be seen that the first-exponential approximation to $\overline{\mathrm{Nu}_{10}}$ replicates Equation 4.19 for essentially all $X > 0$. The first-exponential approximation to $\overline{\mathrm{Nu}_{12}}$ shows significant deviation from Equation 4.20 near the inlet ($X < 0.05$), but very close agreement for $X > 0.05$.

4.3.2 Local Paired Nusselt Numbers

For direct comparison with the local Nusselt numbers reported by Hatton & Turton (1962), a local functionality coefficient may be defined as shown in Equation 4.23, characterizing the influence of T_j on the heat flux q_i at location x.

$$c_{ij} = -\frac{\partial q_i}{\partial T_j}\bigg|_{C_{ik}=\text{const}} \tag{4.23}$$

Accordingly, a local paired Nusselt number, Nu_{ij}, may be defined as shown in Equation 4.24.

$$\mathrm{Nu}_{ij} = \frac{c_{ij}}{k}\big(2H\big) \tag{4.24}$$

The relation between c_{ij} and C_{ij} is shown in Equation 4.25.

$$
\begin{aligned}
c_{ij} = -\frac{\partial q_i}{\partial T_j}\bigg|_{C_{ik}=\text{const}} &= -\left[\frac{\partial}{\partial T_j}\left(\frac{\partial Q_i}{\partial x}\right)\right]_{C_{ik}=\text{const}} \\
&= \frac{\partial}{\partial x}\left(-\frac{\partial Q_i}{\partial T_j}\bigg|_{C_{ik}=\text{const}}\right) \\
&= \frac{\partial\, C_{ij}}{\partial x}
\end{aligned}
\tag{4.25}
$$

Thus, Nu_{ij} and $\overline{\mathrm{Nu}}_{ij}$ are related as shown in Equation 4.26.

$$
\mathrm{Nu}_{ij} = \frac{\mathrm{d}}{\mathrm{d}X}\left(\overline{\mathrm{Nu}}_{ij} X\right) \tag{4.26}
$$

Using Equations 4.13, 4.14 and 4.26, expressions below were found for $\{\mathrm{Nu}_{ij}\}$.

$$
\begin{aligned}
\mathrm{Nu}_{10} &= \frac{\mathrm{d}}{\mathrm{d}X}\left(\overline{\mathrm{Nu}}_{10} X\right) \\
&= 4\sum_{n=1}^{\infty}\frac{1}{\lambda_n^2}\left(\frac{\partial B_n}{\partial \theta_0}\right)\left(\frac{\partial f_n}{\partial Y}\right)_{Y=1}\exp\left(-\frac{8}{3}\lambda_n^2 X\right)
\end{aligned}
\tag{4.27}
$$

$$
\begin{aligned}
\mathrm{Nu}_{12} &= \frac{\mathrm{d}}{\mathrm{d}X}\left(\overline{\mathrm{Nu}}_{12} X\right) \\
&= 4\Bigg\{\sum_{n=1}^{\infty}\frac{1}{\lambda_n^2}\left(\frac{\partial B_n}{\partial \theta_2}\right)\left(\frac{\partial f_n}{\partial Y}\right)_{Y=1}\exp\left(-\frac{8}{3}\lambda_n^2 X\right) \\
&\qquad -1-\sum_{n=1}^{\infty}\frac{B_n}{\lambda_n^2}\left(\frac{\partial f_n}{\partial Y}\right)_{Y=1}\exp\left(-\frac{8}{3}\lambda_n^2 X\right)\Bigg\}
\end{aligned}
\tag{4.28}
$$

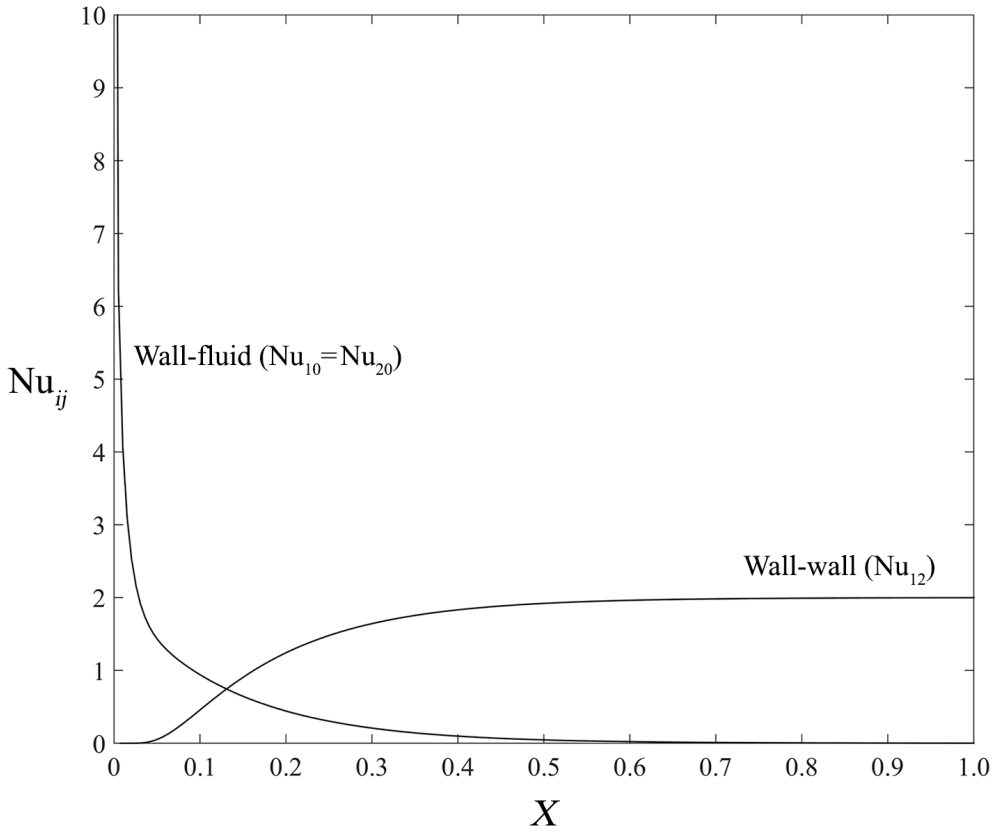

Figure 4.6: Local paired Nusselt numbers of the asymmetric Graetz problem

Comparing $\{\mathrm{Nu}_{ij}\}$ (Equations 4.27 and 4.28) to $\{\mathrm{Nu}_i\}$ (Equations 4.10 and 4.11), it can be seen that the local paired Nusselt numbers are a simpler presentation of the solution. This is better seen by comparing the results presented Hatton & Turton (Figure 4.3) and the dQdT results shown in Figure 4.6. The two curves shown in Figure 4.6 replace the entire family of r_T-dependent curves of Figure 4.3. The local paired Nusselt numbers are also a better representation of the thermal development of the flow. According to Figure 4.6, thermal development is a function of X only; regardless of r_T, the flow becomes essentially thermally developed by $X \approx 0.6$.

The utility and accuracy of the dQdT results are demonstrated in the following example.

4.4 Example: No-Slip Flow in a Microchannel

Consider a flow of water ($\mathrm{Pr} = 6.7$) at $\dot{m} = 0.048\,\mathrm{kg/(m{\cdot}s)}$ and $T_0 = 10°\mathrm{C}$ in a microchannel with $H = 60$ µm, $T_1 = 20°\mathrm{C}$ and $T_2 = 30°\mathrm{C}$. The rate of heat transfer in the channel from the entrance ($x = 0$) to $x = 3\,\mathrm{mm}$ is of interest.

First, calculations using the traditional formulation are presented. The rate of total heat transfer from the fluid per unit channel width, Q_0, can be calculated using an overall energy balance:

$$Q_0 = \dot{m} c_p \big[T_0 - T_\mathrm{m}(x)\big]$$

The mean fluid temperature, T_m, is given in the solution by Hatton & Turton (1962):

$$\begin{aligned} T_\mathrm{m} &= T_\mathrm{wm} + \frac{3}{2}(T_1 - T_2)\theta_\mathrm{m} \\ &= T_\mathrm{wm} + \frac{3}{2}(T_1 - T_2)\Big[0.303\exp(-7.54X) + 0.0177\exp(-85.73X) \\ &\qquad + 0.0051\exp(-249.27X) + 0.0023\exp(-498.15X) \\ &\qquad + 0.0012\exp(-832.39X) + 0.0008\exp(-1251.93X) \\ &\qquad + 0.0005\exp(-1756.80X) + 0.0004\exp(-2347.03X)\Big] \end{aligned}$$

With $\dot{m} = 0.048\,\mathrm{kg/(m \cdot s)}$ and $\mu = 9.6 \times 10^{-2}\,(\mathrm{Ns/m^2})$, the Reynolds number is:

$$\mathrm{Re} = \frac{\rho u_\mathrm{m}(2H)}{\mu} = \frac{2\dot{m}}{\mu} = 100$$

Therefore, at $x = 3\,\mathrm{mm}$, the inverse Graetz number is:

$$X = \frac{2x}{H}\left(\frac{1}{\mathrm{Re\,Pr}}\right) = \frac{2(0.003)}{6 \times 10^{-5}}\left(\frac{1}{100}\right)\left(\frac{1}{6.7}\right) \approx 0.15$$

At $X = 0.15$, the expression for T_{m} yields: $T_{\mathrm{m}} = 20.58°\mathrm{C}$. Therefore, with $c_p = 4.182\,\mathrm{J/(kg\ K)}$, the energy balance leads to:

$$Q_0 = (0.048)(4182)(10 - 20.58) = -2124\,\frac{\mathrm{W}}{\mathrm{m}}$$

Heat transfer at either wall can be obtained by integrating the local Nusselt numbers given by Hatton and Turton (1962). With $k = 0.6\,\mathrm{W/(mK)}$;

$$\begin{aligned} Q_1 &= \int_0^{0.003} q_1\,\mathrm{d}x \\ &= \frac{k}{2}\mathrm{Re}\ \mathrm{Pr}(T_2 - T_1)\int_0^{0.15} \mathrm{Nu}_1\left(\frac{1-\theta_{\mathrm{m}}}{4}\right)\mathrm{d}X \\ &= 657\,\frac{\mathrm{W}}{\mathrm{m}} \end{aligned}$$

$$\begin{aligned} Q_2 &= \int_0^{0.003} q_2\,\mathrm{d}x \\ &= \frac{k}{2}\mathrm{Re}\ \mathrm{Pr}(T_2 - T_1)\int_0^{0.15} \mathrm{Nu}_2\left(\frac{1+\theta_{\mathrm{m}}}{4}\right)\mathrm{d}X \\ &= 1450\,\frac{\mathrm{W}}{\mathrm{m}} \end{aligned}$$

It is evident from Equations 4.10 and 4.11 that integrating Nu_i is not straightforward. Furthermore, since both $\{\mathrm{Nu}_i\}$ and θ_{m} are function of r_T, the tedious task of evaluating the integral must be repeated for every new r_T.

With the wall heat transfer rates known, the total heat transfer rate to the fluid can also be calculated as:

$$Q_0 = -Q_1 - Q_2 = -2107\,\frac{\mathrm{W}}{\mathrm{m}}$$

The slight difference between the result above and the energy-balance calculation is the truncation error caused by evaluating the series expressions for θ_{m} and $\{\mathrm{Nu}_i\}$ using the first eight terms.

Alternatively, the paired Nusselt numbers may be used to calculate $\{Q_i\}$. Substituting $X = 0.15$ in Equations 4.19 and 4.20 (or from Figure 4.5), the average Nusselt paired numbers are: $\overline{\mathrm{Nu}}_{10} = 4.68$, $\overline{\mathrm{Nu}}_{12} = \overline{\mathrm{Nu}}_{21} = 0.30$. The first-exponential approximations (Equations 4.21 and 4.22) give: $\overline{\mathrm{Nu}}_{10} = 4.71$, $\overline{\mathrm{Nu}}_{12} = 0.31$. Note that these values can be used for *any* r_T. The heat transfer rates are therefore:

$$\begin{aligned} Q_0 &= \frac{kx}{2H}\left[\overline{\mathrm{Nu}}_{01}(T_0 - T_1) + \overline{\mathrm{Nu}}_{02}(T_0 - T_2)\right] \\ &= \frac{0.6(0.003)}{2(3\times 10^{-5})}\left[4.68(10-20) + 4.68(10-30)\right] \\ &= -2105\,\frac{\mathrm{W}}{\mathrm{m}} \end{aligned}$$

$$\begin{aligned} Q_1 &= \frac{kx}{2H}\left[\overline{\mathrm{Nu}}_{10}(T_1 - T_0) + \overline{\mathrm{Nu}}_{12}(T_1 - T_2)\right] \\ &= \frac{0.6(0.003)}{2(3\times 10^{-5})}\left[4.68(20-10) + 0.30(20-30)\right] \\ &= 655\,\frac{\mathrm{W}}{\mathrm{m}} \end{aligned}$$

$$\begin{aligned} Q_2 &= \frac{kx}{2H}\left[\overline{\mathrm{Nu}}_{20}(T_2 - T_0) + \overline{\mathrm{Nu}}_{21}(T_2 - T_1)\right] \\ &= \frac{0.6(0.003)}{2(3\times 10^{-5})}\left[4.68(30-10) + 0.30(30-20)\right] \\ &= (T_2 - T_1) = 1450\,\frac{\mathrm{W}}{\mathrm{m}} \end{aligned}$$

The close agreement of the calculations above with the results obtained using the traditional formulation validates the dQdT results. The overall energy balance in the channel can be used as to further check the dQdT results;

$$\sum_i Q_i = Q_0 + Q_1 + Q_2 = -2105 + 655 + 1450 = 0$$

4.5 Summary

The extended Newton formulation of the asymmetric Graetz problem was discussed. The formulation of the problem in terms of paired Nusselt numbers has several advantages over the traditional formulation:

i) The extra singularities observed in the traditional formulation are eliminated.

ii) The paired Nusselt numbers are independent of temperature (and temperature ratio).

iii) The paired Nusselt numbers are a better representation of the physics of the problem; the wall-wall Nusselt numbers start from zero at the entrance and approach the pure-conduction limit in the thermally developed limit, while the wall-fluid Nusselt number starts from infinity at the inlet and smoothly decays to zero in the thermally developed limit.

iv) Two universal Nusselt numbers are obtained that can be applied to any fluid, any laminar flow rate and any temperature ratio.

Furthermore, it was shown due to reciprocity between the functionality coefficients of the problem, the asymmetric Graetz problem can be represented by a network of convective resistors.

Chapter 5

Convection in Hydrodynamically Developed Laminar Flow in an Annulus with Isothermal Walls

Convective heat transfer in concentric annuli is encountered in various applications, most importantly the tube-in-tube heat exchanger. The annulus is therefore a geometry that is extensively studied in the heat transfer literature. Bibliographies of the annulus problem can be found in most advanced heat transfer textbooks, e.g. those by Kays & Crawford (2005) and Kakaç et al. (2014). Recently, the development of microtubes has renewed the interest in this problem.

For fluids with a high Prandtl number (oils, organic liquids, etc.) or cases where the fluid passes through an unheated section first, hydrodynamic development may occur well before thermal development. In this case, the thermal analysis of the flow is performed assuming a fully developed velocity profile.

Hydrodynamically developed laminar flow in a concentric annulus was examined in this work for several reasons. First, the case of isothermal boundary conditions at the

walls constitutes a three-temperature convection problem. Second, this problem has an analytical solution to which the dQdT technique can be applied. Finally, the annulus problem provides an opportunity for validating the results presented in Chapter 4 for the channel problem: in the limit as the curvature of the annulus walls approaches zero, the functionality coefficients of the annulus must approach the functionality coefficients of the parallel-plate channel. This will be demonstrated.

5.1 The Analytical Solution

Consider a hydrodynamically developed laminar flow at a uniform temperature, T_0, entering the annulus formed between two concentric circular pipes of radii r_1 and r_2 with isothermal walls at temperatures T_1 and T_2. This configuration is shown schematically in Figure 5.1.

With constant fluid properties, negligible conduction in the x-direction and negligible viscous dissipation, the energy equation in cylindrical coordinates is reduced to Equation 5.1, subject to the boundary conditions shown in Equation 5.2.

$$\rho u_{\text{fd}} c_p \frac{\partial T}{\partial x} = k\left(\frac{\partial^2 T}{\partial r^2} + \frac{1}{r}\frac{\partial T}{\partial r}\right) \tag{5.1}$$

$$\begin{aligned} x = 0 \quad &; \quad T = T_0 \\ r = r_1 \quad &; \quad T = T_1 \\ r = r_2 \quad &; \quad T = T_2 \end{aligned} \tag{5.2}$$

The fully developed laminar velocity profile, u_{fd}, is given in Equation 5.3.

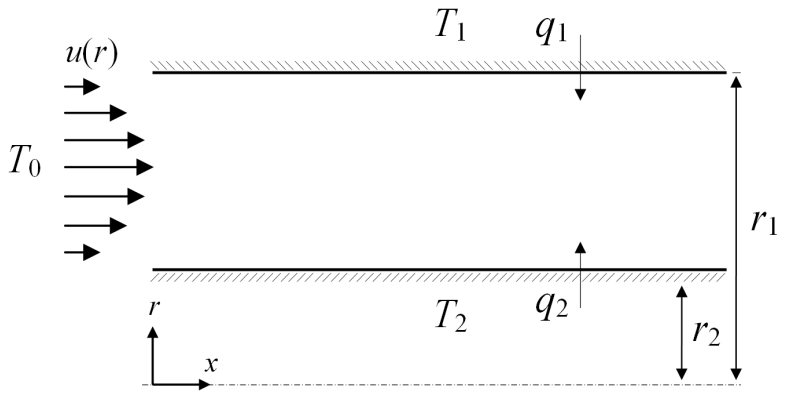

Figure 5.1: Schematic of hydrodynamically developed flow in a concentric annulus with isothermal walls

$$u_{\mathrm{fd}} = -\frac{1}{4\mu}\left(\frac{\mathrm{d}p}{\mathrm{d}x}\right)\left[r_1^2 - r^2 + (r_1^2 - r_2^2)\frac{\ln(r_1/r)}{\ln(r_2/r_1)}\right] \tag{5.3}$$

The flow is characterized by the Reynolds number defined in Equation 5.4. In this equations, D_{h} denotes the hydraulic diameter of the annulus: $D_{\mathrm{h}} = 2(r_1 - r_2)$.

$$\mathrm{Re} = \frac{\rho u_{\mathrm{m}} D_{\mathrm{h}}}{\mu} \tag{5.4}$$

Lundberg et al. (1963) obtained a solution to Equation 5.1 for the special case where one of the annulus walls is maintained at the same temperature as the inlet flow, i.e. for the case of only one non-homogeneous boundary condition. Similar to the solution by Hatton & Turton (1962) for the channel problem, this solution is expressed as the superposition of a one-dimensional solution for the non-homogeneous boundary conditions, i.e. the fully developed solution, θ_{fd}, and a series solution for the homogeneous boundary conditions. See Equation 5.5.

$$\theta_i = \theta_{\mathrm{fd},i} - \sum_{n=1}^{\infty} B_{n,i} f_n \exp(-\lambda_n^2 X) \tag{5.5}$$

In Equation 5.5, θ is dimensionless temperature defined in Equation 5.6 and X is the inverse Graetz number, defined in Equation 5.7. B_n, f_n and λ_n are respectively the eigencoefficients, eigenfunctions and eigenvalues of the series solution. The subscript i denotes the heated wall: θ_2, for example, is the solution to the case where the outer wall is at the same temperature as the inlet flow ($T_1 = T_0$), while the inner wall is heated to a different temperature (T_2). The fully developed temperature profile, θ_{fd}, is given by Equation 5.8 wherein the subscript j designates the unheated wall.

$$\theta_i = \frac{T - T_0}{T_i - T_0} \tag{5.6}$$

$$X = \frac{x}{2(r_1 - r_2)} \left(\frac{1}{\mathrm{Re\,Pr}} \right) \tag{5.7}$$

$$\theta_{\mathrm{fd},i} = \frac{\ln(r/r_j)}{\ln(r_i/r_j)} \tag{5.8}$$

Given the linearity of the energy equation, a solution to the general case where neither wall is at the same temperature as the inlet flow, i.e. for two non-homogeneous boundary conditions, can be constructed using superposition. See Equation 5.9 and Figure 5.2 where the generic solution, $T(x, r)$, is expressed as the sum of "fundamental" solutions, $T_1^{(1)}$ and $T_2^{(1)}$. In accordance with the notation used by Lundberg et al. (1963), the superscript (1) denotes a fundamental solution of the "first kind," i.e. for Dirichlet conditions on all boundaries.

$$T(x,r) = T_1^{(1)}(x,r) + T_2^{(1)}(x,r) \tag{5.9}$$

$T_i^{(1)}$ is known in dimensionless form, θ_i, from the work of Lundberg et al. (1963). Furthermore, with T_i' and T_i'' denoting the boundary conditions of the subproblems, superposition requires:

$$T_i' + T_i'' = T_i$$

Hence, the generic solution is obtained as shown in Equation 5.10.

$$T = (T_1 - T_0)\theta_1 + (T_2 - T_0)\theta_2 + 2T_0 \tag{5.10}$$

Lundberg et al. (1963) have presented their solution in terms of the local Nusselt number defined in Equation 5.11.

$$\mathrm{Nu}_i = \frac{q_i}{T_i - T_\mathrm{m}}\left(\frac{D_\mathrm{h}}{k}\right) \qquad (i = 1, 2) \tag{5.11}$$

Extensive tables are presented, listing the local Nusselt numbers and the mean fluid temperature at different axial locations and for various radius ratios. These tables have become a benchmark in the calculation of heat transfer in concentric annuli and widely cited in prominent references, e.g. *Handbook of Single-Phase Convective Heat Transfer* (Kakaç et al. 1987) and *Handbook of Heat Transfer* (Rohsenow et al. 1998).

The shortcomings of the traditional formulation, i.e. presenting the results in terms of a Nusselt number based on $T_i - T_\mathrm{m}$, were discussed in Chapter 4 for flow in an asymmetrically heated parallel-plate channel. The same problems arise if the traditional formulation is applied to the asymmetrically heated annulus; the Nusselt numbers depend on a temperature ratio and, in some cases, exhibit non-physical singularities for $X > 0$. See

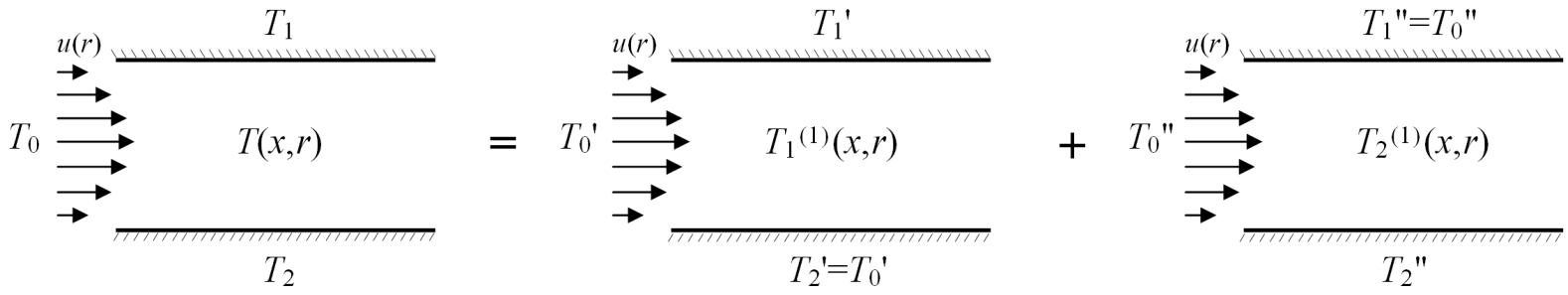

Figure 5.2: Superposition solution to the three-temperature annulus problem

for example the plots of temperature-dependent Nusselt numbers presented by Mitrović & Baletić (2005) and the singularities in the results presented by Mitrović & Baletić (2005) and Coelho & Pinho (2006). See also the plots of fully developed Nusselt numbers in *Handbook of Heat Transfer* (Rohsenow et al. 1998) where different curves are presented for the symmetric ($T_1 = T_2$) and asymmetric ($T_1 \neq T_2$) heating of the annulus walls.

The extended Newton formulation in terms of functionality coefficients is now an alternative approach which, as shown in Chapter 4, addresses the shortcomings of the traditional formulation. In the following, the solution by Lundberg et al. (1963) is used to derive the functionality coefficients of the problem.

5.2 Extended Newton Formulation

Differentiating Equation 5.10, the heat flux at either wall can be calculated as shown in Equations 5.12 and 5.13. In these equations, $\overline{r} = r/r_1$ denotes dimensionless radial location and $\phi = r_2/r_1$ is the radius ratio, characterizing the annulus geometry.

$$\begin{aligned} q_1 &= k\left(\frac{\partial T}{\partial r}\right)_{r=r_1} \\ &= \frac{k}{r_1}\left[(T_1 - T_0)\left(\frac{\partial \theta_1}{\partial \overline{r}}\right)_{\overline{r}=1} + (T_2 - T_0)\left(\frac{\partial \theta_2}{\partial \overline{r}}\right)_{\overline{r}=1}\right] \end{aligned} \tag{5.12}$$

$$\begin{aligned} q_2 &= -k\left(\frac{\partial T}{\partial r}\right)_{r=r_2} \\ &= -\frac{k}{r_1}\left[(T_1 - T_0)\left(\frac{\partial \theta_1}{\partial \overline{r}}\right)_{\overline{r}=\phi} + (T_2 - T_0)\left(\frac{\partial \theta_2}{\partial \overline{r}}\right)_{\overline{r}=\phi}\right] \end{aligned} \tag{5.13}$$

Equations 5.12 and 5.13 must then be integrated along the walls to obtain the heat transfer rate at each wall. See Equation 5.14.

$$
\begin{aligned}
|Q_i| &= \int_0^x |q_i|(2\pi r_i)\,\mathrm{d}x \\
&= \int_0^x \frac{k}{r_1}\left[(T_1 - T_0)\left(\frac{\partial\theta_1}{\partial\overline{r}}\right)_{\overline{r}_i} + (T_2 - T_0)\left(\frac{\partial\theta_2}{\partial\overline{r}}\right)_{\overline{r}_i}\right](2\pi r_i)\,\mathrm{d}x \\
&= 2\pi\overline{r}_i k\left[(T_1 - T_0)\int_0^x \left(\frac{\partial\theta_1}{\partial\overline{r}}\right)_{\overline{r}_i}\mathrm{d}x + (T_2 - T_0)\int_0^x \left(\frac{\partial\theta_2}{\partial\overline{r}}\right)_{\overline{r}_i}\mathrm{d}x\right] \qquad (i = 1, 2)
\end{aligned}
\tag{5.14}
$$

Differentiating Equation 5.5, the gradient terms can be written as shown in Equations 5.15 and 5.16.

$$
\frac{\partial\theta_1}{\partial\overline{r}} = \frac{1/\overline{r}}{\ln(1/\phi)} - \sum_{n=1}^{\infty} B_{n,1}\left(\frac{\partial f_n}{\partial\overline{r}}\right)\exp(-\lambda_n^2 X) \tag{5.15}
$$

$$
\frac{\partial\theta_2}{\partial\overline{r}} = \frac{1/\overline{r}}{\ln(\phi)} - \sum_{n=1}^{\infty} B_{n,2}\left(\frac{\partial f_n}{\partial\overline{r}}\right)\exp(-\lambda_n^2 X) \tag{5.16}
$$

Therefore:

$$
\begin{aligned}
\int_0^x \left(\frac{\partial\theta_1}{\partial\overline{r}}\right)\mathrm{d}x &= 2(r_1 - r_2)\mathrm{Re}\,\mathrm{Pr}\int_0^X \left(\frac{\partial\theta_1}{\partial\overline{r}}\right)\mathrm{d}X \\
&= 2(r_1 - r_2)\mathrm{Re}\,\mathrm{Pr}\left\{\frac{X/\overline{r}}{\ln(1/\phi)} - \sum_{n=1}^{\infty}\frac{B_{n,1}}{\lambda_n^2}\left(\frac{\partial f_n}{\partial\overline{r}}\right)\left[1 - \exp(-\lambda_n^2 X)\right]\right\}
\end{aligned}
\tag{5.17}
$$

$$\begin{aligned}\int_0^x \left(\frac{\partial\theta_2}{\partial\overline{r}}\right)\mathrm{d}x =& 2(r_1-r_2)\mathrm{Re}\,\mathrm{Pr}\int_0^X \left(\frac{\partial\theta_2}{\partial\overline{r}}\right)\mathrm{d}X \\ =& 2(r_1-r_2)\mathrm{Re}\,\mathrm{Pr}\left\{\frac{X/\overline{r}}{\ln(\phi)} - \sum_{n=1}^{\infty}\frac{B_{n,2}}{\lambda_n^2}\left(\frac{\partial f_n}{\partial\overline{r}}\right)\left[1-\exp(-\lambda_n^2 X)\right]\right\}\end{aligned} \tag{5.18}$$

Hence, the heat transfer rates are:

$$\begin{aligned}Q_1 =& 4\pi k(r_1-r_2)\mathrm{Re}\,\mathrm{Pr}\times \\ &\left\{(T_1-T_0)\left[\frac{X}{\ln(1/\phi)} - \sum_{n=1}^{\infty}\frac{B_{n,1}}{\lambda_n^2}\left(\frac{\partial f_n}{\partial\overline{r}}\right)_{\overline{r}=1}\left(1-\exp(-\lambda_n^2 X)\right)\right]\right. \\ &\left.+(T_2-T_0)\left[\frac{X}{\ln(\phi)} - \sum_{n=1}^{\infty}\frac{B_{n,2}}{\lambda_n^2}\left(\frac{\partial f_n}{\partial\overline{r}}\right)_{\overline{r}=1}\left(1-\exp(-\lambda_n^2 X)\right)\right]\right\}\end{aligned} \tag{5.19}$$

$$\begin{aligned}Q_2 =& -4\pi\phi k(r_1-r_2)\mathrm{Re}\,\mathrm{Pr}\times \\ &\left\{(T_1-T_0)\left[\frac{X/\phi}{\ln(1/\phi)} - \sum_{n=1}^{\infty}\frac{B_{n,1}}{\lambda_n^2}\left(\frac{\partial f_n}{\partial\overline{r}}\right)_{\overline{r}=\phi}\left(1-\exp(-\lambda_n^2 X)\right)\right]\right. \\ &\left.+(T_2-T_0)\left[\frac{X/\phi}{\ln(\phi)} - \sum_{n=1}^{\infty}\frac{B_{n,2}}{\lambda_n^2}\left(\frac{\partial f_n}{\partial\overline{r}}\right)_{\overline{r}=\phi}\left(1-\exp(-\lambda_n^2 X)\right)\right]\right\}\end{aligned} \tag{5.20}$$

$$
\begin{aligned}
Q_0 =& - Q_1 - Q_2 \\
&= 4\pi k(r_1 - r_2)\mathrm{Re}\,\mathrm{Pr}\times \\
&\left\{(T_1 - T_0)\sum_{n=1}^{\infty}\frac{B_{n,1}}{\lambda_n^2}\left[\left(\frac{\partial f_n}{\partial \overline{r}}\right)_{\overline{r}=1} - \phi\left(\frac{\partial f_n}{\partial \overline{r}}\right)_{\overline{r}=\phi}\right]\left[1-\exp(-\lambda_n^2 X)\right]\right. \\
&\left.+(T_2 - T_0)\sum_{n=1}^{\infty}\frac{B_{n,2}}{\lambda_n^2}\left[\left(\frac{\partial f_n}{\partial \overline{r}}\right)_{\overline{r}=1} - \phi\left(\frac{\partial f_n}{\partial \overline{r}}\right)_{\overline{r}=\phi}\right]\left[1-\exp(-\lambda_n^2 X)\right]\right\}
\end{aligned}
\tag{5.21}
$$

To find $\{C_{ij}\}$, Equations 5.19-5.21 must be differentiated with respect to $\{T_i\}$. This operation is straightforward because, unlike the asymmetric Graetz problem, the eigencoefficients, $\{B_n\}$, of the present solution do not depend on $\{T_i\}$. See Equations 5.22-5.27.

$$
\begin{aligned}
C_{10} =& -\left.\frac{\partial Q_1}{\partial T_0}\right|_{C_{ik}=\mathrm{const}} \\
&= -4\pi k(r_1 - r_2)\mathrm{Re}\,\mathrm{Pr}\sum_{n=1}^{\infty}\frac{B_{n,1}+B_{n,2}}{\lambda_n^2}\left(\frac{\partial f_n}{\partial \overline{r}}\right)_{\overline{r}=1}\left[1-\exp(-\lambda_n^2 X)\right]
\end{aligned}
\tag{5.22}
$$

$$
\begin{aligned}
C_{12} =& -\left.\frac{\partial Q_1}{\partial T_2}\right|_{C_{ik}=\mathrm{const}} \\
&= -4\pi k(r_1 - r_2)\mathrm{Re}\,\mathrm{Pr}\left\{\frac{X}{\ln(\phi)} - \sum_{n=1}^{\infty}\frac{B_{n,2}}{\lambda_n^2}\left(\frac{\partial f_n}{\partial \overline{r}}\right)_{\overline{r}=1}\left[1-\exp(-\lambda_n^2 X)\right]\right\}
\end{aligned}
\tag{5.23}
$$

$$
\begin{aligned}
C_{20} &= -\left.\frac{\partial Q_2}{\partial T_0}\right|_{C_{ik}=\text{const}} \\
&= 4\pi k\phi(r_1 - r_2)\mathrm{Re}\,\mathrm{Pr}\sum_{n=1}^{\infty}\frac{B_{n,1}+B_{n,2}}{\lambda_n^2}\left(\frac{\partial f_n}{\partial \overline{r}}\right)_{\overline{r}=\phi}\left[1-\exp(-\lambda_n^2 X)\right]
\end{aligned}
\tag{5.24}
$$

$$
\begin{aligned}
C_{21} &= -\left.\frac{\partial Q_2}{\partial T_1}\right|_{C_{ik}=\text{const}} \\
&= 4\pi k\phi(r_1 - r_2)\mathrm{Re}\,\mathrm{Pr}\left\{\frac{X/\phi}{\ln(1/\phi)} - \sum_{n=1}^{\infty}\frac{B_{n,1}}{\lambda_n^2}\left(\frac{\partial f_n}{\partial \overline{r}}\right)_{\overline{r}=\phi}\left[1-\exp(-\lambda_n^2 X)\right]\right\}
\end{aligned}
\tag{5.25}
$$

$$
\begin{aligned}
C_{01} &= -\left.\frac{\partial Q_0}{\partial T_1}\right|_{C_{ik}=\text{const}} \\
&= -4\pi k(r_1 - r_2)\mathrm{Re}\,\mathrm{Pr}\sum_{n=1}^{\infty}\frac{B_{n,1}}{\lambda_n^2}\left[\left(\frac{\partial f_n}{\partial \overline{r}}\right)_{\overline{r}=1} - \phi\left(\frac{\partial f_n}{\partial \overline{r}}\right)_{\overline{r}=\phi}\right]\left[1-\exp(-\lambda_n^2 X)\right]
\end{aligned}
\tag{5.26}
$$

$$
\begin{aligned}
C_{02} &= -\left.\frac{\partial Q_0}{\partial T_2}\right|_{C_{ik}=\text{const}} \\
&= -4\pi k(r_1 - r_2)\mathrm{Re}\,\mathrm{Pr}\sum_{n=1}^{\infty}\frac{B_{n,2}}{\lambda_n^2}\left[\left(\frac{\partial f_n}{\partial \overline{r}}\right)_{\overline{r}=1} - \phi\left(\frac{\partial f_n}{\partial \overline{r}}\right)_{\overline{r}=\phi}\right]\left[1-\exp(-\lambda_n^2 X)\right]
\end{aligned}
\tag{5.27}
$$

Lundberg et al. (1963) presented λ_n and $B_{n,i}(\partial f_n/\partial\overline{r})$ for $n = 1, 2, 3, 4$ and various values of ϕ. The eigencoefficients and eigenfunction derivatives, B_n and $\partial f_n/\partial\overline{r}$, are given by Lundberg et al. (1963) in terms of the group: $2(1-\phi)B_{n,i}(\partial f_n/\partial\overline{r})$. See Appendix B.

These values can be used in conjunction with Equations 5.22-5.27 to evaluate $\{C_{ij}\}$ and show that:

$$C_{ij} = C_{ji}$$

For example, the results of Lundberg et al. (1963) demonstrate that:

$$B_{n,2}\left(\frac{\partial f_n}{\partial \overline{r}}\right)_{\overline{r}=1} = -\phi B_{n,1}\left(\frac{\partial f_n}{\partial \overline{r}}\right)_{\overline{r}=\phi} \tag{5.28}$$

Therefore, Equations 5.23 and 5.25 are equivalent; $C_{12} = C_{21}$.

Furthermore, the data presented by Lundberg et al. (1963) can be used to confirm the relations below, leading to: $C_{10} = C_{01}$, $C_{20} = C_{02}$.

$$(B_{n,1} + B_{n,2})\left(\frac{\partial f_n}{\partial \overline{r}}\right)_{\overline{r}=1} = B_{n,1}\left[\left(\frac{\partial f_n}{\partial \overline{r}}\right)_{\overline{r}=1} - \phi\left(\frac{\partial f_n}{\partial \overline{r}}\right)_{\overline{r}=\phi}\right] \tag{5.29}$$

$$(B_{n,1} + B_{n,2})\left(\frac{\partial f_n}{\partial \overline{r}}\right)_{\overline{r}=\phi} = B_{n,2}\left[-\frac{1}{\phi}\left(\frac{\partial f_n}{\partial \overline{r}}\right)_{\overline{r}=1} + \left(\frac{\partial f_n}{\partial \overline{r}}\right)_{\overline{r}=\phi}\right] \tag{5.30}$$

As discussed in Chapter 3, $C_{ij} = C_{ji}$ means the problem can be represented by a network of convective resistances, in this case a delta network of three resistances connecting three nodes at T_0, T_1 and T_2. See Figure 4.4.

5.3 Average Paired Nusselt Numbers

An average paired Nusselt number may be defined to present the results in dimensionless form. See Equation 5.31.

$$\overline{\mathrm{Nu}}_{ij} = \frac{2(r_1 - r_2)}{A_i}\left(\frac{C_{ij}}{k}\right) \qquad (i = 1, 2) \tag{5.31}$$

Note that in the limit as $\phi \to 1$, the definition above is equivalent to the average paired Nusselt number defined in Chapter 4 (Equation 4.12) for the parallel-plate channel.

Further note that:

$$C_{12} = C_{21} \qquad \Rightarrow \qquad \frac{\overline{\mathrm{Nu}}_{12}}{\overline{\mathrm{Nu}}_{21}} = \frac{A_2}{A_1} = \phi$$

Replacing the results obtained in Equations 5.22-5.27 into Equation 5.31, the wall paired Nusselt numbers are obtained as shown in Equations 5.32-5.34.

$$\overline{\mathrm{Nu}}_{10} = \frac{2(\phi - 1)}{X}\sum_{n=1}^{\infty}\frac{B_{n,1} + B_{n,2}}{\lambda_n^2}\left(\frac{\partial f_n}{\partial \overline{r}}\right)_{\overline{r}=1}\left[1 - \exp(-\lambda_n^2 X)\right] \tag{5.32}$$

$$\overline{\mathrm{Nu}}_{20} = \frac{2(1 - \phi)}{X}\sum_{n=1}^{\infty}\frac{B_{n,1} + B_{n,2}}{\lambda_n^2}\left(\frac{\partial f_n}{\partial \overline{r}}\right)_{\overline{r}=\phi}\left[1 - \exp(-\lambda_n^2 X)\right] \tag{5.33}$$

$$\begin{aligned}\overline{\mathrm{Nu}}_{12} &= \phi\,\overline{\mathrm{Nu}}_{21} \\ &= \frac{2(1 - \phi)}{\ln(1/\phi)} + \frac{2(1 - \phi)}{X}\sum_{n=1}^{\infty}\frac{B_{n,2}}{\lambda_n^2}\left(\frac{\partial f_n}{\partial \overline{r}}\right)_{\overline{r}=1}\left[1 - \exp(-\lambda_n^2 X)\right]\end{aligned} \tag{5.34}$$

The tabulated data presented by Lundberg et al. (1963) can be used to evaluate Equations 5.32-5.34. For instance, at $\phi = 0.5$;

$$\begin{aligned}\overline{\mathrm{Nu}}_{10} = \frac{1}{X}\Big[&0.2127 - 0.1959\exp(-29.65X) - 0.0047\exp(-142.3X) \\ &- 0.0113\exp(-339.6X) - 0.0008\exp(-621.6X)\Big]\end{aligned} \tag{5.35}$$

$$\overline{\mathrm{Nu}}_{20} = \frac{1}{X}\Big[0.2973 - 0.2889\exp(-29.65X) + 0.0070\exp(-142.3X) - 0.0166\exp(-339.6X) + 0.0012\exp(-621.6X)\Big] \tag{5.36}$$

$$\overline{\mathrm{Nu}}_{12} = 1.44 - \frac{1}{X}\Big[0.0723 - 0.0831\exp(-29.65X) + 0.0132\exp(-142.3X) - 0.0048\exp(-339.6X) + 0.0023\exp(-621.6X)\Big] \tag{5.37}$$

The expressions above are plotted in Figure 5.3. The trends are similar to those observed in Chapter 4 for the asymmetric Graetz problem. $\overline{\mathrm{Nu}}_{10}$ and $\overline{\mathrm{Nu}}_{20}$ are infinitely large at the annulus inlet, corresponding to the heat-flux singularity at $X = 0$. As the flow develops thermally, with the temperature profile approaching the fully-developed profile of Equation 5.8, $\overline{\mathrm{Nu}}_{10}$ and $\overline{\mathrm{Nu}}_{20}$ decay continuously. It is clear from Equations 5.32 and 5.33 that:

$$\lim_{X\to\infty} \overline{\mathrm{Nu}}_{10} = \lim_{X\to\infty} \overline{\mathrm{Nu}}_{20} = 0$$

The asymmetry in geometry, i.e. the different curvature of the inner and outer walls, leads to a difference between the two wall-fluid Nusselt numbers; $\overline{\mathrm{Nu}}_{10} < \overline{\mathrm{Nu}}_{20}$. [1]

As thermal boundary layers thicken, the wall-wall Nusselt number, $\overline{\mathrm{Nu}}_{12}$, increases from zero at the inlet to the pure-conduction limit:

$$\lim_{X\to\infty} \overline{\mathrm{Nu}}_{12} = \frac{2(1-\phi)}{\ln(1/\phi)}$$

For $\phi = 0.5$ this limit is: $\overline{\mathrm{Nu}}_{12} \to 1.44$.

[1] Although the problem of hydrodynamically developed laminar flow in a parallel-plate channel with walls at different temperatures is known in the heat transfer literature as the "asymmetric" Graetz problem, it was demonstrated in Chapter 4 that the asymmetry observed in the traditional Nusselt numbers is superficial and problematic. If properly formulated, the problem leads to temperature-independent paired Nusselt numbers which are not affected by the asymmetry in the boundary conditions; the two wall-fluid Nusselt numbers are identical. On the other hand, the asymmetry of geometry in the annulus problem herein examined leads to a difference between the wall-fluid Nusselt numbers. In this light, it is perhaps more suitable to refer to the annulus problem as the asymmetric Graetz problem.

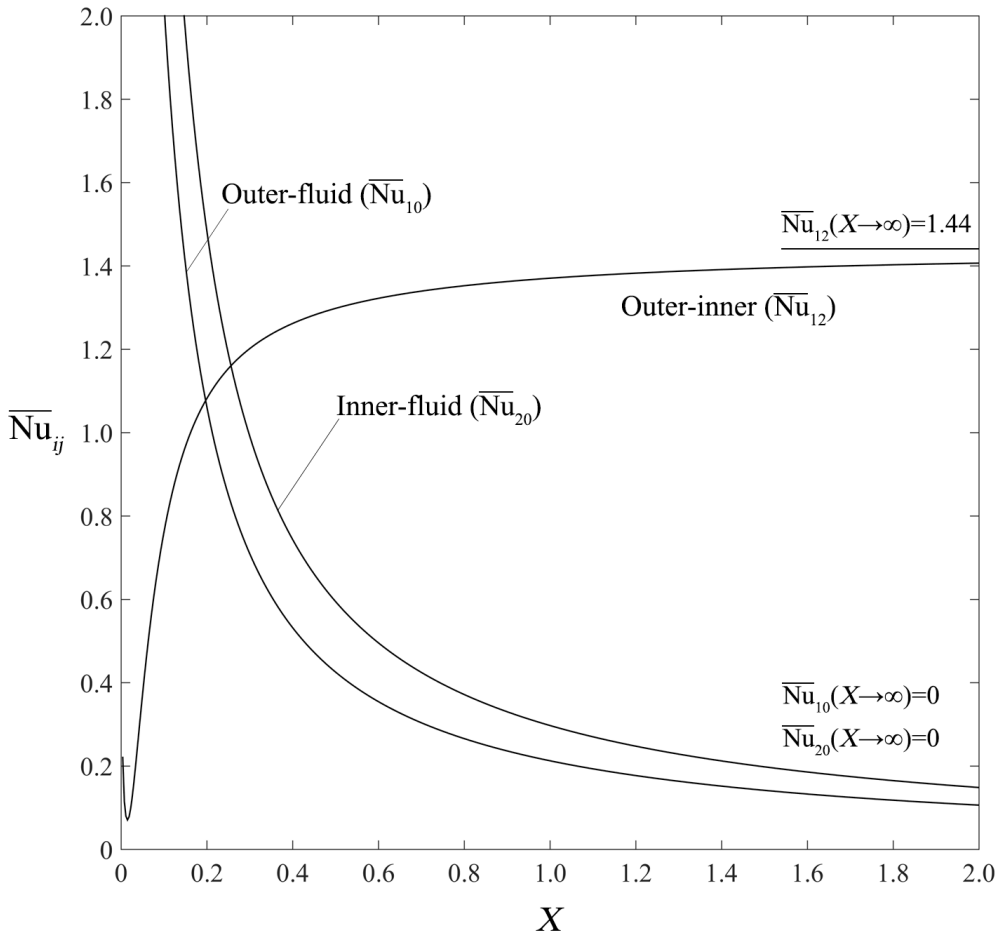

Figure 5.3: Average paired Nusselt numbers of hydrodynamically developed flow in a concentric annulus ($\phi = 0.5$)

Note that this limiting value can be independently established based on the conduction shape factor of two concentric cylinders, S, shown in Equation 5.38, and noting that:

$$\lim_{X \to \infty} C_{12} = Sk$$

$$S = \frac{2\pi x}{\ln(1/\phi)} \tag{5.38}$$

The deviation of the $\overline{\mathrm{Nu}}_{12}$ curve in Figure 5.3 from zero at $X = 0$ is due to the truncation error caused by evaluating the summation in Equation 5.34 using the first four terms only. This truncation error is pronounced near the inlet, i.e. for small X.

If the curvature of both annulus walls approaches zero ($\phi \to 1$), the solution must approach the solution to the flat-plate channel problem. In Figure 5.4, the dQdT results for the outer-fluid Nusselt number are plotted for various radius ratios. Note that non-zero values are reported by Lundberg et al. (1963) for $2(1-\phi)B_{n,i}(\partial f_n/\partial \overline{r})$ in the $\phi \to 1$ limit. See Appendix B. The sign convention observed in the present work must also be taken into account when using the data presented by Lundberg et al. (1963). Further note the difference in the characteristic lengths used to define X in the papers by Hatton & Turton (1962) and Lundberg et al. (1963); compare Equations 4.7 and 5.7. This difference leads to:

$$\lim_{\phi \to 1} X = \frac{X_{\mathrm{Ch}}}{4}$$

In the equation above the subscript "Ch" designates the channel problem, discussed in Chapter 4.

It can be seen from Figure 5.4 that:

$$\lim_{\phi \to 1} \overline{\mathrm{Nu}}_{10} = \left(\overline{\mathrm{Nu}}_{10}\right)_{\mathrm{Ch}} = \left(\overline{\mathrm{Nu}}_{20}\right)_{\mathrm{Ch}}$$

Similarly, it can be shown that:

$$\lim_{\phi \to 1} \overline{\mathrm{Nu}}_{20} = \left(\overline{\mathrm{Nu}}_{20}\right)_{\mathrm{Ch}}$$

The outer-inner Nusselt number, $\overline{\mathrm{Nu}}_{12}$, is plotted in Figure 5.5 for various radius ratios. It is clear from this figure that:

$$\lim_{\phi \to 1} \overline{\mathrm{Nu}}_{12} = \left(\overline{\mathrm{Nu}}_{12}\right)_{\mathrm{Ch}}$$

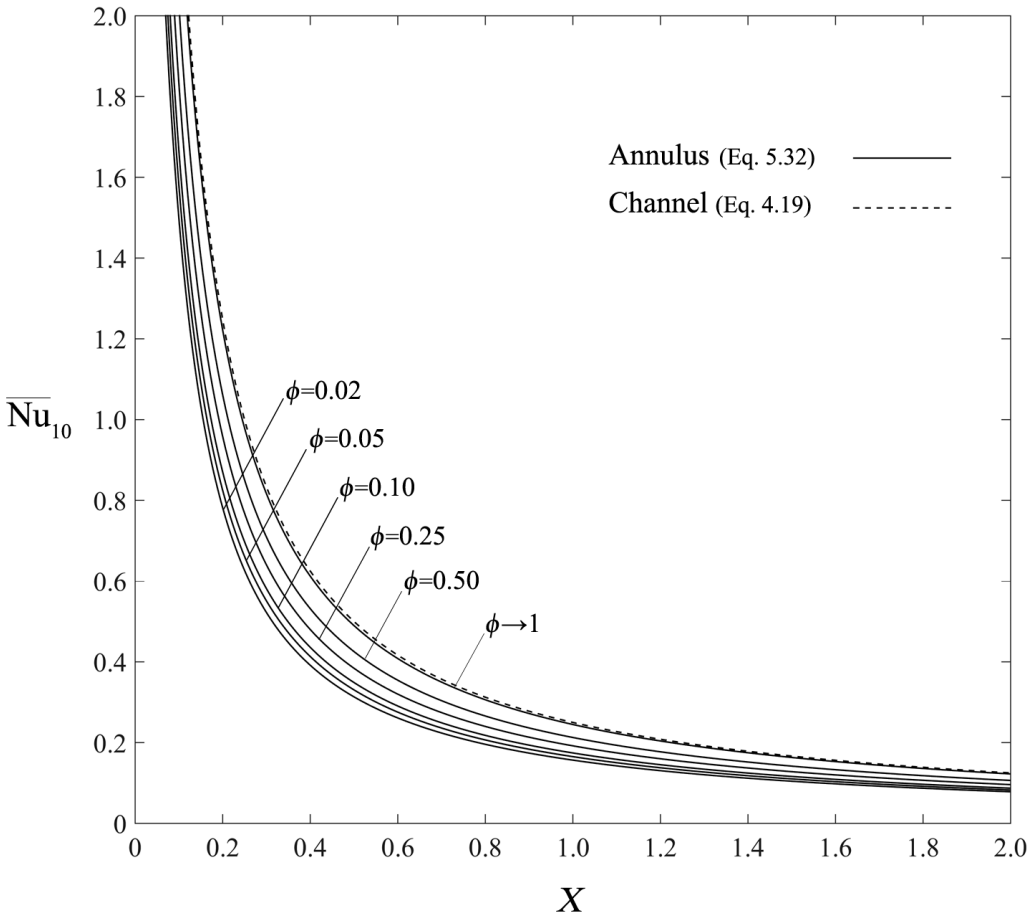

Figure 5.4: Outer-fluid paired Nusselt number of hydrodynamically developed laminar flow in a concentric annulus ($\phi = r_1/r_2$)

The slight discrepancy between the $\phi \rightarrow 1$ curve and the channel-flow curve (dashed) in Figures 5.4 and 5.5 is due to the slight difference between the two sets of eigenvalues [from Hatton & Turton (1962) and Lundberg et al. (1963)] used to generate these curves.

5.4 Curve-Fit Correlations

The accuracy of the series solution shown in Equation 5.5 and the dQdT results obtained using this solution depends on the number of the series terms evaluated. However, since the eigenvalues of the system increase monotonically, the higher-order exponentials become rapidly insignificant as X increases and a very good approximation may be obtained by

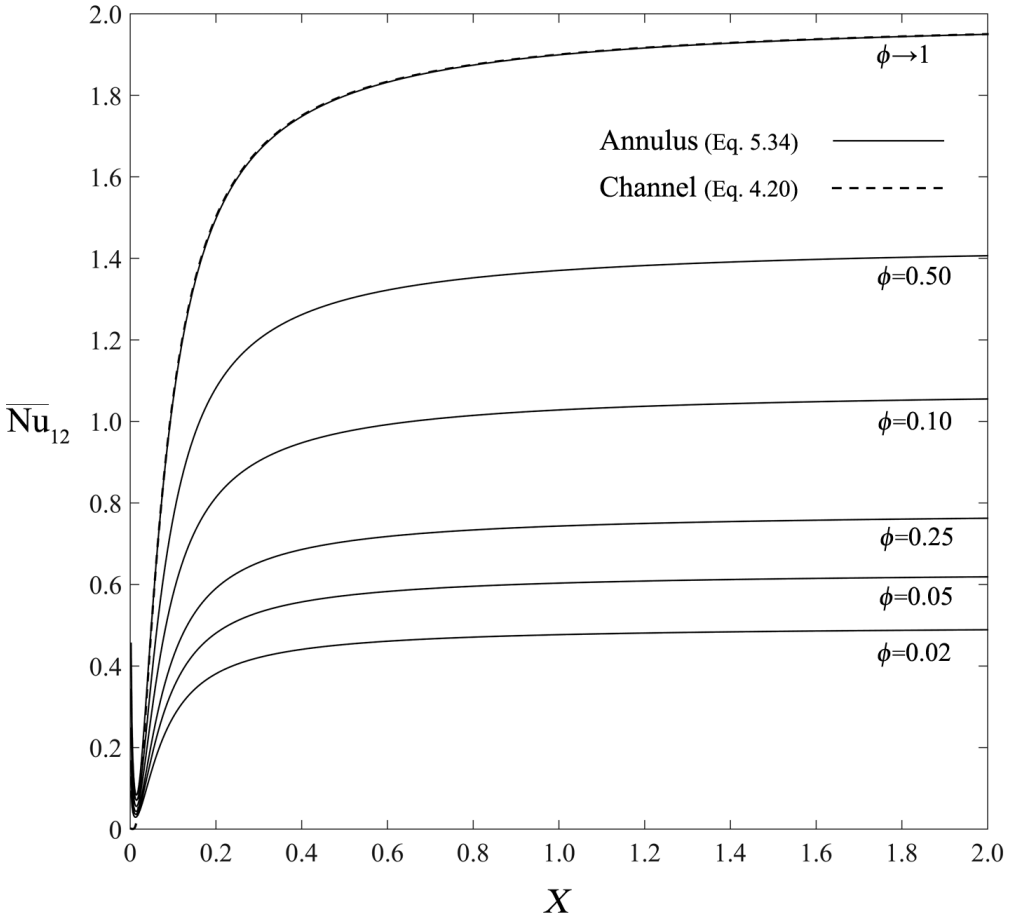

Figure 5.5: Outer-inner paired Nusselt number of hydrodynamically developed laminar flow in a concentric annulus ($\phi = r_1/r_2$)

retaining only the first exponential term. Note that the solution of interest is based on the assumption of negligible axial diffusion which is valid only for large values of X. In Chapter 4, it was shown that the first-exponential approximation to the series expressions for $\{\overline{\mathrm{Nu}}_{ij}\}$ of the channel problem is of good accuracy, especially for $X > 0.05$.

Evaluating only the first exponential terms of the summation components of Equations 5.32-5.34, the average paired Nusselt numbers of the annulus problem can be approximated as:

$$\overline{\mathrm{Nu}}_{10} \approx -2(1-\phi)\left\{ \sum_{n=1}^{4} \left(\frac{B_{n,1}+B_{n,2}}{\lambda_n^2 X} \right) \left(\frac{\partial f_n}{\partial \overline{r}} \right)_{\overline{r}=1} - \left(\frac{B_{0,1}+B_{0,2}}{\lambda_1^2 X} \right) \left(\frac{\partial f_0}{\partial \overline{r}} \right)_{\overline{r}=1} \exp(-\lambda_1^2 X) \right\} \tag{5.39}$$

$$\overline{\mathrm{Nu}}_{20} \approx 2(1-\phi)\left\{ \sum_{n=1}^{4} \left(\frac{B_{n,1}+B_{n,2}}{\lambda_n^2 X} \right) \left(\frac{\partial f_n}{\partial \overline{r}} \right)_{\overline{r}=\phi} - \left(\frac{B_{0,1}+B_{0,2}}{\lambda_1^2 X} \right) \left(\frac{\partial f_0}{\partial \overline{r}} \right)_{\overline{r}=\phi} \exp(-\lambda_1^2 X) \right\} \tag{5.40}$$

$$\overline{\mathrm{Nu}}_{12} \approx \frac{2(1-\phi)}{\ln(1/\phi)} + 2(1-\phi)\left\{ \sum_{n=1}^{4} \left(\frac{B_{n,2}}{\lambda_n^2 X} \right) \left(\frac{\partial f_n}{\partial \overline{r}} \right)_{\overline{r}=1} - \left(\frac{B_{0,2}}{\lambda_1^2 X} \right) \left(\frac{\partial f_0}{\partial \overline{r}} \right)_{\overline{r}=1} \exp(-\lambda_1^2 X) \right\} \tag{5.41}$$

The coefficients and exponents of Equations 5.39-5.41 are all functions of the annulus radius ratio, ϕ. Evaluating these coefficients and exponents for every given ϕ requires solutions to the characteristic differential equation of the Sturm-Liouville system obtained by applying separation of variables to Equation 5.1. Hence the approximate expressions of Equations 5.39-5.41 are of little utility unless the calculation of the coefficients and exponents is simplified. In order to do this, it was first noted that Equations 5.39-5.41 are each comprised of:

i) a fully developed limit which depends only on ϕ,

ii) an "offset" term corresponding to $X = 0$,

iii) an exponential function of X.

This general form is shown in Equation 5.42. The coefficients, E_{ij}, F_{ij} and G_{ij}, are given in Equations 5.43-5.45.

$$\overline{\mathrm{Nu}}_{ij} = E_{ij} + \frac{1}{X}\left[F_{ij} - \frac{G_{ij}}{\lambda_1^2}\exp(-\lambda_1^2 X)\right] \tag{5.42}$$

$$\begin{cases} E_{10} = E_{20} = 0 \\ E_{12} = \dfrac{2(1-\phi)}{\ln(1/\phi)} \end{cases} \tag{5.43}$$

$$\begin{cases} F_{10} = 2(\phi-1)\displaystyle\sum_{n=1}^{4}\left(\frac{B_{n,1}+B_{n,2}}{\lambda_n^2}\right)\left(\frac{\partial f_n}{\partial \overline{r}}\right)_{\overline{r}=1} \\ F_{20} = 2(1-\phi)\displaystyle\sum_{n=1}^{4}\left(\frac{B_{n,1}+B_{n,2}}{\lambda_n^2}\right)\left(\frac{\partial f_n}{\partial \overline{r}}\right)_{\overline{r}=\phi} \\ F_{12} = 2(1-\phi)\displaystyle\sum_{n=1}^{4}\left(\frac{B_{n,2}}{\lambda_n^2}\right)\left(\frac{\partial f_n}{\partial \overline{r}}\right)_{\overline{r}=1} \end{cases} \tag{5.44}$$

$$\begin{cases} G_{10} = 2(\phi-1)\big(B_{0,1}+B_{0,2}\big)\left(\dfrac{\partial f_0}{\partial \overline{r}}\right)_{\overline{r}=1} \\ G_{20} = 2(1-\phi)\big(B_{0,1}+B_{0,2}\big)\left(\dfrac{\partial f_0}{\partial \overline{r}}\right)_{\overline{r}=\phi} \\ G_{12} = 2(1-\phi)B_{0,2}\left(\dfrac{\partial f_0}{\partial \overline{r}}\right)_{\overline{r}=1} \end{cases} \tag{5.45}$$

Analytical expressions were then obtained for λ_1^2, $\{F_{ij}\}$ and $\{G_{ij}\}$ by fitting curves to data points obtained using the results of Lundberg et al. (1963). See Equations 5.46-5.48

Table 5.1: Coefficients and exponents of the curve-fit relations (Eqs. 5.47-5.48)

ij	f_1	f_2	f_3	f_4	g_1	g_2	g_3
10	0.173	-0.041	0.067	0	3.221	0.554	3.634
20	0.073	-0.842	0	0.175	2.420	-0.751	4.709
12	0.072	0.665	0	-0.027	2.928	0.569	0.500

and Table 5.1. The coefficient of determination in all these curve-fit relations is 0.99. Further details can be found in Appendix C.

$$\lambda_1^2 \approx 28.96 \exp(0.042\phi) - 7.62 \exp(-9.240\phi) \tag{5.46}$$

$$F_{ij} = f_1 \phi^{f_2} + f_3 \phi + f_4 \tag{5.47}$$

$$G_{ij} = g_1 \phi^{g_2} + g_3 \tag{5.48}$$

To use Equation 5.42, E_{ij} is first calculated using Equation 5.43; Equation 5.46 is used to estimate λ_1^2; F_{ij} and G_{ij} are then calculated using Equations 5.47 and 5.48 respectively, with constants from Table 5.1. With $\{\overline{\mathrm{Nu}}_{ij}\}$ known, Q_1 and Q_2 can be calculated as shown in Equation 5.49 and Q_0 as: $Q_0 = -Q_1 - Q_2$. This procedure is demonstrated in Section 5.5.

$$\begin{aligned} Q_i &= \sum_j C_{ij}(T_i - T_j) \\ &= \frac{A_i k}{2(r_1 - r_2)} \sum_j \overline{\mathrm{Nu}}_{ij}(T_i - T_j) \qquad (i = 1, 2) \end{aligned} \tag{5.49}$$

5.5 Sample Calculations

The application of the paired Nusselt numbers in heat transfer calculations and the utility and accuracy of the proposed curve-fit correlations are demonstrated in the following examples.

Consider a flow of engine oil ($\mu = 5.13 \times 10^{-2}$ Ns/m^2, $k = 0.139$ W/mK, $c_p = 2.076$ kJ/kgK) at a flow rate of $\dot{m} = 0.05$ kg/s in an annulus with $D_1 = 100$ mm and $D_2 = 50$ mm and a length of $x = 1.6$ m. The inlet temperature is $T_0 = 40°$C and the annulus walls are at $T_1 = 60°$C and $T_2 = 90°$C.

In this case, $D_\mathrm{h} = 0.05$ m, Pr $= 793$ and Re $= 8$. Therefore, at $x = 1.6$ m, the inverse Graetz number is:

$$X = \left(\frac{x}{D_\mathrm{h}}\right)\frac{1}{\mathrm{Re\ Pr}} = \left(\frac{1.6}{0.05}\right)\frac{1}{8 \times 793} = 0.005$$

Because X is very small, relatively large errors are expected when the first-exponent approximations and the proposed curve-fit correlations are used. For larger values of X, i.e. farther from the annulus inlet, the error will be smaller.

The rate of total heat transfer from the fluid can be obtained from an overall energy balance:

$$Q_0 = \dot{m}C_p\big(T_0 - T_\mathrm{m}\big)$$

The change in the mean fluid temperature, $T_\mathrm{m} - T_0$, can be calculated by super-imposing two fundamental solutions, $\theta_{\mathrm{m},1}$ and $\theta_{\mathrm{m},2}$:

$$T_0 - T_\mathrm{m} = (T_0 - T_1)\theta_{\mathrm{m},1} + (T_0 - T_2)\theta_{\mathrm{m},2}$$

According to tabulated data from *Handbook of Heat Transfer* (Rohsenow et al. 1998);

$$\phi = 0.5, X = 0.005 \quad \Rightarrow \quad \begin{cases} \theta_{\mathrm{m},1} = 0.1280 \\ \theta_{\mathrm{m},2} = 0.0782 \end{cases}$$

Therefore:

$$Q_0 = \dot{m} c_p \Big[(T_0 - T_1)\theta_{\mathrm{m},1} + (T_0 - T_2)\theta_{\mathrm{m},2} \Big] = -672\,\mathrm{W}$$

Alternatively, Q_0 may be calculated using Equation 5.49:

$$\begin{aligned} Q_0 &= -Q_1 - Q_2 \\ &= -\frac{\pi r_1 x k}{(r_1 - r_2)} \Big[\overline{\mathrm{Nu}}_{10}(T_1 - T_0) + \phi \overline{\mathrm{Nu}}_{20}(T_2 - T_0) \Big] \end{aligned}$$

At $\phi = 0.5$ and $X = 0.005$, dQdT results (Equations 5.39 and 5.40) yield: $\overline{\mathrm{Nu}}_{10} = 7.88$, $\overline{\mathrm{Nu}}_{20} = 9.72$. Therefore:

$$\begin{aligned} Q_0 &= -\frac{\pi x k}{(1-\phi)} \Big[\overline{\mathrm{Nu}}_{10}(T_1 - T_0) + \phi \overline{\mathrm{Nu}}_{20}(T_2 - T_0) \Big] \\ &= -\frac{\pi (1.6)(0.139)}{(1 - 0.5)} \Big[(7.88)(20) + (0.5)(9.72)(50) \Big] \\ &= -560\,\mathrm{W} \end{aligned}$$

The dQdT result differs from the energy-balance calculation by 17%. This error is large since X is small.

Using the first exponential terms of Equations 5.39 and 5.40, the wall-fluid Nusselt numbers are: $\overline{\mathrm{Nu}}_{10} = 8.77$, $\overline{\mathrm{Nu}}_{20} = 9.64$. The rate of total heat transfer to the fluid is then:

$$Q_0 = -\frac{\pi (1.6)(0.139)}{(1 - 0.5)} \Big[(8.77)(20) + (0.5)(9.64)(50) \Big] = -582\,\mathrm{W}$$

The result above differs from the energy-balance calculation by 13%.

Estimates of $\overline{\mathrm{Nu}}_{10}$ and $\overline{\mathrm{Nu}}_{20}$ now may also be obtained using the proposed curve-fit relations. According to Equation 5.43:

$$E_{10} = E_{20} = 0$$

With $\phi = 0.5$, Equations 5.46-5.48 yield:

$$\lambda_1^2 = 28.96 \exp\left[0.042(0.5)\right] - 7.62 \exp\left[-9.24(0.5)\right] = 29.50$$

$$F_{10} = 0.173(0.5)^{-0.041} + 0.067(0.5) = 0.2122$$

$$F_{20} = 0.073(0.5)^{-0.842} + 0.175 = 0.3066$$

$$G_{10} = 3.221(0.5)^{0.554} + 3.634 = 5.8279$$

$$G_{20} = 2.420(0.5)^{-0.751} + 4.709 = 8.7818$$

Therefore, at $X = 0.005$ Equation 5.42 gives:

$$\overline{\mathrm{Nu}}_{10} = \frac{1}{0.005}\left\{0.2122 - \left(\frac{5.83}{29.50}\right)\exp\left[-29.5(0.005)\right]\right\} = 8.33$$

$$\overline{\mathrm{Nu}}_{20} = \frac{1}{0.005}\left\{0.3066 - \left(\frac{8.78}{29.50}\right)\exp\left[-29.5(0.005)\right]\right\} = 9.96$$

Hence:

$$Q_0 = -581 \text{ W}$$

Note that the result is virtually the same as the value calculated using the first-exponent approximations of $\{\overline{\mathrm{Nu}}_{ij}\}$.

Next, consider a radius ratio for which tabulated data for B_n, $\partial f_n/\partial \bar{r}$ and λ_n are not available, e.g. ϕ=0.3. There is no handbook entry corresponding to $\phi = 0.3$. In this case, to evaluate the paired Nusselt numbers using Equations 5.32-5.34 (or Equations 5.39-5.41), B_n, $\partial f_n/\partial \bar{r}$ and λ_n must first be calculated. The calculation of the eigenvalues specifically is iterative and cumbersome. Alternatively, dQdT may be applied numerically as described in Chapter 2. But this entails at least three numerical solutions to the energy equation. The curve-fit relations developed in this chapter (Equation 5.42) are now a considerably simpler option.

In Figure 5.6 the curve-fit relations for ϕ=0.3 are compared to the results of numerical dQdT based on a finite-volume solution to the energy equation. The curve-fit results were generated in a spreadsheet. The two sets of results for wall-fluid Nusselt numbers are in good agreement, especially for $X \gtrsim 0.05$, while the wall-wall results are virtually identical for $X \gtrsim 0.02$. Note that the dQdT results are based on a numerical solution to the full, elliptic energy equation while the correlations were developed based on a solution to the parabolic energy equation. Therefore, the discrepancy between the results decreases as X increases.

5.6 Summary

The extended Newton formulation of hydrodynamically developed laminar flow in a concentric annulus with isothermal walls leads to functionality coefficients (paired Nusselt numbers) which are independent of temperature, do not have extra singularities and can be applied to any laminar flow rate, any fluid and any set of boundary temperatures. dQdT was applied to obtain analytical expressions for these functionality coefficients. It was shown that there is reciprocity between the functionality coefficients, hence the problem can be represented by a delta network of convective resistors.

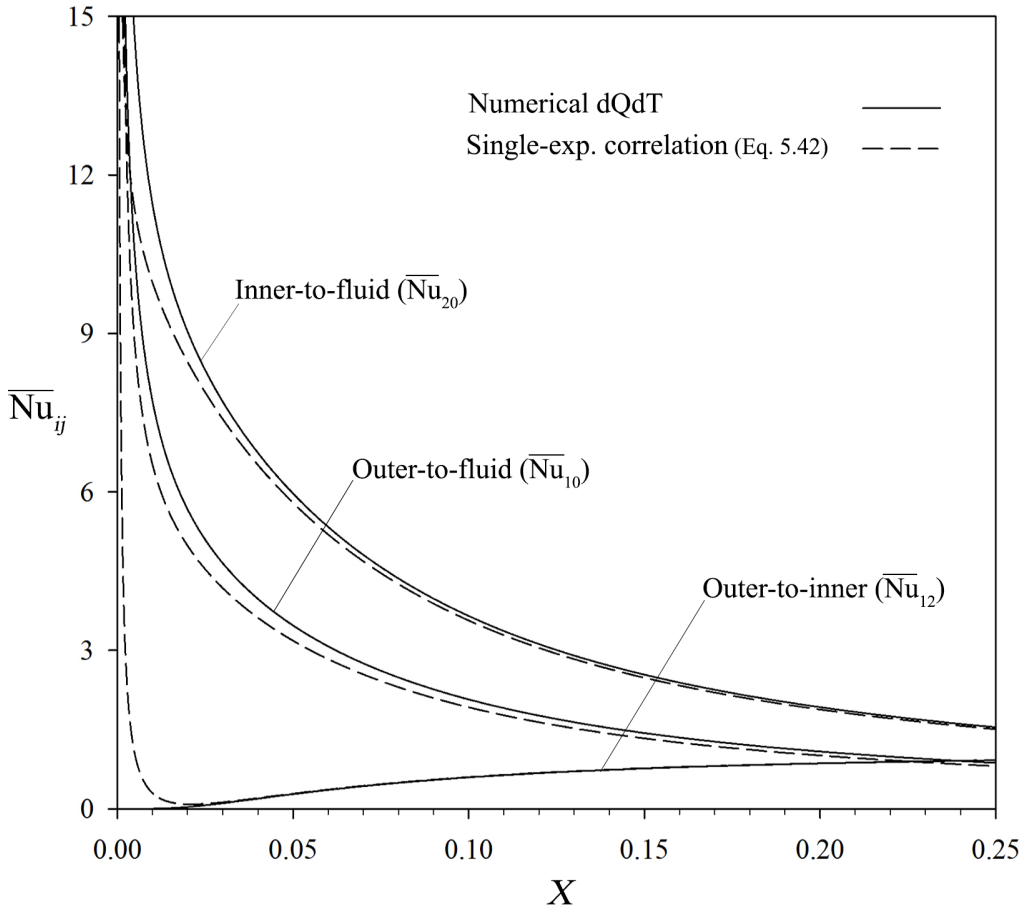

Figure 5.6: Average paired Nusselt numbers of hydrodynamically developed laminar flow in a concentric annulus (ϕ=0.3)

Furthermore, it was shown that as the curvature of the annulus walls approaches zero, i.e. the annulus turns into a parallel-plate channel, the results approach the dQdT results obtained in Chapter 4 for the channel problem. Single-exponent approximations along with curve-fit correlations for the solution constants were developed which may be used to estimate the paired Nusselt numbers with considerable simplicity and reasonable accuracy for any given geometry, i.e. radius ratio.

Chapter 6

Convection in Hydrodynamically Developing Flow in an Annulus with Isothermal Walls

In Chapters 4 and 5, convection in channels and annuli with isothermal walls was examined under hydrodynamically fully developed flow conditions. The assumption of hydrodynamically developed flow reduces the problem to solving the energy equation. Classical analytical solutions from the literature were used in the two preceding chapters to apply dQdT analytically and obtain the functionality coefficients of the multi-temperature problem.

If the flow enters the heated section before reaching full hydrodynamic development, the thermal analysis also entails solution of the momentum equation. No analytical solution was found in the literature for hydrodynamically developing flow in an annulus. Numerical solutions are, nevertheless, relatively easy to obtain. As discussed in Chapter 2, the dQdT technique can also be applied numerically given a valid baseline solution to the problem of interest. In this short chapter, the application of numerical dQdT to CFD solutions of

simultaneously developing flow in an annulus with isothermal walls is demonstrated. Both laminar and turbulent regimes are considered.

Consider the configuration shown in Figure 6.1: fluid flow entering at uniform velocity and temperature, u_0 and T_0, the annulus formed between two concentric circular pipes of radii r_1 and r_2 with isothermal walls at temperatures T_1 and T_2. The flow is characterized by the Reynolds number introduced in Chapter 5:

$$\mathrm{Re} = \frac{\rho u_0 D_\mathrm{h}}{\mu}$$

The ordering of the boundary temperatures, T_0, T_1 and T_2, is characterized by a temperature ratio, defined in Equation 6.1.

$$r_T = \frac{T_1 - T_0}{T_2 - T_0} \tag{6.1}$$

Heat transfer in the annulus is traditionally formulated in terms of the local wall Nusselt number defined in Equations 6.2. In this equation, T_m denotes the mean fluid temperature.

$$\mathrm{Nu}_i = \frac{q_i}{T_i - T_\mathrm{m}} \left(\frac{D_h}{k} \right) \qquad (i = 1, 2) \tag{6.2}$$

6.1 Baseline Solutions

6.1.1 Solution Method

The commercial CFD solver ANSYS Fluent 14.0 (ANSYS 2011a,b) was used to obtain second-order finite volume solutions in an axisymmetric model of the annulus. The

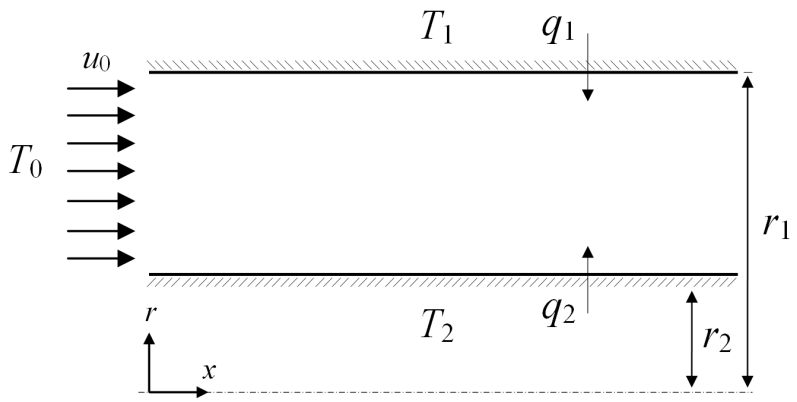

Figure 6.1: Schematic of flow in a concentric annulus with isothermal walls

Standard algorithm for discretizing pressure and the SIMPLE scheme for handling the pressure-velocity coupling were used. The Shear Stress Transformation variation of the k-ω model was used to resolve turbulence.

6.1.2 Computational Domain, Boundary Conditions & Discretization

A rectangular computational domain was used as an axisymmetric model of the annulus. See Figure 6.1. Velocity and temperature were specified at the inlet ($x = 0$). For the turbulent cases, the turbulence intensity and the annulus hydraulic diameter were also specified at the inlet. The other end of the domain was designated a pressure outlet. The annulus walls were modeled as impermeable, no-slip, isothermal solid boundaries.

The computational domain was discretized into a non-uniform rectangular grid of 53,000 control volumes. A Richardson-extrapolation technique (Celik et al. 2008) was used to assess grid dependence of the solutions. Using two additional grids with 28,000 and 200,000 control volumes, and based on the rate of total heat transfer to the fluid

(Q_0), grid convergence indices of 1% and 2% respectively were calculated for $\mathrm{Re} = 50$ and $\mathrm{Re} = 10,000$. The apparent order of the solutions was calculated to be 2.1.

6.1.3 Validation

Two validation studies were performed. In the laminar regime, the baseline CFD solutions were validated against the calculations using the "influence coefficients" derived by Kakaç & Yücel (1974). Unfortunately, details of the solution by Kakaç & Yücel (1974) are not available.[1] Tabulated data from this solution, available in *Handbook of Heat Transfer* (Rohsenow et al. 1998), were used in the present study.

For hydrodynamically developing flows, the axial location in the annulus is customarily reported in dimensionless form as x/D_h. However, the solution by Kakaç & Yücel (1974) is given in terms of the inverse Graetz number, defined in Equation 5.7:

$$X = \frac{x}{D_\mathrm{h}} \left(\frac{1}{\mathrm{Re}\ \mathrm{Pr}} \right)$$

In Figure 6.2 the CFD predictions for $\{\mathrm{Nu}_i\}$ are compared to calculations performed using tabulated data from the *Handbook* for $\phi = r_2/r_1 = 0.5$, $r_T = 0.5$ and $\mathrm{Pr} = 0.7$. It can be seen that, except in the vicinity of the singularity in Nu_1 (caused by $T_\mathrm{m} = T_1$ at $X \approx 0.035$), the two sets of results are nearly identical. The CFD solutions for laminar flow are thus validated.

In the turbulent regime, the CFD solutions were validated against the measurements of Roberts & Barrow (1967) for simultaneously developing flow of air ($\mathrm{Pr} = 0.7$) at $\mathrm{Re} = 55,000$ in an annulus with $\phi = 0.476$, while the inner wall was heated with a uniform heat flux and the outer wall was insulated. In Figure 6.3, the present CFD predictions of Nu_2 using two different turbulence models are compared to the experimental data. The present SST k-ω solution is in generally good agreement with the measurements of Roberts

[1] The thesis by Yücel (1972) is not publicly available and personal correspondence with Professor Kakaç did not reveal further details of the solution.

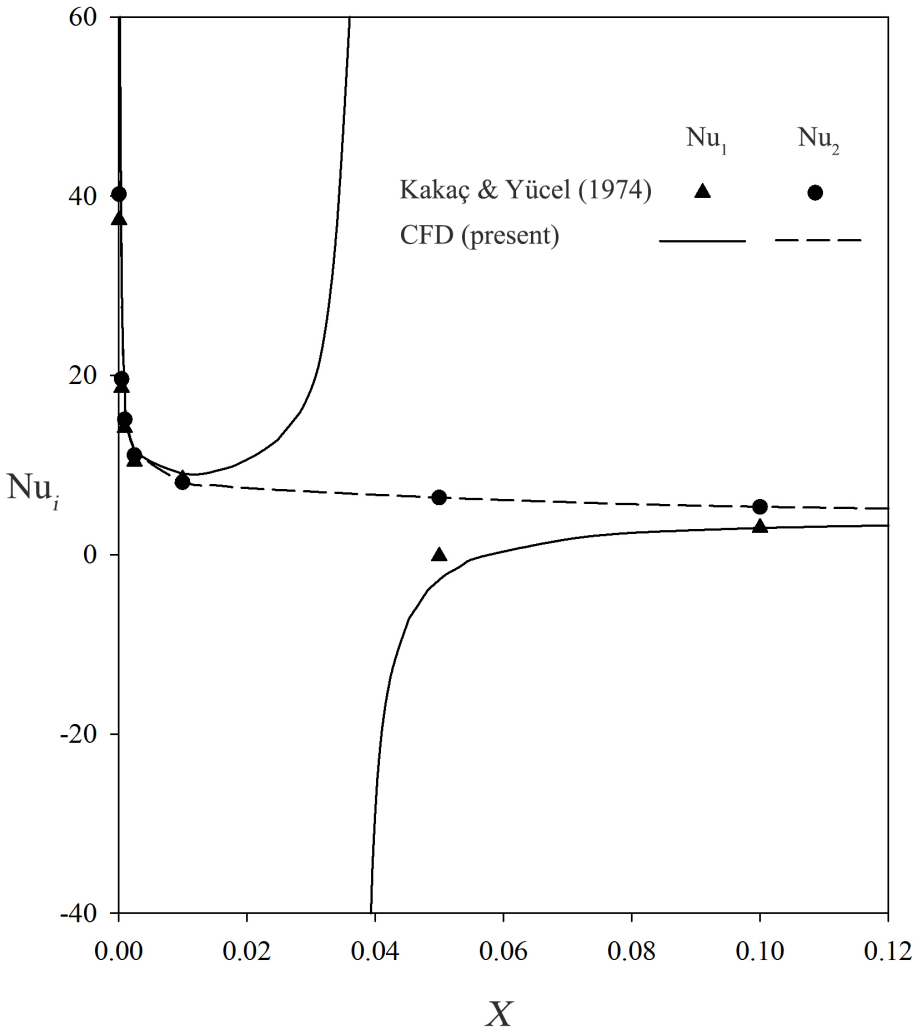

Figure 6.2: Local Nusselt numbers of laminar developing flow in an annulus with isothermal walls ($\phi = 0.5$, $r_T = 0.5$, $\mathrm{Pr} = 0.7$)

& Barrow (1967). Away from the inlet ($x > 5\,D_\mathrm{h}$) the present numerical results are less than 10% higher than the experimental data. Also shown in Figure 6.3 are the results of an earlier numerical study by Malik (1978) compared to which the present k-ω solution seems to be in better agreement with the experimental data.

Unfortunately, Roberts & Barrow (1967) have not reported the turbulence intensity at the inlet. It is stated that the flow is ensured to be fully turbulent by the use of tripping devices at the annulus entrance. Nevertheless, the inlet turbulence is not quantified, merely

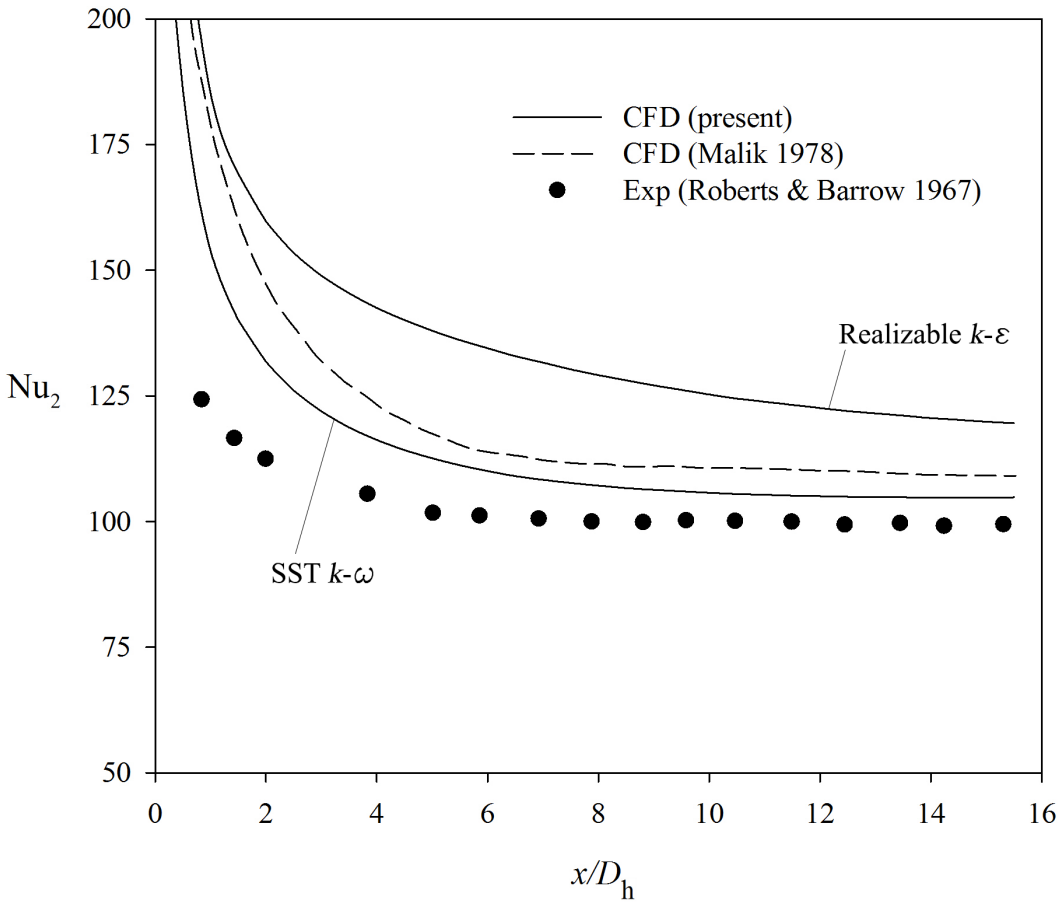

Figure 6.3: Local Nusselt number of turbulent developing flow in an annulus. Inner wall heated with uniform flux, outer wall insulated ($\phi = 0.476$, $\mathrm{Re} = 55,000$, $\mathrm{Pr} = 0.7$)

reported to be "small" (Roberts & Barrow 1967). In the CFD study by Malik (1978) an inlet turbulence intensity of 0.02% has been used. In the present solutions, inlet turbulence intensities between 0.02% and 1% were tested leading to less than 1% difference in the average Nusselt number from $x = 0$ to $x = 15\,D_\mathrm{h}$. Results shown in Figure 6.3 are for an inlet intensity of 1%.

Furthermore, the uncertainty in the measurements of the wall Nusselt number are not reported by Roberts & Barrow (1967). Therefore the comparison between the numerical and experimental results is incomplete. But no better instance of experimental data was

found in the literature. The general agreement between the numerical results and the experimental data was taken as validation of the present CFD solutions.

6.2 Numerical dQdT

For each value of Re, numerical dQdT was implemented following the procedure below:

i) A baseline numerical solution was obtained to the full set of governing equations.

ii) The baseline heat transfer rates, $\{Q_i\}$, were obtained; Q_1 and Q_2 were calculated by integrating the heat flux at the walls, while Q_0 was calculated based on the overall energy balance of the annulus: $Q_0 = -Q_1 - Q_2$.

iii) The boundary temperature T_j was perturbed by a finite amount, δT_j.

iv) The solution to the energy equation was updated.

v) The new heat transfer rates, $\{Q_i^*\}$, and the respective changes were calculated; $\delta Q_i = Q_i^* - Q_i$.

vi) The functionality coefficients corresponding to T_j were calculated using Equation 2.44; $C_{ij} = -\delta Q_i / \delta T_j$.

vii) Steps iii-vi were repeated for $j = 0, 1, 2$.

Note that since this is a constant-property forced-convection problem, the $C_{ik} = \text{const}$ constraint is automatically satisfied. Furthermore, the functionality coefficients obtained for a specific set of boundary temperatures apply to any $\{T_i\}$.

Obtaining the full set of functionality coefficients in an N-temperature problem entails a baseline solution to the full set of governing equations and N subsequent solutions to the energy equation with perturbed boundary conditions. However, because the energy equation is linear, the N additional solutions do not impose significant computational cost.

6.3 Average Paired Nusselt Numbers

Sample dQdT results are shown in Table 6.1 for the flow of air (Pr = 0.7) at various flow rates, $10 \leq \mathrm{Re} \leq 10^4$, in a concentric annulus with $x = 25\,D_\mathrm{h}$ and $\phi = 0.5$. An inlet turbulent intensity of 15% was used to generate the fully turbulent results. As can be seen in this table, there is reciprocity between the functionality coefficients; $C_{ij} \approx C_{ji}$. Therefore, the resistor-network model is applicable. The small (relative) difference between the functionality coefficient pairs is due to numerical error.

The functionality coefficients were converted to dimensionless form using the average paired Nusselt number defined in Equation 6.3.

$$\overline{\mathrm{Nu}}_{ij} = \frac{2(r_1 - r_2)}{A_i}\left(\frac{C_{ij}}{k}\right) \qquad (i = 1, 2) \tag{6.3}$$

In Figures 6.4-6.6, $\{\overline{\mathrm{Nu}}_{ij}\}$ are plotted versus axial location along the annulus. Three key observations can be made regarding the results presented in these figures. First, no dependence on temperature or a temperature ratio is observed. Moreover, the extra singularities of the traditional formulation are eliminated. Finally, the trends of $\{\overline{\mathrm{Nu}}_{ij}\}$ are consistent with the physics of the problem.

Wall-fluid Nusselt numbers, $\overline{\mathrm{Nu}}_{10}$ and $\overline{\mathrm{Nu}}_{20}$, shown in Figures 6.4 and 6.5, start from singularities at the annulus inlet and decay as the flow develops thermally. The general trend is similar to the hydrodynamically-developed case, studied in Chapter 5. Here too, the inner wall has a larger wall-fluid Nusselt number; $\overline{\mathrm{Nu}}_{20} > \overline{\mathrm{Nu}}_{10}$. Transition to turbulence (dashed curves) significantly enhances wall-fluid heat transfer, leading to significant increases in $\overline{\mathrm{Nu}}_{10}$ and $\overline{\mathrm{Nu}}_{20}$.

The wall-wall Nusselt number, $\overline{\mathrm{Nu}}_{12}$, plotted in Figure 6.6, starts from $\overline{\mathrm{Nu}}_{12} = 0$ at $X = 0$ and approaches the pure-conduction limit. In Chapter 5, this limit was shown to

Table 6.1: Sample dQdT results for developing flow in an annulus with isothermal walls [+] ($x = 25\,D_\mathrm{h} = 25\,\mathrm{m}$, $\phi = 0.5$, $\mathrm{Pr} = 0.7$)

Re	C_{12}	C_{21}	C_{10}	C_{01}	C_{20}	C_{02}
10	5.67×10^3	5.68×10^3	6.29×10^2	6.25×10^2	3.70×10^2	3.74×10^2
100	4.96×10^3	4.99×10^3	2.74×10^3	2.72×10^3	1.82×10^3	1.85×10^3
500	2.26×10^3	2.32×10^3	1.14×10^4	1.14×10^4	7.72×10^3	7.78×10^3
1000	8.21×10^2	8.77×10^2	1.78×10^4	1.78×10^4	1.18×10^4	1.18×10^4
5000	2.03×10^3	1.99×10^3	6.56×10^4	6.57×10^4	3.80×10^4	3.79×10^4
10000	2.61×10^3	2.56×10^3	1.14×10^5	1.14×10^5	6.39×10^4	6.39×10^4

[+]All values of C_{ij} are in [W/K].

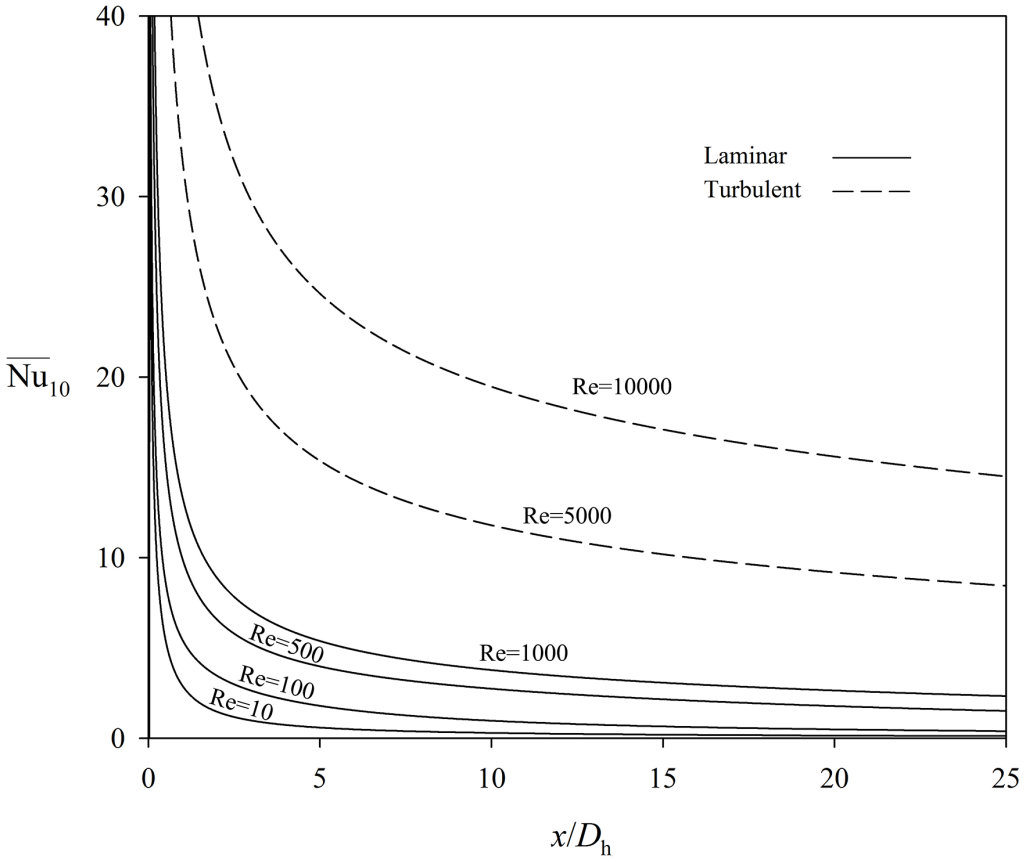

Figure 6.4: Average outer-wall-fluid Nusselt number in developing flow ($\phi = 0.5$, $\mathrm{Pr} = 0.7$)

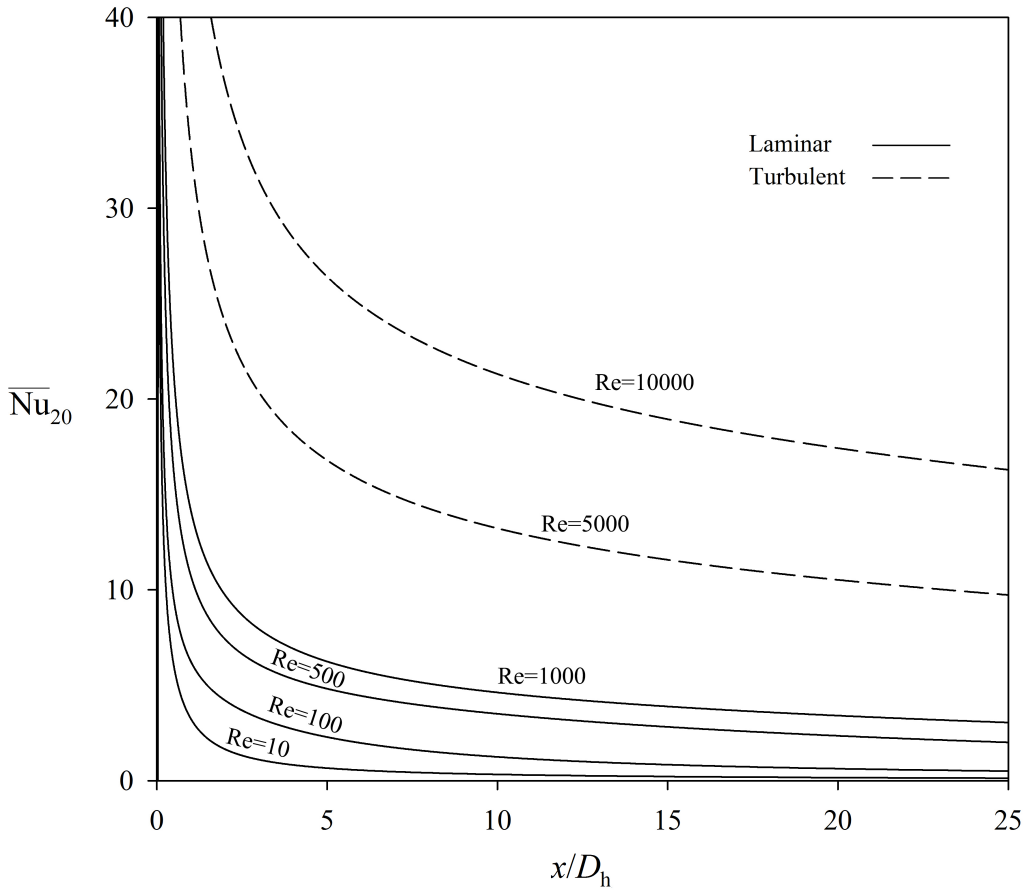

Figure 6.5: Average inner-wall-fluid Nusselt number in developing flow ($\phi = 0.5$, Pr $= 0.7$)

be $\overline{\mathrm{Nu}}_{12} = 1.44$ for laminar flow in an annulus with $\phi = 0.5$. dQdT results also reveal that, similar to the case of hydrodynamically developed flow;

$$\frac{\overline{\mathrm{Nu}}_{12}}{\overline{\mathrm{Nu}}_{21}} = \phi = 0.5$$

As the flow rate increases, the thermal development is pushed farther downstream and, therefore, $\overline{\mathrm{Nu}}_{12}$ at any given location decreases. In the fully turbulent cases (dashed curves), $\overline{\mathrm{Nu}}_{12}$ is enhanced by turbulent mixing. Therefore:

$$\overline{\mathrm{Nu}}_{12}(\mathrm{Re} = 10,000) > \overline{\mathrm{Nu}}_{12}(\mathrm{Re} = 5000) > \overline{\mathrm{Nu}}_{12}(\mathrm{Re} = 1000) \qquad (x/D_\mathrm{h} > 5)$$

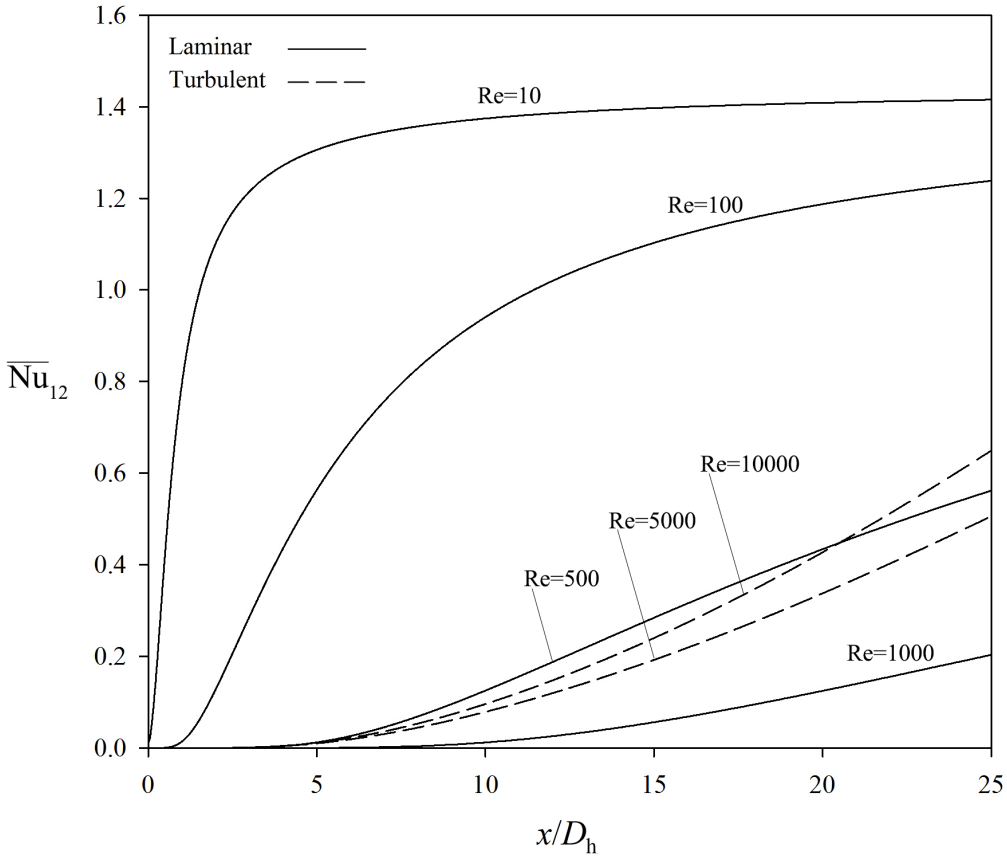

Figure 6.6: Average outer-inner Nusselt number in developing flow ($\phi = 0.5$, $\mathrm{Pr} = 0.7$)

6.4 Summary

The application of numerical dQdT was demonstrated for sample cases of hyrodynamically developing flow in a concentric annulus with isothermal walls. Both laminar and turbulent regimes were considered. It was shown that formulating the multi-temperature problem in terms of paired Nusselt numbers leads to the same advantages as in the case of hyrodynamically developed flow. Further, it was shown that similar to the case of hydrodynamically developed flow, the functionality coefficients of the hydrodynamically developing flow have reciprocity and hence the resistor-network model is applicable. Numerical dQdT results based on RANS baseline solutions were shown to be consistent with the physics of the problem.

Chapter 7

Convection in Laminar Cross Flow over a Pair of Isothermal Cylinders

The problems examined in Chapters 4-6 all entailed internal flow. It was shown in those chapters that the extended Newton formulation of multi-temperature convection problems, made possible by the dQdT technique, is advantageous. In the present chapter, the application of the extended Newton formulation and the dQdT technique to an external-flow multi-temperature convection problem is demonstrated.

Another common feature of the problems studied in Chapters 4-6 is the reciprocity of functionality coefficients: $C_{ij} = C_{ji}$. However, as briefly discussed in Chapter 3, this is not necessarily the case. In the present chapter, a case where $C_{ij} \neq C_{ji}$ is demonstrated and discussed.

Consider a uniform isothermal flow with velocity u_0 and temperature T_0 approaching a pair of parallel, horizontal cylinders of the same diameter, $D_1 = D_2$, with a center-to-center spacing of L and uniform surface temperatures of T_1 and T_2. Two alignments of the cylinders are considered: a) side by side, and b) tandem. See Figure 7.1. These

configurations were briefly discussed in Chapter 3. In the present chapter, they are examined in greater detail.

The flow is characterized by the Reynolds number, Re, defined in Equation 7.1. Heat transfer at the cylinders is typically characterized by total Nusselt numbers, $\{\overline{\mathrm{Nu}}_i\}$, defined in Equation 7.2. In this equation, Q_i denotes heat transfer per unit length of the cylinder at T_i.

$$\mathrm{Re} = \frac{\rho u_0 D_1}{\mu} \tag{7.1}$$

$$\overline{\mathrm{Nu}}_i = \frac{Q_i}{\pi k(T_i - T_0)} \qquad (i = 1, 2) \tag{7.2}$$

In the traditional formulation of external-flow problems, the fluid flow is represented by the free-stream temperature, T_0, i.e. the corresponding boundary condition. Therefore, the extra singularities observed in the traditional Nusselt numbers of internal-flow problems do not occur. Nevertheless, other limitations of the traditional formulation remain unresolved – even with T_0 representing the flow. For example, if one of the cylinders is at the same temperature as the free-stream flow, say $T_2 = T_0$, the corresponding total Nusselt number, $\overline{\mathrm{Nu}}_2$, becomes indefinite; $\overline{\mathrm{Nu}}_2 \to \infty$. Note that the respective heat transfer rate, Q_2, remains finite for any $\{T_i\}$. Moreover, as discussed earlier, heat transfer in a constant-property forced-convection problem is best characterized by "universal" Nusselt numbers that are temperature-independent. The singular behavior of $\overline{\mathrm{Nu}}_2$ in the special case of $T_2 = T_0$ contradicts the physics of the problem. The extended Newton formulation offers an opportunity to address such shortcomings while presenting more details about the heat transfer phenomenon.

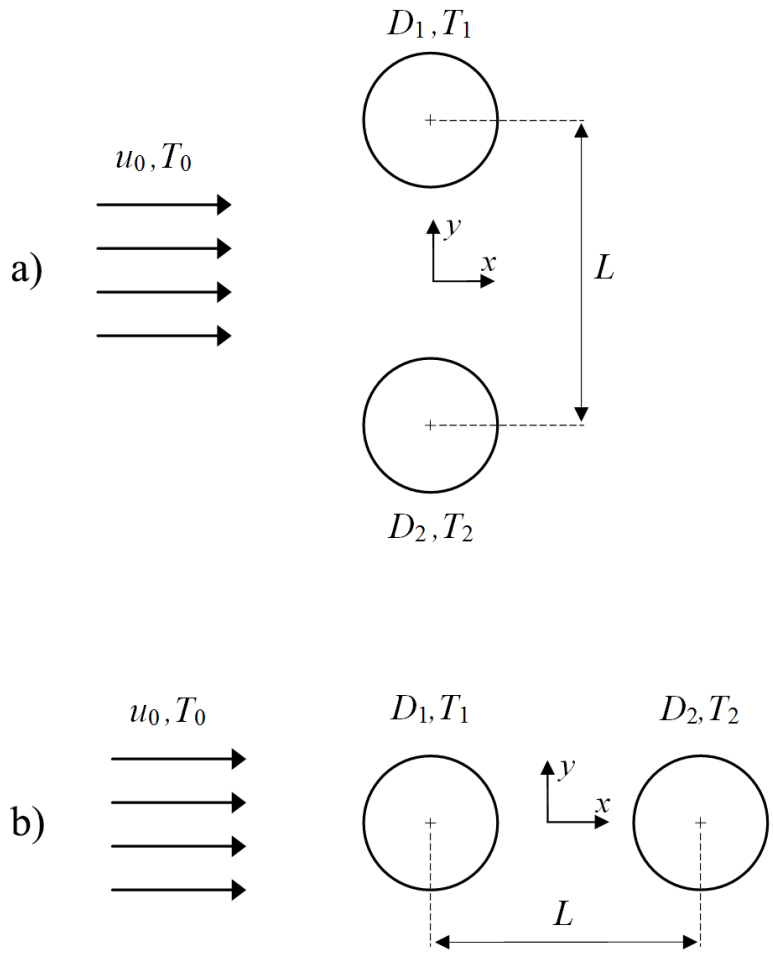

Figure 7.1: Schematic of cross flow over a pair of isothermal cylinders
a) side-by-side alignment, b) tandem alignment

7.1 Extended Newton Formulation

Cross flow over a pair of isothermal cylinders entails three isothermal boundaries: the free-stream flow at T_0 and the two cylinders at T_1 and T_2. Consequently, there are three heat transfer rates of interest: Q_0, Q_1 and Q_2. Each Q_i is in turn characterized by two functionality coefficients. The rate of total heat transfer from the fluid, for instance, can be written as:

$$Q_0 = C_{01}(T_0 - T_1) + C_{02}(T_0 - T_2)$$

The functionality coefficients of the problem, $\{C_{ij}\}$, can be obtained using numerical dQdT.

7.2 Baseline Solutions

7.2.1 Governing Equations

The governing equations under steady laminar flow are shown in Equations 7.3-7.6. These equations are based on the assumption of steady-state, two-dimensional incompressible flow with constant fluid properties and negligible viscous dissipation.

$$\frac{\partial u}{\partial x} + \frac{\partial v}{\partial y} = 0 \tag{7.3}$$

$$\rho u \frac{\partial u}{\partial x} + \rho v \frac{\partial u}{\partial y} = -\frac{\partial p}{\partial x} + \mu \left(\frac{\partial^2 u}{\partial x^2} + \frac{\partial^2 u}{\partial y^2} \right) \tag{7.4}$$

$$\rho u \frac{\partial v}{\partial x} + \rho v \frac{\partial v}{\partial y} = -\frac{\partial p}{\partial y} + \mu \left(\frac{\partial^2 v}{\partial x^2} + \frac{\partial^2 v}{\partial y^2} \right) \tag{7.5}$$

$$\rho u c_p \frac{\partial T}{\partial x} + \rho v c_p \frac{\partial T}{\partial y} = k \left(\frac{\partial^2 T}{\partial x^2} + \frac{\partial^2 T}{\partial y^2} \right) \tag{7.6}$$

7.2.2 Solution Method

The commercial CFD solver ANSYS Fluent 14.0 (ANSYS 2011a,b) was used to obtain second-order finite volume solutions to Equations 7.3-7.6. The Standard algorithm for

discretizing pressure and the SIMPLE scheme for handling the pressure-velocity coupling were used.

7.2.3 Computational Domain, Boundary Conditions & Discretization

A schematic of the computational domain is shown in Figure 7.2. The free-stream velocity and temperature were specified at the domain inlet (1), while the outlet (2) was designated a pressure outlet. The other two sides of the domain (3-4) were designated "symmetry" boundaries. The cylinders were modeled as impermeable, no-slip, isothermal solid boundaries.

The domain was discretized into a non-uniform grid of approximately 84,000 triangular control volumes. Solutions were also obtained using two additional grids with approximately 27,000 and 335,000 control volumes. Based on the Richardson-extrapolation technique proposed by Celik et al. (2008) and the rate of total heat transfer to the fluid (Q_0), a grid convergence index of 1% was calculated for the medium mesh which was used to generate the baseline solutions for dQdT.

7.2.4 Validation

No experimental data on cross flow over cylinder pairs in the steady laminar regime were found in the literature. The existing studies are devoted to unsteady flow – particularly vortex shedding past the cylinders – and turbulent flow. See, for example, the work of Bearman & Wadcock (1973) and Zdravkovich (1977, 1987). Therefore a proper validation of the baseline solutions against measurements was not possible. The CFD solutions were, nonetheless, scrutinized by qualitative inspection of the pressure and shear-stress distributions on the cylinders. This was deemed sufficient verification of the

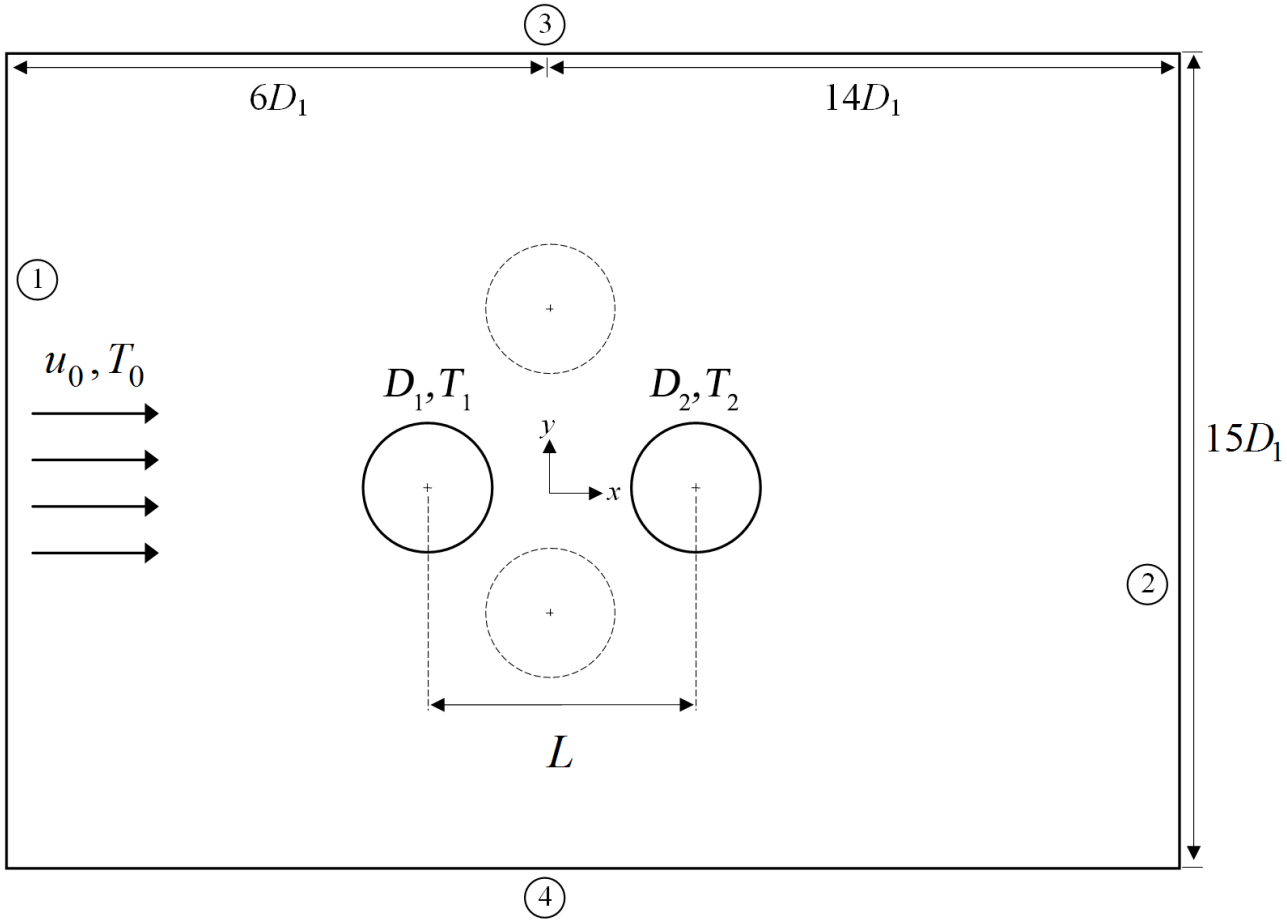

Figure 7.2: Computational domain for cross flow over a pair of horizontal cylinders

baseline solutions since the dQdT results presented in this chapter are intended mainly for demonstration and qualitative discussion.

7.3 Numerical dQdT

Numerical dQdT was implemented as outlined in Section 6.2.

7.4 Average Paired Nusselt Numbers

The functionality coefficients were converted to dimensionless form using the average paired Nusselt number defined in Equation 7.7.

$$\overline{\mathrm{Nu}}_{ij} = \frac{C_{ij}}{\pi k} \tag{7.7}$$

Recall that Q_i denotes the heat transfer rate per unit length of the cylinders. Accordingly, C_{ij} has units of W/(mK).

Sample dQdT results are presented in Tables 7.1-7.2 and Figures 7.3-7.6. These results are very similar to those presented in earlier publication on cross flow over a pair of isothermal spheres (Foroushani et al. 2015b) and free convection from a pair of horizontal isothermal cylinders (Foroushani et al. 2015c).

7.4.1 Side-by-Side Alignment

The paired Nusselt numbers of the side-by-side alignment are listed in Table 7.1. Note that the dQdT results show reciprocity between the functionality coefficients; $\overline{\mathrm{Nu}}_{ij} = \overline{\mathrm{Nu}}_{ji}$. As discussed in Chapter 3, reciprocity between the functionality coefficients indicates that

Table 7.1: Average paired Nusselt numbers of laminar forced convection over a pair of isothermal cylinders – Side-by-side alignment ($D_1 = D_2 = L/2$, $Pr = 0.7$)

Re	$\overline{Nu}_{12}$	$\overline{Nu}_{21}$	$\overline{Nu}_{10}$	$\overline{Nu}_{01}$	$\overline{Nu}_{20}$	$\overline{Nu}_{02}$
0	0.7321	0.7321	0.0000	0.0000	0.0000	0.0000
5	0.3590	0.3591	1.1406	1.1406	1.1405	1.1406
11	0.1559	0.1558	1.8977	1.8978	1.8977	1.8976
22	0.0236	0.0236	2.7456	2.7455	2.7456	2.7457
34	0.0038	0.0038	3.3308	3.3310	3.3311	3.3310
52	0.0007	0.0007	3.9858	3.9858	3.9856	3.9857

the problem can be represented by a network of convective resistances — in this case a delta network of three resistances.

In Figure 7.3, the cylinder-cylinder Nusselt number of the side-by-side alignment (Figure 7.1a) is plotted for $D_1 = D_2 = L/2$, Pr = 0.7 and $0 \leq$ Re $<$ 60. At Re=0, i.e. when there is no flow, $\overline{Nu}_{12}$ characterizes conduction between two parallel cylinders in an infinite medium. Therefore: $\overline{Nu}_{12} = S/\pi$.

For Re $>$ 0, as Re (representing the flow rate) increases, the thermal boundary layers around the cylinders become thinner and the thermal interaction between the cylinders diminishes. Hence, $\overline{Nu}_{12}$ decreases.

In the side-by-side configuration, the cylinders are positioned symmetrically in the flow field. Therefore the paired Nusselt numbers must be symmetrical. The dQdT results confirm this observation; $\overline{Nu}_{12} = \overline{Nu}_{21}$.

The cylinder-fluid Nusselt numbers, plotted in Figure 7.4, start from $\overline{Nu}_{10} = \overline{Nu}_{20} = 0$ at Re $= 0$ and increase as the flow rate increases. As seen in Figure 7.4, the cylinder-fluid Nusselt numbers are symmetrical; $\overline{Nu}_{10} = \overline{Nu}_{20}$. Note also that the curves of Figure 7.4 closely follow the general expression for the total Nusselt number in external flow, shown in Equation 7.8.

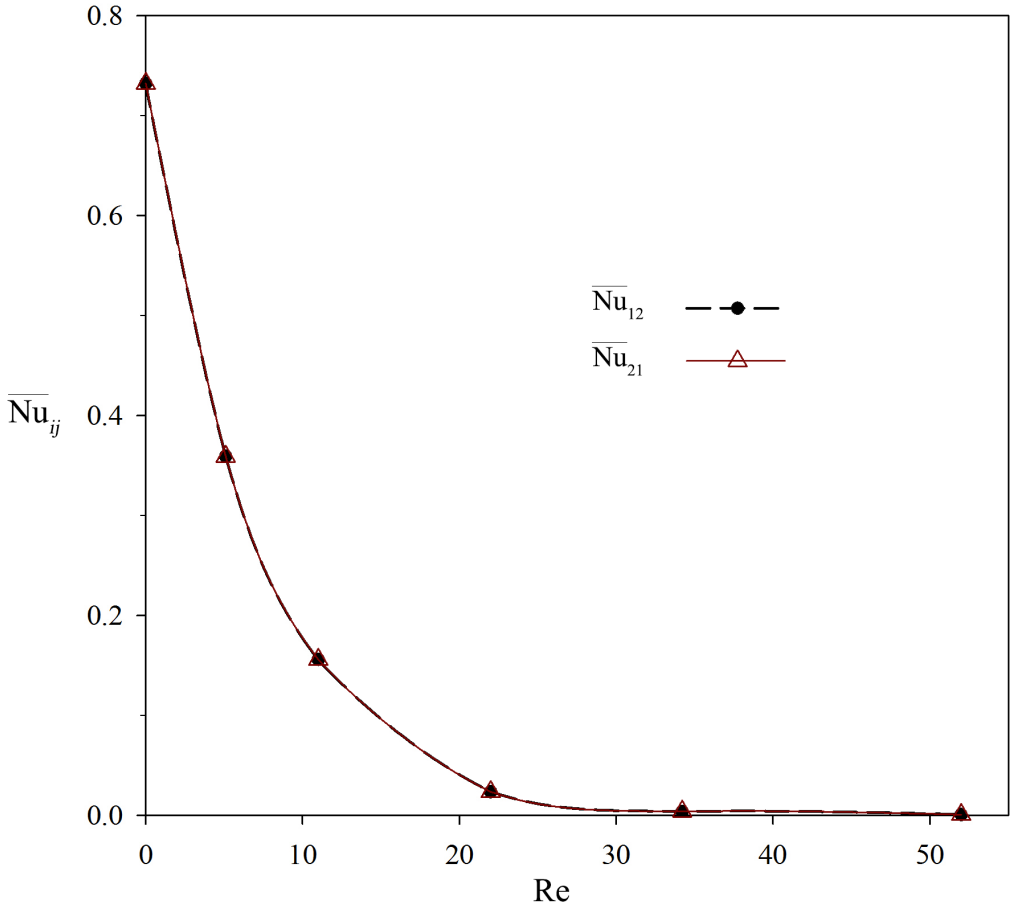

Figure 7.3: Average cylinder-cylinder Nusselt number – Side-by-side alignment ($D_1 = D_2 = L/2$, $\mathrm{P}r = 0.7$)

$$\overline{\mathrm{Nu}}_i = c\,\mathrm{Re}^m \qquad (i = 1, 2) \tag{7.8}$$

Since this is a constant-property forced convection problem, i.e. the energy equation is linear, the functionality coefficients can be obtained using "numerical experiments" as described in Section 2.6.2. Further note that in case of $D_1 = D_2$, the functionality coefficients can also be obtained using the algebraic expressions derived in Section 2.6.1 for the special case of symmetry. Using these alternative methods, results identical to the dQdT results were obtained, confirming the validity of the dQdT results.

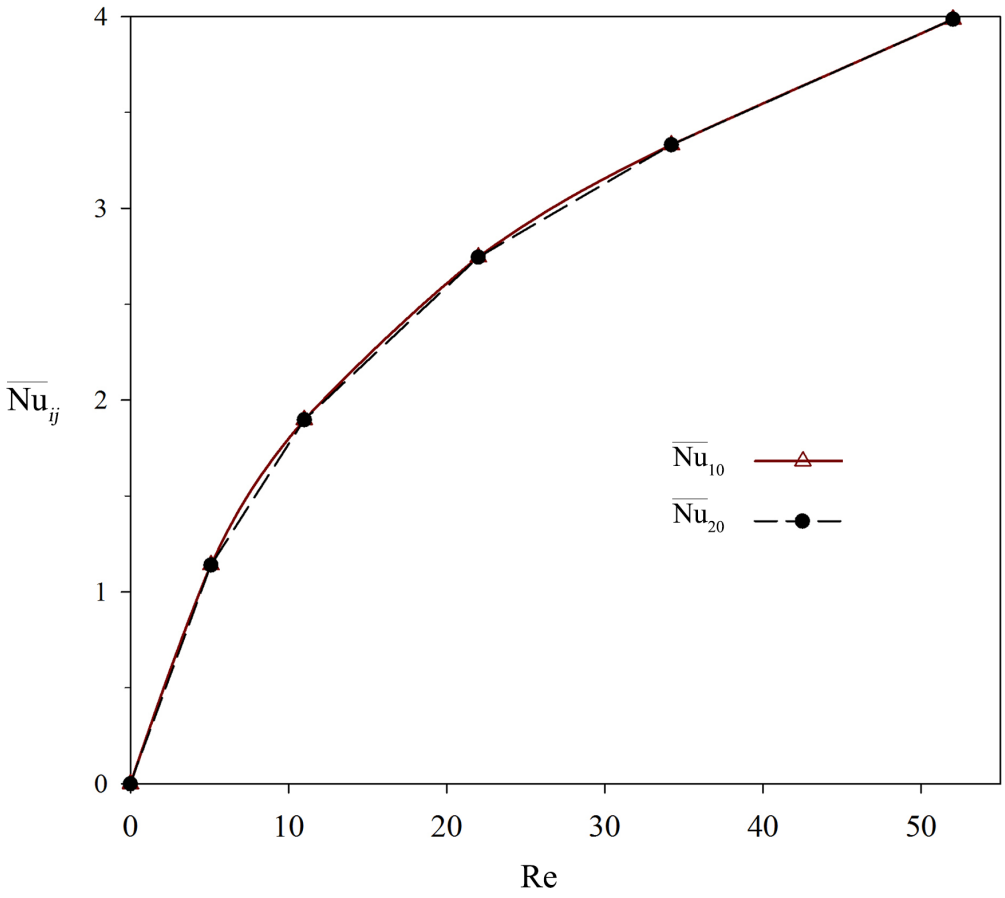

Figure 7.4: Average cylinder-fluid Nusselt number – Side-by-side alignment ($D_1 = D_2 = L/2$, $\mathrm{Pr} = 0.7$)

7.4.2 Tandem Alignment

In the tandem configuration (Figure 7.1b), there is symmetry in both the geometry and the flow field with respect to the $y = 0$ line. Nevertheless, the cylinders are not symmetrically positioned with respect to the *flow field*; the upstream cylinder (T_1) is exposed to the undisturbed free-stream flow while blocking the flow in front of the downstream cylinder (T_2). Therefore, the thermal interaction of the isothermal boundaries – the cylinders and the free-stream flow – is expected to be asymmetrical.

The paired Nusselt numbers of the tandem alignment with $D_1 = D_2 = L/2$, $\mathrm{Pr} = 0.7$ and $0 \leq \mathrm{Re} < 60$ are listed in Table 7.2. As can be seen from these results; $\overline{\mathrm{Nu}}_{ij} \neq$

Table 7.2: Average paired Nusselt numbers of laminar forced convection over a pair of isothermal cylinders – Tandem alignment ($D_1 = D_2 = L/2$, $\mathrm{P}r = 0.7$)

Re	$\overline{\mathrm{Nu}}_{12}$	$\overline{\mathrm{Nu}}_{21}$	$\overline{\mathrm{Nu}}_{10}$	$\overline{\mathrm{Nu}}_{01}$	$\overline{\mathrm{Nu}}_{20}$	$\overline{\mathrm{Nu}}_{02}$
0	0.7321	0.7321	0.0000	0.0000	0.0000	0.0000
5	0.2072	0.7141	1.4531	0.9462	0.7576	1.2645
10	0.1490	0.8017	1.9469	1.2941	0.9487	1.6015
22	0.1201	0.9206	2.6094	1.8089	1.2084	2.0089
34	0.1296	1.0108	3.1481	2.2669	1.4210	2.3023
58	0.1958	1.1392	3.9147	2.9713	1.7264	2.6698

$\overline{\mathrm{Nu}}_{ji}$. Hence, the resistor-network model is not applicable to the tandem configuration. Interestingly, the difference $C_{ij} - C_{ji}$ for each Re is a constant. In Appendix D, a mathematical proof for this observation is presented.

Consider the cylinder-cylinder Nusselt numbers, plotted in Figure 7.5. For Re=0, i.e. in the absence of fluid flow, the symmetry of geometry leads to symmetry of the paired Nusselt numbers; $\overline{\mathrm{Nu}}_{12} = \overline{\mathrm{Nu}}_{21} = S/\pi$. However, as the flow rate increases, $\overline{\mathrm{Nu}}_{12}$ and $\overline{\mathrm{Nu}}_{21}$ become considerably different, even in the creeping flow regime ($\mathrm{Re} \approx 1$). This difference can be explained by recalling that the functionality coefficient C_{ij} characterizes the sensitivity of the heat transfer rate Q_i to the boundary temperature T_j. In this light, $\overline{\mathrm{Nu}}_{21} > \overline{\mathrm{Nu}}_{12}$ is due simply to the fact that T_1 is upstream of T_2; whereas T_1 has a strong impact on the temperature field and hence the rate of heat transfer downstream, T_2 can barely impact heat transfer at the upstream cylinder – only through diffusion.

Note that for $0 \leq \mathrm{Re} \lesssim 25$, $\overline{\mathrm{Nu}}_{12}$ (characterizing the effect of T_2 on Q_1) decreases with the increase of the flow rate. However, with the onset of flow recirculation between the cylinders at $\mathrm{Re} \approx 25$, this trend is reversed. Note also the slight slight drop in $\overline{\mathrm{Nu}}_{21}$ between $\mathrm{Re} = 0$ and $\mathrm{Re} = 5$ which is likely due to the formation of boundary layers around the cylinders.

The cylinder-fluid Nusselt numbers of the tandem alignment are plotted in Figure 7.6. Similar to the side-by-side alignment, the curves of Figure 7.6 follow the general expression

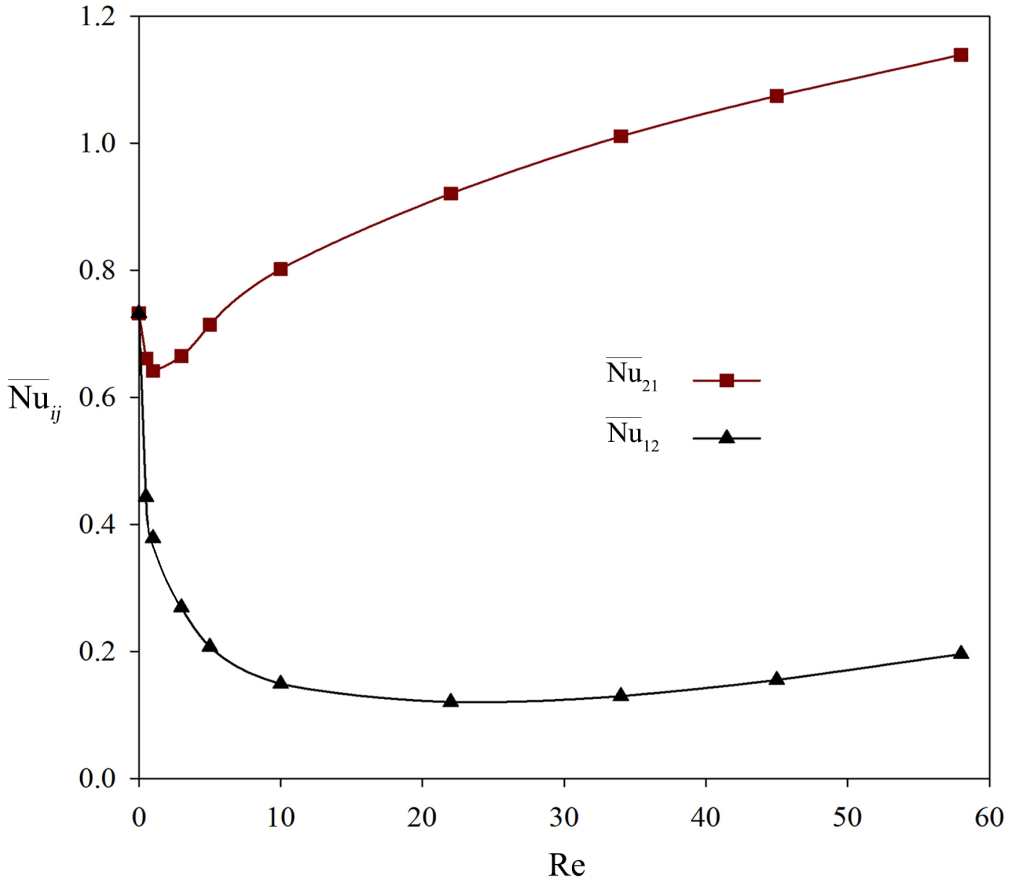

Figure 7.5: Average cylinder-cylinder Nusselt numbers – Tandem alignment ($D_1 = D_2 = L/2$, $\mathrm{P}r = 0.7$)

of Equation 7.8. Four distinct curves were obtained for $\overline{\mathrm{Nu}}_{10}$, $\overline{\mathrm{Nu}}_{01}$, $\overline{\mathrm{Nu}}_{20}$ and $\overline{\mathrm{Nu}}_{02}$. Recall that in the side-by-side arrangement, the cylinder-fluid Nusselt numbers collapsed to a single curve.

All four curves shown in Figure 7.6 exhibit a monotonic increase with Re; as the flow rate increases, advection enhances the influence of each boundary temperature on heat transfer. The discrepancy between each pair of cylinder-fluid Nusselt numbers also increases with Re. Moreover, since T_1 is upstream of T_2, its corresponding heat transfer rate, Q_1, is more sensitive to the free-stream temperature (T_0) than Q_2 is; $\overline{\mathrm{Nu}}_{10} > \overline{\mathrm{Nu}}_{20}$. But the influence of the cylinder temperatures on the rate of total heat transfer to the

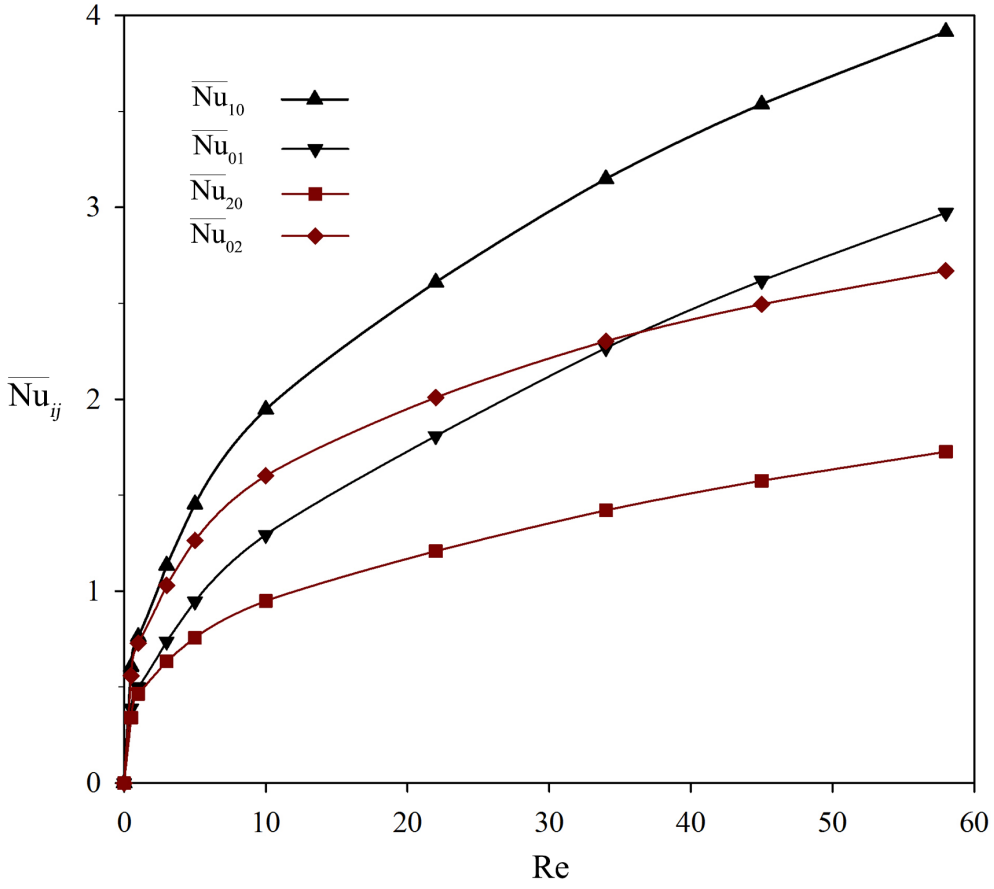

Figure 7.6: Average cylinder-fluid Nusselt numbers – Tandem alignment ($D_1 = D_2 = L/2$, $\mathrm{Pr} = 0.7$)

fluid is not as straightforward. For $\mathrm{Re} \lesssim 35$, T_2 has a stronger influence; $\overline{\mathrm{Nu}}_{02} > \overline{\mathrm{Nu}}_{01}$. In contrast, for $\mathrm{Re} \gtrsim 35$, the influence of T_1 is larger; $\overline{\mathrm{Nu}}_{02} < \overline{\mathrm{Nu}}_{01}$.

The lack of reciprocity between the functionality coefficients means that the multi-temperature problem cannot be represented by a network of convective resistors. Nonetheless, as discussed above, the paired Nusselt numbers obtained using dQdT provide a means of quantifying the thermal interaction of the cylinders and the flow. Moreover, the average paired Nusselt numbers can be used to calculate the heat transfer rates for any set of boundary temperatures:

$$Q_i = \sum_j C_{ij}(T_i - T_j) = \pi\, k \sum_j \overline{\mathrm{Nu}}_{ij}(T_i - T_j)$$

The rate of heat transfer at the upstream cylinder, for example, can be calculated using $\overline{\mathrm{Nu}}_{10}$ and $\overline{\mathrm{Nu}}_{12}$;

$$Q_1 = \pi\, k \left[\overline{\mathrm{Nu}}_{10}(T_1 - T_0) + \overline{\mathrm{Nu}}_{12}(T_1 - T_2) \right]$$

Likewise, to calculate the rate of total heat transfer to the fluid, $\overline{\mathrm{Nu}}_{01}$ and $\overline{\mathrm{Nu}}_{02}$ must be used;

$$Q_0 = \pi\, k \left[\overline{\mathrm{Nu}}_{01}(T_1 - T_0) + \overline{\mathrm{Nu}}_{02}(T_0 - T_2) \right]$$

7.5 Local Paired Nusselt Numbers

A *local* functionality coefficient, c_{ij}, may also be defined to characterize the influence of the boundary temperature T_j on the heat *flux* q_i. See Equation 7.9.

$$c_{ij} = -\left.\frac{\partial q_i}{\partial T_j}\right|_{c_{ik}=\text{const}} \qquad (i = 1, 2) \tag{7.9}$$

Accordingly, a local paired Nusselt number may be defined as shown in Equation 7.10.

$$\mathrm{Nu}_{ij} = \left(\frac{c_{ij}}{k}\right) D_1 \qquad (i = 1, 2) \tag{7.10}$$

Sample dQdT results for $\{\mathrm{Nu}_{ij}\}$ are plotted in Figures 7.7-7.11 for $D_1 = D_2 = L/2$, $\mathrm{Pr} = 0.7$ and $\mathrm{Re} = 10$. The following discussion aims to demonstrate the meaning of local paired Nusselt numbers and their utility in understanding multi-temperature convection, even in the absence of reciprocity and failure of the resistor-network model.

7.5.1 Side-by-Side Alignment

The local cylinder-cylinder Nusselt number of the upper cylinder (T_1) in the side-by-side arrangement (Figure 7.1a) is plotted in Figure 7.7. The dashed curve corresponds to the lower half, facing the lower cylinder. As expected, Nu_{12} is larger on the lower half, while almost a third of the upper half (the solid curve, $30 \lesssim \theta \lesssim 90°$) is thermally isolated from the lower cylinder; $\mathrm{Nu}_{12} = 0$. Note also that Nu_{12} is larger on the "leeward" side of the cylinder, i.e. for $90° \leq \theta \leq 180°$. In other words, the thermal interaction of the cylinders is enhanced in the wake behind the cylinders. Interestingly, at least for this particular spacing and flow rate, $\mathrm{Nu}_{12} > 0$ around the stagnation point ($0 \leq \theta \lesssim 30°$).

dQdT confirms that in the side-by-side alignment, the local Nusselt numbers too are symmetric; $\mathrm{Nu}_{ij} = \mathrm{Nu}_{ji}$. Therefore, Figure 7.7 also depicts the circumferential distribution of Nu_{21}, with the dashed curve corresponding to the upper half of the lower cylinder (T_2).

The distribution of the local cylinder-fluid Nusselt number on the upper cylinder is plotted in Figure 7.8. Again, the dashed curve corresponds to the lower half, facing the lower cylinder. As expected, Nu_{10} is largest at the stagnation point ($\theta = 0$) and decreases monotonically over both sides. Due to the acceleration of the flow between the cylinders, for $0 < \theta \lesssim 110°$, Nu_{10} is larger on the lower half than on the upper half. For $\theta \gtrsim 110°$, however, as the flow expands, i.e. decelerates, Nu_{10} on the the lower half (dashed curve) is smaller.

7.5.2 Tandem Alignment

The local cylinder-cylinder Nusselt numbers of the tandem alignment are plotted in Figure 7.9. As discussed earlier, in the tandem configuration there is asymmetry in the paired Nusselt numbers. Therefore, two distinct curves are obtained for Nu_{12} and Nu_{21}.

The windward side of the upstream cylinder ($0° \leq \theta < 90°$) is isolated from the downstream cylinder; $\mathrm{Nu}_{12} = 0$. On the leeward half, however, q_1 is influenced by T_2 and

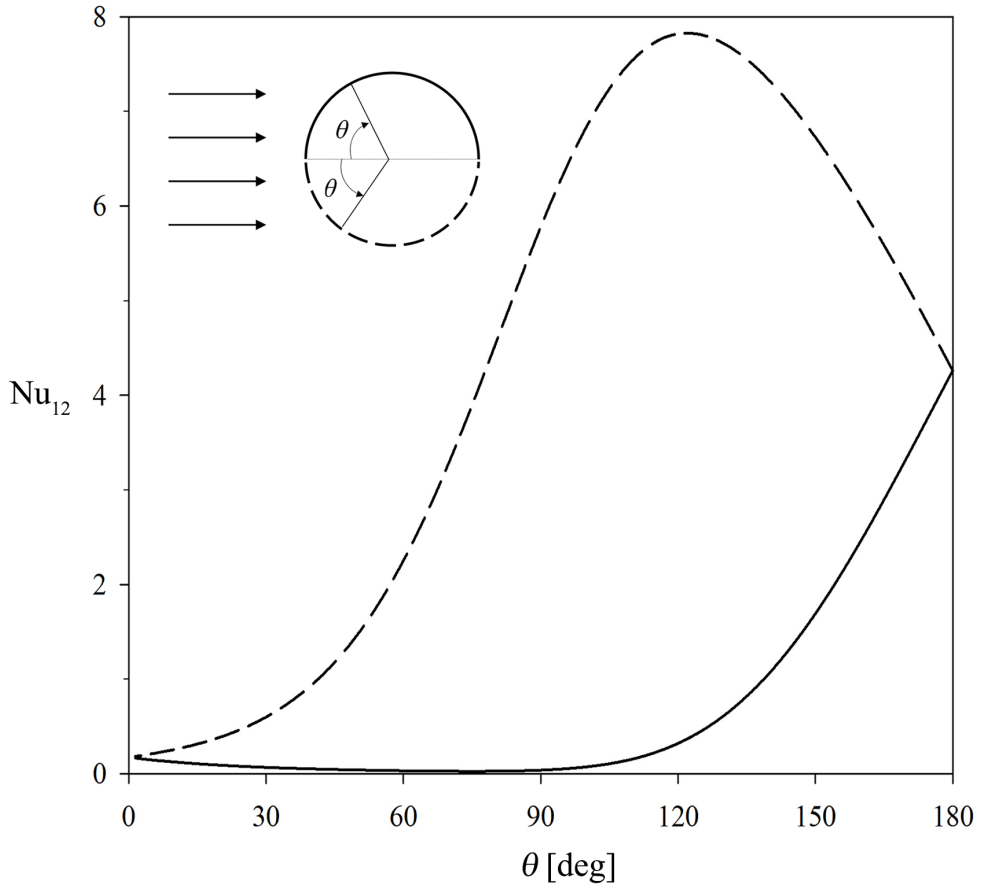

Figure 7.7: Local cylinder-cylinder Nusselt number
Upper cylinder, Side-by-side alignment ($D_1 = D_2 = L/2$, Pr = 0.7, Re = 10)

therefore: $\mathrm{Nu}_{12} > 0$. Heat flux at all circumferential positions on the downstream cylinder, q_2, on the other hand, is influenced by T_1; $\mathrm{Nu}_{21} > 0$. As expected, Nu_{21} is maximum at $\theta = 0$ and decreases smoothly as θ increases. It is interesting, however, that $\mathrm{Nu}_{21} > 0$ even at $\theta = 180°$.

In Figure 7.10, the variation of Nu_{12} with the flow rate is illustrated. Note that on the windward side of the upstream cylinder, $90° \leq \theta \leq 180°$, Nu_{12} decreases as the flow rate increases from Re=5 to Re=10 due to the dominance of advection and weakening of upstream diffusion — the only mechanism for influence of T_2 on q_1. As Re further increases, however, a region of flow recirculation is formed between the cylinders. In this case, T_2 impacts q_1 also through advection. Therefore, Nu_{12} increases. Note that for

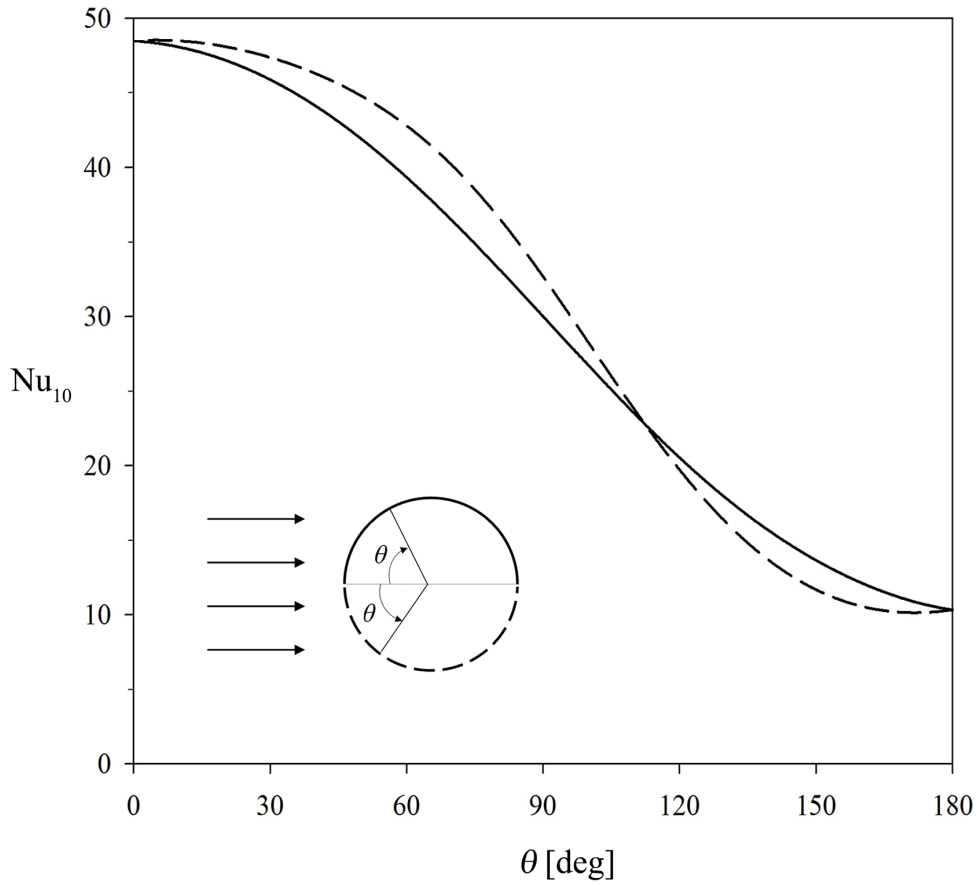

Figure 7.8: Local cylinder-fluid Nusselt numbers
Upper cylinder, Side-by-side alignment ($D_1 = D_2 = L/2$, Pr = 0.7, Re = 10)

$175° \lesssim \theta \leq 180°$, Re=45 has the largest Nu_{12}. This is further evidence that recirculating flow between the cylinders enhances the influence of T_2 on q_1.

Finally, the local cylinder-fluid Nusselt numbers of the tandem alignment are plotted in Figure 7.11. Nu_{10} starts from a maximum at the stagnation point ($\theta = 0$) and decays smoothly as θ increases. Note that Nu_{10} of the tandem alignment is almost identical to the solid curve in Figure 7.8. The variation of Nu_{20} on the downstream cylinder is significantly different, with its maximum occurring at $\theta \approx 80°$. Interestingly, for $150° \leq \theta \leq 180°$, q_2 is more sensitive to T_0 than q_1 is; $\mathrm{Nu}_{20} > \mathrm{Nu}_{10}$.

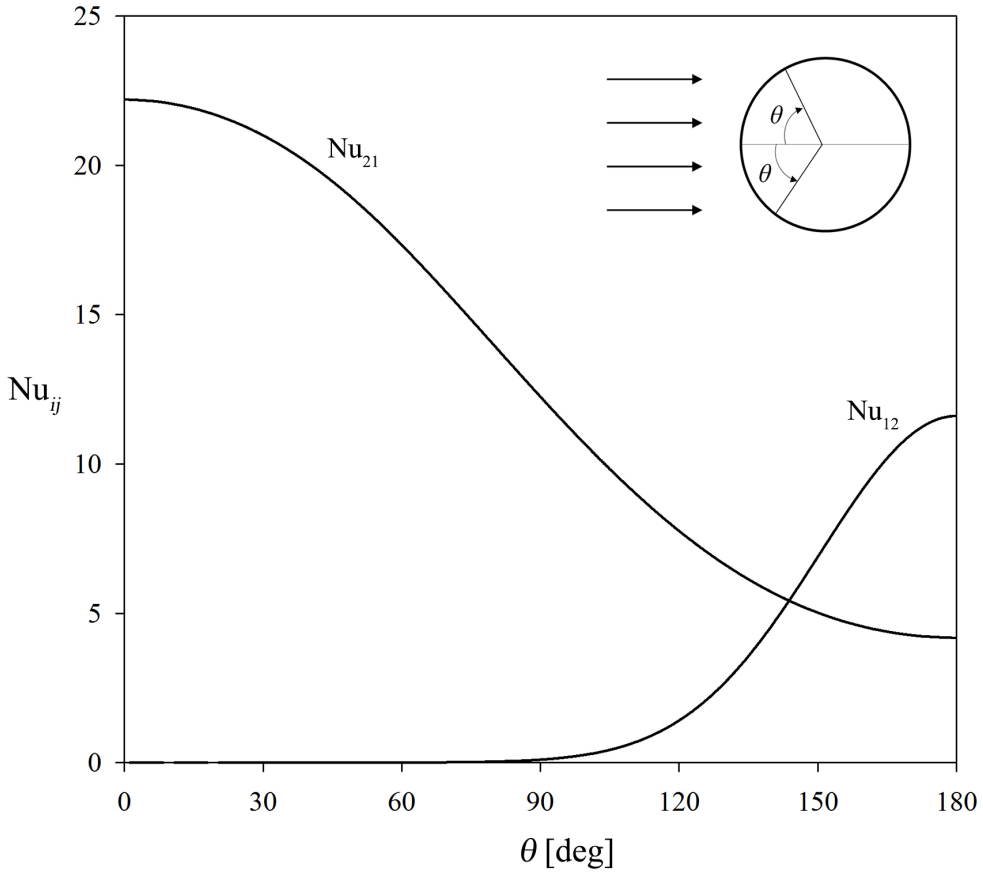

Figure 7.9: Local cylinder-cylinder Nusselt numbers – Tandem alignment ($D_1 = D_2 = L/2$, Pr = 0.7, Re = 10)

7.6 Summary

Numerical dQdT was utilized to calculate the functionality coefficients of the three-temperature problem of convection in cross flow over a pair of isothermal cylinders. Cylinders of the same size placed in side-by-side alignment, i.e. with their centers aligned along a line normal to the free-stream flow, are symmetric with respect to the flow. Therefore, as shown by dQdT, there is symmetry and reciprocity between the functionality coefficients. Consequently, the problem can be represented by a network of three convective resistors. Two universal paired Nusselt numbers fully characterize the three-temperature problem.

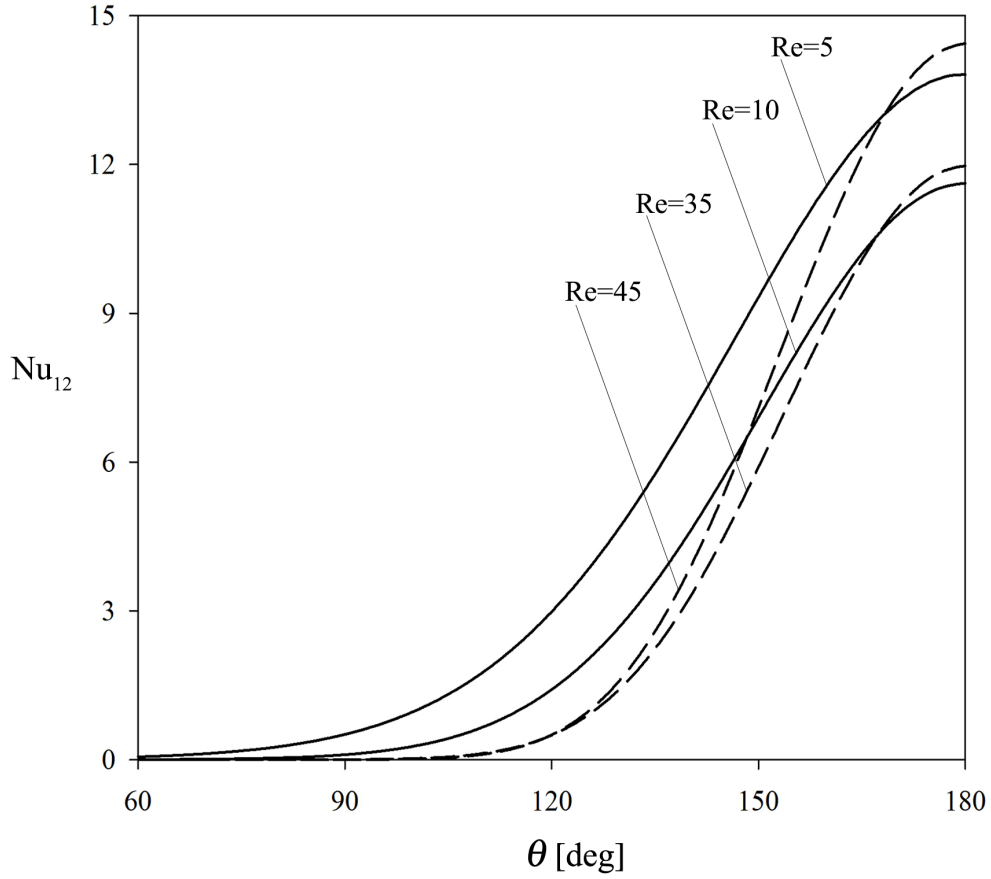

Figure 7.10: Local upstream-downstream Nusselt number at different flow rates Tandem alignment ($D_1 = D_2 = L/2$, Pr = 0.7, Re = 10)

In tandem alignment, i.e. when the cylinder centers are aligned along a line parallel to the free-stream flow, the cylinders are asymmetrically positioned in the flow. Therefore, there is asymmetry between the functionality coefficients. dQdT yields six distinct functionality coefficients. Although the tandem configuration cannot be represented by a resistor network, the functionality coefficients are still physically meaningful, while revealing important details about the heat transfer phenomenon. Moreover, the functionality coefficients obtained using dQdT can be used to calculate the heat transfer rates, $\{Q_i\}$, for any set of boundary temperatures.

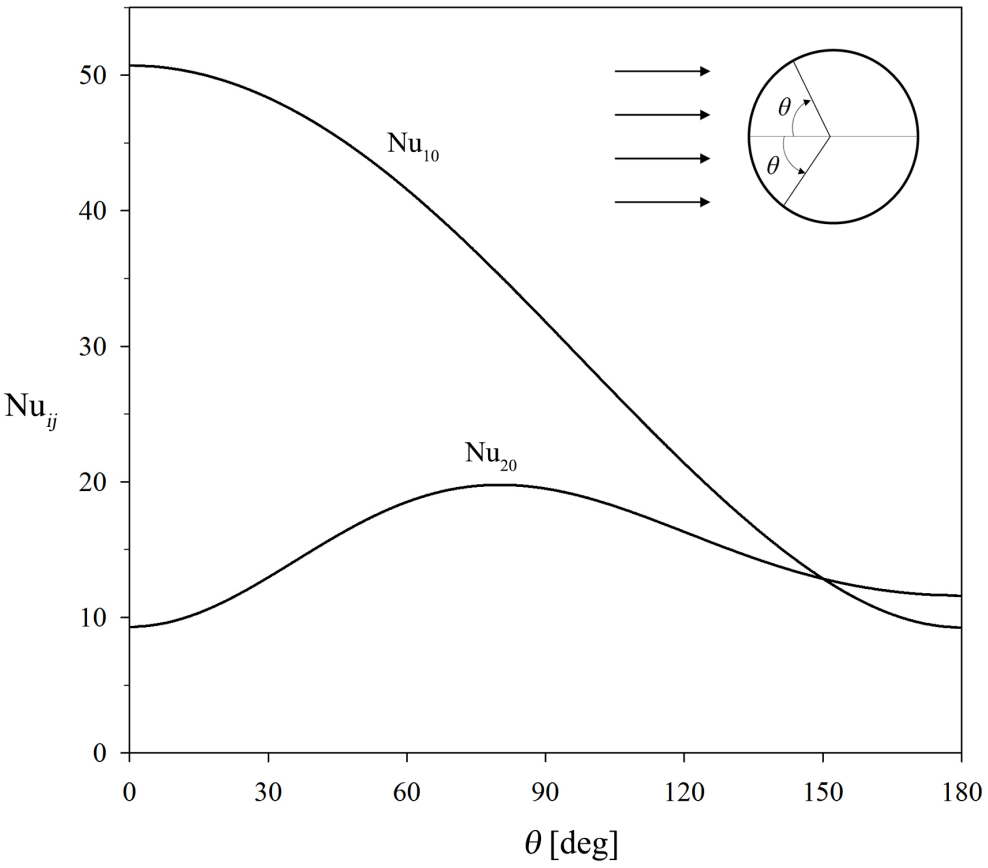

Figure 7.11: Local cylinder-fluid Nusselt numbers – Tandem alignment ($D_1 = D_2 = L/2$, Pr = 0.7, Re = 10)

Chapter 8

Laminar Free Convection in a Vertical Channel with Isothermal Walls

In Chapters 4-7, the extended Newton formulation and the dQdT technique were presented for constant-property forced convection problems, i.e. cases where the energy equation is linear. In Chapters 8-10, examples of free convection, i.e. nonlinear, multi-temperature problems will be examined.

Free-convective heat transfer in vertical channels is encountered in various applications, e.g. electronics cooling, nuclear reactors, solar collectors and building envelope assemblies. In building science, specifically, free convection in vertical heated passages is encountered in building-integrated photovoltaic systems and windows with attachments such as roller blinds. With its broad application in energy systems, this problem has seen great interest from researchers, especially with the growing demand and attention to renewable energy in the past two decades. Many studies have been published of the different variations of the problem – isoflux or isothermal conditions at the channel walls, laminar or turbulent flow regimes, different aspect ratios, etc.

The case of isoflux heating of the walls in channels of low aspect ratio has been the subject of the majority of published studies. This is because most applications – electronic, nuclear and solar – entail relatively short channels with walls heated in a way best modeled as isoflux. Moreover, compared to the isothermal boundary condition, the isoflux condition is easier to produce experimentally. Furthermore, the local heat transfer coefficient at an isoflux surface can be simply measured with only a thermocouple. But free convection in tall vertical channels with isothermally heated walls too has been the subject of several studies, e.g. the work of Roeleveld et al. (2009, 2014).

Extensive bibliographies on free convection in vertical channels can be found in the papers by Yilmaz & Fraser (2007) and Lau et al. (2011). Roeleveld (2013) presents a brief review of free convection in vertical channels with walls at different temperatures. An overview of numerical studies of free convection in vertical channels is provided by Manca et al. (2000).

In this chapter, numerical dQdT is applied to calculate the functionality coefficients of laminar free convection in a vertical channel with walls heated to uniform temperatures. It is shown that the extended Newton formulation of the problem is advantageous over the traditional formulation and leads to improved heat transfer correlations.

8.1 Traditional Formulation

Consider buoyancy-driven flow in a vertical channel with isothermal walls, shown in Figure 8.1. The flow is characterized by the modified channel Rayleigh number, Ra, defined in Equation 8.1. In this equation, $T_{\text{wm}} = (T_1 + T_2)/2$.

$$\text{Ra} = \frac{g\beta(T_{\text{wm}} - T_0)W^3}{\nu^2}\left(\frac{W}{H}\right)\text{Pr} \tag{8.1}$$

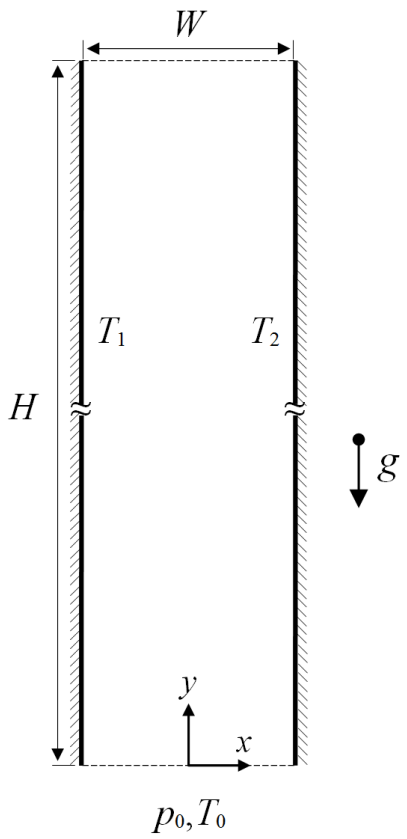

Figure 8.1: Schematic of a vertical channel with isothermal walls

A temperature ratio, r_T, is typically used to characterize the heating of the walls. A common definition is given in Equation 8.2.

$$r_T = \frac{T_2 - T_0}{T_1 - T_0} \tag{8.2}$$

It is assumed in this chapter that the channel walls are hotter both than the ambient air; $T_1 \geq T_2 \geq T_0$. The proceeding analysis and results are nonetheless applicable also to the general case of $r_T \geq 0$, including the case of both walls colder than the ambient air. The case of $r_T < 0$ has been excluded from the present study. In this case, two "opposing" boundary layers develop along the channel which may lead to complex flow structures and instability.

Convection in isothermal channels is traditionally formulated in terms of local and average wall Nusselt numbers, defined in Equations 8.3 and 8.4. Note that Q_i denotes heat transfer rate *per unit depth* of the channel.

$$\mathrm{Nu}_i = \frac{q_i}{T_i - T_0}\left(\frac{W}{k}\right) \qquad (i = 1, 2) \tag{8.3}$$

$$\overline{\mathrm{Nu}}_i = \frac{Q_i}{H(T_i - T_0)}\left(\frac{W}{k}\right) \qquad (i = 1, 2) \tag{8.4}$$

It was discussed in Chapters 4 and 5 that forced convection in heated passages is traditionally formulated using the mean fluid temperature to represent the fluid flow and construct effective temperature differences. Note however that the definitions presented in Equations 8.3 and 8.4 are based on the representation of the fluid by the "ambient" or "far-field" temperature, i.e. the corresponding boundary condition. As a result, the extra singularities discussed in Chapters 4 and 5 do not arise in the traditional Nusselt numbers, Nu_i and $\overline{\mathrm{Nu}}_i$. See for example the overview of heat transfer correlations for open-ended channels in *Handbook of Heat Transfer* (Rohsenow et al. 1998) and the more detailed review by Roeleveld (2013). Credit is due to Aung (1972) who recognized T_0 as the appropriate temperature to represent the fluid and used $T_{\mathrm{wm}} - T_0$ as the effective temperature difference for characterizing free convection in a channel with isothermal walls.

Moreover, the dependence of the traditional Nusselt numbers on r_T is not problematic; it is consistent with the physics of a free-convection problem. The rate of flow in the channel, the development of hydrodynamic and thermal boundary layers and their relative size are all functions of the boundary temperatures. Therefore, it is expected that the Nusselt numbers depend on r_T.

Nonetheless, the formulation of the multi-temperature problem in terms of "total" Nusselt numbers based on effective temperature differences, i.e. a combination of T_0, T_1 and T_2, is problematic. For example, although numerical and experimental results are often presented in terms of average wall Nusselt numbers, $\overline{\mathrm{Nu}}_1$ and $\overline{\mathrm{Nu}}_2$, separate correlations for heat transfer at each wall are rare. Such correlations are needed for building-energy calculations, e.g. in modeling heat transfer in complex fenestration systems. Instead, correlations are often developed for the overall heat transfer in the channel. See for instance Equation 8.5, recommended by Raithby & Hollands (1998) for air ($\mathrm{Pr} = 0.7$).

$$\begin{aligned} \overline{\mathrm{Nu}}_0 &= \frac{Q_1 + Q_2}{2H(T_{\mathrm{wm}} - T_0)} \left(\frac{W}{k}\right) \\ &= \left[\left(\overline{\mathrm{Nu}}_{\mathrm{fd}}\right)^{-1.9} + \left(0.618\,\mathrm{Ra}^{1/4}\right)^{-1.9} \right]^{-\frac{1}{1.9}} \end{aligned} \tag{8.5}$$

The two terms comprising the correlation shown in Equation 8.5 represent two limiting cases of the problem:

i) The thermally fully developed limit ($\mathrm{Ra} \to 0$) where maximum heat transfer to the fluid has been achieved and heat transfer from one wall is conducted across the fluid layers to the other wall. An expression for this limit is given by Aung (1972) as shown in Equation 8.6.

$$\lim_{\mathrm{Ra}\to 0} \overline{\mathrm{Nu}}_0 = \overline{\mathrm{Nu}}_{\mathrm{fd}} = \left[\frac{4r_T^2 + 7r_T + 4}{90(1 + r_T)^2} \right] \mathrm{Ra} \tag{8.6}$$

ii) The limit of $\mathrm{Ra} \to \infty$ (infinitely wide channel or infinitely large flow rate), corresponding to two "isolated" isothermal flat plates. The respective term in Equation 8.5 is based on the boundary-layer solution by Ostrach (1953) for free convection at an isothermal vertical flat plate;

$$\lim_{\mathrm{Ra}\to\infty} \overline{\mathrm{Nu}_0} = 0.618\,\mathrm{Ra}^{1/4}$$

As pointed out by Roeleveld et al. (2009), a possible reason for the lack of separate correlations for $\overline{\mathrm{Nu}_1}$ and $\overline{\mathrm{Nu}_2}$ is that Q_1 and Q_2 do not correlate "conveniently" with $T_{\mathrm{wm}} - T_0$. A main reason for this difficulty is that the asymptotic values of $\overline{\mathrm{Nu}_1}$ and $\overline{\mathrm{Nu}_2}$ for $\mathrm{Ra} \to 0$ and $\mathrm{Ra} \to \infty$ depend on r_T. The sign change of $\overline{\mathrm{Nu}_2}$ also poses a challenge. These features are apparent in Figure 8.2, where the wall Nusselt numbers, $\overline{\mathrm{Nu}_1}$ and $\overline{\mathrm{Nu}_2}$, are plotted for various r_T. These results were generated using the CFD solutions described in Section 8.3.

Recognizing the importance of the representative temperatures, Roelveled et. al (2009) tried two alternative effective temperature differences in search of Nu and Ra that would be easier to correlate. See Equations 8.7 and 8.8.

$$\Delta T_{\mathrm{walls}} = T_1 - T_2 \tag{8.7}$$

$$\Delta T_{\mathrm{max}} = T_1 - T_0 \tag{8.8}$$

Nevertheless, even Nusselt numbers based on $\Delta T_{\mathrm{walls}}$ or ΔT_{max} do not collapse to the same asymptotes for all r_T. To obtain universal, i.e. r_T-independent, asymptotes at the $\mathrm{Ra} \to 0$ and $\mathrm{Ra} \to \infty$ limits, Roelveled et. al (2009) eventually constructed an "effective" temperature difference by introducing a weighting function, α. See Euaqtion 8.9.

$$\Delta T_{\mathrm{eff}} = \alpha(\Delta T_{\mathrm{walls}}) + (1-\alpha)(\Delta T_{\mathrm{max}}) \tag{8.9}$$

Based on ΔT_{eff}, Roeleveld et al. (2009) defined an effective Nusselt number as shown in Equation 8.10.

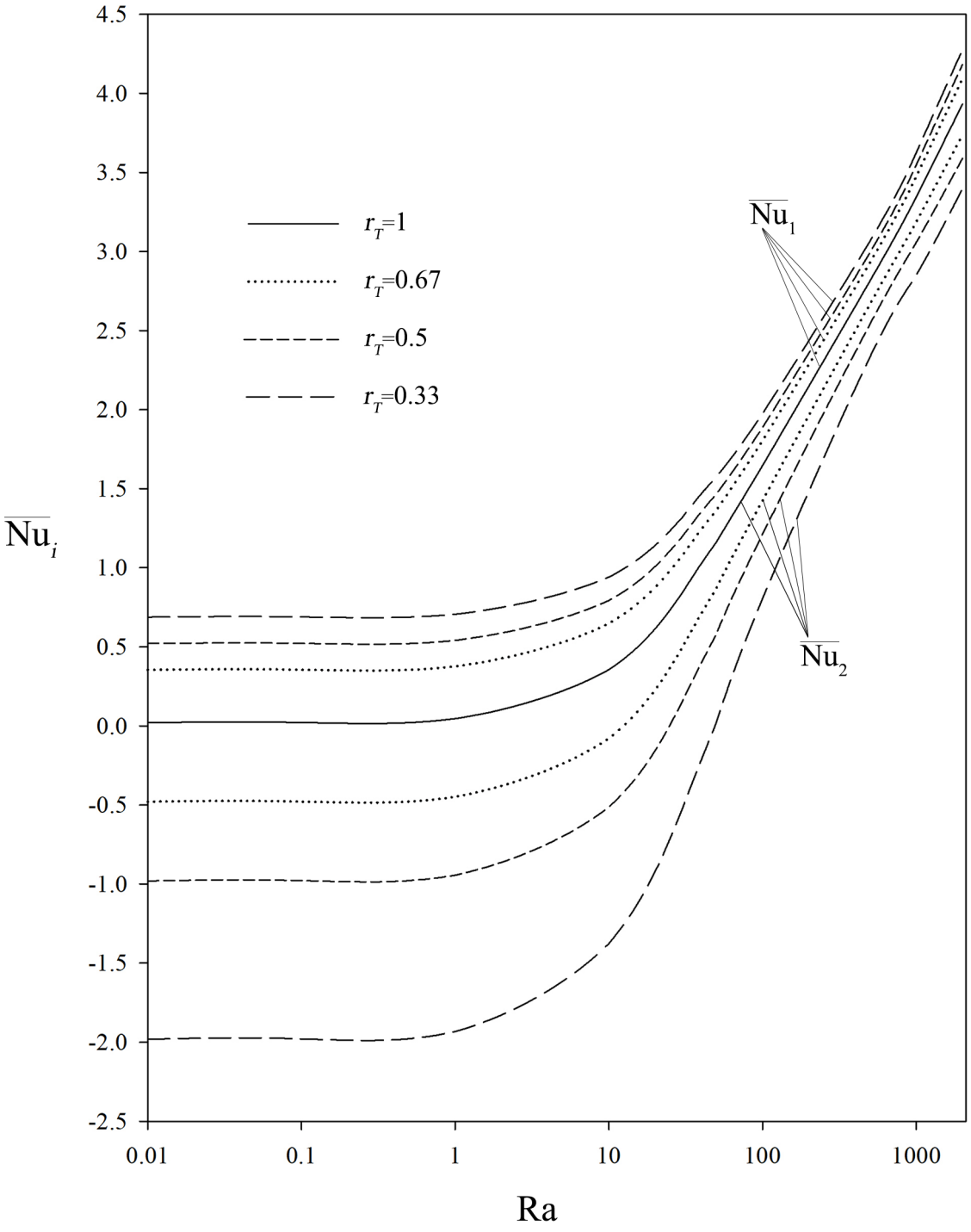

Figure 8.2: Average Nusselt numbers of laminar free convection in a vertical channel with isothermal walls (Pr = 0.7)

$$\overline{\mathrm{Nu}}_{\mathrm{eff},i} = \frac{Q_i}{H\,\Delta T_{\mathrm{eff}}}\left(\frac{W}{k}\right) \qquad (i = 1, 2) \tag{8.10}$$

An expression for α was also presented based on a best least-square fit to numerical data (Roeleveld et al. 2009);

$$\alpha = \frac{38.583}{\left[\mathrm{Ra}\left(\frac{2}{1+r_T}\right)\right]^{1.128} + 38.583} \tag{8.11}$$

The correlations developed by Roeleveld et al. (2009) are reproduced in Equations 8.12 and 8.13. Recall that the subscript 1 denotes the largest temperature ($T_1 \geq T_2 \geq T_0$). Further, note that Equation 8.12 correlates $\overline{\mathrm{Nu}}_{\mathrm{eff},1}$ (based on ΔT_{eff}) with Ra which is based on $T_{\mathrm{wm}} - T_0$.

$$\overline{\mathrm{Nu}}_{\mathrm{eff},1} = \left[1 + \left(0.618\,\mathrm{Ra}^{1/4}\right)^{3.011}\right]^{\frac{1}{3.011}} \tag{8.12}$$

$$\overline{\mathrm{Nu}}_2 = 2\overline{\mathrm{Nu}}_0 - 2\overline{\mathrm{Nu}}_{\mathrm{eff},1}\left[\frac{\alpha(\Delta T_{\mathrm{walls}}) + (1-\alpha)(\Delta T_{\mathrm{max}})}{1 + r_T}\right] \tag{8.13}$$

Roelveled et al. (2009) have reported good accuracy for the correlations above: a standard deviation of $\pm 5\%$ and a maximum RMS error of $\pm 10\%$ compared to CFD solutions. Nevertheless, with α incorporated in $\overline{\mathrm{Nu}}_{\mathrm{eff},1}$, Equations 8.12 and 8.13 are complex in form, while lacking physical significance or meaning. As will be shown, the complexity of these equations is merely an artifact of formulating the three-temperature problem in terms of total Nusselt numbers, which requires the construction of an effective temperature difference. The extended Newton formulation of the problem in terms of paired Nusselt

numbers has the potential to simplify the solution and eliminate the extra parameters, ΔT_{eff} and α.

8.2 Extended Newton Formulation

The problem of free convection in a channel with isothermal walls entails three boundary temperatures: the far-field ambient at T_0 and the two channel walls at T_1 and T_2. Accordingly, there are three heat transfer rates of interest: Q_0, Q_1 and Q_2. Each heat transfer rate Q_i is characterized by two functionality coefficients C_{ij} and C_{ik}. The full set of functionality coefficients, $\{C_{ij}\}$, can be obtained using numerical dQdT.

Because this is a free convection problem, it is expected that $\{C_{ij}\}$ be a function of $\{T_i\}$. Moreover, because the velocity field is temperature-dependent, the asymmetry in the temperature field ($r_T \neq 1$) is expected to cause asymmetry in the functionality coefficients; $C_{ij} \neq C_{ji}$. Finally, the two wall-fluid functionality coefficients are expected to be different except in the case of the symmetric heating of the walls ($r_T = 1$). These features will all be explored using dQdT.

8.3 Baseline Solutions

In order to perform the dQdT operation to evaluate $\{C_{ij}\}$, baseline solutions to the full set of governing equations must first be obtained and validated. Assuming steady, incompressible and two-dimensional flow with negligible viscous dissipation, the equations governing free convection in a vertical channel are as shown in Equations 8.14-8.17.

$$\frac{\partial u}{\partial x} + \frac{\partial v}{\partial y} = 0 \tag{8.14}$$

$$\rho u\frac{\partial u}{\partial x}+\rho v\frac{\partial u}{\partial y}=-\frac{\partial \bar{p}}{\partial x}+\mu\left(\frac{\partial^2 u}{\partial x^2}+\frac{\partial^2 u}{\partial y^2}\right) \tag{8.15}$$

$$\rho u\frac{\partial v}{\partial x}+\rho v\frac{\partial v}{\partial y}=-\frac{\partial \bar{p}}{\partial y}+\mu\left(\frac{\partial^2 v}{\partial x^2}+\frac{\partial^2 v}{\partial y^2}\right)+(\rho_0-\rho)g \tag{8.16}$$

$$\rho u c_p\frac{\partial T}{\partial x}+\rho v c_p\frac{\partial T}{\partial y}=k\left(\frac{\partial^2 T}{\partial x^2}+\frac{\partial^2 T}{\partial y^2}\right) \tag{8.17}$$

In deriving these equations the fluid properties were assumed to be constant except for density which was handled by the Boussinesq approximation. In Equations 8.15 and 8.16, $\bar{p}$ denotes the pressure "defect" between the local pressure in the channel and the ambient pressure:

$$\bar{p}=p-p_0$$

8.3.1 Solution Method

The commercial CFD solver ANSYS Fluent (ANSYS 2011a,b) was utilized to obtain second-order finite volume solutions to Equations 8.14-8.17 using the PRESTO! algorithm for discretizing pressure and SIMPLE scheme for handling the pressure-velocity coupling.

8.3.2 Computational Domain, Boundary Conditions & Discretization

Different computational domains have been used in the CFD modeling of free convection in heated channels. The channel with no extensions, the channel with upstream and/or downstream extensions of different shapes (rectangular, semicircular, etc.) and the channel

within an "infinite" extension (channel in a cavity) are most common. A review of the typical computational domains used for free convection in vertical channels is given by Manca et al. (2000). In the present study, based on the work of Naylor et al. (1991), semicircular inlet and outlet sections of the same size were added to the channel. See Figure 8.3.

The channel walls (1-2) were modeled as impermeable, no-slip, isothermal solid boundaries. The four horizontal segments of the inlet/outlet extensions (3-6) were modeled as impermeable, no-slip, adiabatic solid boundaries. The semicircular segments (7-8) were designated pressure boundaries at the ambient pressure and temperature. The inlet flow direction was specified as normal to the boundaries (7-8).

If the channel is tall ($H/W \gtrsim 10$), axial diffusion of heat can be neglected and heat transfer in the channel is nearly independent of the channel aspect ratio. The present numerical results were generated for an aspect ratio of $H/W = 50$, except for cases with $r_T = 0$ and $\mathrm{Ra} \geq 500$ which were solved in a shorter computational domain ($H/W = 20$) to facilitate convergence. The results are, however, generally applicable for $H/W \geq 10$.

The domain was discretized into approximately 100,000 non-uniform rectangular control volumes. A structured grid was generated in the rectangle representing the channel while unstructured cells were generated in the inlet and outlet extensions. A Richardson-extrapolation-based technique (Celik et al. 2008) was used to assess the grid dependence of the solutions. Using two additional grids with 4,400 and 27,600 control volumes and the same pattern, and based on the rate of total heat transfer to the fluid

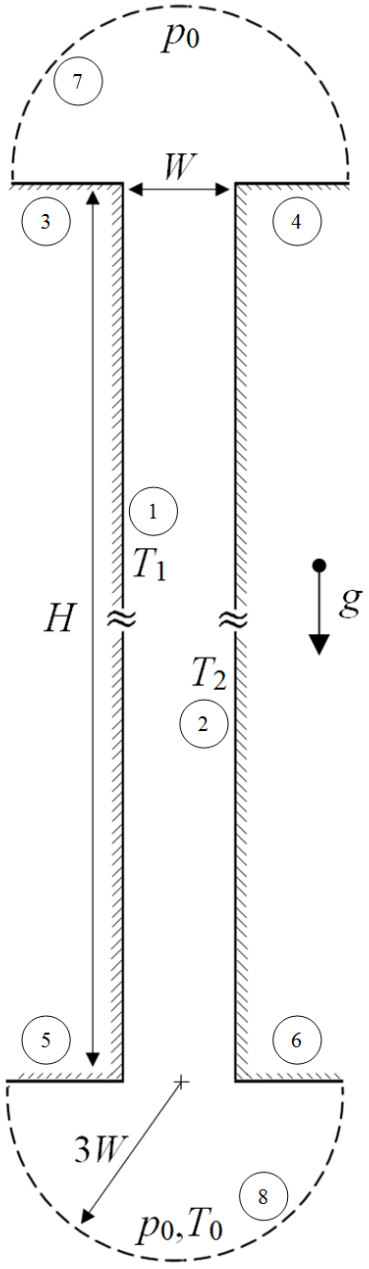

Figure 8.3: Computational domain for laminar free convection in a vertical channel

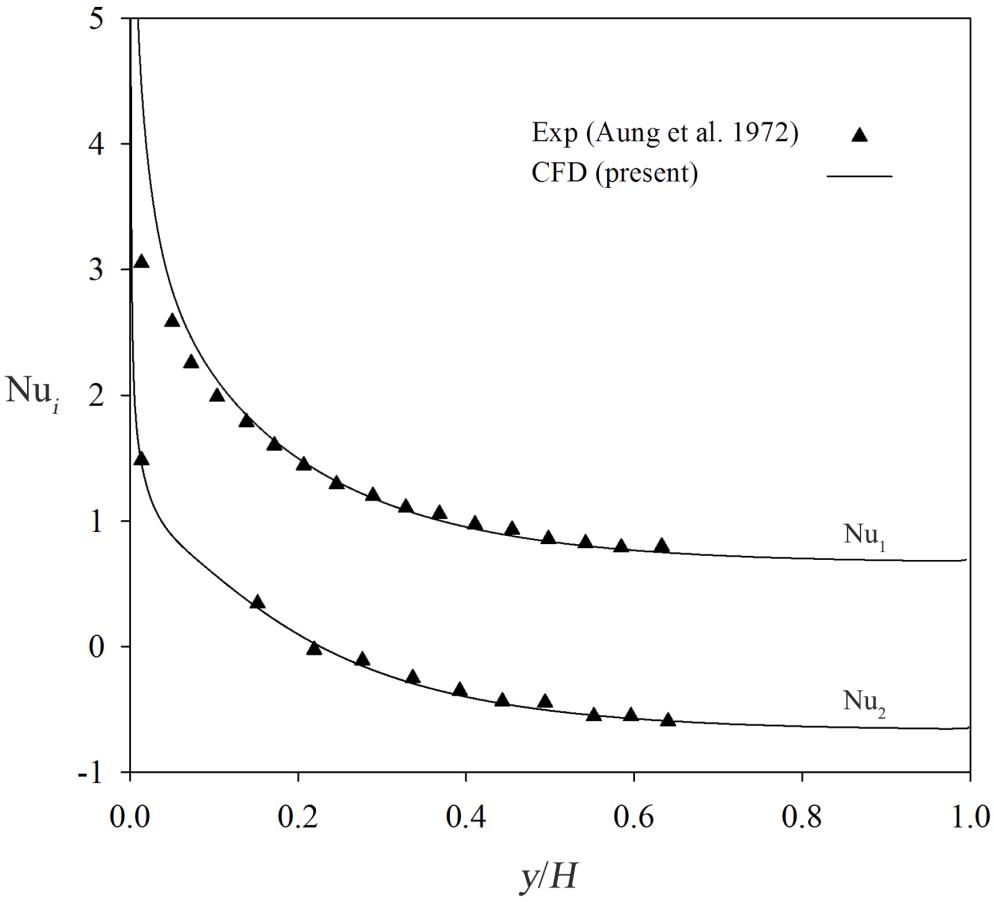

Figure 8.4: Local Nusselt numbers of laminar free convection in a vertical channel with isothermal walls (Ra = 24, Pr = 0.7, $r_T = 0.33$)

(Q_0), a grid convergence index of 3% was calculated for the fine grid which was used to generate the results. The apparent order of the solution was found to be 1.9.

8.3.3 Validation

The baseline CFD solutions were validated against the experimental data of Aung et al. (1972). In Figure 8.4, the local wall Nusselt numbers (defined in Equation 8.3) are shown for Ra = 24, Pr = 0.7 and $r_T = 0.33$.

Away from the channel inlet ($y/H \gtrsim 0.1$), the present numerical results are in very close agreement with the measurements. Aung et al. (1972) have reported a drop in the channel wall temperature near the inlet "due to the construction of the apparatus".

This experimental error explains the pronounced discrepancy between numerical and experimental results near the inlet ($y/H < 0.1$).

At higher Rayleigh numbers, Aung et al. (1972) have only reported average Nusselt numbers. At Ra = 2000, for example, and with the walls heated symmetrically ($r_T = 1$), the measured average wall Nusselt number is: $\overline{\mathrm{Nu}_1} = \overline{\mathrm{Nu}_2} = 4.27$. The current CFD solutions predict $\overline{\mathrm{Nu}_1} = \overline{\mathrm{Nu}_2} = 3.93$, within 8% of the measurements.

Unfortunately, the uncertainty in the measured Nusselt numbers is not reported by Aung et al. (1972). Therefore, the comparison is incomplete. The general agreement shown in Figure 8.4 was nonetheless taken as validation of the baseline CFD solutions.

8.4 Numerical dQdT

For each combination of Ra and r_T, numerical dQdT was implemented as follows:

i) A baseline solution was obtained by solving the full set of governing equations numerically.

ii) The baseline heat transfer rates, $\{Q_i\}$, were calculated; Q_1 and Q_2 were calculated by integrating the heat flux at the walls, while Q_0 was calculated based on the overall energy balance in the channel: $Q_0 = -Q_1 - Q_2$.

iii) The boundary temperature T_j was perturbed by a finite amount, δT_j.

iv) The solution to the energy equation *only* was updated by retaining the velocity field of the baseline solution. In Fluent, this can be readily done by selecting the energy equation only in the "Equations" section, under "Solution Controls".

v) The new heat transfer rates, $\{Q_i^*\}$, and the respective changes were calculated; $\delta Q_i = Q_i^* - Q_i$.

vi) The functionality coefficients corresponding to T_j were calculated using Equation 2.44; $C_{ij} = -\delta Q_i / \delta T_j$.

vii) Steps iii-vi were repeated for $j = 0, 1, 2$.

The functionality coefficients thus obtained apply to the original set of boundary temperatures, $\{T_i\}$.

The implementation of steps ii-vi in Fluent was automated using "journal" files. A sample journal routine can be found in Appendix E.

Note that by retaining the velocity field of the baseline solution (step iv), the $C_{ik} =$ const constraint in Equation 2.44 was satisfied. Since the fluid properties were assumed to be constant, no action was necessary to fix the fluid properties. Imposing the $C_{ik} =$ const constraint for cases of variable fluid properties will be discussed in Chapter 9.

Further note that obtaining the full set of functionality coefficients in an N-temperature problem entails a baseline solution to the full set of governing equations and N subsequent solutions to the energy equation with perturbed boundary conditions. Nevertheless, because the N additional solutions are sought only for the linearized energy equation, the additional computational cost is insignificant.

8.5 Average Paired Nusselt Numbers

An average paired Nusselt may be defined to present the results in dimensionless form. See Equation 8.18.

$$\overline{\mathrm{Nu}}_{ij} = \left(\frac{C_{ij}}{k}\right)\frac{W}{H} \tag{8.18}$$

Sample dQdT results are reported in Table 8.1 for $r_T = 0.5$, and in Appendix F for several other r_T. dQdT results confirm that:

$$r_T \neq 1 \Rightarrow \overline{\mathrm{Nu}}_{ij} \neq \overline{\mathrm{Nu}}_{ji}$$

As mentioned earlier, the asymmetry in the temperature field leads to asymmetry in the flow field. The asymmetrical position of the channel walls within the flow field leads to $C_{ij} \neq C_{ji}$ and hence, $\overline{\mathrm{Nu}}_{ij} \neq \overline{\mathrm{Nu}}_{ji}$. When $r_T = 1$, on the other hand, the flow field is symmetrical with respect to the channel centerline ($x = 0$). Therefore, the walls are symmetrically positioned in the flow field and hence: $\overline{\mathrm{Nu}}_{ij} = \overline{\mathrm{Nu}}_{ji}$.

Note that because the difference between $\overline{\mathrm{Nu}}_{ij}$ and $\overline{\mathrm{Nu}}_{ji}$ is very small, it is reasonable to assume $\overline{\mathrm{Nu}}_{ij} = \overline{\mathrm{Nu}}_{ji}$. Consequently, the resistor-network model is applicable.

In Figure 8.5 numerical dQdT results are plotted for $\mathrm{Pr} = 0.7$, $0 < r_T \leq 1$ and $0.01 \leq \mathrm{Ra} \leq 2000$. The curves of Figure 8.5 have a clear physical interpretation. The trends are similar to those observed for the forced-convection problems studied in Chapters 4-6. For low flow rates, $\mathrm{Ra} \lesssim 1$, heat transfer in the channel is dominated by conduction between the walls, leading to $\overline{\mathrm{Nu}}_{12} \approx \overline{\mathrm{Nu}}_{21} \approx 1$. As the flow rate increases, the thermal boundary layers become thinner and the thermal interaction between the walls diminishes. Therefore:

$$\lim_{\mathrm{Ra}\to\infty} \overline{\mathrm{Nu}}_{12} = \lim_{\mathrm{Ra}\to\infty} \overline{\mathrm{Nu}}_{21} = 0$$

Note that the wall-wall Nusselt number $\overline{\mathrm{Nu}}_{12}$ is nearly independent of r_T.

At low flow rates ($\mathrm{Ra} < 1$), there is almost zero net heat transfer to the fluid, reflected by:

$$\lim_{\mathrm{Ra}\to 0} \overline{\mathrm{Nu}}_{10} = \lim_{\mathrm{Ra}\to 0} \overline{\mathrm{Nu}}_{20} = 0$$

The slight departure of the numerical results for $\overline{\mathrm{Nu}}_{10}$ and $\overline{\mathrm{Nu}}_{20}$ from zero in the low-Ra limit is due to the axial diffusion of heat out of the channel inlet.

Table 8.1: Sample dQdT results for laminar free convection in a vertical channel with isothermal walls ($r_T = 0.5$, Pr = 0.7)

Ra	$\overline{\mathrm{Nu}}_{12}$	$\overline{\mathrm{Nu}}_{21}$	$\overline{\mathrm{Nu}}_{10}$	$\overline{\mathrm{Nu}}_{01}$	$\overline{\mathrm{Nu}}_{20}$	$\overline{\mathrm{Nu}}_{02}$
0.01	1.0010	1.0010	0.0206	0.0206	0.0206	0.0205
0.1	1.0007	1.0007	0.0213	0.0213	0.0212	0.0212
1	0.9896	0.9891	0.0462	0.0467	0.0456	0.0452
10	0.8642	0.8614	0.3616	0.3644	0.3488	0.3460
100	0.3875	0.3691	1.6939	1.7122	1.5818	1.5634
1000	0.0404	0.0297	3.5269	3.5376	3.0867	3.0759

The wall-fluid Nusselt numbers, $\overline{\mathrm{Nu}}_{10}$ and $\overline{\mathrm{Nu}}_{20}$, both increase with Ra. Since this is a free-convection problem, the asymmetry in the temperature field leads to asymmetry between the paired Nusselt numbers. Heat transfer at the hotter wall is more sensitive to the inlet temperature; $\overline{\mathrm{Nu}}_{10} > \overline{\mathrm{Nu}}_{20}$. Moreover, the difference between $\overline{\mathrm{Nu}}_{10}$ and $\overline{\mathrm{Nu}}_{20}$ increases as Ra increase and as r_T decreases. Note that in the limiting case of symmetric heating of the walls ($r_T = 1$) there is symmetry between the wall-fluid Nusselt numbers; $\overline{\mathrm{Nu}}_{10} = \overline{\mathrm{Nu}}_{20}$.

With the channel aspect ratio incorporated in the channel Rayleigh number (see Equation 8.1), Ra is also an indication of the thermal development length of the flow. In this interpretation, small values of Ra (Ra $\to$ 0) correspond to essentially thermally developed flow wherein the net heat transfer rate to the fluid is zero; heat transfer at one wall is entirely conducted to the other wall. Large values of Ra (Ra $\to \infty$) represent the entrance region wherein there is enhanced heat transfer between the channel walls and the fluid, while because the thermal boundary layers are thin, there is very little thermal interaction between the walls.

To further establish the validity of the dQdT results, two limiting cases may be examined. First, as explained in Chapter 2, if the walls are symmetrically heated ($r_T = 1$), the functionality coefficients can be obtained algebraically — without using dQdT. In

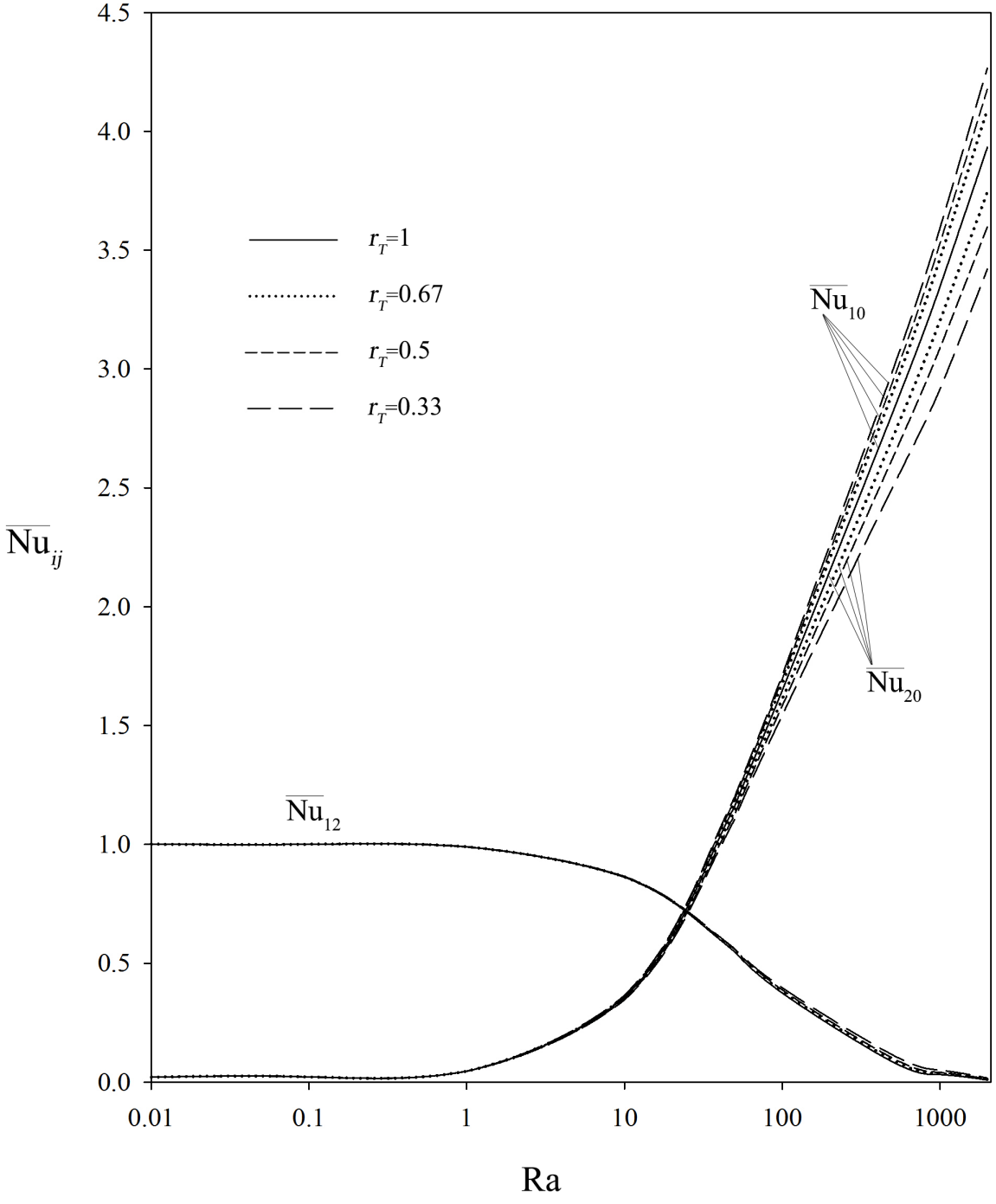

Figure 8.5: Average paired Nusselt numbers of laminar free convection in a vertical channel with isothermal walls (Pr = 0.7)

Section 2.6.1, an algebraic expression was obtained for C_{10} of a symmetric problem as shown in Equation 8.19.

$$C_{10} = C_{20} = \frac{Q_1 + Q_2}{T_1 + T_2 - 2T_0} \tag{8.19}$$

In Table 8.2 the dQdT results for C_{10} and C_{20} are compared to the algebraic results (Equation 8.19) for various Rayleigh numbers. The two sets of results are *identical*, indicating the validity of the dQdT results. For clarity, results in Table 8.2 are presented in dimensional form. Note the small discrepancy between Q_1 and Q_2 which is due to numerical errors. This error, however, does not propagate to the dQdT results.

The second limiting case is the case of thermally developing flow, i.e. heat transfer in the entrance region; $\mathrm{Ra} \to \infty$. In this limit, the thermal boundary layers are separated by a core of fluid flow at T_0 and do not thermally communicate. Hence, as shown earlier:

$$\lim_{\mathrm{Ra}\to\infty} \overline{\mathrm{Nu}}_{12} = 0$$

Therefore, the wall-fluid functionality coefficients can be calculated as:

$$C_{i0} = \frac{Q_i}{T_i - T_0} \qquad (\mathrm{Ra} \to \infty \; ; \; i = 1, 2)$$

For $r_T = 0.5$, $\mathrm{Pr} = 0.7$ and $\mathrm{Ra} = 2000$, for example, dQdT gives: $\overline{\mathrm{Nu}}_{10} = 4.18$. Using the equation above, an identical result is obtained, again indicating the validity of the dQdT technique.

Alternatively, adopting the resistor-network model, the functionality coefficients C_{10} and C_{20} can be obtained by considering the thermal current in the legs connecting T_1 and T_2 to T_0;

Table 8.2: Wall-fluid functionality coefficients of laminar free convection in a vertical channel with isothermal walls – The special case of symmetry $\left[r_T = 1,\ \mathrm{Pr} = 0.7,\ H/W = 50,\ k = 0.0255\ \mathrm{W/(mK)}\right]$

Ra	i	T_i [K]	Q_i [W/m]	C_{i0} (Eq. 8.19) [W/(mK)]	T_i^* [K]	Q_i^* [W/m]	C_{i0} (dQdT) [W/(mK)]
	0	300	0.5240	–	301	0.4716	–
0.01	1	310	0.2622	0.0262	310	0.2360	0.0262
	2	310	0.2618	0.0262	310	0.2356	0.0262
	0	300	0.5426	–	301	0.4883	–
0.1	1	310	0.2713	0.0271	310	0.2442	0.0271
	2	310	0.2713	0.0271	310	0.2441	0.0271
	0	300	1.1703	–	301	1.0533	–
1	1	310	0.5849	0.0585	310	0.5265	0.0585
	2	310	0.5854	0.0585	310	0.5268	0.0586
	0	300	9.0791	–	301	8.1712	–
10	1	310	4.5395	0.4540	310	4.0856	0.4540
	2	310	4.5396	0.4540	310	4.0856	0.4540
	0	300	42.0002	–	301	37.8002	–
100	1	310	21.0000	2.1000	310	18.9000	2.1000
	2	310	21.0002	2.1000	310	18.9002	2.1000
	0	300	85.3232	–	301	76.7909	–
1000	1	310	42.6616	4.2662	310	38.3954	4.2662
	2	310	42.6616	4.2662	310	38.3955	4.2662

$$C_{i0} = \frac{Q_{i0}}{T_i - T_0}$$

To use the preceding equation, the *paired* thermal currents Q_{10} and Q_{20} can be estimated by evaluating the enthalpy change inside the respective boundary layers;

$$Q_{i0} = \int_{x_i}^{\delta_i} \rho v c_p (T - T_0)\,\mathrm{d}x \qquad (\mathrm{Ra} \to \infty\ ;\ i = 1, 2)$$

In the equation above, δ_i denotes the thickness of the thermal boundary layer developed along the wall at T_i, and v is the velocity in the y-direction. Q_{10}, for instance, can be estimated as:

$$Q_{10} = \int_{-\frac{W}{2}}^{\delta_1} \rho v c_p (T - T_0)\, \mathrm{d}x \qquad (\mathrm{Ra} \to \infty)$$

For the example examined earlier ($r_T = 0.5$, $\mathrm{Pr} = 0.7$ and $\mathrm{Ra} = 2000$), using the boundary-layer integral to estimate Q_{10} leads to $\overline{\mathrm{Nu}}_{10} = 4.24$. In this calculation, δ_1 was estimated as the lateral location where $T_1 - T = 0.99\,(T_1 - T_0)$. The close agreement with the dQdT result ($\overline{\mathrm{Nu}}_{10} = 4.18$) indicates, again, the validity of the dQdT technique.

8.5.1 The Special Case of $r_T = 0$

When both channel walls are hotter than the ambient temperature, $T_1 \geq T_2 > T_0$, two boundary layers develop along the channel walls. The development and interaction of these boundary layers determine heat transfer in the channel. As discussed earlier, the paired Nusselt numbers are a good representation of this physics.

The case of $r_T = 0$, i.e. when one of the channel walls is unheated ($T_2 = T_0$), is a special case. For $r_T = 0$, a hydrodynamic boundary layer is developed along the heated wall. As a result of the induced flow, a "secondary" hydrodynamic boundary layer develops along the unheated wall. Nevertheless, only one thermal boundary layer is formed — along the heated wall. The development of this boundary layer and its interaction with the unheated wall, i.e. a physical boundary, determine heat transfer in the channel. Moreover, CFD results indicate that for $r_T = 0$ and $\mathrm{Ra} \gtrsim 500$, some fluid is drawn into the channel from the top, near the unheated wall. In other words, there is some back-flow at the top of the channel. These features are in several ways apparent in the paired Nusselt numbers of the case of $r_T = 0$. See Table 8.3.

First, the difference between $\overline{\mathrm{Nu}}_{ij}$ and $\overline{\mathrm{Nu}}_{ji}$ can be considerable, especially when there is back-flow at the top, i.e. for $\mathrm{Ra} \gtrsim 500$. Recall that for $r_T > 0$, this difference was

Table 8.3: Sample dQdT results for laminar free convection in a vertical channel with isothermal walls (Pr = 0.7) – The special case of $r_T = 0$

Ra	$\overline{\mathrm{Nu}}_{12}$	$\overline{\mathrm{Nu}}_{21}$	$\overline{\mathrm{Nu}}_{10}$	$\overline{\mathrm{Nu}}_{01}$	$\overline{\mathrm{Nu}}_{20}$	$\overline{\mathrm{Nu}}_{02}$
0.01	1.0010	1.0010	0.0206	0.0206	0.0206	0.0206
0.1	1.0007	1.0007	0.0213	0.0213	0.0213	0.0212
1	0.9901	0.9887	0.0467	0.0482	0.0452	0.0437
10	0.8684	0.8600	0.3716	0.3800	0.3331	0.3248
100	0.4413	0.3816	1.7358	1.7955	1.4032	1.3434
500	0.2240	0.1177	2.9995	3.1057	1.9603	1.8540
1000	0.1861	0.0654	3.5826	3.7033	2.1043	1.9836
2000	0.1748	0.0336	4.2266	4.3678	2.2828	2.1416

negligibly small. Clearly, in the case of $r_T = 0$, there is notable asymmetry in the flow field. The onset of back-flow at the top of the channel enhances this asymmetry, leading to increased disparity between $\overline{\mathrm{Nu}}_{ij}$ and $\overline{\mathrm{Nu}}_{ji}$. Note that, as observed in flow over cylinders in tandem, for a given flow rate, the difference between each pair is a constant. See Appendix D.

Second, for $r_T = 0$ and $\mathrm{Ra} \geq 100$, the wall-wall Nusselt number $\overline{\mathrm{Nu}}_{12}$ is significantly larger than the $r_T > 0$ cases. This is apparent in Figure 8.6 where $\overline{\mathrm{Nu}}_{12}$, $\overline{\mathrm{Nu}}_{10}$ and $\overline{\mathrm{Nu}}_{20}$ are plotted for $r_T = 0$ and $r_T = 0.5$. Recall that, as shown in Figure 8.5, the variation of $\overline{\mathrm{Nu}}_{ij}$ with Ra is qualitatively the same for all $r_T > 0$. Hence the $r_T = 0.5$ curves shown in Figure 8.6 are representative of $r_T > 0$. The other wall-wall Nusselt number $\overline{\mathrm{Nu}}_{21}$, however, follows a trend very similar to that of the $r_T > 0$ cases. It was noted earlier that, for $r_T > 0$, the wall-wall Nusselt numbers, $\overline{\mathrm{Nu}}_{12}$ and $\overline{\mathrm{Nu}}_{21}$, closely follow a "universal" curve which is independent of r_T. For $r_T = 0$, $\overline{\mathrm{Nu}}_{21}$ follows the same curve.

Finally, the variation of the wall-fluid Nusselt number $\overline{\mathrm{Nu}}_{20}$ with Ra for $r_T = 0$ is notably different from the $r_T > 0$ cases. On the other hand, as seen in Figure 8.6, $\overline{\mathrm{Nu}}_{10}$, is similar to the $r_T > 0$ cases.

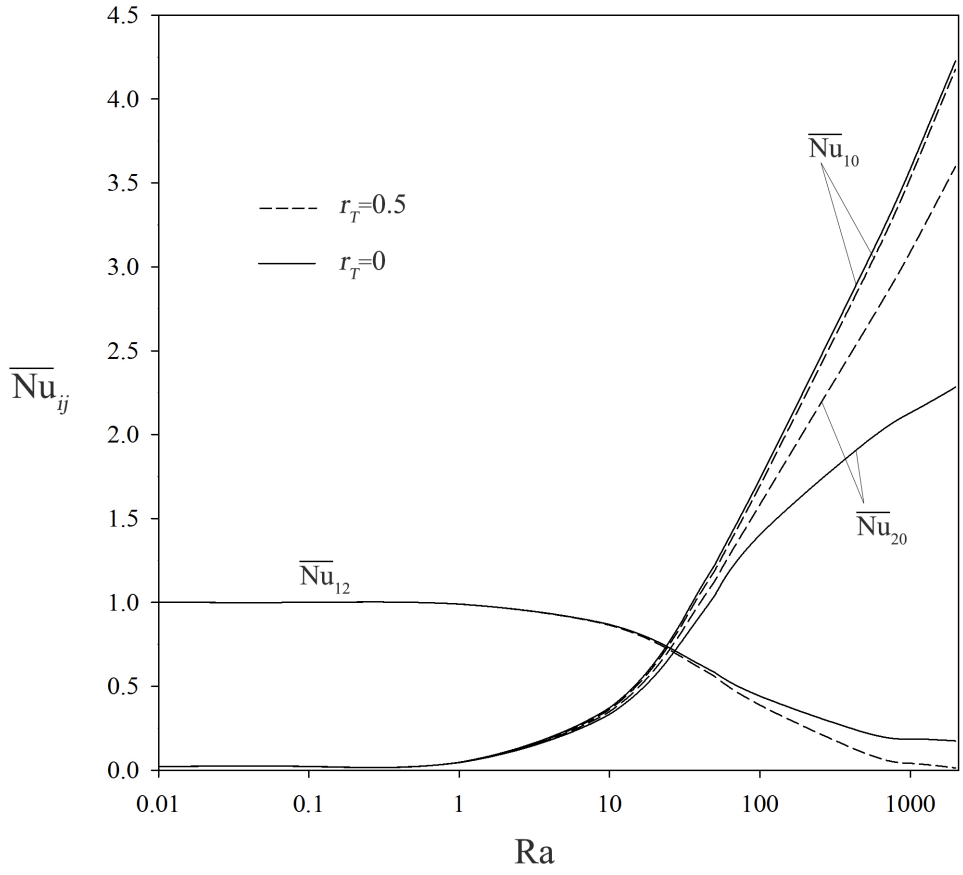

Figure 8.6: Average paired Nusselt numbers of laminar free convection in a vertical channel with isothermal walls (Pr = 0.7) – The special case of $r_T = 0$

It is noteworthy that the traditional Nusselt number does not reflect the peculiarities of the $r_T = 0$ case; although Q_2 is finite and non-zero, $\overline{\mathrm{Nu}}_2$ becomes indefinite because $T_2 = T_0$. See Equation 8.4. This is a non-physical feature and another shortcoming of the traditional total Nusselt numbers in characterizing multi-temperature convection.

8.6 Alternative Correlations

Comparing Figures 8.2 and 8.5, important differences between $\{\overline{\mathrm{Nu}}_i\}$ and $\{\overline{\mathrm{Nu}}_{ij}\}$ are observed:

i) Whereas the total wall Nusselt numbers, $\overline{\mathrm{Nu}}_1$ and $\overline{\mathrm{Nu}}_2$, have distinct, r_T-dependent asymptotic values at both ends ($\mathrm{Ra} \to 0$ and $\mathrm{Ra} \to \infty$), the paired wall-fluid Nusselt numbers, $\overline{\mathrm{Nu}}_{10}$ and $\overline{\mathrm{Nu}}_{20}$, approach the same r_T-independent limit as $\mathrm{Ra} \to 0$.

ii) Contrary to the total Nusselt number of the colder wall ($\overline{\mathrm{Nu}}_2$), the paired Nusselt numbers do not change sign; $\overline{\mathrm{Nu}}_{ij} \geq 0$.

iii) The wall-wall paired Nusselt number, $\overline{\mathrm{Nu}}_{12}$, is nearly independent of r_T.

These features offer an opportunity for developing improved correlations which are free of the extra parameters of the existing correlations discussed in Section 8.1, while having clear physical interpretations.

8.6.1 Asymptotes

Wall-Fluid Nusselt Numbers

The limiting values of $\overline{\mathrm{Nu}}_{10}$ and $\overline{\mathrm{Nu}}_{20}$ were discussed in Section 8.5. The asymptotic behavior of $\overline{\mathrm{Nu}}_{10}$ and $\overline{\mathrm{Nu}}_{20}$ in approaching those limits is better seen in Figure 8.7 where the dQdT results for the wall-fluid Nusselt numbers a sample case ($r_T = 0.3$) are plotted in log-log scale. According to Figure 8.7, in thermally developed limit, $\overline{\mathrm{Nu}}_{10}$ and $\overline{\mathrm{Nu}}_{20}$ both follow the same asymptote[1]:

$$\lim_{\mathrm{Ra}\to 0} \overline{\mathrm{Nu}}_{10} = \lim_{\mathrm{Ra}\to 0} \overline{\mathrm{Nu}}_{20} = \overline{\mathrm{Nu}}_{\mathrm{fd}}$$

Note that as can be seen from Equation 8.6, for $0 \leq r_T \leq 1$, $\overline{\mathrm{Nu}}_{\mathrm{fd}}$ is very weakly dependent on r_T and can be approximated as shown in Equation 8.20. For a detailed discussion of the fully developed limit, see the work of Martin et al. (1991).

[1] As mentioned earlier, due to axial diffusion at the channel inlet, the numerical results for $\overline{\mathrm{Nu}}_{10}$ and $\overline{\mathrm{Nu}}_{20}$ deviate from the asymptote, $\overline{\mathrm{Nu}}_{\mathrm{fd}}$, for $\mathrm{Ra} < 1$. Numerical results obtained in a domain with an infinitely large inlet section would closely follow this asymptote all the way to $\mathrm{Ra} = 0$.

$$\overline{\mathrm{Nu}}_{\mathrm{fd}} \approx \frac{\mathrm{Ra}}{24} \qquad (0 \leq r_T \leq 1) \tag{8.20}$$

In the other limit ($\mathrm{Ra} \to \infty$), $\overline{\mathrm{Nu}}_{10}$ and $\overline{\mathrm{Nu}}_{20}$ approach the respective isothermal plate limits, $\overline{\mathrm{Nu}}_{\mathrm{p}1}$ and $\overline{\mathrm{Nu}}_{\mathrm{p}2}$;

$$\lim_{\mathrm{Ra}\to\infty} \overline{\mathrm{Nu}}_{i0} = \overline{\mathrm{Nu}}_{\mathrm{p}i}$$

To obtain $\overline{\mathrm{Nu}}_{\mathrm{p}i}$, the boundary-layer solution to the isothermal flat plate problem (Ostrach 1953) was evaluated at the respective Rayleigh number, Ra_i. See Equations 8.21 and 8.22.

$$\mathrm{Ra}_i = \frac{g\beta(T_i - T_0)W^3}{\nu^2}\left(\frac{W}{H}\right)\mathrm{Pr} \tag{8.21}$$

$$\mathrm{Nu}_{\mathrm{p}i} = 0.618\,\mathrm{Ra}_i^{1/4} \tag{8.22}$$

Wall-Wall Nusselt Numbers

As discussed in Section 8.5, the wall-wall Nusselt number, $\overline{\mathrm{Nu}}_{12}$, varies between the following limits:

$$\lim_{\mathrm{Ra}\to 0} \overline{\mathrm{Nu}}_{12} = 1$$

$$\lim_{\mathrm{Ra}\to\infty} \overline{\mathrm{Nu}}_{12} = 0$$

In the thermally developed limit, $\overline{\mathrm{Nu}}_{12}$ describes conduction between parallel plates, following the constant function: $\overline{\mathrm{Nu}}_{12} = 1$. In the other limit ($\mathrm{Ra} \to \infty$), the dQdT results seem to follow a function of the form: $\overline{\mathrm{Nu}}_{12} = a_{12}/\mathrm{Ra}$, with $a_{12} = \text{const}$.

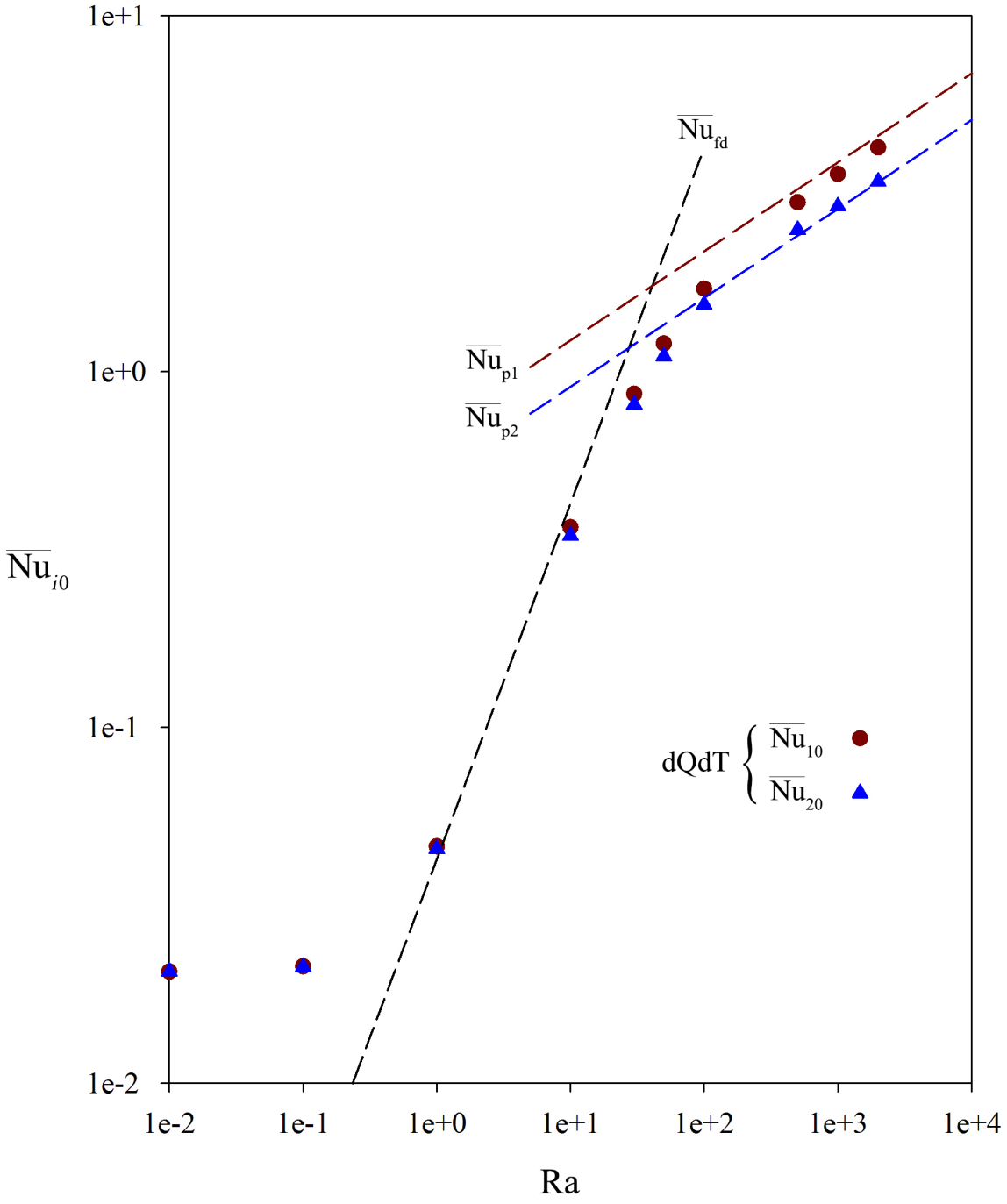

Figure 8.7: Average wall-fluid Nusselt numbers of laminar free convection in a vertical channel with isothermal walls ($r_T = 0.33$, $\mathrm{Pr} = 0.7$)

8.6.2 Correlations

With the asymptotic behavior of $\{\overline{\mathrm{Nu}}_{ij}\}$ established, the method of asymptotes (Churchill & Usagi 1972) was applied to correlate the dQdT results. See Equations 8.23-8.25.

$$\overline{\mathrm{Nu}}_{10} = \left[\left(\overline{\mathrm{Nu}}_{\mathrm{fd}}\right)^{-1.3} + \left(0.618\,\mathrm{Ra}_1^{1/4}\right)^{-1.3}\right]^{-\frac{1}{1.3}} \tag{8.23}$$

$$\overline{\mathrm{Nu}}_{20} = \left[\left(\overline{\mathrm{Nu}}_{\mathrm{fd}}\right)^{-1.3} + \left(0.618\,\mathrm{Ra}_2^{1/4}\right)^{-1.3}\right]^{-\frac{1}{1.3}} \tag{8.24}$$

$$\overline{\mathrm{Nu}}_{12} = \left(1 + 0.0165\,\mathrm{Ra}\right)^{-1} \tag{8.25}$$

The fully developed limit, $\overline{\mathrm{Nu}}_{\mathrm{fd}}$, can be evaluated using Equation 8.6 or simply approximated using Equation 8.20. The relation between the wall Rayleigh numbers, Ra_1 and Ra_2, and the channel Rayleigh number, Ra, is shown in Equation 8.26. The constant $a_{12} = 0.0165$ in Equation 8.25 was obtained from a curve-fit to the numerical dQdT results reported in Section 8.5.

$$\begin{cases} \mathrm{Ra}_1 = \dfrac{2\,\mathrm{Ra}}{1 + r_T} \\ \mathrm{Ra}_2 = \dfrac{2\,\mathrm{Ra}}{1 + 1/r_T} \end{cases} \tag{8.26}$$

For $0 < r_T \leq 1$, Equations 8.23-8.25 fit the numerical dQdT results notably well, with a maximum RMS error of $\pm\,5\%$.

With $\overline{\mathrm{Nu}}_{10}$, $\overline{\mathrm{Nu}}_{20}$ and $\overline{\mathrm{Nu}}_{12}$ obtained from Equations 8.23-8.25, and recalling that for $r_T > 0$; $\overline{\mathrm{Nu}}_{ij} \approx \overline{\mathrm{Nu}}_{ji}$, the individual heat transfer rates, $\{Q_i\}$, can be obtained as shown in Equation 8.27.

$$
\begin{aligned}
Q_i &= \sum_j C_{ij}(T_i - T_j) \\
&= k\left(\frac{H}{W}\right) \sum_j \overline{\mathrm{Nu}}_{ij}(T_i - T_j)
\end{aligned}
\tag{8.27}
$$

Note that Equation 8.27 is applicable for all three heat transfer rates, including Q_0. Alternatively, Q_1 and Q_2 can be calculated using Equation 8.27, and Q_0 using the overall energy balance of the channel:

$$Q_0 = -Q_1 - Q_2$$

The proposed correlations can hence replace Equations 8.5, 8.12 and 8.13, while simplifying the calculations by eliminating the intermediate parameters, ΔT_{eff} and α.

8.6.3 The Special Case of $r_T = 0$: Extension of the Correlations

It was discussed in Section 8.5.1 that if one of the channel walls in unheated, i.e. $r_T = 0$, the physics of the problem changes considerably. Consequently, the paired Nusselt numbers, particularly $\overline{\mathrm{Nu}}_{12}$ and $\overline{\mathrm{Nu}}_{20}$, exhibit trends that are different from the $r_T > 0$ cases. Nevertheless, introducing a few corrections, the correlations presented in Section 8.6.2 can be extended to the special case of $r_T = 0$.

One of the difficulties of the $r_T = 0$ case is the unusual trend of $\overline{\mathrm{Nu}}_{20}$. See Figure 8.6. Nevertheless, since $\Delta T_{20} = 0$, the paired Nusselt number $\overline{\mathrm{Nu}}_{20}$ is not required for the calculation of $\{Q_i\}$. Therefore, no adjustments were introduced in Equation 8.24.

The other difficulty arises from the notable deviation of $\overline{\mathrm{Nu}}_{12}$ from the universal curve obtained for $r_T > 0$. Again, see Figure 8.6. This was remedied by noting that if $r_T = 0$;

$$
\begin{aligned}
Q_1 &= k\left(\frac{H}{W}\right)\left[\overline{\mathrm{Nu}}_{10}(T_1 - T_0) + \overline{\mathrm{Nu}}_{12}(T_1 - T_2)\right] \qquad (r_T = 0) \\
&= k\left(\frac{H}{W}\right)\left(\overline{\mathrm{Nu}}_{10} + \overline{\mathrm{Nu}}_{12}\right)(T_1 - T_0)
\end{aligned}
\tag{8.28}
$$

Furthermore, although $\overline{\mathrm{Nu}}_{12}$ shows a different trend when $r_T = 0$, $\overline{\mathrm{Nu}}_{21}$ is virtually the same for $r_T = 0$ and $r_T > 0$. See the tabulated data in Appendix F. Equation 8.28 was thus rewritten as:

$$
\begin{aligned}
Q_1 &= k\left(\frac{H}{W}\right)\left(\overline{\mathrm{Nu}}_{10} + \overline{\mathrm{Nu}}_{12}\right)(T_1 - T_0) \qquad (r_T = 0) \\
&= k\left(\frac{H}{W}\right)\left[\overline{\mathrm{Nu}}_{10} + \left(\overline{\mathrm{Nu}}_{12} - \overline{\mathrm{Nu}}_{21}\right) + \overline{\mathrm{Nu}}_{21}\right](T_1 - T_0)
\end{aligned}
\tag{8.29}
$$

The dQdT results for $\overline{\mathrm{Nu}}_{10}$ were then adjusted to: $\overline{\mathrm{Nu}}_{10} + \left(\overline{\mathrm{Nu}}_{12} - \overline{\mathrm{Nu}}_{21}\right)$. In other words, the deviation of $\overline{\mathrm{Nu}}_{12}$ from the universal wall-wall curve of Figure 8.5 was at one point neglected, but then compensated by adjusting $\overline{\mathrm{Nu}}_{10}$. This is permissible since the driving temperature differences are equal; $\Delta T_{10} = \Delta T_{12}$. Fortunately, the modified group $\left(\overline{\mathrm{Nu}}_{10} + \overline{\mathrm{Nu}}_{12} - \overline{\mathrm{Nu}}_{21}\right)$ follows Equation 8.23 very closely, with an RMS error of $\pm 5\%$.

Therefore, Equations 8.23 and 8.25 can also be used for $r_T = 0$. It must be re-emphasized however that Equations 8.23 and 8.25 are applicable to the case of $r_T = 0$ *only for calculating the total heat transfer rates using Equation* 8.27; they do not reproduce the dQdT results for $\overline{\mathrm{Nu}}_{10}$ and $\overline{\mathrm{Nu}}_{12}$.

8.7 Summary

Numerical dQdT was implemented in CFD solutions of laminar free convection in a vertical channel with isothermal walls. The functionality coefficients of the problem were calculated for various flow rates and heating scenarios. Due to asymmetry in the flow field, the functionality coefficients do not have perfect reciprocity. However, the difference between each pair is very small and hence the resistor-network model can be applied.

The dQdT results were used to developed new correlations for the individual heat transfer rates at the channel walls. These correlations are applicable to laminar flow of air for the case of both channel walls heated or cooled isothermally ($r_T \geq 0$). Such correlations are needed in building energy simulation, particularly in the modeling convective heat transfer in complex fenestration systems. Excellent agreement between these correlations and numerical dQdT results was achieved. The proposed correlations are notably simpler than the existing correlations while having a clear physical meaning.

Chapter 9

Turbulent Free Convection in a Vertical Channel with Isothermal Walls

In Chapter 8, the extended Newton formulation of laminar free convection in a vertical channel with isothermal walls was presented. Numerical dQdT was applied to obtain the functionality coefficients of the problem; the results were used to develop improved heat transfer correlations.

Compared to the laminar case, less attention has been devoted to turbulent free convection in vertical channels with isothermal walls. Examples include the work of Yilmaz & Fraser (2007), Ayinde et al. (2008) and Roeleveld (2013). The shortcomings of the traditional formulation, discussed in the previous chapter, are relevant also in the case of turbulent flow. In this chapter, the three-temperature problem of turbulent free convection of air in a tall vertical channel with isothermal walls is studied using the dQdT technique. The application of numerical dQdT to turbulent free convection and the implementation of the $C_{ik} = \text{const}$ constraint in the case of variable fluid properties are demonstrated.

9.1 Baseline Solutions

Consider buoyancy-driven flow in a vertical channel with walls at uniform temperatures T_1 and T_2, both greater than the far-field ambient temperature, T_0.

The flow was assumed to be steady, incompressible and two-dimensional. Viscous dissipation was neglected. Except for density, the fluid properties were assumed to be constant. Instead of invoking the Boussinesq approximation, the variation of density with temperature was considered in all of the governing equations. There were two reasons for adopting this approach. First, the numerical solutions were to be validated against experimental data entailing large temperature differences, far beyond the range established by Gray & Giorgini (1976) for the validity of the Boussinesq approximation. Second, the present study was intended partly to demonstrate the application of dQdT to a variable-property problem. The ideal-gas equation was used to evaluate the variation of the density with temperature. Turbulence was resolved using the k-ε model.

The problem was thus formulated in terms of the Reynolds-averaged governing equations shown in Equations 9.1-9.7. With the introduction of the turbulence kinetic energy, k, in this chapter thermal conductivity is denoted by λ.

$$\rho = \frac{p_0}{\mathcal{R}_{\text{air}} T} \tag{9.1}$$

$$\frac{\partial(\rho u)}{\partial x} + \frac{\partial(\rho v)}{\partial y} = 0 \tag{9.2}$$

$$u\frac{\partial(\rho u)}{\partial x} + v\frac{\partial(\rho u)}{\partial y} = -\frac{\partial \bar{p}}{\partial x} + \frac{\partial}{\partial x}\left[(\mu + \mu_t)\frac{\partial u}{\partial x}\right] + \frac{\partial}{\partial y}\left[(\mu + \mu_t)\frac{\partial u}{\partial y}\right] \tag{9.3}$$

$$u\frac{\partial(\rho v)}{\partial x}+v\frac{\partial(\rho v)}{\partial y}=-\frac{\partial \bar{p}}{\partial y}+\frac{\partial}{\partial x}\left[(\mu+\mu_t)\frac{\partial v}{\partial x}\right]+\frac{\partial}{\partial y}\left[(\mu+\mu_t)\frac{\partial v}{\partial y}\right]-(\rho-\rho_0)g \qquad (9.4)$$

$$uc_p\frac{\partial(\rho T)}{\partial x}+vc_p\frac{\partial(\rho T)}{\partial y}=\frac{\partial}{\partial x}\left[(\lambda+\frac{c_p\mu_t}{\sigma_t})\frac{\partial T}{\partial x}\right]+\frac{\partial}{\partial y}\left[(\lambda+\frac{c_p\mu_t}{\sigma_t})\frac{\partial T}{\partial y}\right] \qquad (9.5)$$

$$u\frac{\partial(\rho k)}{\partial x}+v\frac{\partial(\rho k)}{\partial y}=\frac{\partial}{\partial x}\left[(\mu+\frac{\mu_t}{\sigma_k})\frac{\partial k}{\partial x}\right]+\frac{\partial}{\partial y}\left[(\mu+\frac{\mu_t}{\sigma_k})\frac{\partial k}{\partial y}\right]+G_k+G_b-\rho k \qquad (9.6)$$

$$u\frac{\partial(\rho \varepsilon)}{\partial x}+v\frac{\partial(\rho \varepsilon)}{\partial y}=\frac{\partial}{\partial x}\left[(\mu+\frac{\mu_t}{\sigma_\varepsilon})\frac{\partial \varepsilon}{\partial x}\right]+\frac{\partial}{\partial y}\left[(\mu+\frac{\mu_t}{\sigma_\varepsilon})\frac{\partial \varepsilon}{\partial y}\right]+B_{1\varepsilon}\frac{\varepsilon}{k}G_k-B_{2\varepsilon}\rho\frac{\varepsilon^2}{k} \qquad (9.7)$$

In the equations above, $\mathcal{R}_{\text{air}} = 287\,\text{J/(kg K)}$ is the gas constant of air and $\bar{p}$ is the pressure defect, introduced in Chapter 8. The turbulence (eddy) viscosity, μ_t, was calculated using the low-Reynolds differential relation of the k-ε model (ANSYS 2011a). The energy, turbulence kinetic energy and turbulence dissipation rate Prandtl numbers are respectively: $\sigma_t = 0.85$, $\sigma_k = 1$ and $\sigma_\varepsilon = 1.3$. These values are empirical constants in the turbulence model. The source terms G_k and G_b represent respectively the generation of turbulence kinetic energy due to mean velocity gradients and buoyancy. Other model constants are $B_{1\varepsilon} = 1.44$ and $B_{2\varepsilon} = 1.92$. Further details of the low-Reynolds k-ε model used in the present solutions can be found in the ANSYS Fluent documentation (ANSYS 2011a).

9.1.1 Solution Method

The commercial solver ANSYS Fluent (ANSYS 2011a,b) was used to obtain second-order finite volume solutions to Equations 9.1-9.7. The PRESTO! algorithm for discretizing pressure and the SIMPLE scheme for handling the pressure-velocity coupling were used. The ideal-gas model for density and the low-Reynolds k-ε model for turbulence were utilized. No special criterion for transition to turbulence was adopted. The k-ε transport equations were solved throughout the domain.

The k-ω turbulence model and various models for the variation of the fluid properties with temperature were also tested, as discussed in Section 9.1.3.

9.1.2 Computational Domain, Boundary Conditions & Discretization

The computational domain is an important factor in the numerical solutions of turbulent free convection. The boundaries of the domain must ideally be locations at which some data regarding the "background" turbulence (turbulence intensity, kinetic energy, etc.) is available. Furthermore, as discussed by Desrayaud et al. (2013), the inlet geometry can significantly influence the solution.

The present solutions were to be validated against cases for which measurements of the turbulence kinetic energy at the channel inlet are available. These measured turbulence parameters were used to set the inlet boundary conditions in the numerical solution. Therefore, a rectangular computational domain confined to the channel, as shown in Figure 9.1, was used. Similar domains are used by other researchers, e.g. Fedorov & Viskanta (1997), Yilmaz & Fraser (2007) and Yilmaz & Gilchrist (2007).

The channel walls (1-2) were treated as no-slip, impermeable solid boundaries at uniform temperatures. In some of the cases examined in the validation study, constant

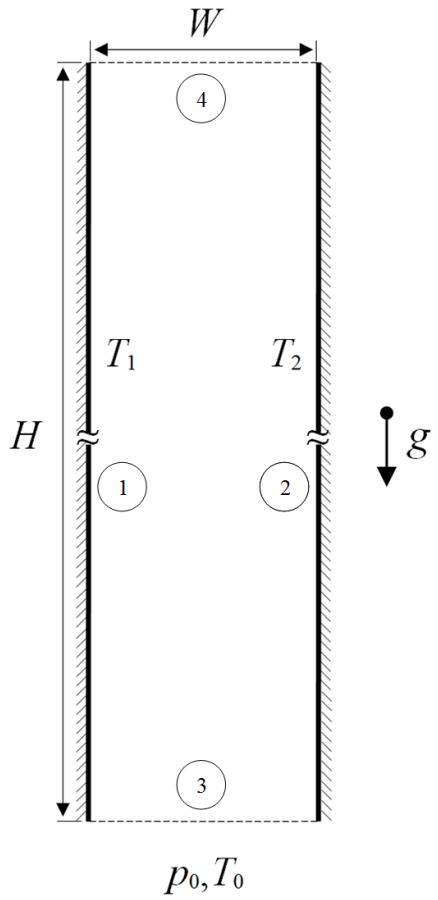

Figure 9.1: Computational domain for turbulent free convection in a vertical channel

heat flux was prescribed at the walls. Pressure and temperature were set to the far-field values, p_0 and T_0, at the channel inlet (3). In Fluent, the temperature gradient normal to the inlet boundary is, by default, set to zero. In the following validation study, turbulence kinetic energy and dissipation rate were used to specify the inlet turbulence conditions. See Section 9.1.3. But to generate the baseline solutions for dQdT, i.e. in the "production" runs, a turbulence intensity of 10% and the hydraulic diameter were specified as the inlet turbulence conditions. Back-flow parameters matching the inlet conditions were set at the channel outlet (4).

Note that in the present model, the axial diffusion of heat at the channel inlet was neglected. On the other hand, if an upstream extension were considered (as in Chapter

8), matching the turbulence kinetic energy at the channel inlet would become an iterative process and, due to the nonlinearities involved, cumbersome. Numerical tests showed that despite errors arising from the omission of axial heat diffusion at the inlet, a rectangular domain with matched turbulence kinetic energy at the inlet yields acceptable agreement with experimental data.

The computational domain was discretized into a non-uniform grid of approximately 300,000 rectangular control volumes. The grid dependence of the solutions was assessed based on the Richardson-extrapolation technique proposed by Celik et al. (2008). Using two finer grids with about 600,000 and 800,000 control volumes, and based on the rate of total heat transfer to the fluid (Q_0), a grid convergence index of 4% was obtained for the coarse mesh which was used to generate the results.

9.1.3 Validation

The numerical solutions were validated against the experimental data of Yilmaz & Fraser (2007). To perform the validation study, a numerical solution was obtained for a channel with $H/W = 30$ and one wall heated to $T_1 = 100°C$. In the experiments conducted by Yilmaz & Fraser (2007) the thermal condition at the other wall was uncontrolled; the temperature of this wall was reported to rise 2-5°C above the inlet temperature, $T_0 = 22.5°C$ (Yilmaz & Fraser 2007). In the numerical solutions, radiant exchange was neglected and the unheated wall was assumed to be adiabatic. The low-Reynolds-number (LR) variations of the k-ε and k-ω models were used to resolve turbulence. The inlet kinetic turbulence energy was set as the average of the values measured by Yilmaz & Fraser (2007) at $y/H = 0.03$. A solution was also obtained by specifying a profile for the inlet turbulence kinetic energy using the experimental data points and a user-defined function (UDF). The turbulence dissipation rate at the inlet was calculated based on the relation given by Yilmaz & Fraser (2007). The fluid properties were assumed to be constant, evaluated at $(T_1 + T_0)/2$, except for density which was evaluated using the ideal-gas equation. Solutions

were also obtained using variable fluid properties based on the linear interpolation of data compiled by Hilsenrath (1955) and Touloukian (1970, 1975).

In Table 9.1 the predictions of the CFD solutions for the induced mass flow rate and the average wall heat flux are compared with the measurements of Yilmaz & Fraser (2007). Results of a numerical solution from the literature (Yilmaz & Fraser 2007) are also presented in Table 9.1. The uncertainty in the experimental data are reported from the source (Yilmaz & Fraser 2007). The errors in the numerical results are calculated based on the experimental data. It can be seen that the various schemes used for handling turbulence and variation of the fluid properties all yield results within the experimental uncertainty of the measurements ($\sim 10\%$). This is in agreement with the conclusion of Yilmaz & Fraser (2007) that, despite considerable discrepancy in the local results such as temperature and velocity profiles, different RANS models predict the overall heat and mass flow rates within 10-15% of the measurements.

In Figure 9.2, the temperature profile near the channel outlet ($y/H = 0.98$) is shown in terms of the excess temperature, $T - T_0$. Solution "CFD-2" (see Table 9.1) was compared to experimental and numerical (CFD-1) data from the literature. The uncertainty in the temperature measurements by Yilmaz & Fraser (2007) has been reported to be respectively 0.2°C and 0.9°C for the flow and surface temperatures. As can be seen in Figure 9.2, solutions using both k-ε and k-ω models are in good agreement with the benchmark data.

Based on the results presented in Table 9.1 and Figure 9.2, the low-Reynolds k-ε turbulence and ideal-gas models for turbulence and density were chosen to generate baseline solutions for dQdT.

Table 9.1: Induced mass flow rate and average wall heat flux
($H = 30W = 3\,\text{m}$, $T_1 = 100°\text{C}$, $q_2 = 0$, $T_0 = 22°\text{C}$, $p_0 = 1\,\text{atm}$)

Study	Turbulence Model	Inlet Turbulence	Fluid Properties	$\dot{m}$ [gr/s]	Error	q [W/m^2]	Error
Exp$^+$	—	—	—	85.4	10.0%$^{++}$	360.3	7.0%$^{++}$
CFD-1$^+$	LR k-ε	constant	Ideal gas ρ	91.4	7.0%	331.5	8.0%
CFD-2	LR k-ε	constant	Ideal gas ρ	89.7	5.0%	361.0	0.2%
CFD-3	LR k-ω	constant	Ideal gas ρ	86.5	1.3%	337.6	6.3%
CFD-4	LR k-ε	$k_0 = k_0(x)$	Ideal gas ρ	89.3	4.6%	359.7	0.2%
CFD-5	LR k-ε	constant	Linear	82.1	3.9%	353.8	1.8%

$^+$ Yilmaz & Fraser (2007)

$^{++}$ Estimate of experimental uncertainty (Yilmaz & Fraser 2007)

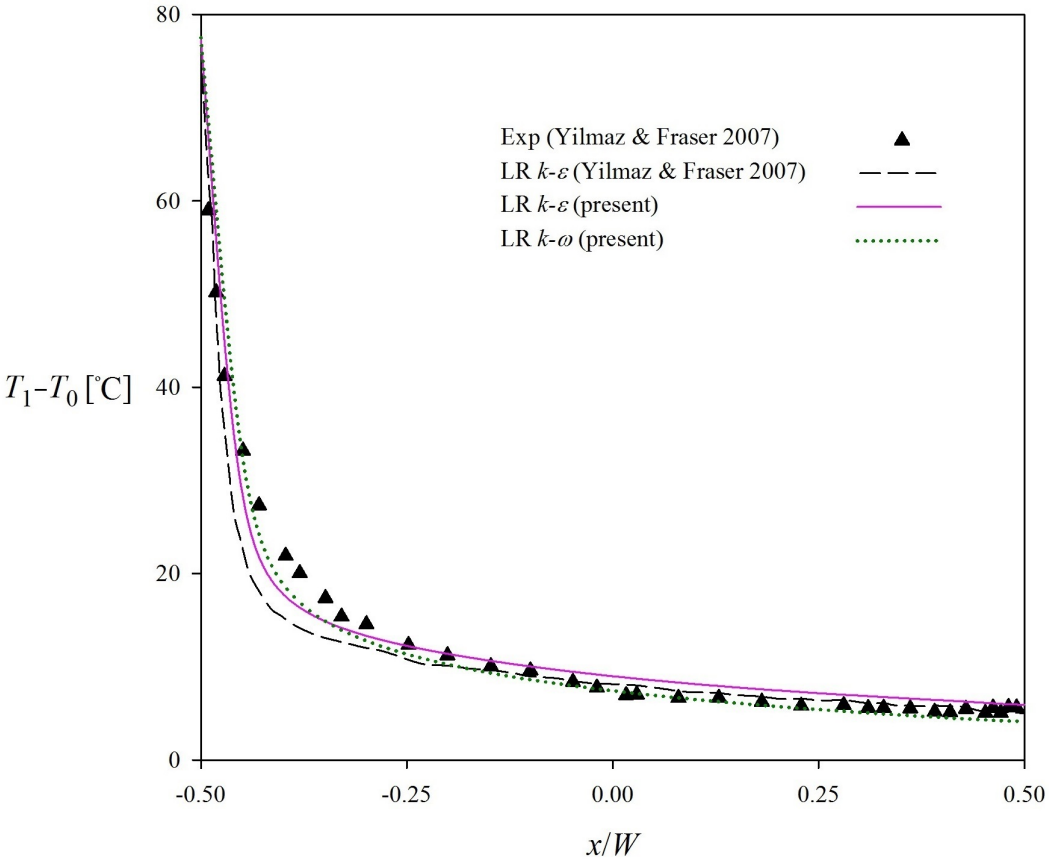

Figure 9.2: Temperature distribution near the channel outlet ($y/H = 0.98$)
($H = 30W = 3\,\text{m}$, $T_1 = 100°\text{C}$, $q_2 = 0$, $T_0 = 22°\text{C}$, $p_0 = 1\,\text{atm}$)

9.2 Numerical dQdT

If the Boussinesq approximation for density were invoked, the variation of density in the energy equation would be neglected and hence the $C_{ik} = \text{const}$ constraint would be satisfied by retaining only the velocity field of the baseline solution. As mentioned in Chapter 8, this can be readily done in Fluent. In the present solutions, however, the variation of density with temperature is considered in all terms of the energy equation (Equation 9.5). Therefore, to enforce the $C_{ik} = \text{const}$ constraint, the density field of the baseline solution too must be retained when obtaining subsequent solutions to the energy equation with perturbed boundary conditions.

9.2.1 Fixing the Fluid Properties

Retaining the fluid properties in Fluent is not straightforward; none of the default features of the solver provide control over the updating of the fluid properties in the course of a solution. In principle, the fluid properties can be retained by extracting the property fields of the baseline solution, e.g. in the form of an ASCII file, and then importing this data when obtaining subsequent solutions to the energy equation, e.g. through a user-defined function. Nevertheless, this approach is complicated and computationally expensive. Instead, a custom finite-difference solver was used to obtain baseline and subsequent solutions to the energy equation using the velocity and property fields of the elliptic baseline solutions obtained in Fluent.

To further simplify the procedure, the energy equation was parabolized by dropping the axial diffusion terms. This is a close approximation since the problem involves large Peclet numbers ($\text{Pe} \approx 1500$). Hence a simple, forward-marching solution scheme could be utilized to solve the energy equation. The MATLAB code developed for this purpose can be found in Appendix G. The error introduced by parabolizing the energy equation was up to 3% in the total heat transfer rates. Less than 1% difference in results was observed

when dQdT was carried out based on solutions to elliptic and parabolic energy equations using the Boussinesq approximation for density.

9.2.2 The dQdT Procedure

Numerical dQdT was implemented following the steps below:

i) A baseline solution to the full set of governing equations was obtained in Fluent.

ii) The velocity, density and turbulent viscosity[1] fields were interpolated at the grid nodes (control volume corners) and exported into the finite-difference solver (FDS).

iii) A baseline solution to the parabolic energy equation was obtained using FDS.

iv) The baseline heat transfer rates, $\{Q_i\}$, were calculated.

v) The boundary temperature T_j was perturbed by a finite amount, δT_j.

vi) The FDS solution to the parabolic energy equation was updated using the baseline velocity and property fields, obtained in step (ii).

vii) The new heat transfer rates, $\{Q_i^*\}$, and the respective changes were calculated; $\delta Q_i = Q_i^* - Q_i$.

viii) The functionality coefficients corresponding to T_j were calculated; $C_{ij} = -\delta Q_i / \delta T_j$.

ix) Steps v-viii were repeated for $j = 0, 1, 2$.

The functionality coefficients thus obtained apply to the original boundary temperatures, $\{T_i\}$.

To verify the enforcement of the $C_{ik} = \text{const}$ constraint, the results obtained for a sample laminar case (Ra = 400, $r_T = 0.5$, Pr = 0.7) following the procedure above were

[1] Turbulent viscosity is needed for calculating the effective thermal conductivity when solving the energy equation. See Equation 9.5.

compared to dQdT results based on a parabolic solution to the energy equation while invoking the Boussinesq approximation in the baseline solution, i.e. with no need to fix the density field. Less than 1% difference between the results was observed, indicating that the $C_{ik} = \text{const}$ constraint was properly implemented.

9.3 Average Paired Nusselt Numbers

The functionality coefficients were converted to dimensionless form using the average paired Nusselt number introduced in Chapter 8:

$$\overline{\mathrm{Nu}}_{ij} = \left(\frac{C_{ij}}{\lambda}\right)\frac{W}{H} \tag{9.8}$$

The modified channel Rayleigh number, defined in Equation 9.9, and the temperature ratio defined in Equation 9.10 were used to characterize respectively the flow and the ordering of boundary temperatures.

$$\mathrm{Ra} = \frac{g\beta(T_{\mathrm{wm}} - T_0)W^3}{\nu^2}\left(\frac{W}{H}\right)\mathrm{Pr} \tag{9.9}$$

$$r_T = \frac{T_2 - T_0}{T_1 - T_0} \tag{9.10}$$

Obtaining baseline solutions to turbulent free convection is computationally very expensive. Therefore, sample results were obtained in a narrow range of Ra: $10^4 \leq \mathrm{Ra} \leq 2 \times 10^5$. In the numerical solutions. Ra was modified by changing the gravitational acceleration, g.

Similar to the laminar case, discussed in Chapter 8, the asymmetry in the temperature field leads to asymmetry in the velocity and density fields, and hence: $\overline{\mathrm{Nu}}_{ij} \neq \overline{\mathrm{Nu}}_{ji}$. According to the results presented in Table 9.2, for a given value of Ra, the difference $\overline{\mathrm{Nu}}_{ij} - \overline{\mathrm{Nu}}_{ji}$ is a constant;

$$\overline{\mathrm{Nu}}_{12} - \overline{\mathrm{Nu}}_{21} = \overline{\mathrm{Nu}}_{01} - \overline{\mathrm{Nu}}_{10} = \overline{\mathrm{Nu}}_{20} - \overline{\mathrm{Nu}}_{02}$$

This is in agreement with the results reported in Chapters 7 and 8, and the theorem presented in Appendix D.

Note however that the difference between $\overline{\mathrm{Nu}}_{ij}$ and $\overline{\mathrm{Nu}}_{ji}$ is very small. Consequently, it is a close approximation to assume $\overline{\mathrm{Nu}}_{ij} = \overline{\mathrm{Nu}}_{ji}$. Therefore, the resistor-network model is applicable and the problem can be represented by a delta network.

dQdT results for $r_T = 0.5$ and $\mathrm{Pr} = 0.7$ are plotted in Figure 9.3. Since $\overline{\mathrm{Nu}}_{ij} \approx \overline{\mathrm{Nu}}_{ji}$, only three of the paired Nusselt numbers were plotted. Note that the channel geometry affects the complex turbulence structures of the flow. For instance, the size of turbulent eddies is restricted by the length scale of the channel. Hence, a very small channel width may prohibit the formation and propagation of eddies, suppressing turbulent heat transfer. As a result, heat transfer in the turbulent regime depends on the channel geometry (aspect ratio). The results presented in Figure 9.3 are for a sample aspect ratio of $H/W = 30$.

The wall-fluid Nusselt numbers, $\overline{\mathrm{Nu}}_{10}$ and $\overline{\mathrm{Nu}}_{20}$, increase as Ra increases. Also plotted in Figure 9.3 are the predictions of the correlations developed in Chapter 8 (Equations 8.23-8.24). Although these correlations were extrapolated beyond their range of applicability, i.e. the laminar regime, they are helpful in demonstrating the enhancement of heat transfer due to turbulence; both $\overline{\mathrm{Nu}}_{10}$ and $\overline{\mathrm{Nu}}_{20}$ are larger than the laminar predictions. Note that similar to the laminar case, the hotter wall has a larger wall-fluid Nusselt number; $\overline{\mathrm{Nu}}_{10} > \overline{\mathrm{Nu}}_{20}$. Nevertheless, the difference between $\overline{\mathrm{Nu}}_{10}$ and $\overline{\mathrm{Nu}}_{20}$ decreases as Ra increases.

Table 9.2: Sample dQdT results for turbulent free convection in a vertical channel with isothermal walls ($H/W = 30$, $r_T = 0.5$, $p_0 = 1\,\text{atm}$)

Ra	$\overline{\text{Nu}}_{12}$	$\overline{\text{Nu}}_{21}$	$\overline{\text{Nu}}_{10}$	$\overline{\text{Nu}}_{01}$	$\overline{\text{Nu}}_{20}$	$\overline{\text{Nu}}_{02}$
10^4	0.0319	0.0122	6.7993	6.8190	5.9139	5.8944
2×10^4	0.0418	0.0145	8.3105	8.3379	7.3218	7.2945
5×10^4	0.0632	0.0215	11.0155	11.0570	9.9259	9.8841
10^5	0.0838	0.0296	13.7125	13.7666	12.7233	12.6690
2×10^5	0.1074	0.0398	17.3020	17.3696	17.0410	16.9735

Recall that in the laminar regime, the difference between the wall-fluid Nusselt numbers increases with Ra (see Figure 8.5).

In Figure 9.3, the wall-wall Nusselt number, $\overline{\text{Nu}}_{12}$, is plotted versus the scale shown on the right. Similar to the laminar case, $\overline{\text{Nu}}_{12}$ is much smaller than $\overline{\text{Nu}}_{10}$ and $\overline{\text{Nu}}_{20}$. However, contrary to the laminar case, $\overline{\text{Nu}}_{12}$ increases as Ra increases. In other words, the thermal interaction between the walls is enhanced as the flow rate increases. The universal wall-wall correlation developed for laminar flow gives: $\overline{\text{Nu}}_{12,\text{lam}} = 0$ for $\text{Ra} \geq 10^4$. This was attributed to the thinning of the thermal boundary layers with the increase of the flow. The reverse trend of $\overline{\text{Nu}}_{12}$ in the turbulent regime can be attributed to the increase in the effective thermal conductivity of the fluid due to turbulent mixing. Similar results were observed in Chapter 6 for turbulent flow in an annulus.

9.4 Summary

dQdT was applied to calculate the functionality coefficients of turbulent free convection of air in a vertical channel with isothermal walls. The implementation of the $C_{ik} = \text{const}$ constraint in the case of variable fluid properties was demonstrated. Since Fluent does not have a built-in feature which can be used to retain the property fields of the baseline solution, a separate finite-difference solver was developed for solving the energy equation using the baseline velocity and property fields of the baseline finite-volume solution

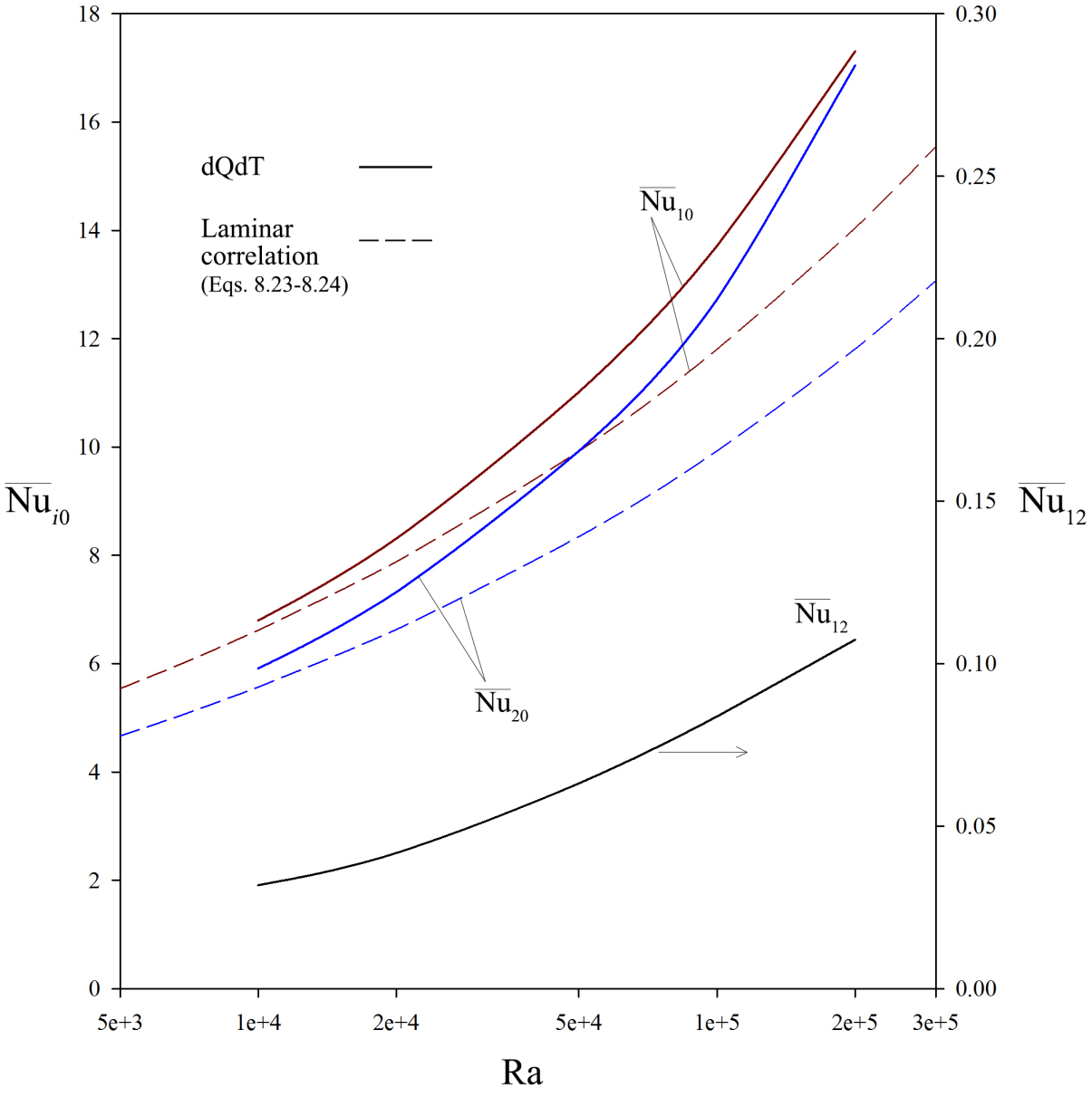

Figure 9.3: Average paired Nusselt numbers of turbulent free convection in a vertical channel with isothermal walls ($H/W = 30$, $r_T = 0.5$, $\mathrm{Pr} = 0.7$)

obtained in Fluent. The proper implementation of the C_{ik} = const constraint in this dual-scheme solution was verified. The dQdT results thus obtained show that:

i) There is reciprocity between the functionality coefficients; $\overline{\mathrm{Nu}}_{ij} \approx \overline{\mathrm{Nu}}_{ji}$. Therefore, a delta resistor network can be used to model the three-temperature problem.

ii) The paired Nusselt numbers are all enhanced by transition to turbulence.

iii) Due to turbulent mixing, the wall-wall fluid Nusselt numbers of turbulent flow increase as the flow rate increases.

Chapter 10

Free Convection at the Indoor Side of Complex Fenestration Systems

In Chapter 1, the ASHWAT models for heat transfer in glazing systems with attachments were introduced. The combination of glazing layers and attachments, i.e. shades and insect screens, is known as a Complex Fenestration System (CFS). The thermal-resistor network used in ASHWAT for modeling convection at the indoor side of a CFS was also introduced in Chapter 1. See Figure 10.1. Calculating the paired heat transfer coefficients that characterize the delta network of Figure 10.1 was the original motivation for the body of work presented in this thesis.

In Chapters 2-9, the class of multi-temperature convection problems was investigated using a general formulation based on an extension of the Newton law of cooling. The dQdT technique was developed for calculating the multiple functionality coefficients that characterize heat transfer in a multi-temperature setting. Advantages of the extended Newton formulation and validity of the dQdT technique were demonstrated and discussed for several classical problems.

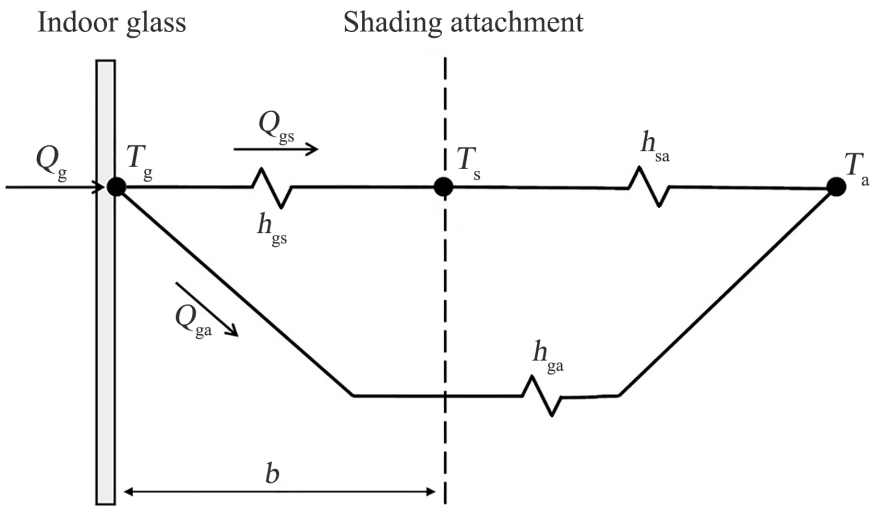

Figure 10.1: The resistor network of convection at the indoor side of a complex fenestration system (g: glazing, s: shading attachment, a: indoor air)

In this chapter, the dQdT technique is applied to obtain the functionality coefficients of the multi-temperature problem of convection at the indoor side of a CFS. In light of the developments reported in the preceding chapters, the present study was conducted mainly to answer two questions:

i) Is the resistor-network model applicable to the three-temperature problem of convection at the indoor side of complex fenestration systems? In other words, is there reciprocity between the functionality coefficients of the problem?

ii) How good are the approximate relations currently used in ASHWAT for the paired heat transfer coefficients of the delta network of Figure 10.1?

10.1 Current ASHWAT Estimates

Currently, estimates of the three convection coefficients that characterize the delta network of Figure 10.1 are used in ASHWAT. Based on known limits and experience, correlations

have been developed that give the indoor convection coefficients as functions of the glass-shade spacing, b (Wright et al. 2009, Barnaby et al. 2009).

The glass-shade convection coefficient, h_{gs}, is estimated assuming laminar flow in the channel formed between the glass and attachment. Furthermore, assuming a relatively short thermal development length, heat transfer is assumed to be dominated by conduction across the vertical flow. Equation 10.1 is therefore taken as a reasonable estimate for h_{gs} (Wright et al. 2009).

$$h_{\mathrm{gs}} = \frac{k}{b} \tag{10.1}$$

Equation 10.1 is plotted in Figure 10.2. As can be seen in this figure, when the shading attachment is spaced well away from the window, h_{gs} will be small and its influence unimportant.

The glass-air and shade-air convection coefficients, h_{ga} and h_{sa}, are evaluated based on a user-specified "run-off" value, h_{c}. This approach allows for the effects of different flow conditions, e.g. forced or free convection, to be taken into account by adjusting h_{c}. To incorporate the effect of b, two limiting cases were considered. When $b \to \infty$, the convective heat transfer at one layer, glass or shade, will not be influenced by the presence of the other layer and mimics convection at an isolated flat plate. When $b \to 0$, on the other hand, the thermal communication between the glass and the indoor air is blocked, while one side of the attachment layer remains exposed, hence thermally communicating with air. An exponential function was introduced to represent this behavior and make a smooth transition between the limits. This transition was scaled by assuming that the boundary layers at the glass and shading layer surfaces will not interfere for $b > 0.1\,\mathrm{m}$ (Wright et al. 2009). See Equations 10.2 and 10.3.

$$h_{\mathrm{ga}} = h_{\mathrm{c}}\left\{1 - \exp\left[-4.6\left(\frac{b}{0.1}\right)\right]\right\} \tag{10.2}$$

$$\begin{aligned} h_{\mathrm{sa}} &= h_{\mathrm{ga}} + h_{\mathrm{c}} \\ &= h_{\mathrm{c}}\left\{2 - \exp\left[-4.6\left(\frac{b}{0.1}\right)\right]\right\} \end{aligned} \tag{10.3}$$

Note that h_{sa} is based on $A_{\mathrm{g}} = A_{\mathrm{s}}/2$. Further note that the attachment layer is exposed to air on both sides. In developing Equation 10.3, it has been assumed that the right side of the shading attachment (the side facing the indoors) has a heat transfer coefficient of h_{c}, unaffected by the glazing layer.

In Figure 10.2, Equations 10.2 and 10.3 are plotted using the run-off value recommended in the ASHWAT documentation (Wright et al. 2009): $h_{\mathrm{c}} = 3.5\,\mathrm{W/(m^2K)}$ — "a typical value for natural convection".

In the case of venetian blinds (VB), the glass-shade spacing is defined as distance from the glass to a point on the slat that is 70% of the way from the slat center to the slat tip (Wright et al. 2008):

$$b_{\mathrm{VB}} = L - 0.7\left(\frac{w}{2}\right)\cos\phi$$

Moreover, an adjustment has been introduced to take into account the enhanced buoyancy-driven flow through the slats (Wright et al. 2009) and allow for up to 20% increase in h_{sa}. See Equation 10.4 where ϕ denotes the slat angle, measured from horizontal.

$$h_{\mathrm{sa,VB}} = h_{\mathrm{c}}\left\{2 - \exp\left[-4.6\left(\frac{b_{\mathrm{VB}}}{0.1}\right)\right]\right\}\left[1 + 0.2\left|\sin(2\phi)\right|\right] \tag{10.4}$$

Although no difficulty has been reported regarding the ASHWAT three-resistor network and the approximate correlations above, Equations 10.1-10.4 do not have the

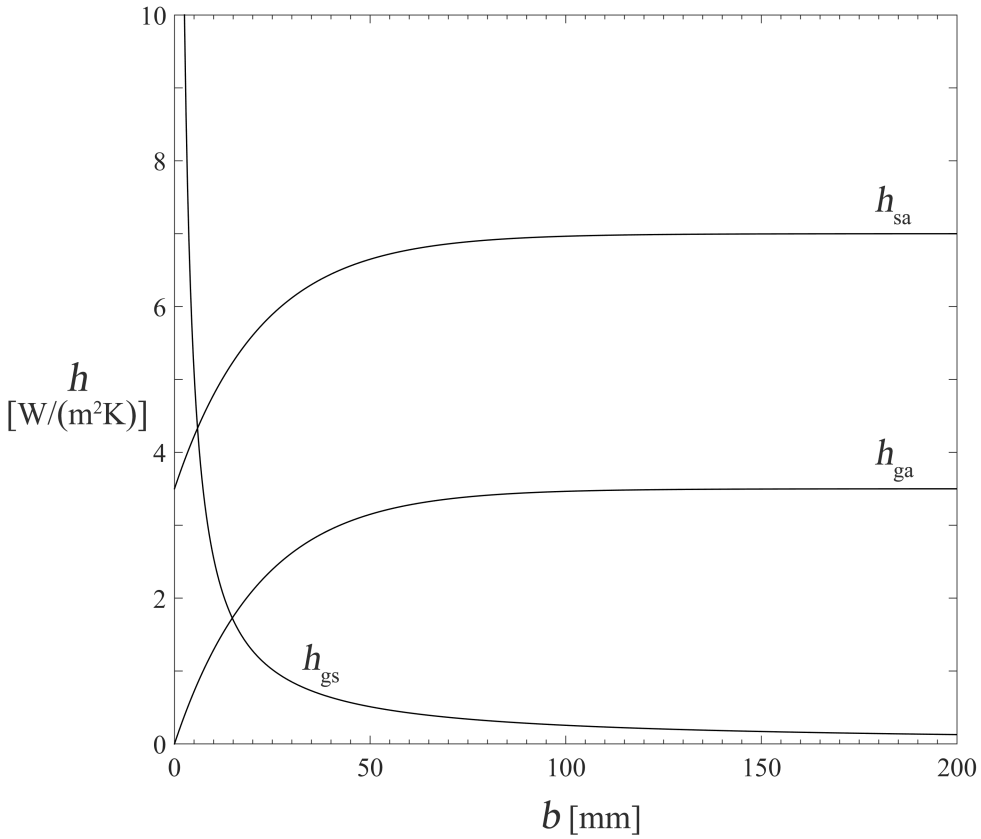

Figure 10.2: ASHWAT estimates for the indoor-side convection coefficients of a complex fenestration system (Wright et al. 2009) $\left[h_{\mathrm{c}} = 3.5\,\mathrm{W/(m^2K)}\right]$

same level of fundamental grounding as the other components of ASHWAT. At the time of the development of ASHWAT, virtually no information was available on the resistor-network modeling of multi-temperature convection problems and the evaluation of the corresponding paired heat transfer coefficients. The dQdT technique is now a powerful tool for the accurate calculation of $\{h_{ij}\}$.

10.2 Extended Newton Formulation

Convection at the indoor side of a CFS comprises three isothermal boundaries: the glazing surface, the attachment and the ambient air. Accordingly, the problem is characterized by

six functionality coefficients. These functionality coefficients are converted to the paired heat transfer coefficients discussed above through division by the reference heat-transfer surface area.

As discussed in Chapter 3, the validity of the resistor-network model is contingent on reciprocity of the functionality coefficients; $C_{ij} = C_{ji}$. As shown in Chapters 7-9, reciprocity exists in multi-temperature configurations where the isothermal surfaces are positioned symmetrically in the flow field. The existence of reciprocity, and hence validity of the resistor-network model, can be explored using dQdT.

10.3 Baseline Solutions

10.3.1 Solution Method

The commercial solver ANSYS Fluent (ANSYS 2011a,b) was used to obtain second-order finite volume baseline solutions. The PRESTO! algorithm for discretizing pressure and the SIMPLE scheme for handling the pressure-velocity coupling were used. The Boussinesq approximation for density was invoked, while other thermophysical properties of air were assumed to be constant, evaluated at T_{a} ($\mathrm{Pr} = 0.7$). The Shear Stress Transformation (SST) k-ω model with low-Reynolds-number correction was used for resolving turbulence.

10.3.2 Computational Domain, Boundary Conditions & Discretization

A schematic of the computational domain is shown in Figure 10.3. The glazing (1) and shading layer (2) were modeled as impermeable, no-slip, isothermal solid boundaries. The venetian blind slats were assumed to be flat and infinitesimally thin. The window glazing was assumed to be flush-mounted, i.e. the window "setback" was ignored. Two adiabatic

walls (3-4) were added at the top and bottom of the window, each the same height as the window. The blinds (2) were "hanging" in the domain, i.e. not attached to the domain boundaries.

Pressure, temperature, and turbulent parameters (kinetic energy, k, and specific dissipation rate, ω) were specified at the far-field boundaries (5-7). The solver's default values were used for the far-field turbulence boundary conditions: $k = 1\ \mathrm{m^2/s^2}$ and $\omega = 1\ \mathrm{s^{-1}}$. Numerical tests were performed to ensure the far-field boundaries (5-7) are placed sufficiently far to have negligible effect on the solutions.

Depending on the CFS aspect ratio, the domain was discretized into a non-uniform unstructured mesh of approximately 345,000-590,000 control volumes. The mesh was constructed with a higher density in the vicinity of the glazing and the shading layer. The difference between the number of control volumes used for different configurations corresponds to the difference in b as well as the attachment type — roller or venetian blind.

The grid dependence of the solutions was assessed using the Richardson-extrapolation technique proposed by Celik et al. (2008). Using three grids with approximately 140,000, 355,000 and 590,000 control volumes for a CFS entailing a venetian blind with $H/L = 17$, and based on the rate of total heat transfer to the air (Q_a), a convergence index of 5% was calculated for the fine grid.

10.3.3 Validation

To validate the baseline solutions, the present CFD solutions were compared to an experimental study from the literature. Machin et al. (1998) used interferometry to measure the local heat transfer coefficient, h_g, at an isothermal flat plate (representing the glazing layer) with an adjacent venetian blind. The plate had a height of $H = 380\,\mathrm{mm}$. The blind consisted of 17 slats of width $w = 25.4\,\mathrm{mm}$ at an angle of $\phi = 45°$, and was mounted at a distance of $L = 14.5\,\mathrm{mm}$ from the plate. The plate was maintained at

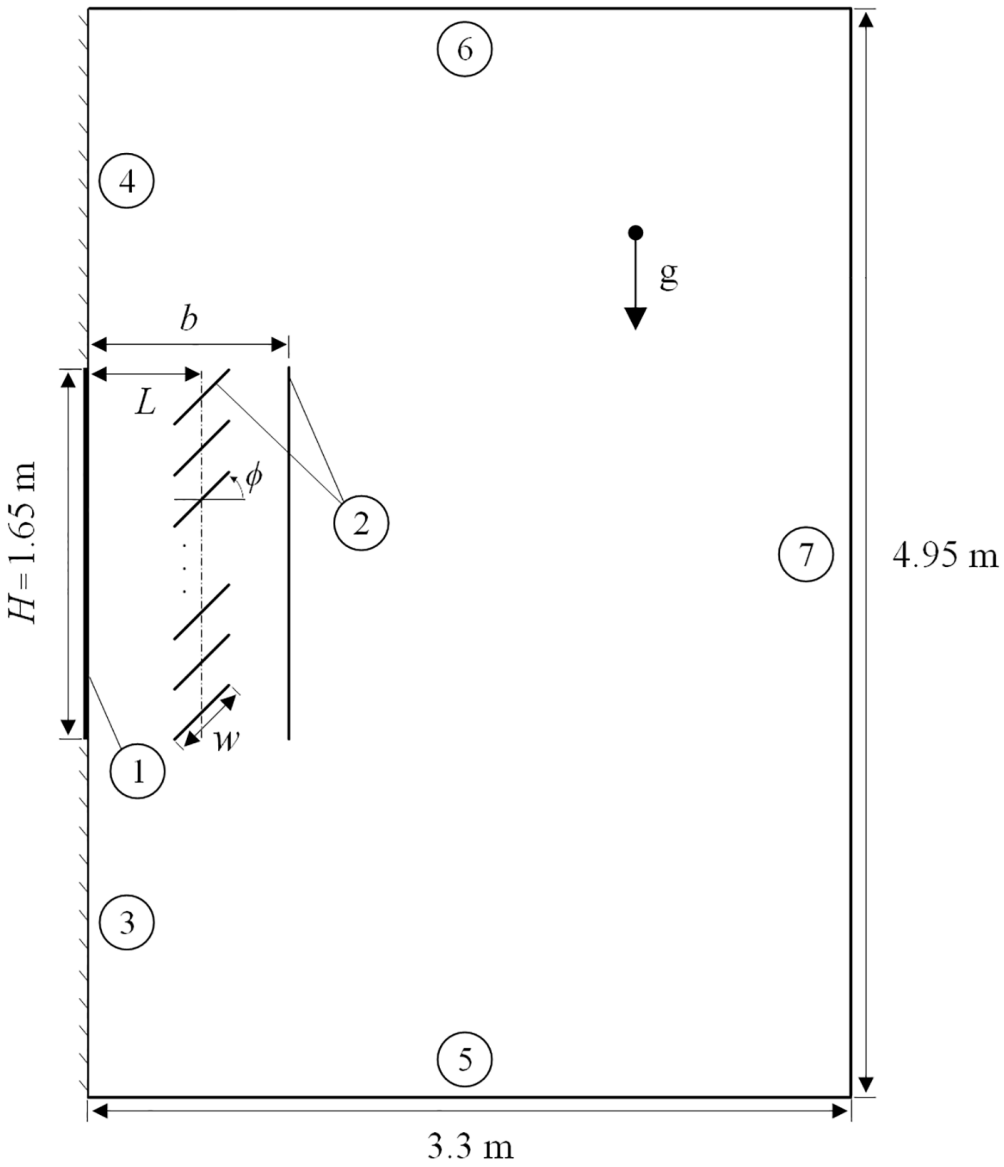

Figure 10.3: Computational domain for a flush-mounted glazing (1) with an indoor-mounted roller OR venetian blind (2)

$T_g = 41°C$, about 20°C above the ambient temperature. The thermal condition at the blind slats was uncontrolled in the experiments by Machin et al. (1998). Consequently, in the CFD solutions, the slats were set as conjugate ("coupled") walls with zero thickness. Thermal radiation was ignored in the CFD solutions.

In Figure 10.4, the FVM solution is compared to the measurements of Machin et al. (1998) and a laminar FEM solution from the literature (Ye et al. 1999). Due to experimental restrictions, Machin et al. (1998) have reported h_g only up to $y/H \approx 0.71$. Therefore, in Figure 10.4 the results were plotted for $0 \leq y/H \leq 0.8$.

The present CFD solution captures the overall trend of h_g along the plate. Nevertheless, the CFD solution under-predicts h_g, especially away from the leading edge ($y/H > 0.5$). This is likely due to the neglect of radiation in the CFD solutions. The radiant blind performs as a "heat sink" in the flow field, lowering the temperature of the air flowing along the plate and hence increasing h_g. In the experiments by Machin et al. (1998), the plate was polished to achieve a low emissivity and reduce radiation to the blind. The blind slats, on the other hand, were painted and hence had a significantly higher emissivity. As a result, the blind slats radiated heat to the essentially "black", cold environment. Thus, a no-radiation CFD solution would over-predict the equilibrium temperature of the blind slats, hence under-predicting h_g.

Compared to the laminar solution by Ye et al. (1999), the present turbulent solution is in better agreement with the measurements, especially for $y/H > 0.5$. Note that Ye et al. (1999) too have ignored radiation. The overall agreement of the current CFD predictions with the data from the literature indicates validity of the baseline solutions.

10.4 Numerical dQdT

Numerical dQdT was implemented following the procedure described in Section 8.4.

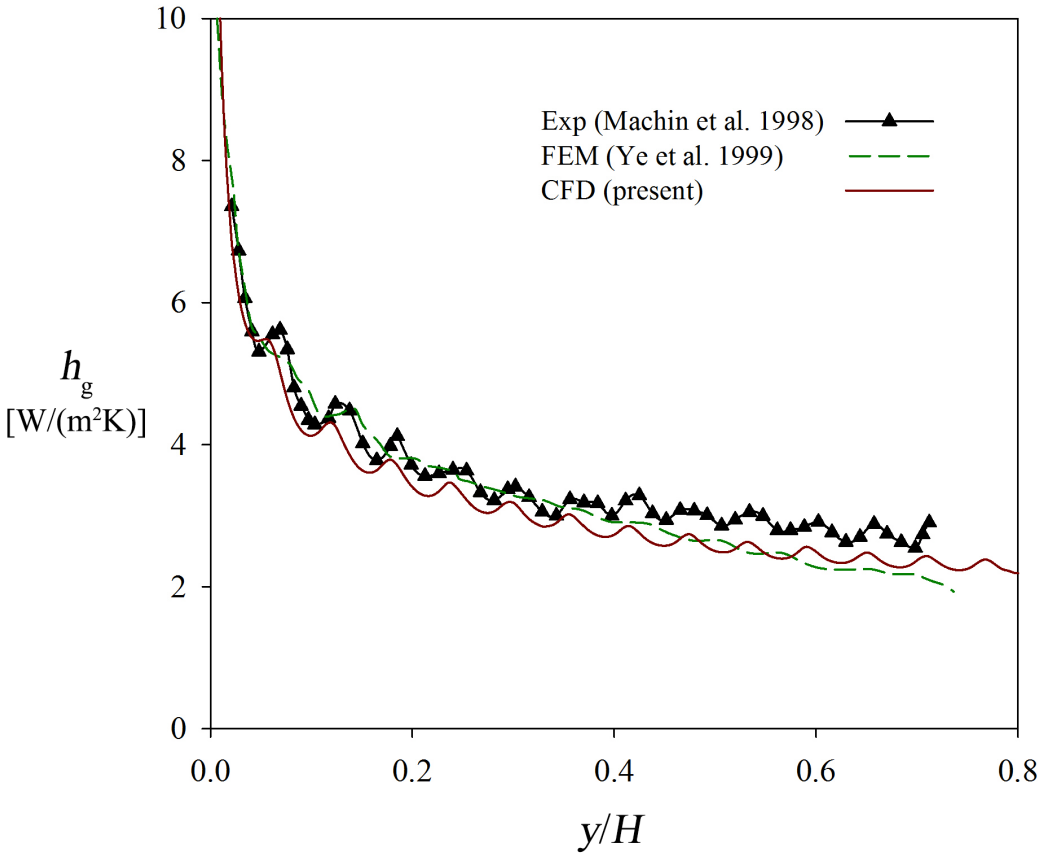

Figure 10.4: Heat transfer coefficient of a glazing with an adjacent venetian blind ($T_g - T_a = 20°C$, $H = 380\,mm$, $L = 14.5\,mm$, $\phi = 45°$)

10.5 dQdT Results

Two configurations were studied: a flush-mounted glazing with 1) a roller blind and 2) a venetian (louver) blind. A window height of $H = 1.65\,m$ and different glass-shade distances in the range 25-150 mm were considered. In the case of venetian blinds, the distance, L, was measured from the center of the slats, as shown in Figure 10.3. The venetian blind consisted of 75 uniformly spaced flat slats of width $w = 2.54\,mm$, at an angle of $\phi = 45°$.

Because the effects of shading attachments are usually of interest in calculating cooling loads, results were generated for boundary temperatures of a typical double-glazing window with a low-ϵ coating, under the design summer condition. Using the window simulation

software VISION5 (Wright & Sullivan 1987, Wright 2011), the following temperatures were obtained: $T_g = 35°C$, $T_s = 28°C$ and $T_a = 24°C$.[1] In this case, the average Rayleigh number based on $(T_g + T_s)/2 - T_a$ and H is: $Ra = 3.9 \times 10^9$.

10.5.1 CFS with a Roller Blind

The dQdT results for the complex fenestration system with a roller blind (RB) are shown in Table 10.1. As can be seen in this table, $C_{ij} \approx C_{ji}$ for the RB configuration. Recall that in Chapters 8 and 9 too, small differences between C_{ij} and C_{ji} were observed in the case of free convection in a vertical channel. Since $C_{ij} \approx C_{ji}$, the resistor-network model is valid for the three-temperature problem.

Note that as observed in Chapters 8 and 9 and proven in Appendix D, in a three-temperature setting, the difference between each pair, $C_{ij} - C_{ji}$, is constant. So the relative difference can be quite large when C_{ij} and C_{ji} are small. For instance, see the entries in Table 10.1 for C_{gs} and C_{sg} at $b = 150\,mm$.

Further note that when performing the dQdT operation, both sides of the blind were treated as a single isothermal surface. Therefore: $A_s = 2A_g$. The substantial difference between C_{ga} and C_{sa}, and C_{ag} and C_{as} is therefore partly due to the difference between the surface areas. However, since heat transfer at the right side of the blind is almost not affected at all by the presence of the glazing[2], the difference between A_g and A_s does not lead to as large a difference between C_{gs} and C_{sg}.

In Figure 10.5, the dQdT results are compared to the ASHWAT estimates (Equations 10.1-10.3). Instead of using the default value of $h_c = 3.5\,W/(m^2K)$ (Wright et al. 2009), h_c was calculated using the correlation shown in Equation 10.5 (Churchill & Chu 1975) for

[1] Note that these temperatures depend on the glass-shade spacing. Representative values are used here.

[2] This can be confirmed by treating the two sides of the roller blind (denoted by L and R) as separate isothermal surfaces when applying dQdT. For example, at $b = 75\,mm$: $C_{sLg} = 0.2418$ and $C_{sRg} = 0.0184$. Note that: $C_{sLg} > C_{sRg}$ and $C_{sLg} + C_{sRg} = C_{sg}$

Table 10.1: dQdT results for the CFS with a roller blind
($T_g = 35°C$, $T_s = 28°C$, $T_a = 24°C$, $H = 1.65\,m$)

b [mm]	C_{gs}	C_{sg}	C_{ga}	C_{ag}	C_{sa}	C_{as}
25	1.3642	1.2902	3.6336	3.7077	13.3296	13.2569
50	0.5357	0.4244	4.7560	4.8673	14.8091	14.6978
75	0.3892	0.2602	5.3012	5.4298	15.1606	15.0312
97	0.3101	0.1901	5.3094	5.4294	14.9718	15.1236
127	0.2672	0.1502	5.5295	5.6475	15.4907	15.3779
150	0.2533	0.1395	5.8463	5.9605	15.5504	15.4393

free convection at an isothermal flat plate. At $\mathrm{Ra} = 3.9 \times 10^9$ and $\mathrm{Pr} = 0.7$, this correlation yields: $h_c = 2.81\ \mathrm{W/(m^2K)}$.

$$\mathrm{Nu}_c = \frac{h_c H}{k} = \left\{ 0.825 + \frac{0.387\,\mathrm{Ra}^{1/6}}{\left[1 + (0.492/\mathrm{Pr})^{9/16}\right]^{8/27}} \right\}^2 \tag{10.5}$$

The functionality coefficients were converted to paired heat transfer coefficients using Equation 10.6.

$$\begin{cases} h_{ga} = \dfrac{C_{ga}}{A_g} \\ h_{sa} = \dfrac{C_{sa}}{A_s} \\ h_{gs} = \dfrac{C_{gs}}{A_g} \end{cases} \tag{10.6}$$

As seen in Figure 10.5, there is good agreement between Equation 10.1 and the dQdT results for h_{gs}. Recall that Equation 10.1 was developed based on the assumption of laminar flow. In the turbulent regime, the thermal boundary layers are thinner and hence the thermal interaction between the glazing and the blind is weaker. Thus, Equation 10.1 overestimates h_{gs}, especially for small spacings, $b < 60\,\mathrm{mm}$. Recall that in Chapter 9, the

wall-wall functionality coefficients of free convection in a vertical channel were reported to be enhanced due to turbulent mixing. However, such enhancement is not observed in the results presented in Figure 10.5 because the flow is only mildly turbulent.

The discrepancy between the dQdT results and ASHWAT estimates for h_{ga} and h_{sa} is significant; compared to the dQdT results, Equation 10.2 underestimates h_{ga} and Equation 10.3 overestimates h_{sa}.

Note that in Equations 10.2 and 10.3, the same run-off value is assigned to h_{ga} and h_{sa}. Taking note of the asymptotic limits observed in Chapter 8 for the wall-fluid Nusselt numbers of free convection in a vertical channel, a correction was introduced in Equations 10.2 and 10.3: the run-off values were calculated separately, by evaluating Equation 10.5 with the respective Rayleigh numbers based on $T_{\mathrm{g}} - T_{\mathrm{a}}$ and $T_{\mathrm{s}} - T_{\mathrm{a}}$. Hence, replacing $\mathrm{Ra}_{\mathrm{ga}} = 5.8 \times 10^9$ and $\mathrm{Ra}_{\mathrm{sa}} = 1.9 \times 10^9$ in Equation 10.5;

$$\lim_{b \to \infty} h_{\mathrm{ga}} = 3.29 \text{ W/(m}^2\text{K)}$$

$$\lim_{b \to \infty} h_{\mathrm{sa}} = 2.33 \text{ W/(m}^2\text{K)}$$

Note that the default value of $h_{\mathrm{c}} = 3.5$ W/(m^{2}K) used in ASHWAT overestimates both limits, especially that of h_{sa}.

The ASHWAT estimates modified with the correction above are also plotted in Figure 10.5; excellent agreement with the dQdT results is obtained, with the exception of h_{ga} at $b = 150\,\mathrm{mm}$.

It is noteworthy that preliminary results (Foroushani et al. 2015a) obtained based on laminar baseline solutions to a shorter CFS with a roller blind had indicated notable discrepancy between the dQdT results and the ASHWAT estimates.

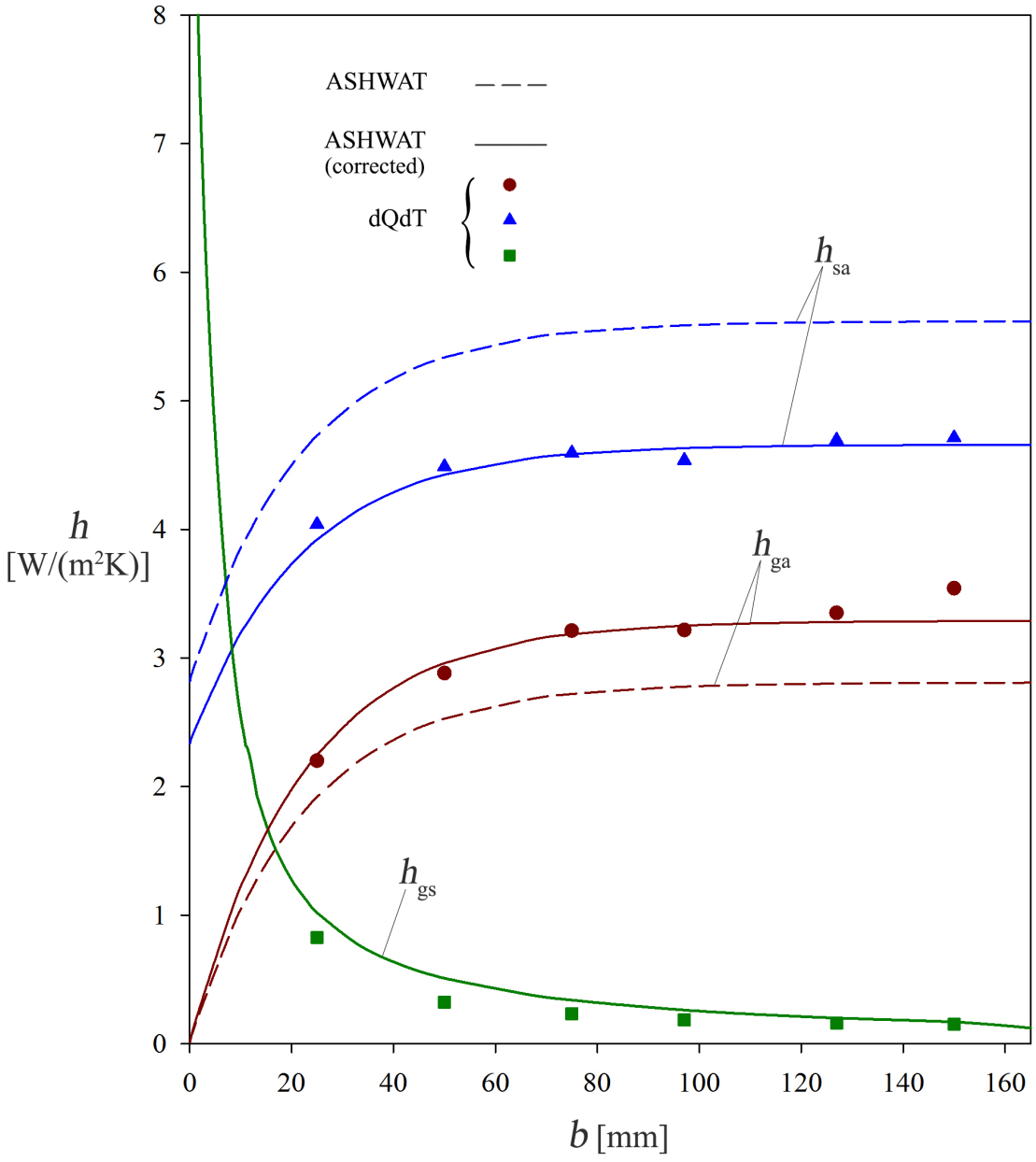

Figure 10.5: Paired heat transfer coefficients of the CFS with a roller blind ($T_g = 35°C$, $T_s = 28°C$, $T_a = 24°C$, $H = 1.65\,m$)

10.5.2 CFS with a Venetian Blind

The dQdT results for the complex fenestration system with a venetian blind (VB) are shown in Table 10.2. Again, the difference between the surface areas must be noted when interpreting these results; $A_{\mathrm{g}} = H$ and $A_{\mathrm{s}} = 2 \times 75\, w$. Most notably, the results presented in Table 10.2 show a lack of reciprocity between the functionality coefficients of the VB configuration: $C_{ij} \neq C_{ji}$. In the VB configuration, especially for $\phi < 90°$, there is significant asymmetry in the position of the glazing and the slats with respect to the buoyancy-driven flow. As discussed in Chapter 7, asymmetric position of the isothermal surfaces with respect to the flow field precludes reciprocity.

In Figure 10.6, sample streamlines for the VB configuration are shown; air is drawn towards the glazing from the bottom and right boundaries. Therefore, the blind slats are, in a sense, "upstream" of the the glazing. It is therefore expected that the upstream temperature T_{s} have a significant impact on the temperature field and hence the heat transfer rates. For instance, as can be seen in Table 10.2; $C_{\mathrm{gs}} > C_{\mathrm{sg}}$. This result is similar to the results presented in Chapter 7 for cylinders in tandem: $C_{21} > C_{12}$, with subscripts 1 and 2 denoting respectively the upstream and downstream cylinders.

In Figure 10.7, the dQdT results for the six paired heat transfer coefficients of the VB configuration are compared to the ASHWAT estimates with and without the correction introduced in Section 10.5.1 for h_{c}. The dQdT results for functionality coefficients were converted to paired heat transfer coefficients using Equation 10.7.

$$\begin{cases} h_{ga} = \dfrac{C_{ga}}{A_g}\,, \qquad h_{ag} = \dfrac{C_{ag}}{A_g} \\ h_{ga} = \dfrac{C_{sa}}{A_s}\,, \qquad h_{as} = \dfrac{C_{as}}{A_s} \\ h_{gs} = \dfrac{C_{gs}}{A_g}\,, \qquad h_{sg} = \dfrac{C_{sg}}{A_s} \end{cases} \tag{10.7}$$

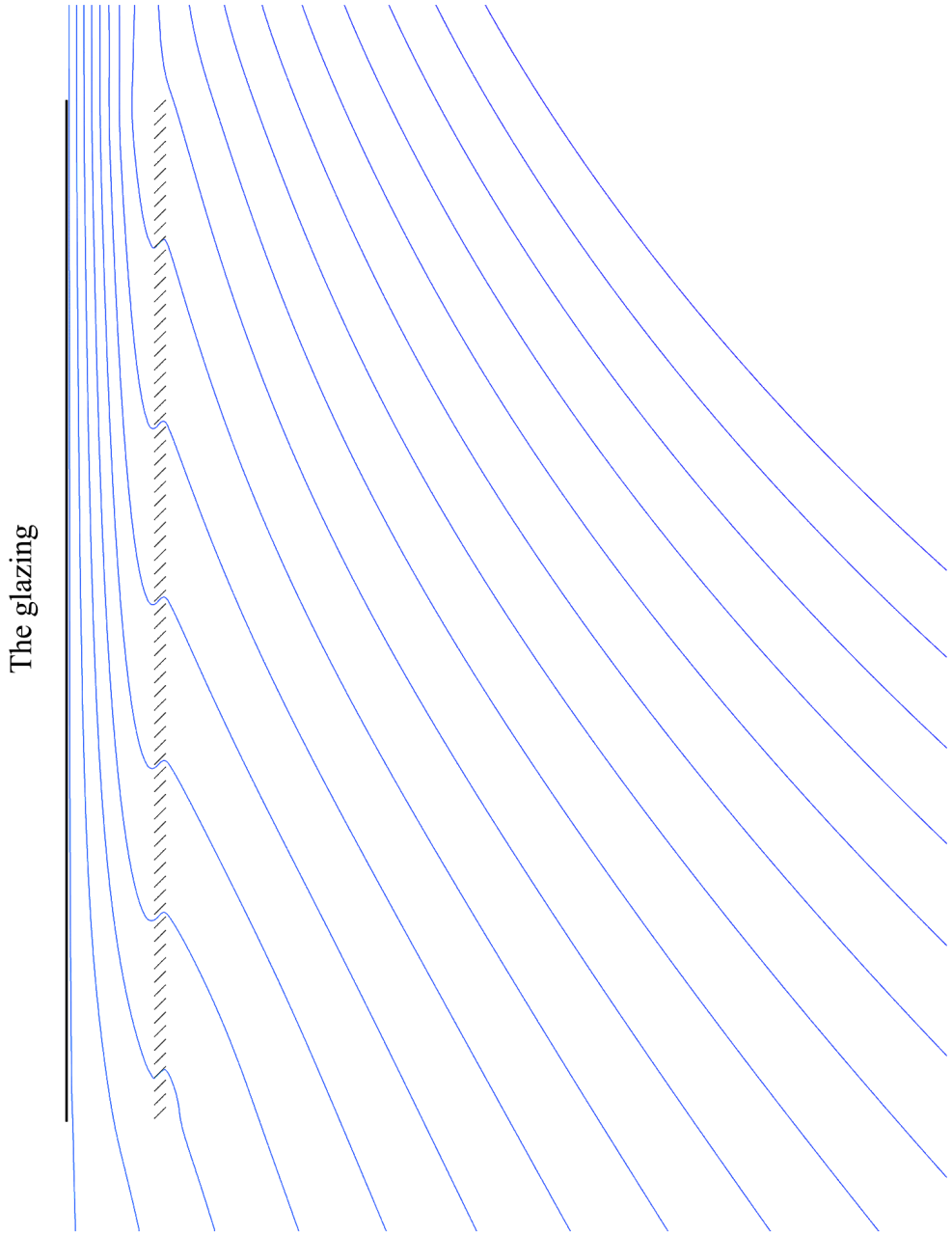

Figure 10.6: Streamlines of free convection in a CFS with a venetian blind ($T_{\mathrm{g}} = 35°\mathrm{C}$, $T_{\mathrm{s}} = 28°\mathrm{C}$, $T_{\mathrm{a}} = 24°\mathrm{C}$, $H = 11\,L = 1.65\,\mathrm{m}$, $\phi = 45°$)

Table 10.2: dQdT results for the CFS with a venetian blind
($T_g = 35°C$, $T_s = 28°C$, $T_a = 24°C$, $H = 1.65\,m$, $\phi = 45°$)

L [mm]	C_{gs}	C_{sg}	C_{ga}	C_{ag}	C_{sa}	C_{as}
25	2.5633	1.1212	1.2587	2.7632	12.7115	11.2768
50	2.0735	0.1752	2.7760	4.6735	18.8556	16.8978
75	1.3925	0.0428	3.3906	4.7405	21.5207	20.1728
97	1.0751	0.0345	3.7303	4.7711	23.1315	22.0925
127	0.8223	0.0262	4.0597	4.8558	24.0857	23.2902
150	0.7460	0.0295	4.3430	5.0595	26.3522	25.6354

The shade-air heat transfer coefficients, h_{sa} and h_{as}, are closer to the corrected ASHWAT curve for $b < 100\,mm$. The air-glass coefficient, h_{ga}, on the other hand, is closer to the ASHWAT curve [$h_c = 2.81\ W/(m^2K)$]. The glass-air coefficient is significantly lower than the predictions of both ASHWAT curves, except at $b = 150\,mm$ where there is good agreement between the dQdT results and the ASHWAT estimate.

Finally, while the overall trend of variation of the dQdT results for h_{gs} and h_{sg} is in agreement with the ASHWAT curve, the actual values are, respectively, notably higher and lower than the ASHWAT estimate.

Note that in the $b \to \infty$ limit, the three-temperature problem degenerates into two independent two-temperature problems: free convection from a vertical isothermal flat plate and free convection from a set of inclined isothermal flat plates. Therefore, the difference between h_{ij} and h_{ji} decreases as b increases;

$$\begin{cases} \lim\limits_{b\to\infty} h_{gs} = \lim\limits_{b\to\infty} h_{sg} = 0 \\ \lim\limits_{b\to\infty} h_{ga} = \lim\limits_{b\to\infty} h_{ag} \\ \lim\limits_{b\to\infty} h_{sa} = \lim\limits_{b\to\infty} h_{as} \end{cases}$$

The ASHWAT estimates (Equations 10.1-10.4) are based on a significantly simplified model, assuming laminar flow and one-dimensional heat transfer, leaving out many details

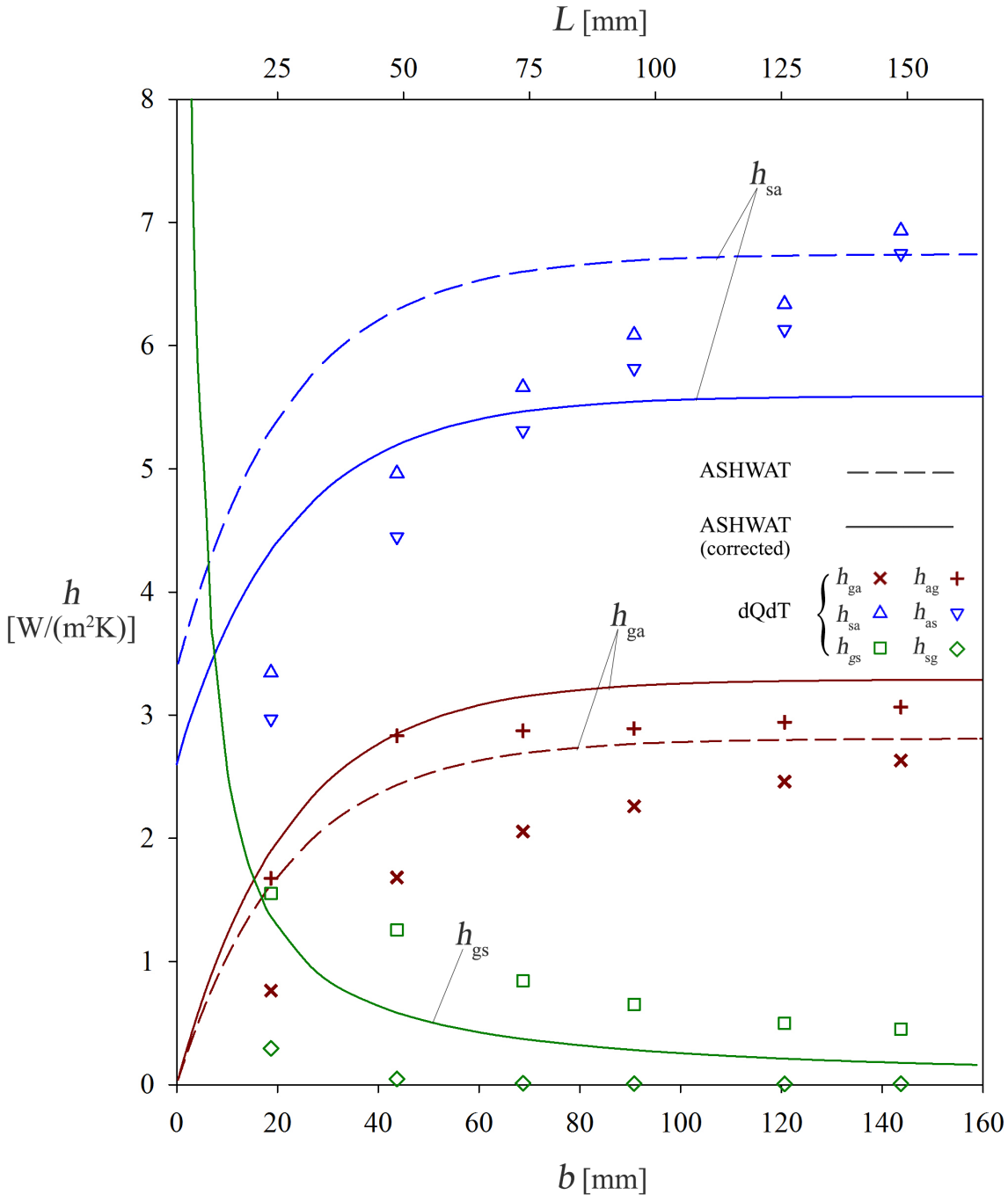

Figure 10.7: Paired heat transfer coefficients of the CFS with a venetian blind ($T_g = 35°C$, $T_s = 28°C$, $T_a = 24°C$, $H = 1.65\,m$, $\phi = 45°$)

of physics of the problem. For example, the current ASHWAT models predict that as $b \to 0$, heat transfer at the glazing is totally "blocked" by the shading layer and hence:

$$\lim_{b \to 0} h_{\text{ga}} = 0$$

This is obviously not the case for an open venetian blind ($\phi < 90°$).

Therefore, it is not surprising that the ASHWAT estimates have large errors for a complex problem such as turbulent free convection in the VB configuration.

However, it must be noted that the results presented here are limited to a single slat angle, a single window height and a simplified CFS geometry. Further investigation is needed before a conclusive assessment of the ASHWAT estimates; dQdT provides the means. Moreover, it is noteworthy that, as shown by Foroushani et al. (2016), the solar heat gain coefficient and the overall heat transfer coefficient of typical complex fenestration systems are almost insensitive to the indoor-side convection coefficients, $\{h_{ij}\}$. Therefore, the large differences observed between the ASHWAT estimates and the dQdT results can be expected to have a small effect on the overall performance of whole-building energy models.

Aside from the accuracy of the ASHWAT estimates, the observation that $C_{ij} \neq C_{ji}$ raises an important question regarding the validity of the resistor-network model. With $C_{ij} \neq C_{ji}$, this model must be used cautiously. In particular, a modeling decision must be made regarding the resistance (conductance) between T_i and T_j. The arithmetic mean of the two corresponding functionality coefficients, C_{ij} and C_{ji}, is one possibility:

$$C_{iji} = \frac{C_{ij} + C_{ji}}{2} \tag{10.8}$$

In Table 10.3, heat transfer calculations using the energy balance of a delta resistor-network with $\{C_{iji}\}$ as its conductances (Equation 10.9) and the current ASHWAT estimates are compared to the CFD results. The error in each case is calculated based on the CFD results.

$$Q_i = \sum_j C_{iji}(T_i - T_j) \tag{10.9}$$

The ASHWAT calculations were performed using Equations 10.10-10.12, with the paired heat transfer coefficients evaluated based on Equations 10.1, 10.2 and 10.4 with $h_c = 2.81$ (W/m^{2}K).

$$Q_g = h_{ga} A_g (T_g - T_a) + h_{gs} A_g (T_g - T_s) \tag{10.10}$$

$$Q_s = h_{sa} \frac{A_s}{2} (T_s - T_a) + h_{gs} \frac{A_s}{2} (T_s - T_g) \tag{10.11}$$

$$Q_a = h_{ga} A_g (T_g - T_a) + h_{sa} \frac{A_s}{2} (T_s - T_a) \tag{10.12}$$

Recall that h_{sa} given by Equation 10.4 corresponds to both sides of the blind. Hence, in Equations 10.11 and 10.12, A_s is divided by 2.

As can be seen in Table 10.3, Equation 10.9 gives a good estimate of $\{Q_i\}$, especially for $b \geq 75$ mm.[3] The current ASHWAT estimates, on the other hand, lead to significant errors, especially for Q_s. Therefore:

[3]The heat transfer rates calculated using the full set of functionality coefficients, $\{C_{ij}\}$, are identical to the CFD results.

Table 10.3: Heat transfer rates in the CFS with a venetian blind[+] ($T_g = 35°C$, $T_s = 28°C$, $T_a = 24°C$, $H = 1.65\,m$, $\phi = 45°$)

L [mm]	—	CFD	Res net	Error	ASHWAT	Error
25	Q_g	32.13	35.02	9.0%	45.17	40.6%
	Q_s	43.00	35.08	-18.4%	22.29	-48.2%
	Q_a	75.13	70.10	-6.7%	69.85	-7.0%
50	Q_g	45.05	48.84	8.4%	50.91	13.0%
	Q_s	74.28	63.64	-14.3%	40.06	-46.1%
	Q_a	119.32	112.48	-5.7%	91.99	-22.9%
75	Q_g	47.05	49.74	5.7%	53.12	12.9%
	Q_s	85.78	78.36	-8.6%	45.23	-47.3%
	Q_a	132.83	128.11	-3.6%	99.00	-25.5%
97	Q_g	48.56	50.64	4.3%	53.46	10.1%
	Q_s	92.28	86.56	-6.2%	47.12	-48.9%
	Q_a	140.84	137.21	-2.6%	101.07	-28.2%
127	Q_g	50.41	52.01	3.2%	53.24	5.5%
	Q_s	96.16	91.78	-4.6%	48.34	-49.6%
	Q_a	146.57	143.79	-1.9%	101.95	-30.4%
150	Q_g	53.00	54.43	2.7%	52.98	0.0%
	Q_s	105.21	101.26	-3.7%	48.85	-53.6%
	Q_a	158.20	155.69	-1.6%	102.14	-35.4%

[+]All values of Q_i are in [W/m].

i) A delta resistor-network with $\{C_{iji}\}$ as its conductances is a reasonable engineering model for calculating the total heat transfer rates.

ii) Using the dQdT results for the VB configuration, the accuracy of the heat transfer calculations can be notably improved.

In Figure 10.8, the mean heat transfer coefficients, h_{gsg}, h_{gag} and h_{sas}, are compared to the ASHWAT estimates with and without the correction of h_c. While neither of the ASHWAT curves are in reasonable proximity of the dQdT results for h_{sas}, there is good overall agreement between the original ASHWAT curve [$h_c = 2.81$ W/(m^{2}K)] and the

dQdT results for h_{gag}. For $b > 40\,\mathrm{mm}$, very good agreement is observed between the ASHWAT estimate and the dQdT results for h_{gsg}.

10.6 Summary

Numerical dQdT was applied to calculate the functionality coefficients of free convection at the indoor side of complex fenestration systems comprised of a flush-mounted glazing and two types of indoor-mounted attachments: 1) a roller blind (RB) and 2) a venetian blind (VB). The dQdT results show that:

i) There is reciprocity between the functionality coefficients of the RB configuration. The use of a delta resistor network to represent the three-temperature problem is therefore justified.

ii) The ASHWAT estimates are in very good agreement with the dQdT results for the RB configuration after a minor correction: using a correlation for free convection at an isothermal vertical flat plate, separate run-off values for h_{ga} and h_{sa} were evaluated.

iii) The functionality coefficients of the VB configuration do not show reciprocity. This is due to the asymmetric position of the gazing and blind with respect to the flow

iv) A delta resistor network with $(C_{ij} + C_{ji})/2$ as its conductances is a reasonable model for calculating the total heat transfer rates of the VB configuration, especially for $L \geq 75\,\mathrm{mm}$.

v) For the VB configuration, there is significant difference between the ASHWAT estimates and the dQdT results for $\{h_{ij}\}$ and the heat transfer rates calculated accordingly.

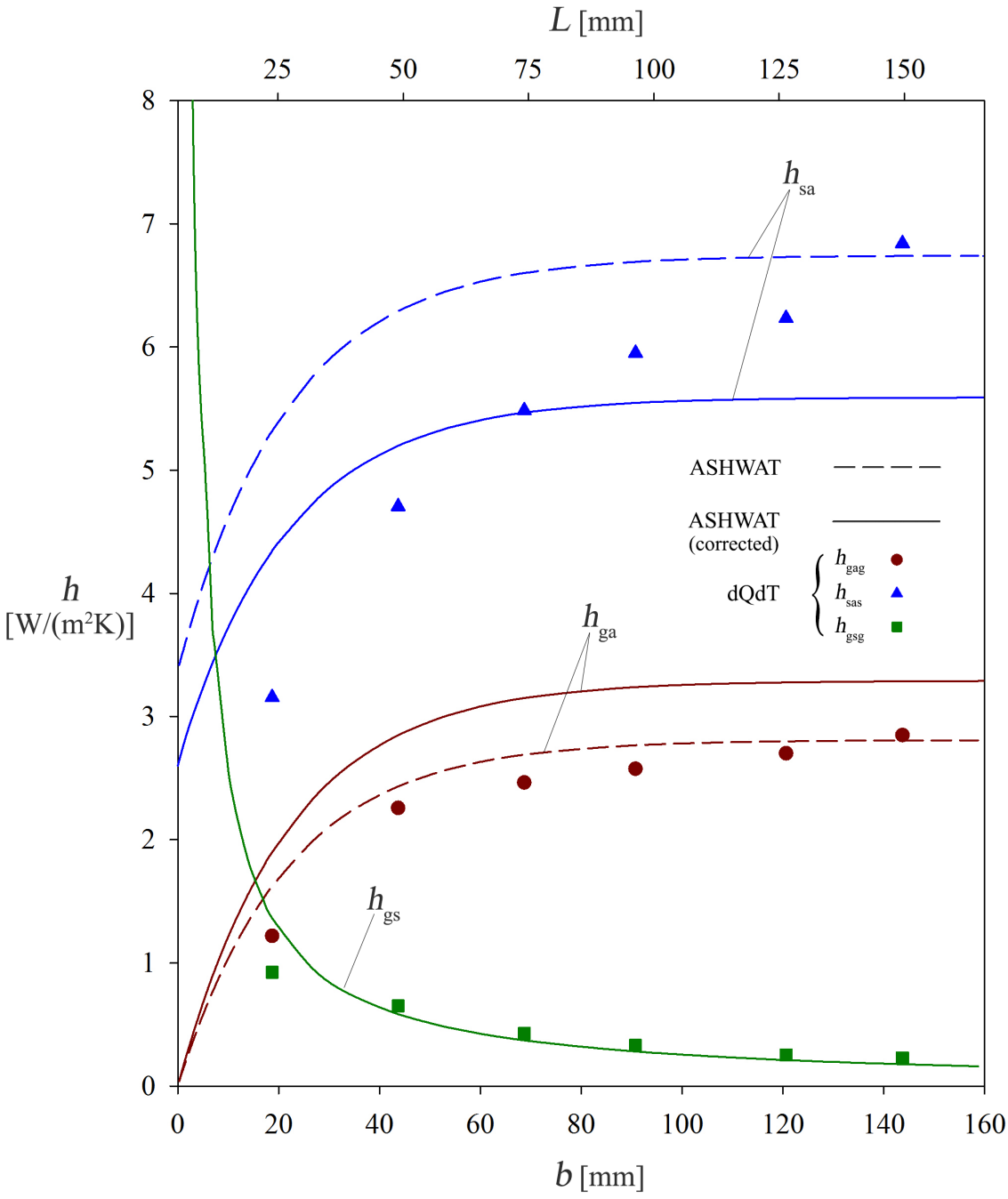

Figure 10.8: Mean paired heat transfer coefficients of the CFS with a venetian blind ($T_g = 35°C$, $T_s = 28°C$, $T_a = 24°C$, $H = 1.65\,m$, $\phi = 45°$)

vi) There is a potential for improving the current ASHWAT estimates using dQdT. However, further investigation of various CFS configurations is needed before comprehensive corrections can be developed.

Chapter 11

Conclusion

11.1 Summary of Findings

Many convection heat transfer problems entail exclusively isothermal and adiabatic boundary conditions. Moreover, in many cases, heat transfer takes place between more than two isothermal boundaries. This class was identified under the title of multi-temperature convection problems.

In the ASHWAT models for heat transfer in a complex fenestration system (CFS), convection at the indoor side is modeled as a three-temperature problem, characterized by three heat transfer coefficients. Motivated by the desire to calculate these coefficients with improved accuracy, the research reported in this thesis was devoted to the study of the general problem of multi-temperature convection.

The Newton law of cooling formulates the rate of convective heat transfer in terms of a temperature difference. For multi-temperature convection problems, this formulation must be reconciled with the presence of more than two representative temperatures. Traditionally, this is done by constructing an effective temperature difference, i.e. a combination of the independent, and sometimes dependent, temperatures of the problem.

It was shown in this thesis that the traditional formulation based on a single driving temperature difference is not a proper representation of the multi-temperature problem mainly because:

i) It leads to non-physical peculiarities (singularities, etc.) in the presentation of the solution.

ii) It does not reflect the thermal phenomenon in full detail.

An extension of the Newton formulation was proposed to address these shortcomings. The principal idea of the extended Newton formulation is the representation of the multiple driving temperature differences in separate terms. Hence, instead of using an amalgam of independent and dependent temperatures to construct a single effective temperature difference, the extended Newton formulation is based on a linearized summation of multiple terms, each entailing a distinct driving temperature difference. Consequently, heat transfer is characterized by multiple "functionality coefficients", each characterizing the thermal interaction between a specific pair of isothermal boundaries.

In general, the functionality coefficients that characterize a multi-temperature convection problem cannot be calculated based only on the knowledge of total heat transfer rates; an under-determined system of equations is encountered. The dQdT technique was developed to overcome this difficulty.

In the rare occasion that an analytical solution for the energy equation is available, the dQdT technique can be implemented by differentiating analytical expressions for the total heat transfer rates with respect to the boundary temperatures. This was demonstrated for classical convection problems: convection at an isothermal flat plate and in hydrodynamically developed laminar flow in channels and annuli with isothermal walls.

The dQdT technique can also be implemented numerically. This entails a baseline solution to the full set of governing equations and subsequent solutions to the linearized

energy equation with perturbed boundary conditions. The unique opportunity that numerical methods, specifically CFD, provide for the numerical implementation of dQdT must be highlighted. In a numerical study, solutions to the energy equation can be obtained using any desired velocity and property field. In numerical dQdT, this capacity is utilized to obtain solutions to the energy equation with perturbed boundary conditions, while retaining the velocity and property fields of the solution for the original boundary conditions. With the velocity and property fields fixed, the energy equation is linearized and hence the heat transfer coefficients are held constant. The following procedure summarizes the numerical implementation of dQdT:

i) A baseline solution to the full set of governing equations is obtained.

ii) The heat transfer rates are calculated.

iii) One of the boundary temperatures is perturbed by a finite amount.

iv) Retaining the velocity and property fields of the baseline solution (step i), the solution to the energy equation *only* is updated.

v) The new heat transfer rates are calculated. The change in each heat transfer rate gives a corresponding functionality coefficient.

vi) Steps iii-v are repeated for all boundary temperatures.

Numerical dQdT was verified against the analytical technique and then applied to CFD solutions to different multi-temperature convection problems: hydrodynamically developing flow in an annulus with isothermal walls, cross flow over isothermal cylinders, and free convection in a vertical channel with isothermal walls.

As demonstrated for various examples, the extended Newton formulation has several advantages over the traditional formulation. For instance, the superficial, non-physical singularities of the classical analytical solution to the asymmetric Graetz problem were

eliminated when the extended Newton formulation was applied. In the case of laminar free convection in a vertical channel with isothermal walls, the extended Newton formulation led to heat transfer correlations which are both more accurate and more physically meaningful than the existing correlations. In general, compared to the traditional formulation, the extended Newton formulation is a better representation of the physics of a multi-temperature convection problem, while revealing more detail about the thermal phenomenon.

The accurate calculation of the heat transfer coefficients of convection at the indoor side of a CFS was the original motivation for the research reported in this thesis. Currently, estimates based on known limits and experience are used to evaluate the convection coefficients of the CFS problem. However, with dQdT these coefficients can now be calculated more accurately. Sample dQdT results for a CFS entailing a roller blind demonstrated the good accuracy of the existing ASHWAT estimates. For a CFS with a venetian blind, however, dQdT results revealed potential for the improvement of the ASHWAT estimates.

In addition to giving the functionality coefficients of a multi-temperature convection problem and hence enabling the extended Newton formulation, the dQdT technique also provides a basis for assessing the resistor-network model of convection. As discussed for several examples, when the two functionality coefficients corresponding to each pair of isothermal boundaries are equal (or reasonably close), the multi-temperature problem can be represented by a network of convective resistors. Otherwise, the resistor-network is not applicable. Nonetheless, the functionality coefficients can still be used to quantify the thermal interaction between the isothermal boundaries and to calculate the total heat transfer rates.

11.2 Highlights

In relation to the general goals defined in Chapter 1, the highlights of this thesis can be summarized as follows:

i) The Newton law of cooling was extended to formulate the general problem of multi-temperature convection.

ii) The dQdT technique was developed and validated to calculate the paired heat transfer coefficients of a multi-temperature convection problem, including the CFS problem.

iii) The dQdT technique provides a basis for assessing the current ASHWAT estimates for the convection coefficients of the CFS problem. The dQdT results presented in this thesis suggest that while the ASHWAT estimates are remarkably accurate for a CFS with a roller blind, there is a potential for improving the estimates for a CFS with a venetian blind.

11.3 Future Work

The promising performance of the extended Newton formulation and the dQdT technique for the examples examined in this thesis encourage the application of this new approach to other multi-temperature convection problems. Examples include free convection in a vertical channel with one wall colder and one wall hotter than the ambient ($r_T < 0$), the CFS problem with forced convection (e.g. with a diffuser) and jets impinging on an isothermal surface in an isothermal medium.

The mathematical development of the extended Newton formulation and the dQdT technique was presented for the general case of an N-temperature problem. However, the examples studied in this thesis were all two- or three-temperature problems. The

application of dQdT to cases of $N > 3$, e.g. flow over more than two isothermal cylinders, is a natural step forward.

In some of the cases presented in this thesis, the numerical accuracy of the dQdT results seemed to be (slightly) better than the numerical accuracy of the baseline solution. This observation calls for further investigation. The formal accuracy of numerical dQdT, i.e. the relation between the numerical accuracy of the baseline solution and the accuracy of numerical dQdT results, is a subject for future research.

Finally, there is evidence in support of the idea that the split of heat transfer at an isothermal boundary can be resolved using the functionality coefficients. Calculations using the boundary-layer integral at early stages of thermal development and conduction shape factors in the thermally developed limit, and the asymptotic behavior of the wall-fluid Nusselt numbers of free convection in a vertical channel are examples of such evidence. Nevertheless, since there are currently no alternative methods that can be used to calculate (or measure) the split of heat transfer, the calculations based on functionality coefficients have not been verified for the general case. Moreover, the physical meaning of the split of convective heat transfer remains to be further examined. Is it meaningful, particularly from a thermodynamic point of view, to interpret the thermal current between two nodes of a resistor network as the paired convective heat transfer, i.e. the exchange of thermal energy, between the respective isothermal boundaries?

References

American Society of Heating, Refrigeration & Air Conditioning Engineers (2013), *ASHRAE Handbook: Fundamentals*, ASHRAE, Atlanta, GA.

ANSYS (2011*a*), *ANSYS Fluent 14.0 Theory Guide*, Canonsburg, PA.

ANSYS (2011*b*), *ANSYS Fluent 14.0 User Guide*, Canonsburg, PA.

Aung, W. (1972), 'Fully developed laminar free convection between vertical plates heated asymmetrically', *International Journal of Heat and Mass Transfer* **15**(8), 1577–1580.

Aung, W., Fletcher, L. and Sernas, V. (1972), 'Developing Laminar Free Convection Between Vertical Flat Plates with Asymmetric Heating', *International Journal of Heat and Mass Transfer* **15**(11), 2293–2308.

Ayinde, T. F., Said, S. A. M. and Habib, M. A. (2008), 'Turbulent Natural Convection Flow in a Vertical Channel with Anti-Symmetric Heating', *Heat and Mass Transfer* **44**(10), 1207–1216.

Barnaby, C. S., Wright, J. L. and Collins, M. R. (2009), 'Improving Load Calculations for Fenestration with Shading Devices', *ASHRAE Transactions* **115 (Part 2)**, 31–44.

Bearman, P. W. and Wadcock, A. J. (1973), 'The Interaction between a Pair of Circular Cylinders Normal to a Stream', *Journal of Fluid Mechanics* **61**(03), 499.

Blasius, H. (1908), 'Grenzschichten in Flüssigkeiten mit kleiner Reibung', *Zeitschrift für angewandte Mathematik und Physik* **26**, 1–37. [In German].

Celik, I. B. et al. (2008), 'Procedure for Estimation and Reporting of Uncertainty Due to Discretization in CFD Applications', *Journal of Fluids Engineering* **130**(7), 78001:1–4.

Churchill, S. and Chu, H. (1975), 'Correlating Equations for Laminar and Turbulent Free Convection from a Vertical Plate', *International Journal of Heat and Mass Transfer* **18**(11), 1323–1329.

Churchill, S. W. and Usagi, R. (1972), 'A General Expression for the Correlation of Rates of Transfer and Other Phenomena', *AIChE Journal* **18**(6), 1121–1128.

Coelho, P. and Pinho, F. (2006), 'Fully-Developed Heat Transfer in Annuli with Viscous Dissipation', *International Journal of Heat and Mass Transfer* **49**(19-20), 3349–3359.

Collins, M. R. and Wright, J. L. (2006), 'Calculating Center-Glass Performance Indices of Windows', *ASHRAE Transactions* **112 (Prat 2)**, 22–29.

Desrayaud, G. et al. (2013), 'Benchmark Solutions for Natural Convection Flows in Vertical Channels Submitted to Different Open Boundary Conditions', *International Journal of Thermal Sciences* **72**, 18–33.

Fedorov, A. G., Viskanta, R. and Mohamad, A. A. (1997), 'Turbulent Natural Convection Heat Transfer in an Asymmetrically Vertical Parallel-Plate Channel', *International Journal of Heat and Mass* **40**(16), 3849–3860.

Foroushani, S., Naylor, D. and Wright, J. L. (2015c), Laminar Free Convection from a Pair of Horizontal Cylinders : A Three-Temperature Problem, *in* '23rd Annual Conference of the CFD Society of Canada', Waterloo, ON.

Foroushani, S., Naylor, D. and Wright, J. L. (2017b), 'Resistor-Network Formulation of Multitemperature Forced-Convection Problems', *Journal of Thermophysics and Heat Transfer* **31**(2), 443–450.

Foroushani, S., Wright, J. L., Collins, M. R. and Naylor, D. (2015a), Assessing Convective Heat Transfer Coefficients Associated with Indoor Shading Attachments Using a New Technique Based on Computational Fluid Dynamics, *in* 'ASHRAE Winter Conference 2015', Chicago, Il. Paper CH-15-C046.

Foroushani, S., Wright, J. L., Collins, M. R. and Naylor, D. (2017d), Indoor-Side Convection Coefficients for Complex Fenestration Systems with Roller Blinds, *in* 'ASHRAE Winter Conference 2017', Las Vegas, NV. Paper LV–17–C080.

Foroushani, S., Wright, J. L. and Naylor, D. (2015b), Forced Convection from a Pair of Spheres: A Three-Temperature Problem, *in* '8th Int. Conf. Computational Heat & Mass Transfer', Istanbul, Turkey. Paper#119.

Foroushani, S., Wright, J. L. and Naylor, D. (2016), Sensitivity of the Solar Heat Gain Coefficient of Complex Fenestration Systems to the Indoor Convection Coefficient, *in* 'eSim 2016 Building Performance Simulation Conference', Hamilton, ON, pp. 277–285.

Foroushani, S., Wright, J. L. and Naylor, D. (2017a), 'Asymmetric Graetz Problem: The Analytical Solution Revisited', *Journal of Thermophysics and Heat Transfer* **31**(1), 237–242.

Foroushani, S., Wright, J. L. and Naylor, D. (2017c), 'Resistor-Network Formulation of Multitemperature Free-Convection Problems', *Journal of Thermophysics and Heat Transfer* **31**(3), [In press].

Graetz, L. (1882), 'Ueber die Wärmeleitungsfähigkeit von Flüssigkeiten', *Annalen der Physik* **245**, 79–94. [In German].

Gray, D. D. and Giorgini, A. (1976), 'The Validity of the Boussinesq Approximation for Liquids and Gases', *International Journal of Heat and Mass Transfer* **19**(5), 545–551.

Haddout, Y. and Lahjomri, J. (2015), 'The Extended Graetz Problem for a Gaseous Slip Flow in Micropipe and Parallel-plate Microchannel with Heating Section of Finite Length: Effects of Axial Conduction, Viscous Dissipation and Pressure Work', *International Journal of Heat and Mass Transfer* **80**, 673–687.

Hatton, A. and Turton, J. (1962), 'Heat Transfer in the Thermal Entry Length with Laminar Flow between Parallel Plates at Unequal Temperatures', *International Journal of Heat and Mass Transfer* **5**, 673–679.

Hilsenrath, J. (1955), Tables of Thermal Properties of Gases, Technical Report 564, National Bureau of Standards.

Incropera, F. P., DeWitt, D. P., Bergman, T. L. and Lavine, A. S. (2007), *Fundamentals of Heat and Mass Transfer*, 6th edn, Wiley & Sons, Hoboken, NJ.

Kakaç, S., Shah, K. R. and Aung, W. (1987), *Handbook of Single-Phase Convective Heat Transfer*, Wiley & Sons, New York, NY.

Kakaç, S. and Yücel, O. (1974), Laminar Flow Heat Transfer in an Annulus with Simultaneous Development of Velocity and Temperature Fields, Technical Report No. 19, Technical and Scientific Council of Turkey, Ankara, Turkey.

Kakaç, S., Yener, Y. and Pramuanjaroenkij, A. (2014), *Convective Heat Transfer*, 3rd edn, CRC Press, Boca Raton, FL.

Kays, W. M. and Crawford, M. E. (2005), *Convective Heat and Mass Transfer*, 4th edn, McGraw-Hill, New York, NY.

Kimura, S. and Bejan, A. (1983), 'The "Heatline" Visualization of Convective Heat Transfer', *Journal of Heat Transfer* **105**, 916–919.

Kotey, N., Wright, J. L., Barnaby, C. and Collins, M. (2009), 'Solar Gain through Windows with Shading Devices: Simulation versus Measurement', *ASHRAE Transactions* **115 (Part 2)**, 18–30.

Lau, G. E., Yeoh, G. H., Timchenko, V. and Reizes, J. A. (2011), 'Large-Eddy Simulation of Turbulent Natural Convection in Vertical Parallel-Plate Channels', *Numerical Heat Transfer — Part B: Fundamentals* **59**(4), 259–287.

Lomanowski, B. A. and Wright, J. L. (2012), 'The Complex Fenestration Construction: A Practical Approach for Modelling Windows with Shading Devices in ESP-r', *Journal of Building Performance Simulation* **5**(3), 185–198.

Lundberg, R. E. and McCuen, P. (1963), 'Heat Transfer in Annular Passages. Hydro-Dynamically Developed Laminar Flow With Arbitrarily Prescribed Wall Temperatures or Heat Fluxes', *International Journal of Heat and Mass Transfer* **6**, 495–529.

Machin, A. D., Naylor, D., Harrison, S. J. and Oosthuizen, P. H. (1998), 'Experimental Study of Free Convection at an Indoor Glazing Surface with a Venetian Blind', *HVAC&R Research* **4**(2), 153–166.

Malik, M. R. (1978), Prediction of Laminar and Turbulent Flow Heat Transfer in Annular Passages, PhD thesis, Iowa State University.

Manca, O., Morrone, B., Nardini, S. and Naso, V. (2000), *Natural Convection in Open Channels*, in Computational Analysis of Convection Heat Transfer (Sunden & Comini), WIT Press, Southampton, UK, pp. 235–278.

Martin, L., Raithby, G. and Yovahovich, M. (1991), 'On the Low Rayleigh Number Asymptote for Natural Convection Through an Isothermal, Parallel-Plate Channel', *Journal of Heat Transfer* **113**, 899–905.

Mitrović, J. and Maletić, B. (2005), 'Effect of Thermal Asymmetry on Heat Transfer in a Laminar Annular Flow', *Chemical Engineering & Technology* **28**(10), 1144–1150.

Mitrović, J., Maletić, B. and Bačlić, B. S. (2006), 'Some Peculiarities of the Asymmetric Graetz Problem', *International Journal of Engineering Science* **44**(7), 436–455.

Naylor, D., Floryan, J. M. and Tarasuk, J. D. (1991), 'A Numerical Study of Developing Free Convection Between Isothermal Vertical Plates', *Journal of Heat Transfer* **113**(3), 620–626.

Nield, D. A. (2004), 'Forced Convection in a Parallel Plate Channel with Asymmetric Heating', *International Journal of Heat and Mass Transfer* **47**(25), 5609–5612.

Oosthuizen, P. H. and Naylor, D. (1999), *Introduction to Convective Heat Transfer Analysis*, McGraw–Hill, New York, NY.

Ostrach, S. (1953), An Analysis of Laminar Free-Convection Flow and Heat Transfer About a Flat Plate Parallel to the Direction of the Generating Body Force, Technical report, NACA Technical Reptort 1111.

Raithby, G. D. and Hollands, K. G. T. (1998), *Natural Convection*, in Handbook of Heat Transfer (Rohsenhow et. al), McGraw-Hill, New York, NY, chapter 4, pp. 4.1–4.99.

Roberts, A. and Barrow, H. (1967), 'Turbulent Heat Transfer to Air in the Vicinity of the Entry of an Internally Heated Annulus', *Proceedings of the Institution of Mechanical Engineers* **182**(8), 268–276.

Roeleveld, D. (2013), Experimental and Numerical Study of Free Convection in a Vertical Channel with Opposing Buoyancy Forces, PhD thesis, Ryerson University.

Roeleveld, D., Naylor, D. and Leong, W. H. (2014), 'Free Convection in Antisymmetrically Heated Vertical Channels', *Journal of Heat Transfer* **136**(1), 012502:1–7.

Roeleveld, D., Naylor, D. and Oosthuizen, P. H. (2009), 'Empirical Correlations for Free Convection in an Isothermal Asymmetrically Heated Vertical Channel', *Heat Transfer Engineering* **30**(3), 189–196.

Rohsenow, W. M., Hartnett, J. P. and Cho, Y. I. (1998), *Handbook of Heat Transfer*, 3rd edn, McGraw–Hill, New York, NY.

Ryzhkov, I. I. (2013), 'The Extended Graetz Problem with Specified Heat Flux for Multicomponent Fluids with Soret and Dufour Effects', *International Journal of Heat and Mass Transfer* **66**, 461–471.

Touloukian, Y. S., Liley, P. E. and Saxena, S. C. (1970), Thermal Conductivity: Nonmetallic Liquids and Gases, Technical Report 3, Plenum Publishing Corporation, New York, NY.

Touloukian, Y. S., Saxena, S. C. and Hestermans, P. (1975), Viscosity: Non- metallic Liquids and Gases, Technical Report 11, Plenum Publishing Corporation, New York, NY.

Trevisan, O. and Bejan, A. (1987), 'Combined Heat and Mass Transfer by Natural Convection in a Vertical Enclosure', *Journal of Heat Transfer* **109**(1), 104–112.

Wright, J. L. (2011), 'A User Friendly Program for the Solar/Thermal Analysis of Glazing Systems with Shading Devices', Performance of Shading Devices in Commercial Buildings Seminar (Montréal, QC). [Invited talk].

Wright, J. L., Barnaby, C. S., Niles, P. and Rogalsky, C. J. (2011), Efficient Simulation of Complex Fenestration Systems in Heat Balance Room Models, *in* '12th International Conference of the International Building Performance Simulation Association', Sydney, NSW, Australia, p. 2851–2858.

Wright, J. L., Collins, M. R. and Huang, N. Y. T. (2008), 'Thermal Resistance of a Window with an Enclosed Venetian Blind: A Simplified Model', *ASHRAE Transactions* **114 (Part 1)**, 471–482.

Wright, J. L., Collins, M. R., Kotey, N. A. and Barnaby, C. S. (2009), Improving Load Calculations for Fenestration with Shading Devices, Technical report, ASHRAE 1311-RP Final Report.

Wright, J. L. and Sullivan, H. F. (1987), VISION: A Computer Program for the Detailed Simulation of the Thermal Performance of Innovative Glazing Systems, *in* 'International Conference on Building Energy Management', Lausanne, Switzerland, pp. 179–185.

Wright J.L. (2008), 'Calculating Centre-Glass Performance Indices of Glazing Systems with Shading Devices', *ASHRAE Transactions* **114 (Part 2)**, 199–209.

Yücel, O. (1972), Laminar Flow Heat Transfer In the Combined Entrance Region of Concentric Circular Annulus, Master's thesis, Middle East Technical University (Ankara, Turkey).

Ye, P., Harrison, S., Oosthuizen, P. H. and Naylor, D. (1999), 'Convective Heat Transfer from a Window with a Venetian Blind: Detailed Modeling', *ASHRAE Transactions* **105 (Part 2)**, 1031–1037.

Yilmaz, T. and Fraser, S. M. (2007), 'Turbulent Natural Convection in a Vertical Parallel-Plate Channel with Asymmetric Heating', *International Journal of Heat and Mass Transfer* **50**(13-14), 2612–2623.

Yilmaz, T. and Gilchrist, A. (2007), 'Temperature and Velocity Field Characteristics of Turbulent Natural Convection in a Vertical Parallel-Plate Channel with Asymmetric Heating', *Heat and Mass Transfer* **43**(7), 707–719.

Zdravkovich, M. M. (1977), 'Review of Flow Interference Between Two Circular Cylinders in Various Arrangements', *Journal of Fluids Engineering* **99**(4), 618–633.

Zdravkovich, M. M. (1987), 'The Effects of Interference Between Circular Cylinders in Cross-Flow', *Journal of Fluids and Structures* **1**(2), 239–261.

APPENDICES

Appendix A

MATLAB Code for the Asymmetric Graetz Problem

```
X=1;              % Domain size
Y=2;
% Discretization:
Nx=1001;          % Number of nodes
Ny=21;
dX=X/(Nx-1);      % Grid size
dY=Y/(Ny-1);
% Initialization:
T=ones(Nx,Ny);
% Boundary conditions:
T(1,:)=1;         % T0=0 @ X=0
T(:,Ny)=0;        % T1=1 @ Y=1
T(:,1)=1;         % T2=rT @ Y=-1
% Forward-marching scheme:
for i=2:Nx
```

```
16      n=1;                    % Iteration counter
17      res=1;                  % Residual
18      while res>0.0001        % Convergence criterion
19          n=n+1;
20          Tn=T;
21          for j=2:Ny-1
22              Y=(j-1)*dY;
23              U=1.5*Y*(2-Y);
24              a=U/4/dX+2/dY^2;
25              b=(Tn(i,j+1)+Tn(i,j-1))/dY^2+U*Tn(i-1,j)/4/dX;
26              T(i,j)=b/a;
27          end
28          res=max(abs(T(:,j)-Tn(:,j)));
29      end
30  end
31  Ty1=-(T(:,Ny)-T(:,Ny-1))/dY;      % Calculate gradient at walls
32  Ty2=(T(:,2)-T(:,1))/dY;
33
34  for i=1:Nx
35      % Integrate q to find Q (walls):
36      Q1(i,1)=-sum(Ty1(1:i))*dX;
37      Q2(i,1)=-sum(Ty2(1:i))*dX;
38      % Energy balance gives Q0:
39      Q0(i,1)=Q1(i)+Q2(i);
40  end
```

Appendix B

Parameters of the Solution to the Annulus Problem: Eigencoefficients, Eigenvalues and Eigenfunction-Derivatives

Table B.1: Parameters of the fundamental series solution of the first kind for the annulus problem (Lundberg et al. 1963)

ϕ	n	λ_n	λ_n^2	$2(1-\phi)B_{n,2}\times$ $(\partial f_n/\partial\overline{r})_{\overline{r}_2}$	$2(1-\phi)B_{n,2}\times$ $(\partial f_n/\partial\overline{r})_{\overline{r}_1}$	$2(1-\phi)B_{n,1}\times$ $(\partial f_n/\partial\overline{r})_{\overline{r}_2}$	$2(1-\phi)B_{n,1}\times$ $(\partial f_n/\partial\overline{r})_{\overline{r}_1}$
0.02	0	4.748	22.54	-10.22	0.8076	-40.25	3.179
	1	10.87	118.2	-6.392	-0.5494	27.37	2.353
	2	16.99	228.8	-5.065	0.4524	-22.55	2.014
	3	23.10	533.8	-4.353	-0.3978	19.82	1.811
0.05	0	4.939	24.39	-6.697	1.038	-20.77	3.221
	1	11.18	125.0	-4.457	-0.7306	14.62	2.397
	2	17.40	303.0	-3.647	0.6117	-12.24	2.053
	3	23.62	538.3	-3.200	-0.5437	10.88	1.848
0.1	0	5.105	26.06	-5.171	1.297	-12.97	3.255
	1	11.43	130.7	-3.618	-0.9387	9.389	2.435
	2	17.75	315.3	-3.029	0.7956	-7.958	2.090
	3	24.07	579.4	-2.694	-0.7122	7.124	1.883
0.25	0	5.323	28.33	-5.056	1.829	-7.317	3.299
	1	11.75	138.2	-3.008	-1.370	5.480	2.496
	2	18.19	331.0	-2.513	1.176	-4.703	2.149
	3	24.63	606.6	-2.315	-1.059	4.237	1.938
0.5	0	5.445	29.65	-3.636	2.465	-4.931	3.343
	1	11.75	142.3	-2.770	-1.881	3.762	2.554
	2	18.19	339.6	-2.388	1.622	-3.245	2.204
	3	24.93	621.6	-2.156	-1.465	2.930	1.990
1	0	5.492	30.16	-3.432	3.432	-3.432	3.432
	1	11.99	143.8	-2.608	-2.608	2.608	2.608
	2	18.51	342.9	-2.277	2.277	-2.277	2.277
	3	25.04	627.3	-2.058	-2.058	2.058	2.058

Appendix C

Curve Fits for the Correlation Constants of the Annulus Problem

Equations C.1-C.7 show the curve-fit relations developed for the first eigenvalue of the annulus problem, discussed in Chapter 5, and the coefficients of the correlations presented in Section 5.4. In Figures C.1-C.7, these relations are compared to the numerical data presented by Lundberg et al. (1963). The quality of the fits are reported in the figure captions in terms of the coefficient of determination (R^2) and the RMS error (RMSE).

$$\lambda_1^2 = 28.96\exp(0.042\,\phi) - 7.62\exp(-9.240\,\phi) \tag{C.1}$$

$$F_{10} = 0.1734\,\phi^{-0.0413} + 0.0676\,\phi \tag{C.2}$$

$$F_{20} = 0.0734\,\phi^{-0.8417} + 0.175 \tag{C.3}$$

$$F_{12} = 0.07164\,\phi^{0.6647} + 0.0271 \tag{C.4}$$

$$G_{10} = 3.221\,\phi^{0.5536} + 3.634 \tag{C.5}$$

$$G_{20} = 2.420\,\phi^{-0.7511} + 4.709 \tag{C.6}$$

$$G_{12} = 2.928\,\phi^{0.5691} + 0.4996 \tag{C.7}$$

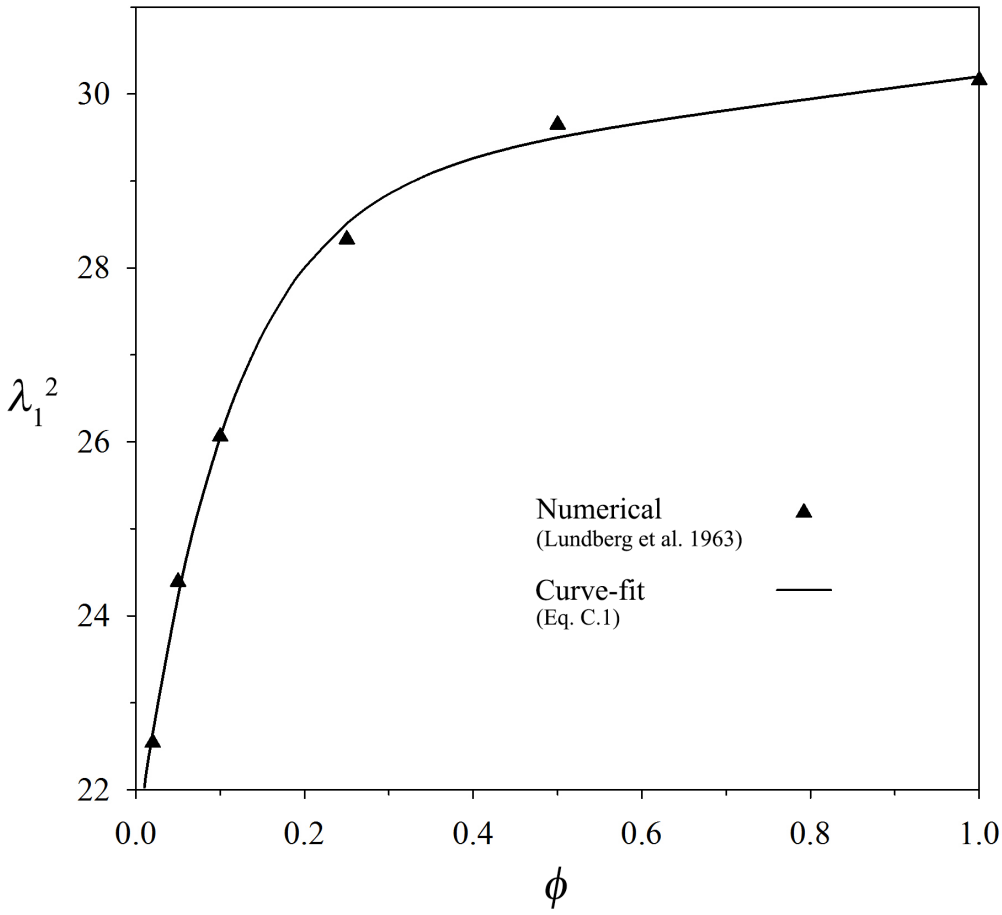

Figure C.1: Curve-fit vs. numerical data for the first eigenvalue of the annulus problem
Goodness of the fit: $R^2 = 0.99$, RMSE $= 0.2208$

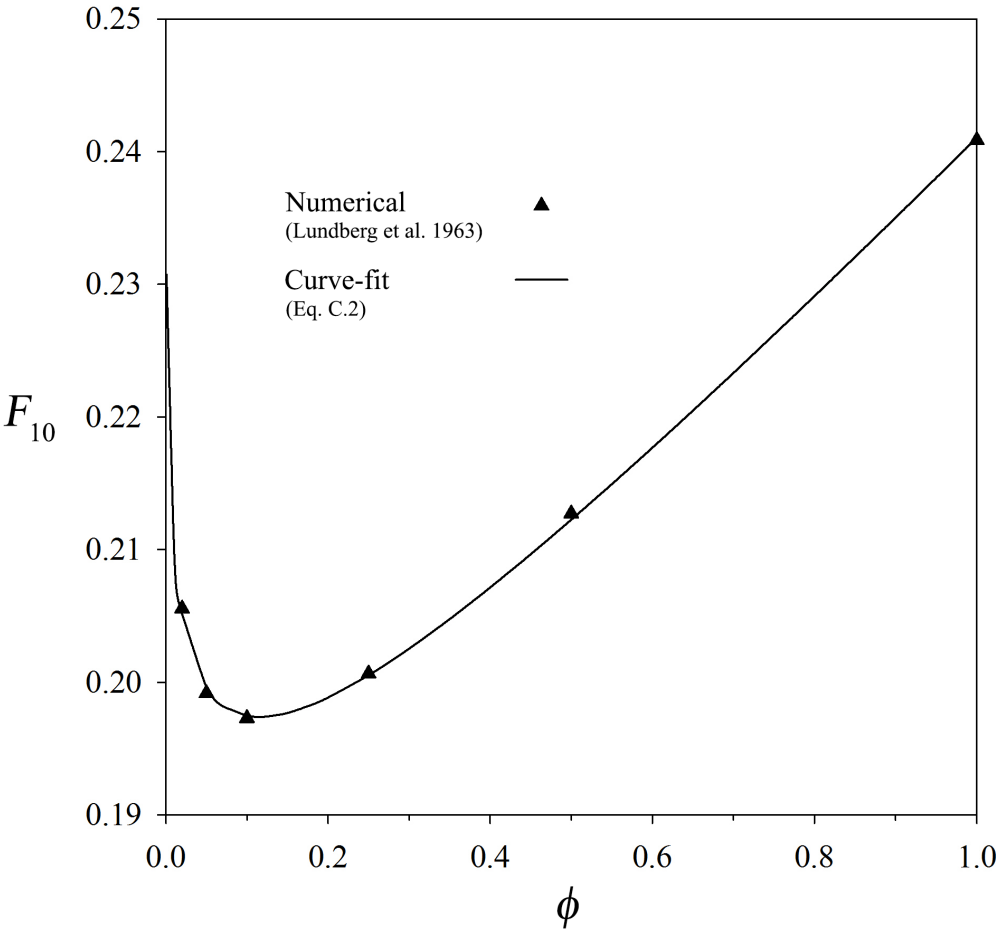

Figure C.2: Curve-fit vs. numerical data for the correlation constant F_{10}
Goodness of the fit: $R^2 = 0.99$, RMSE $= 0.0004$

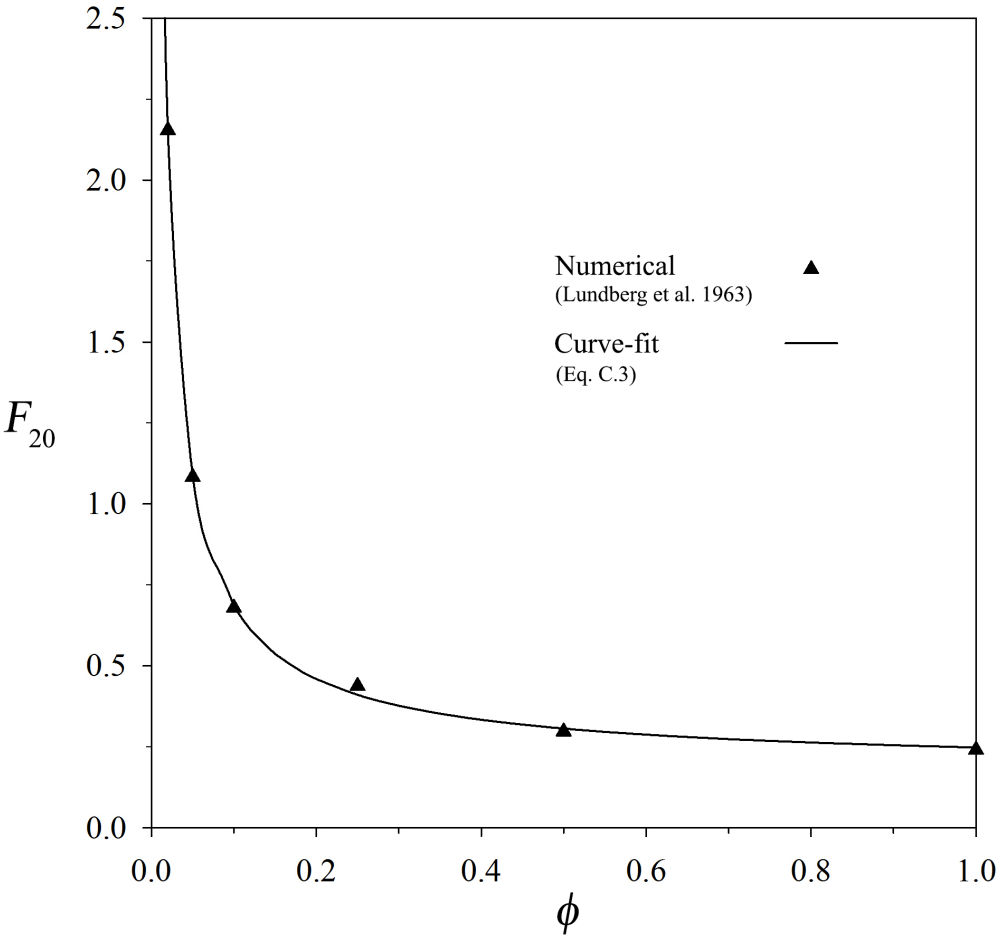

Figure C.3: Curve-fit vs. numerical data for the correlation constant F_{20}
Goodness of the fit: $R^2 = 0.99$, RMSE $= 0.0176$

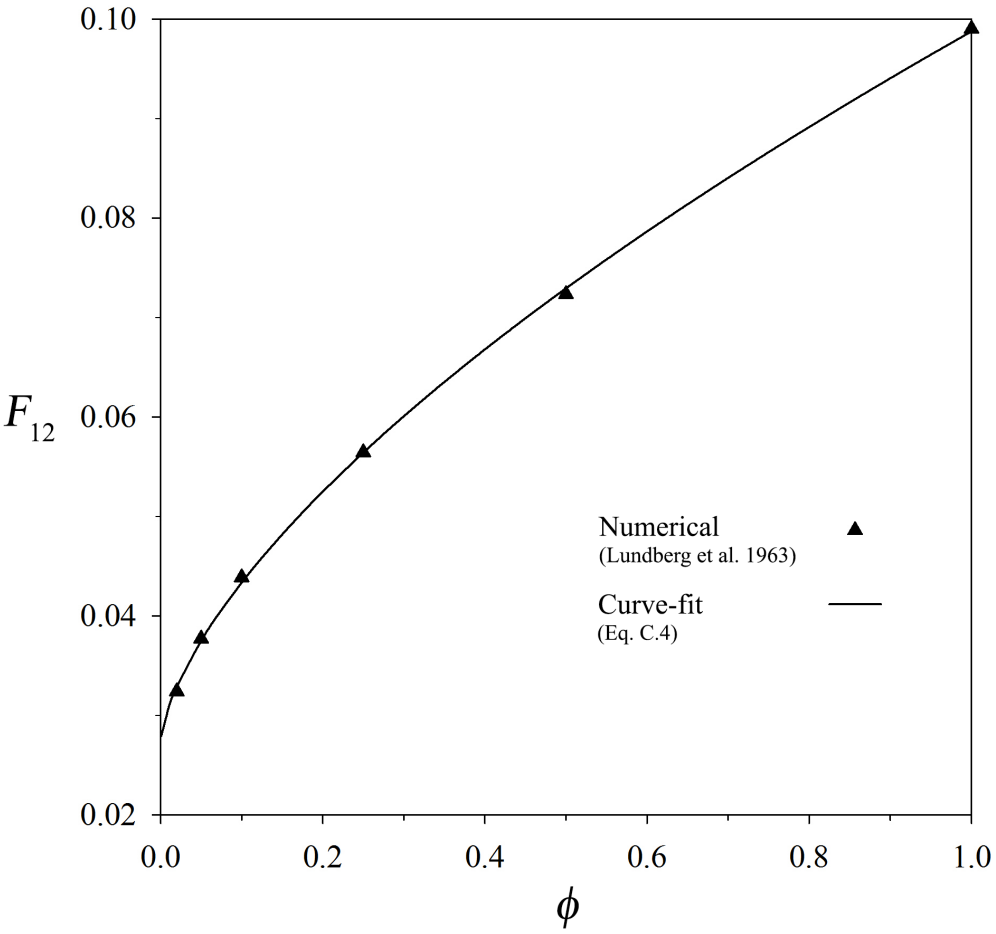

Figure C.4: Curve-fit vs. numerical data for the correlation constant F_{12}
Goodness of the fit: $R^2 = 0.99$, RMSE = 0.0006

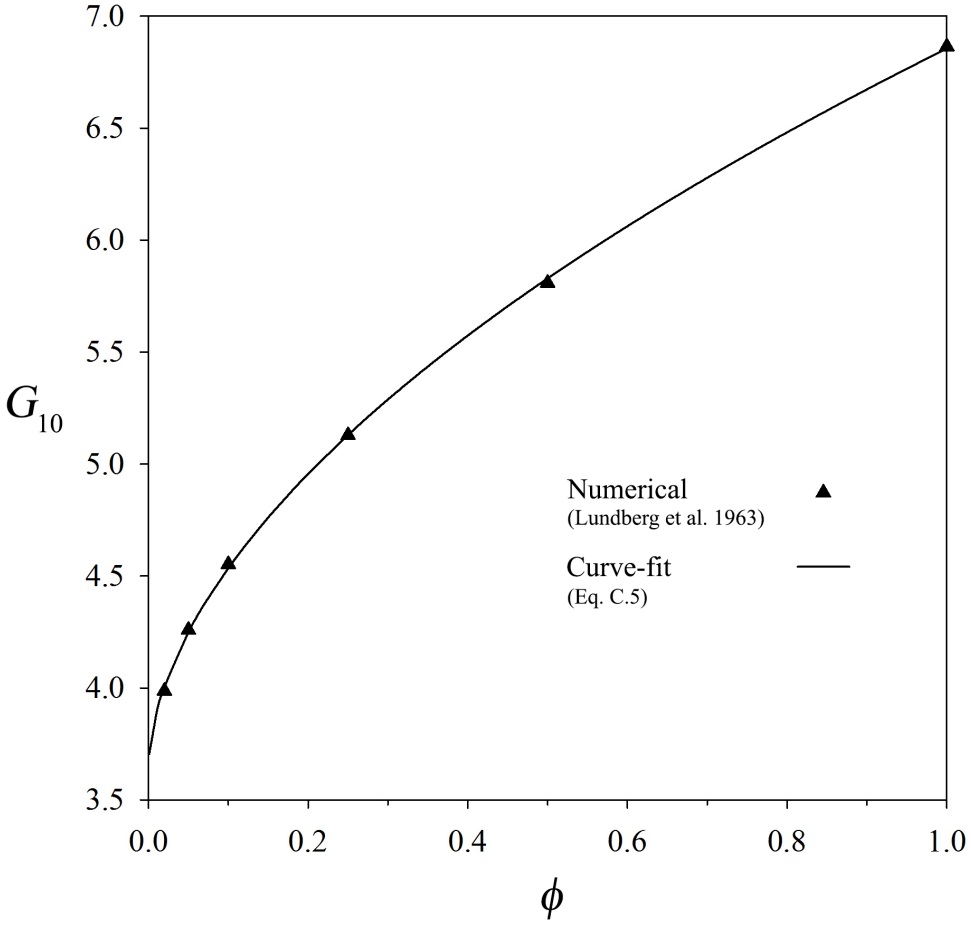

Figure C.5: Curve-fit vs. numerical data for the correlation constant G_{10}
Goodness of the fit: $R^2 = 0.99$, RMSE = 0.0203

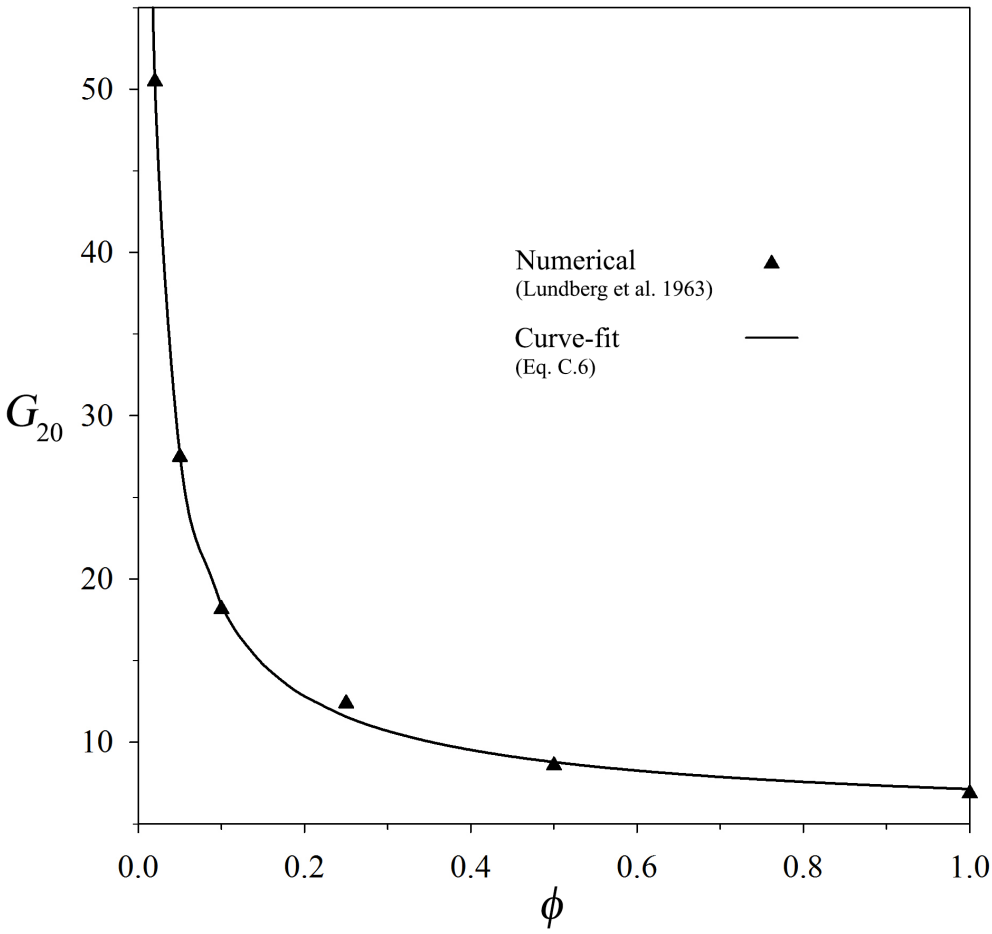

Figure C.6: Curve-fit vs. numerical data for the correlation constant G_{20}
Goodness of the fit: $R^2 = 0.99$, RMSE $= 0.5356$

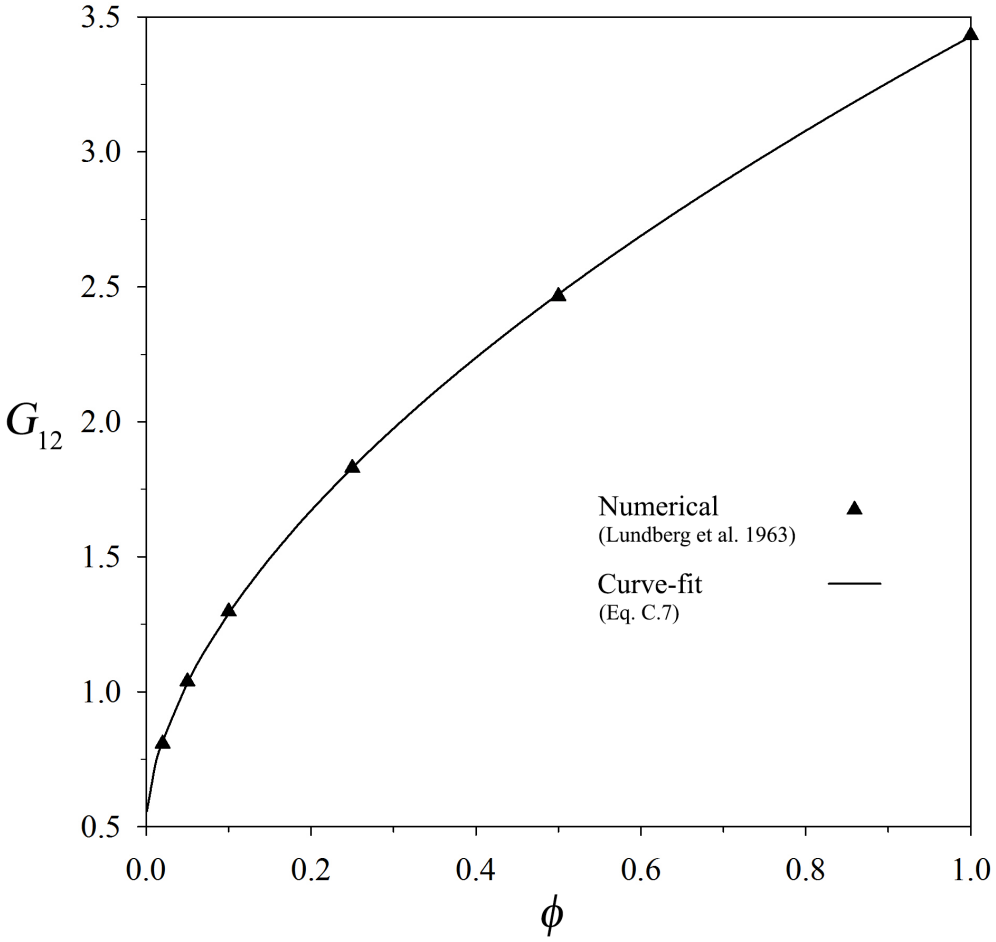

Figure C.7: Curve-fit vs. numerical data for the correlation constant G_{10}
Goodness of the fit: $R^2 = 0.99$, RMSE $= 0.0091$

Appendix D

Theorem: In Three-Temperature Problems $C_{ij} - C_{ji} = \text{const}$

The results presented in Chapters 7-10 reveal that, for a three-temperature problem, even in the absence of reciprocity between the functionality coefficients ($C_{ij} \neq C_{ji}$), the difference between each pair is a constant value for a given combination of geometry, flow and fluid properties. In this appendix, a mathematical proof is presented for this observation.[1]

Consider, for instance, the results presented in Chapter 7 for flow over isothermal cylinders. According to these results;

$$C_{20} - C_{02} = C_{01} - C_{10} = C_{12} - C_{21} \tag{D.1}$$

Next, consider the extended Newton formulation of a three-temperature problem:

[1]The contribution of Dr. Marilyn Lightstone to the material presented in this appendix is hereby gratefully acknowledged.

$$\begin{cases} Q_0 = C_{01}(T_0 - T_1) + C_{02}(T_0 - T_2) \\ Q_1 = C_{10}(T_1 - T_0) + C_{12}(T_1 - T_2) \\ Q_2 = C_{20}(T_2 - T_0) + C_{21}(T_2 - T_1) \end{cases} \tag{D.2}$$

The overall energy balance of the problem requires:

$$Q_0 + Q_1 + Q_2 = 0$$

Therefore:

$$\begin{aligned} & C_{01}(T_0 - T_1) + C_{02}(T_0 - T_2) \\ & + C_{10}(T_1 - T_0) + C_{12}(T_1 - T_2) \\ & + C_{20}(T_2 - T_0) + C_{21}(T_2 - T_1) = 0 \end{aligned} \tag{D.3}$$

Equation D.3 can be rearranged to obtain Equation D.4.

$$\begin{aligned} & \big(C_{01} - C_{10} + C_{02} - C_{20}\big)T_0 \\ & + \big(C_{10} - C_{01} + C_{12} - C_{21}\big)T_1 \\ & + \big(C_{20} - C_{02} + C_{21} - C_{12}\big)T_2 = 0 \end{aligned} \tag{D.4}$$

Because T_0, T_1 and T_2 are independent variables, Equation D.4 is valid if and only if the individual terms on the LHS are zero;

$$
\begin{aligned}
&\big(C_{01} - C_{10} + C_{02} - C_{20}\big)T_0 \\
=&\big(C_{10} - C_{01} + C_{12} - C_{21}\big)T_1 \\
=&\big(C_{20} - C_{02} + C_{21} - C_{12}\big)T_2 = 0
\end{aligned}
\tag{D.5}
$$

Furthermore, because Equation D.4 is valid for *any* $\{T_i\}$, Equation D.5 leads to:

$$
\begin{cases}
C_{01} - C_{10} + C_{02} - C_{20} = 0 \\
C_{10} - C_{01} + C_{12} - C_{21} = 0 \\
C_{20} - C_{02} + C_{21} - C_{12} = 0
\end{cases}
\tag{D.6}
$$

Hence:

$$
C_{20} - C_{02} = C_{01} - C_{10} = C_{12} - C_{21} \qquad \text{(Q.E.D)}
$$

Appendix E

Journal File for the implementation of Numerical dQdT in Fluent

```
report/surface-integrals/integral left right
heat-flux n
define/boundary-conditions/wall left 0 n 0 n n n 311 n n
define/boundary-conditions/wall right 0 n 0 n n n 305 n n
define/boundary-conditions/pressure-inlet btm y n 0 n 0 n 300 n y
define/boundary-conditions/pressure-outlet top n 0 n 300 n y n n
define/operating-conditions/operating-temperature 300
solve/set/equations/flow n
solve/monitors/residual/check-convergence n
solve/iterate 100
report/surface-integrals/integral left right
heat-flux n
```

Appendix F

dQdT Results for Laminar Free Convection of Air in a Vertical Channel with Isothermal Walls

Table F.1: dQdT results for laminar free convection in a vertical channel with isothermal walls ($r_T = 0$, Pr = 0.7)

Ra	$\overline{\mathrm{Nu}}_{12}$	$\overline{\mathrm{Nu}}_{21}$	$\overline{\mathrm{Nu}}_{10}$	$\overline{\mathrm{Nu}}_{01}$	$\overline{\mathrm{Nu}}_{20}$	$\overline{\mathrm{Nu}}_{02}$
0.01	1.0010	1.0010	0.0206	0.0206	0.0206	0.0206
0.1	1.0007	1.0007	0.0213	0.0213	0.0213	0.0212
1	0.9901	0.9887	0.0467	0.0482	0.0452	0.0437
10	0.8684	0.8600	0.3716	0.3800	0.3331	0.3248
100	0.4413	0.3816	1.7358	1.7955	1.4032	1.3434
500	0.2240	0.1177	2.9995	3.1057	1.9603	1.8540
1000	0.1861	0.0654	3.5826	3.7033	2.1043	1.9836
2000	0.1748	0.0336	4.2266	4.3678	2.2828	2.1416

Table F.2: dQdT results for laminar free convection in a vertical channel with isothermal walls ($r_T = 0.25$, Pr = 0.7)

Ra	$\overline{\mathrm{Nu}}_{12}$	$\overline{\mathrm{Nu}}_{21}$	$\overline{\mathrm{Nu}}_{10}$	$\overline{\mathrm{Nu}}_{01}$	$\overline{\mathrm{Nu}}_{20}$	$\overline{\mathrm{Nu}}_{02}$
0.01	1.0010	1.0010	0.0206	0.0206	0.0206	0.0206
0.1	1.0007	1.0007	0.0213	0.0213	0.0212	0.0212
1	0.9898	0.9889	0.0464	0.0473	0.0455	0.0446
10	0.8655	0.8605	0.3665	0.3715	0.3433	0.3383
100	0.4033	0.3697	1.7179	1.7514	1.5156	1.4821
500	0.1255	0.0860	3.0080	3.0474	2.4120	2.3726
1000	0.0588	0.0333	3.6196	3.6451	2.7891	2.7636
2000	0.0216	0.0096	4.3039	4.3159	3.2560	3.2440

Table F.3: dQdT results for laminar free convection in a vertical channel with isothermal walls ($r_T = 0.3$, Pr = 0.7)

Ra	$\overline{\mathrm{Nu}}_{12}$	$\overline{\mathrm{Nu}}_{21}$	$\overline{\mathrm{Nu}}_{10}$	$\overline{\mathrm{Nu}}_{01}$	$\overline{\mathrm{Nu}}_{20}$	$\overline{\mathrm{Nu}}_{02}$
0.01	1.0010	1.0010	0.0206	0.0206	0.0206	0.0206
0.1	1.0007	1.0007	0.0213	0.0213	0.0212	0.0212
1	0.9898	0.9890	0.0463	0.0470	0.0455	0.0448
10	0.8649	0.8607	0.3649	0.3691	0.3456	0.3414
100	0.3967	0.3690	1.7103	1.7380	1.5419	1.5142
500	0.1141	0.0833	2.9893	3.0201	2.4994	2.4686
1000	0.0499	0.0312	3.5910	3.6097	2.9139	2.8952
2000	0.0166	0.0090	4.2648	4.2724	3.3783	3.3707

Table F.4: dQdT results for laminar free convection in a vertical channel with isothermal walls ($r_T = 0.5$, Pr = 0.7)

Ra	$\overline{\mathrm{Nu}}_{12}$	$\overline{\mathrm{Nu}}_{21}$	$\overline{\mathrm{Nu}}_{10}$	$\overline{\mathrm{Nu}}_{01}$	$\overline{\mathrm{Nu}}_{20}$	$\overline{\mathrm{Nu}}_{02}$
0.01	1.0010	1.0010	0.0206	0.0206	0.0206	0.0205
0.1	1.0007	1.0007	0.0213	0.0213	0.0212	0.0212
1	0.9896	0.9891	0.0462	0.0467	0.0456	0.0452
10	0.8642	0.8614	0.3616	0.3644	0.3488	0.3460
100	0.3875	0.3691	1.6939	1.7122	1.5818	1.5634
500	0.1006	0.0817	2.9433	2.9622	2.6224	2.6035
1000	0.0404	0.0297	3.5269	3.5376	3.0867	3.0759
2000	0.0123	0.0083	4.1765	4.1805	3.5975	3.5936

Table F.5: dQdT results for laminar free convection in a vertical channel with isothermal walls ($r_T = 0.67$, Pr = 0.7)

Ra	$\overline{\mathrm{Nu}}_{12}$	$\overline{\mathrm{Nu}}_{21}$	$\overline{\mathrm{Nu}}_{10}$	$\overline{\mathrm{Nu}}_{01}$	$\overline{\mathrm{Nu}}_{20}$	$\overline{\mathrm{Nu}}_{02}$
0.01	1.0010	1.0010	0.0206	0.0206	0.0206	0.0206
0.1	1.0007	1.0007	0.0213	0.0213	0.0213	0.0213
1	0.9895	0.9892	0.0461	0.0464	0.0457	0.0454
10	0.8633	0.8616	0.3598	0.3614	0.3521	0.3504
100	0.3815	0.3705	1.6773	1.6882	1.6101	1.5991
500	0.0927	0.0818	2.8998	2.9106	2.7086	2.6977
1000	0.0357	0.0297	3.4628	3.4687	3.2018	3.1958
2000	0.0103	0.0083	4.0907	4.0928	3.7438	3.7417

Table F.6: dQdT results for laminar free convection in a vertical channel with isothermal walls ($r_T = 1$, Pr = 0.7)

Ra	$\overline{\mathrm{Nu}}_{12}$	$\overline{\mathrm{Nu}}_{21}$	$\overline{\mathrm{Nu}}_{10}$	$\overline{\mathrm{Nu}}_{01}$	$\overline{\mathrm{Nu}}_{20}$	$\overline{\mathrm{Nu}}_{02}$
0.01	1.0010	1.0010	0.0206	0.0206	0.0205	0.0205
0.1	1.0007	1.0007	0.0213	0.0213	0.0213	0.0213
1	0.9894	0.9894	0.0459	0.0459	0.0459	0.0459
10	0.8624	0.8624	0.3560	0.3560	0.3560	0.3560
100	0.3747	0.3747	1.6471	1.6471	1.6471	1.6471
500	0.0852	0.0852	2.8148	2.8150	2.8148	2.8150
1000	0.0314	0.0314	3.3460	3.3461	3.3460	3.3461
2000	0.0088	0.0088	3.9331	3.9331	3.9332	3.9332

Appendix G

Finite-Difference Solver for the Parabolic Energy Equation in Turbulent Free Convection: The MATLAB Code

G.1 Forward-Marching Solution Scheme

```
% Read Fluent data file and normalize solution
sort_data;              % See Section G.2
% Initialize
T=zeros(Nx,Ny);
% Boundary conditions
T(1,1:Ny)=1;
T(Nx,:)=rT;
T(:,1)=0;
```

```
% Forward-marching scheme:
for j=2:Ny
    n=1;                    % Iteration counter
    while n<200             % Convergence criterion
        n=n+1;
        Tn=T;
        for i=2:Nx-1
            dX=DX(i);
            b=g(i,j)*(Tn(i+1,j)+Tn(i-1,j))/dX^2;
            c=(rho(i,j)*U(i,j)-gx(i,j))*(Tn(i+1,j)-Tn(i-1,j))/2/dX;
            a=(rho(i,j)*V(i,j)-gy(i,j))/dY+2*g(i,j)/dX^2;
            d=(rho(i,j)*V(i,j)-gy(i,j))*Tn(i,j-1)/dY;
            T(i,j)=(b-c+d)/a;
        end
    end
end
Tx1=(T(2,:)-T(1,:))/dX;                 % Calulcate gradient at walls
Tx2=-(T(Nx,:)-T(Nx-1,:))/dX;
Q1=sum(-Tx1)*dY*0.02865*(T1-T0)         % Integrate q to find Q (walls)
Q2=sum(-Tx2)*dY*0.02865*(T1-T0)
Q0=Q1+Q2                                % Energy balance to find Q0
```

G.2 Importing Fluent Data

```
% Dimensional boundary conditions -- change these for dQdT:
T1=310;
T2=305;
```

```
4  T0=300;
5  rT=(T2-T0)/(T1-T0);
6  % Read Fluent data file:
7  D=importdata('data_Ra=5e+5');
8  D=D.data;
9  % Solution parameters:
10 W=0.1;                    % Characteristic length
11 A=30;
12 mu=2.01e-05;              % Viscosity
13 rho_0=1.1769;             % Density @ T=T_0
14 k=0.02865;                % Conductivity (molecular)
15 Pr=0.707;                 % Molecular Prandtl number
16 Pr_t=0.85;                % Turbulence Prandtl number (energy)
17 U_ref=mu/rho_0/W;         % Ref velocity
18 % Discretization:
19 Nx=100;
20 Ny=3000;
21 % Normalize solution data:
22 D(:,1)=[];                          % Erase cell number
23 D(:,[1,2])=D(:,[1,2])/W;            % Normalize x,y wrt W
24 D(:,3)=D(:,3)/rho_0;                % Normalize rho
25 D(:,[4,5])=D(:,[4,5])/U_ref;        % Normalize u,v
26 D(:,6)=(D(:,6)-T0)/(T1-T0);         % Normalize T
27 % Sort data file by coordinate (x,y):
28 [Z,I]=sort(D(:,2));                 % Sort by y
29 D=D(I,:);
30 [Z,I]=sort(D(:,1));                 % Sort by x
```

```
31 D=D(I,:);
32 clear Z I;
33 % Grid size:
34 dY=D(2,2)-D(1,2);
35 % Sorting data -- nonuniform grids:
36 [Z,I]=sort(D(:,2));                    % Sort by y
37 B=D(I,:);
38 % Grid size -- nonuniform grids:
39 for i=2:Nx                             % Sort by x
40     DX(i)=B(i,1)-B(i-1,1);
41 end
42 DX(1)=DX(Nx);
43 % Generate rho,u,v,1/Pr matricies
44 for i=1:Nx
45     for j=1:Ny
46         rho(i,j)=D((i-1)*Ny+j,3);
47         U(i,j)=D((i-1)*Ny+j,4);
48         V(i,j)=D((i-1)*Ny+j,5);
49         % Effective conductivity:
50         g(i,j)=1/Pr+D((i-1)*Ny+j,7)/mu/Pr_t;
51     end
52 end
53 % Calculate k_eff gradient
54 gx([1,Nx],1)=0;
55 gy([1,Nx],1)=0;
56 for j=2:Ny
57         for i=2:Nx-1
```

```
58              gx(i,j)=(g(i+1,j)-g(i-1,j))/2/DX(i);
59              gy(i,j)=(g(i,j)-g(i,j-1))/dY;
60          end
61      end
```